Design of polarimeters based on liquid crystals and biaxial crystals for polarization metrology

by Alba Peinado Capdevila

To obtain the title of PhD in Physics

Universitat Autònoma de Barcelona

Bellaterra, September 2014

Don Juan Campos Coloma, Catedrático de Óptica de la Universitat Autònoma de Barcelona y don Angel Lizana Tutusaus, Investigador Postdoctoral de la Universitat Autònoma de Barcelona

CERTIFICAN

Que Doña Alba Peinado Capdevila, graduada en Física, ha realizado bajo su dirección y en el Departamento de Física de la Universitat Autònoma de Barcelona, el trabajo "*Design of polarimeters based on liquid crystals and biaxial crystals for polarization metrology*", que se recoge en esta memoria para optar al grado de Doctor en Física.

Y para que conste, de acuerdo con la legislación vigente, firman este certificado en Bellaterra, a 23 de septiembre de 2014.

Prof. Juan Campos Dr. Angel Lizana

Als meus pares, la Carme i el Miguel,

i a les meves germanes, la Laura i la Marina.

Agraïments / Acknowledgments

Jo que sóc de família muntanyenca, he viscut aquests quatre anys de doctorat com si hagués estat pujant una imponent muntanya.

Comences molt il·lusionada i amb una ruta relativament planificada. A mesura que vas pujant van sorgint imprevistos, però amb un bon equip d'expedició es van trobant solucions i rutes alternatives. En aquest equip, hi ha excursionistes veterans amb una gran i valuosa experiència muntanyenca, la qual admires i intentes nodrir-te d'ella, i d'altres més novells amb una empenta i il·lusió contagiosa. A més a més, pel camí et vas trobant gent ben diversa però amb un sentiment comú, la passió per la muntanya: els que ja baixen et donen consells pràctics del tram que et queda, i els que pugen comparteixen amb tu esbufecs i paraules d'ànims mutus, fins i tot potser fas algun tram conjuntament. És veritat que a mesura que puges les forces van disminuint, però les vistes són cada cop més espectaculars i l'esperit de superació et dóna força per continuar fins al cim. Un cop a dalt, inspires profundament i gaudeixes de la bellesa del lloc on et trobes, amb una satisfacció personal per l'esforç esmerçat que costa de descriure amb paraules. Al cap d'una estona, reprens el camí de tornada, més cansada però feliç, feliç d'haver fet cim. De baixada et sorprens sent tu la que dóna consells als que pugen. Un cop a baix, mires enrere i absorbeixes els últims instants de l'experiència viscuda i desitges arribar a casa per compartir-la amb els teus.

Moltes gràcies als que heu format part de l'equip d'expedició, als excursionistes que m'he trobat pel camí i als que m'espereu a casa pel vostre suport. Tots heu fet possible aquest somni.

En primer lloc m'agradaria deixar constància del meu profund agraïment als meus directors de tesi, al Dr. Juan Campos i al Dr. Angel Lizana.

Al Dr. Juan Campos per haver-me donat l'oportunitat de realitzar el doctorat sota la seva direcció, per la seva gran dedicació i entrega, per haver confiat en mi, per tenir sempre la porta oberta per resoldre qualsevol dubte que tingués i pels coneixements que m'ha transmès.

Al Dr. Angel Lizana, per contagiar-me el seu positivisme i pel suport que m'ha donat en tot moment, com a company de despatx, com a director de tesi i sobretot com amic.

A la Dra. María J. Yzuel, per compartir la seva experiència, per la seva proximitat i pels seus inestimables consells tant a nivell professional com a nivell personal.

Als coautors dels articles que formen aquesta tesi. A tots aquells amb qui he treballat al laboratori, amb els que he analitzat els resultats que he anat obtenint i amb qui he compartit i gaudit hores de docència i de divulgació de l'Òptica; per la seva dedicació i per contribuir en la meva formació com a investigadora i docent. Al Dr. Claudio Iemmi, al Dr. Ignacio Moreno, al Dr. Andrés Márquez, al Dr. Asticio Vargas, al Dr. Juan Carlos Escalera, al Dr. Jordi Mompart, al Dr. Todor K. Kalkandjiev, al Dr. Francesc Pi, al Dr. Jose Luis Martínez, a l'Alex Turpin i a l'Estefania Fernández.

A tots els professors i estudiants de doctorat del grup d'Òptica, per fer-me sentir com a casa. En especial, als meus companys de despatx, per tots els bons moments que hem passat junts i pels moments més complicats en que han estat al meu costat. A l'Angel i al Josep, per fer que la meva entrada al grup fos tan agradable, per la seva cura de germans grans a porta tancada, i perquè amb el temps m'han fet partícip del seu cercle. Al Josep, per tenir un paper important a l'inici i la fi d'aquesta etapa. A la Irene per portar alegria al despatx i al Claudio per estar sempre disposat a ajudar.

Als quàntics, per complementar-nos als clàssics, a l'Albert, al Ricard, al Dani, a l'Alex, al Juan Luis i al Joan, per les hores compartides, pelis, dinars, alguna classe de spinning, i bastants cafès.

To Prof. Russell Chipman for giving me the opportunity to learn from his knowledge. To all Polarization Laboratory members for their support: Dr. McClain, Dr. Crabtree, Stacey, Christine, Tiffany, Paula, Lena and Brian. Also to all my friends who were my tucsonian family and took care of me: Johanna, Stacey, Eduardo, Guillaume, Jessica, Anael, Laura and Zach.

To Prof. Bahram Javidi, for giving me the opportunity to stay in his laboratory. I am very thankful to my labmates and friends for their warmth during my time in Connecticut: Xiaoxi, Xin, Chen, Jingang, Kaleel, Xiao, Carolina, Covi and Archna.

A la Celia Martínez, Montse Galán, Francesc Poblet i Rafael Moraira, per donar-me el suport necessari en tasques administratives i tècniques.

Als meus amics de la carrera, al Sebastià, al Dani, al Sergi, a l'Albert, a l'Alberto, al Guillem i al Jordi, per tots els dinars, hores al SAF, sortides a la muntanya, per cuidar-me, i sobretot per les seves paraules de suport i d'ànim durant aquest últim tram. A la Sabina i a la Irene, pels sopars de retrobada. Al Cristian, perquè sempre l'he sentit al meu costat.

A les meves companyes i professores de flamenc, per posar color als meus dilluns i dimecres.

A la Laura, per ser una amiga tan especial, per saber el que dir-me en tot moment i per les innumerables vivències compartides i les que vindran.

A les meves amigues i amics de Sant Cugat, a l'Elena, la Sílvia, la Cris, la Mire, la Júlia Costa, la Júlia Mateos, l'Amaya, l'Albert i l'Ignasi, per tot el que he compartit amb elles i ells, per haver-me fet costat sempre, per les innumerables trucades telefòniques i perquè em fan sentir especial i estimada.

A la meva família, pel seu amor incondicional i pel seu suport. Als meus padrins, per les seves converses. A les meves tietes, tiets i cosins, per ser una família tan unida i per la seva visita a Arizona. A les meves germanes, per ser com són, úniques i per com em complementen. Als meus pares, per la seva estimació, per ser el meu model i...

... per transmetre'm la passió per la muntanya.

This work has been financed by the following research projects:

i) Advanced techniques of optical metrology. Application of liquid crystal modulators. FIS2009-13955-C02-01. Ministerio de Ciencia e Innovación

ii) Development of systems and methods for surface metrology and polarimetric characterization based on liquid crystals modulators. FIS2012-39158-C02-01. Ministerio de Economía y Competitividad

A. Peinado thanks the Ministerio de Ciencia e Innovación for the grant "*Formación Personal Investigador*" (FPI) BES-2010-031696.

Contents

Abstract

Polarimetry provides crucial information in many applications in diverse fields, including medicine, biology, remote sensing, material characterization, astronomy, etc. Polarimeters are the basic instruments for polarization metrology. Several polarimeters architectures have been analyzed in the literature, each one presenting its own drawbacks and strengths. In general, the parameters of the polarimeter set-up are optimized in order to reduce the amplification of noise present at the radiometric measurements to the final polarization measurement. Moreover, experimental errors, as misalignment or miscalibration, lead to a polarimeter accuracy reduction to the measure of such polarization content. Recently, liquid crystal (LC) devices have been introduced in polarimeters architectures, taking advantage of their appealing features of changing their optical properties dynamically and at high rates. Because architectures based on LC have no moving parts, experimental errors related to mechanical movements are avoided, and those due to misalignments may be significantly reduced after a calibration of the whole system.

This thesis is framed in the field of polarimetry, focusing on the optical design, optimization, analysis and comparative of polarimeters based on materials presenting index anisotropy. In particular, it reviews some existing LC based polarimeter architectures popular in the literature, introduces some variants to those polarimeter layouts in order to improve some aspects in their performance such as noise minimization, and presents new designs of LC based polarimeters. In particular, we use three different types of LC cells: parallel aligned nematic, twisted nematic and ferroelectric. Moreover, it presents a new static polarimeter able to measure any state of polarization. This last architecture is based on the conical refraction (CR) phenomenon occurring when light propagates along one of the optical axes of a biaxial crystal.

For each polarimeter prototype we conduct a comprehensive analysis of its design, including a noise optimization, robustness study, tolerance analysis, as well as we detail the implementation of the polarimeter, including its experimental calibration and measurements. A comparative between the different implemented prototypes is conducted, giving a very valuable review of the main features of LC based polarimeters as well as the CR based polarimeter.

From this comparative, the best candidate for imaging polarimetry is selected. Finally, in this thesis it is proposed a new experimental configuration which combines an imaging polarimeter and a module used to achieve sub-pixel-resolution imaging in a system where the resolution is limited by detector pixel size. Crucial experimental results are provided, validating the resolution enhancement achieved in polarization images.

Chapter 1 **Introduction**

This introductory chapter defines the framework of the current thesis and reviews the state of art of the particular research field. In order to motivate the development of polarimeters, a summary of the principal applications of these instruments is given, including diverse fields such as biomedicine, remote sensing, astronomy and material characterization. Following, an overview of the different types of polarimeters is provided. Afterwards, we introduce the main materials to be used in the design of the polarimeters explained in next chapters of this thesis: liquid crystals and biaxial crystals. First, a general description of liquid crystals is given, focusing later on the main liquid crystals types commonly used in polarimeter designs. Second, the biaxial crystals are reviewed, and the conical refraction phenomenon occurring on such materials is explained in detail. Finally, the main goals of this thesis are exposed and the structure of this thesis is detailed.

Light is characterized by its fundamental properties: intensity, frequency, coherence and polarization. Light polarization describes the transverse nature of electromagnetic waves, indicating how their electric and magnetic field vectors are orientated [1,2]. The polarized behavior of light was first reported in 1669 by Erasmus Bartholinus who observed the double refraction of light in calcite crystals [3]. Since then, several scientists have focused their research in polarimetry, the science of measuring the polarization state of a light beam and how this polarized light is altered and manipulated by optical elements or matter interactions [4]. Indeed, the analysis of the interaction of light with matter in terms of polarization provides valuable

information related to the optical features of the material, such as index of refraction, retardance, diattenuation or depolarization. Over the years, polarization metrology has been widespread used in many and diverse research fields [5–50], ranging from the monitoring of cells to the detection of extra-solar planets. In the following section 1.1, a summary of the main applications of polarimetry is provided.

Due to the great interest of polarization data in such applications, research and development of polarimeters (i.e. the basic instruments for polarization metrology) are still very active with the aim of improving the robustness of their performances, as well as their accuracy, resolution, architecture simplicity, measurements speed, among others technical features.

Section 1.2 gives a general overview of the different types of polarimeters. In particular, polarimeter architectures with no moving parts are very attractive for many applications because these architectures avoid experimental errors associated to systems with rotating elements, such as orientational misalignment or beam wander. With this goal, some works have proposed to use liquid crystal cells as dynamically varying polarization controllers in the polarimeter layout. In addition, liquid crystal based polarimeters operate at high rates, very appealing feature for applications requiring short-term measurements. Under this scenario, a thorough study of polarimeters based on liquid crystals becomes very significant.

This thesis presents an exhaustive analysis of different polarimeters based on liquid crystals cells. In particular, they are based on three types of liquid crystals: parallel aligned nematic, twisted nematic and ferroelectric. Moreover, we include a new design of static polarimeter based on the conical refraction phenomenon occurring when light travels along one of the optical axes of a biaxial crystal. Liquid crystals and biaxial crystals features are revised in section 1.3 and 1.4, respectively. Following, the main goals of this thesis are given in section 1.5. Finally, the structure of this thesis is detailed in section 1.6.

Most of the scientific contributions included in this thesis are of interest in the scientific community, so they have been disclosed through different international journals in the field of Optics [PAPER A - PAPER F], as well as through a number of international conferences. In addition, the current thesis has also give rise to the application of a patent [PAPER G].

1.1 Polarimetry applications

Polarimetric techniques are widespread used in many research fields, where the knowledge of the state of polarization of light beams or the polarizing properties of samples is

essential. Following, we review some examples of the main applications of polarimeters grouped in four fields: biomedicine, remote sensing, astronomy and material characterization.

- *Biomedicine:*

The use of polarimetric approaches for biological tissue assessment has recently received considerable attention not only for enhancing image contrast, but also because the intrinsic tissue polarimetry characteristics contain a wealth of morphological and functional information of potential biomedical importance [5,6]. Imaging polarimeters described in [7,8] are used to image the living human eye, specifically they measure spatially polarization properties at the retina plane. Significant differences in degree of polarization between normal and glaucoma affected eyes are measured in [9]. Moreover, polarimetric imaging is studied as a tool for cancer diagnosis and determining the stage of the disease, including cervical cancer [10,11], human colon cancer [12,13] and skin cancer [14,15]. Experimental studies on the application of polarization-scattering techniques to the physiological monitoring of cells, bacteria and other microorganism are widely described in the literature [16,17]. Another appealing application of polarimeters is to measure the optical activity of certain solutions with chiral molecules, such as glucose. There are some works related to the development of a noninvasive optical polarimetry sensing systems to monitor in vivo glucose concentrations [18,19], very promising technique for diabetic patients.

- *Remote sensing*

Polarimetry is used as an important remote sensing technique which complements spectroscopic and hyperspectral imaging, offering additional information related to the surface features, shape, shading and roughness [20,21]. For instance, in [22] they illustrate that retardance orientation and diattenuation orientation provide a clear indication of the shape of the surface. Moreover, in [23] they differentiate manmade objects with natural backgrounds due to the different polarization signatures. The polarization distribution of diverse scenes have been investigated, such as vegetation and soil [24], forest [25], oceans [26], and skies [27]. In addition, the study of linear polarization in more traditional lidar remote sensing systems provides information about the presence of ice in clouds or non-spherically shaped dust particles in the atmosphere [28,29]. Recently, some studies have shown how adding polarimetric data in a hyperspectral infrared (IR) camera can more effectively detect partially exposed anti-personnel mines [30].

- *Astronomy*

The polarization study of celestial objects is a valuable part of optical astronomy [31]. For instance, a very high sensitive polarization measurement of the Sun was reported in [32]. In

[33], a polarimeter for a stratospheric mission in Antarctica was designed for analyzing polarimetric data from the incoming light through the telescope, related with the magnetic fields in the Sun via de Zeeman effect. One way of investigating the structure of the interstellar magnetic field is to measure the linear polarization of starlight with high accuracy [34,35]. Additionally, polarimetry is a powerful technique for extra-solar planet detection because radiation is generally polarized by the molecules of the planetary atmosphere in contrast with the unpolarized background radiation [36–38]. A novel way to measure the distance to external galaxies, including supernovae, was proposed in [39] using polarimetry.

- *Material characterization*

Ellipsometry is a polarimetric technique which uses the change in the polarization state upon reflection or transmission to characterize the complex refractive index of surfaces and interfaces, and refractive indices and thicknesses of thin films [40–42]. The recent development of "generalized ellipsometry" uses Jones matrix or Mueller matrix measurements to determine the optical properties of more general anisotropic structures such as birefringent crystals and polarizing films [43–45]. Polarimetric characterization of liquid crystal modulators has been reported in [46–48], in order to optimize such devices as phase-only or amplitude-only modulators. An imaging polarimeter is implemented in [49] for characterization of strain in transparent crystals in the near IR range. Also, polarimetry plays an important role for determining the polarization-mode dispersion in optical fibers [50], critical parameter as it leads to system performance degradation.

1.2 Polarimeters

Polarimeters are the basic instruments for polarization metrology. Basically, they determine the polarimetric information by means of radiometric measurements when analyzing the light beam with polarizing elements. The mathematical formulation of the measurement principle of a polarimeter is described in depth in next chapter (section 2.2). However, in this section we provide a general overview of the different types of polarimeters.

Polarimeters can be sub-divided into different categories depending on their specifications [4], for instance, by the type of information that they provide, by the methodology used to acquire the measurements, by the specific characteristics of the polarimeter constituent elements or by the spectral range analyzed, among others. Regarding the specification requirements imposed by a given application in which the instrument will be used (such as velocity, spectral data, cost, accuracy and area of measurement), a particular type of polarimeter will be the best suited for

such application. Let us review the different categories and illustrate them with some examples present in the literature.

- *Light-measuring polarimeters and sample-measuring polarimeters*

Light-measuring polarimeters determine the state of polarization (SOP) of a light beam. Thus, they characterize the polarization parameters defining the polarization ellipse [1] (azimuth and ellipticity), as well as the degree of polarization. In the literature they are well-known as Stokes polarimeters (due to any SOP can be described by a Stokes vector [1]). The light-measuring polarimeter is composed by a set of polarizing elements (typically retarders), followed by a polarizer and the detector, which takes flux measurements. This set of elements is known as polarization state analyzer (PSA). The light is analyzed by the PSA in different configurations (for instance different orientations of a rotating waveplate or different retardances introduced by a variable retarder), leading to different flux measurements. The different configurations of a PSA are called polarization analyzers (PAs) because they are analyzing particular polarization components in the incident beam. Some examples of light-measuring polarimeters are given in [51–64].

Sample-measuring polarimeters describe how a light beam changes its polarization due to an interaction with a sample. It refers to a general light-mater interaction, including transmission, reflection, diffraction or scattering. Hence, the instrument determines the polarizing properties of the sample, such as depolarization, polarizance, diattenuation and retardance [1]. In the literature they are well-known as Mueller polarimeters (due to any sample can be described by a Mueller matrix [1]). It consists of a polarization state generator (PSG), which controls the input polarization to the sample and a PSA which analyzes the output polarization, finally the radiometer or camera which takes the flux measurements. There are numerous examples of sample-measuring polarimeters [7,13,65–72].

- *Complete and incomplete polarimeters*

A light-measuring (sample-measuring) polarimeter is complete when the Stokes vector (Mueller matrix) is fully determined. On the contrary, it is said incomplete when only a part of the whole polarimetric information is available. A typical example of incomplete light-measuring polarimeter is a rotating linear polarizer in front of the detector. This architecture only allows measuring the azimuth of the incident beam, but no information about the ellipticity can be obtained. This type of polarimeters is attractive for its simplicity to applications focused on the linear polarization content [51,53,56,73].

- *Punctual and imaging polarimeters*

When the Mueller (Stokes) polarimeter uses a punctual detector to take flux measurements, the polarization information is related to a particular position of the sample (beam) analyzed. This type of polarimeter is suitable when homogeneous samples (or uniform beams) are of interest. When there is a small spatial variation on the polarization properties of the sample (beam) under study, and the light coming from that area is averaged by the detector (due to the detector sensor always has some finite area), it will lead to a measurement with certain content of depolarization. This issue needs to be considered as a source of spatial effective depolarization when using punctual polarimeters. Nevertheless, when dealing with samples (beams) presenting significant polarization spatial distributions, an imaging polarimeter is required. This instrument uses a camera as a detector, allowing us to measure the flux distribution pixel by pixel, and consequently to characterize the polarization distribution, with a given spatial resolution, along the whole area imaged at the camera sensor.

- *Wavelength and incidence angle dependence*

Polarization parameters of samples depend on the wavelength used during the measurement as well as to the incident angle selected. For this reason, different polarimeters working at different spectrum ranges are designed, such those devised for the visible [70], infrared [74,75] or vacuum-ultraviolet [76]. Some polarimeters take the measurement for a particular wavelength and others provide the Stokes vector (Mueller matrix) spectra [59].

Moreover, some Mueller polarimeters include two microscope objectives of large aperture (in the PSG and in the PSA), in order to obtain the Mueller matrix for different incident angles [45]. Other architectures utilize mechanical arms to vary the angular position of the PSG and PSA systems, leading to polarimetric measurements for different angles of incidence. This information is crucial for applications measuring anisotropic materials, such in [45] where the dielectric tensor is characterized, as well as to minimize the effect of mathematical correlations between parameters when performing optical models based on experimental data [42].

1.2.1 Polarimeter architectures

Several architectures using different types of polarizing elements can be designed as polarimeters. The goal of all architectures is to be able to determine the polarimetric data (Stokes vector or Mueller matrix) by projecting the light beam with different configurations, leading to different flux measurements. How we project the light over these configurations, and consequentially, how we obtain the different flux measurements, is what we are classifying here. Polarimeter architectures can be grouped in three main categories, depending on the method by

which the flux measurements are acquired. For the sake of simplicity, we will mostly focus on Stokes polarimeters (i.e. PSAs). Nevertheless, architectures described below can be extended to Mueller polarimeters by including a PSG with similar characteristics to the PSA (traditionally, PSG uses the same elements as the PSA but in inverse order, although hybrid systems could be also designed).

- *Division of amplitude*

The polarimeter has some elements (typically beam splitters) dividing the amplitude of the entire incident light beam into sub-beams and next, the different sub-beams are analyzed in parallel with their corresponding polarization analyzers and detectors. In this way, this polarimeter architecture allows measuring the flux measurements simultaneously, leading to a snapshot polarimeter, suitable for measuring time-varying polarization beams. An accurate alignment of the detectors is important to ensure that all detectors are analyzing the same point in the space (punctual polarimeter), or that the raw images obtained by the cameras are well aligned and coincide pixel by pixel (imaging polarimeter).

There exist different designs of amplitude division polarimeters. A traditional division of amplitude polarimeter architecture uses beam splitters (B-Ss) to split the light beam. For instance, in [77] by means of a B-S and two cameras, a polarimeter to sense two orthogonal states of polarization was designed; in [57] three polarizing B-S were used to simultaneously analyze four sub-beams; or in [64] an appropriately coated B-S, whose optical parameters are optimized, and two Wollaston prisms are used in the polarimeter layout. Another example is the four-detector polarimeter [55,61], where light beam strikes four detectors in sequence. Moreover, diffraction gratings are used in polarimeters designs in order to split a single incident beam into multiple sub-beams [62], in particular polarization gratings introduce a polarization dependence to the different diffraction orders [52,60]. In [59], a polarimeter uses a planar dielectric slab to produce multiple internal reflections within the slab, resulting in a set of parallel outgoing beams which are simultaneously analyzed.

- *Division of wavefront*

The polarimeter analyzes different parts of a wavefront with separate polarization elements, operating side by side. This type of architecture also constitutes a snapshot polarimeter, since all measurements are taken simultaneously, ensuring that time is not a dependent factor in the result. The reduction in resolution of the detector by the number of different polarization elements and the spatial displacement of information within the polarization element pattern are disadvantages.

Different examples of wavefront-division polarimeter are present in the literature. A typical example is a polarimeter using a pattern of micro linear polarizers in front of the imaging sensor, leading to an incomplete polarimeter for linear polarization metrology. In such systems, the polarization is calculated for defined macropixels, which contain a set of micropolarizers (typically 4 polarizers orientated at 0º, 45º, 90º and 135º). In [56] they use a wire-grid polarizer array fabricated on a separate substrate, whereas in [51] it is directly set on the sensor. An alternative using birefringent crystals as micropolarizers is described in [53]. A complete Stokes polarimeter is built in [78], where two layers of patterned liquid crystal polymer are used.

- *Division of time*

The polarimeter takes flux measurements sequentially in time. In this way, the architecture generally uses a single detector. When designing this type of architectures, fast polarization modulators are desired to avoid false polarization artifacts due to polarization variations during flux measurements.

A first group of division of time polarimeters uses rotating polarization elements to take the different flux measurements. Numerous polarimeters are based on a rotating retarder with fixed polarizer. In [79,80], four rotation angles of the retarder are selected. Whereas in [66,81], it is described a Mueller polarimeter with two retarders which are continuously rotating at given frequencies, leading to a modulated output flux which is Fourier analyzed to determine the polarization parameters. Mechanically rotating elements may cause vibration and beam wander, and ultimately limit the maximum speed at which measurement can be acquired. Beam wander can result if there is a wedge in the rotating element or if the element wobbles in any senses, and a special care needs to be addressed in such systems [82].

A second group of division of time polarimeters incorporates active polarization elements (i.e. electrically addressable polarization controllers), constituting an interesting alternative to mechanical polarimeters. Several examples are present in the literature, such as architectures based on photo-elastic modulators [58,65,83], Pockels cells [71,72], Faraday cells [63], and liquid crystal cells. A review of polarimeters based on liquid crystals is given in next section, after introducing the different types of liquid crystals.

1.3 Liquid crystals

Liquid crystals (LCs) [84,85] describe a distinct state of matter that has properties observed between the crystalline solids and the isotropic liquids. A distinguishing characteristic of LC state

is the tendency of the constituent molecules to point along a common axis, called the director. This structure is in contrast to molecules in the liquid state which have no intrinsic order, and to molecules in the solid state which are highly ordered. LCs can show in different intermediate states between these two matter states, called mesophases. Liquid crystals were reported for the first time at the late 19th century by Friedrich Reinitzer [86], who discovered a strange material that exhibited a mesophase between solid state and liquid state.

The LC constituent molecules exhibit a high degree of shape anisotropy: rod-like (calamitic) or disk-like (discotic) [84]. We will focus of calamitic (rod-like) LC because of their importance in LC based technology.

Because of the ordering of calamitic molecules, LC exhibits a uniaxial symmetry (i.e. the axis of symmetry is parallel to the axis of the molecules, the LC director) which manifests itself in many other ways, such as dielectric anisotropy and optical anisotropy.

As a consequence of this uniaxial symmetry, the dielectric constant along the long axis ($\varepsilon_{\parallel}$) differ from the dielectric constant perpendicular to it ($\varepsilon_{\perp}$). The dielectric anisotropy is defined as follows:

$$\Delta\varepsilon = \varepsilon_{\parallel} - \varepsilon_{\perp} \ . \tag{1-1}$$

As consequence of the dielectric anisotropy described above, the LC molecules vary their orientation when applying external fields. Mostly commonly, LC exhibits a positive dielectric anisotropy, resulting in a tendency of the LC molecules to align parallel to the electrical field.

Moreover, LC molecules also exhibit optical anisotropy. The extraordinary refraction index, n_e, is experienced by light with polarization parallel to the long molecular axis, whereas ordinary refraction index, n_o, is experienced by light with polarization perpendicular to the long molecular axis. In this way, the birefringence (or optical anisotropy) is defined as:

$$\Delta n = n_e - n_o \tag{1-2}$$

For polarized light impinging at the LC cell at an angle θ to the long molecular axis, the effective birefringence is calculated by taking into account the effective extraordinary refraction index, $n_e(\theta)$, using the following expression [84]:

$$\frac{1}{n_e^2(\theta)} = \frac{\cos^2\theta}{n_e^2} + \frac{\sin^2\theta}{n_o^2} \tag{1-3}$$

The ability to realign LC molecules with an external field enables to manipulate the effective birefringence and ultimately, to modify dynamically the polarization of light beams, which is the basis for most liquid crystals based optical technology.

1.3.1 Types of liquid crystals

According to the physical parameters responsible for driving the mesophase transition in a LC, they can be divided into thermotropic and lyotropic phases. Thermotropic LCs are dependent on temperature variations. Whereas lyotropic LCs are dependent on both temperature and concentration of the LC molecules in a solvent. This last group is very important in biology but as they are not commonly used for manufacturing LC cells and displays, suitable to be present in polarimetric applications, lyotropic LCs will not be here discussed as they are out of the scope of this thesis.

The typical phase sequence of calamitic thermotropic liquid crystals as the temperature increases is represented in Figure 1-1.

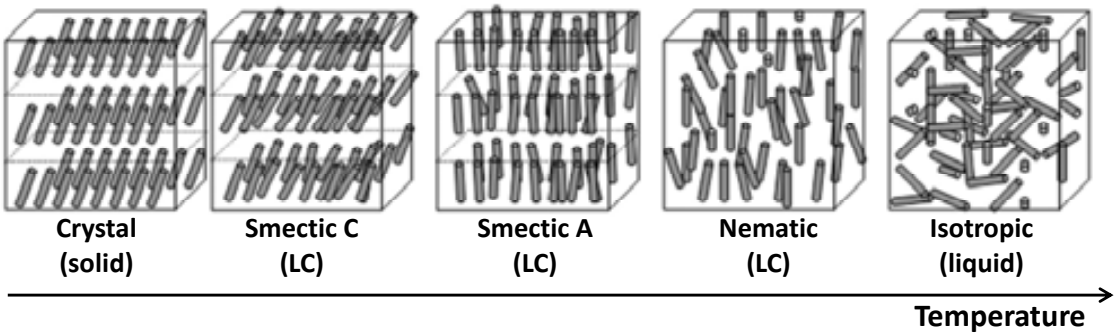

Figure 1-1: Phase sequence from the crystalline phase to the isotropic liquid for a thermotropic calamitic liquid crystal [85].

The isotropic liquid phase does not have either positional or orientational order. The nematic phase lacks positional order although there is a long-range orientational order, characterized by the LC director defining the average direction of the ensemble molecules. The smectic A phase besides the orientational order, characterized by the LC director, the molecules have partial positional order forming a layered structure. In particular, LC director is perpendicular to the layers. The smectic C phase has the same structure as smectic A phase, but LC director is no longer perpendicular to the layer but tilted. Finally, crystal solid phase has both positional and orientational orders.

Following, we explain in detail the structure of the three main LC types used in polarimeter architectures, as well as we provide the mathematical model describing the polarization properties of such LC cells. Specifically, two nematic LC cells whose internal structure depends on the surface anchoring conditions on the cell walls, and a smectic C LC with chiral molecules.

1.3.1.1 Parallel aligned nematic LC

A parallel aligned nematic liquid crystal (PA-LC) cell consists of nematic LC sandwiched between two glass substrates, and the molecules anchored in both substrates are parallel aligned. In this way, in absence of external field, the LC molecules lie parallel to the glass substrates (see Figure 1-2(a)). Thus, light impinging the LC cell in such condition sees the molecules arranged as the one plotted in Figure 1-2(c), where the extraordinary and ordinary refraction indices are perpendicular to the light propagation direction. Therefore, the effective birefringence is maximum, achieving a maximum of retardation. When an external field is applied, LC molecules start to tilt in direction of the electrical field. In this way, the effective birefringence is reduced, achieving a smaller retardance. In Figure 1-2(b) we show the particular case when internal molecules are completely aligned to the electric field, corresponding to a high voltage. Under this scenario, light going through the LC cell finds the molecules distributed as the one plotted in Figure 1-2(d), where light only sees the ordinary refraction index independent of its polarization (i.e. light propagates along the molecules optical axis). Therefore, in the ideal case where the light sees all LC molecules oriented as that plotted in Figure 1-2(d), the system acts as an isotropic material, and so, the birefringence is null, and zero retardance is obtained. However, in the real case, even for the highest voltage addressed, the molecules at the surface are pinned at the alignment layer and they are unable to rotate freely, as sketched in Figure 1-2(b). As a result, a residual retardance at high voltage is always present.

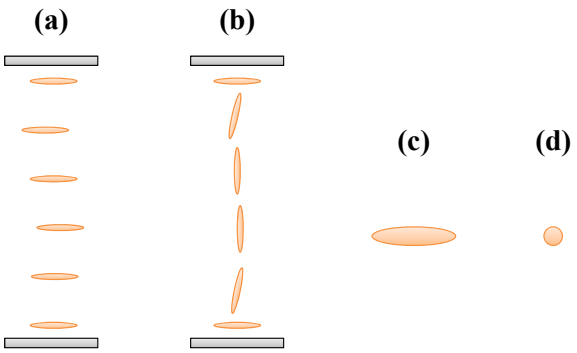

Figure 1-2: PA-LC cell showing molecules arrangement (a) without and (b) with a high voltage addressed. LC molecule orientation at the perpendicular plane to the light propagation direction: (c) without and (d) with a high voltage addressed.

Therefore, a PA-LC can be modeled as a linear retarder with variable retardance, tunable with the voltage applied to the cell. The Mueller matrix describing a linear retarder [1] depends on the orientation of the fast axis (θ) and the retardance (δ):

$$M_{LR}(\delta,\theta)=\begin{pmatrix}1 & 0 & 0 & 0\\ 0 & \cos^2 2\theta+\cos\delta\sin^2 2\theta & (1-\cos\delta)\sin 2\theta\cos 2\theta & -\sin\delta\sin 2\theta\\ 0 & (1-\cos\delta)\sin 2\theta\cos 2\theta & \sin^2 2\theta+\cos\delta\cos^2 2\theta & \sin\delta\cos 2\theta\\ 0 & \sin\delta\sin 2\theta & -\sin\delta\cos 2\theta & \cos\delta\end{pmatrix}, \quad (1\text{-}4)$$

where the orientation of the PA-LC cell is constant, and retardance is a non linear function of the applied voltage and needs to be calibrated.

1.3.1.2 Twisted nematic LC

A twisted nematic liquid crystal (TN-LC) cell consists of nematic LC sandwiched between two glass substrates, and the molecules anchored in both walls are defining an angle, called twist angle (α). In absence of external electrical field, LC molecules are parallel to the surface substrates, although internal LC molecules twist at a constant rate from the bottom to the top of the cell due to the anchored molecules, as shown in Figure 1-3(a). Generally, the twist angle is about 90º. When an electrical field is applied to the cell, the internal molecules tilt as they tend to align parallel to the electrical field, as shown in Figure 1-3(b).

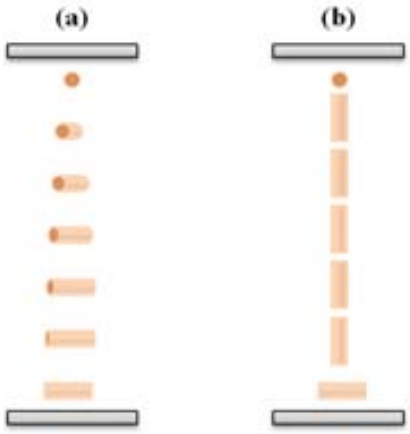

Figure 1-3: TN-LC cell, with a twist of 90º, showing molecules arrangement (a) without and (b) with a high voltage addressed.

A simple model of a TN-LC cell given in [87] describes the LC cell as a stack of thin uniaxial crystal layers, presenting a uniform optical axis direction in each sublayer. The direction of the optical axis changes by a small angle between adjacent layers, following the twist structure. Each layer can be represented by a Jones matrix, and the overall Jones matrix describing the whole system is the result of the cascade product of the individual Jones matrices, leading to the following expression:

$$M_{TN-LC}(\alpha,\beta)=e^{-i\beta}\cdot R(-\alpha)\cdot M(\alpha,\beta)\ , \quad (1\text{-}5)$$

where R is the 2x2 rotation matrix and the matrix M is given by:

$$M(\alpha,\beta)=\begin{bmatrix} X-iY & Z \\ -Z & X+iY \end{bmatrix} \tag{1-6}$$

where $X=\cos(\gamma)$, $Y=\beta\sin(\gamma)/\gamma$, $Z=\alpha\sin(\gamma)/\gamma$ and $\gamma^2=\alpha^2+\beta^2$. The twist angle of the molecules is α, and the birefringence parameter, β, is defined as function of the thickness of the display d, the incident wavelength λ, and the difference between the extraordinary and ordinary indices of refraction for the LC molecules Δn:

$$\beta=\pi d\Delta n/\lambda \ . \tag{1-7}$$

The birefringence parameter β takes its maximum value when no voltage is applied. In fact, under the effect of an external field, LC molecules tilt and the effective birefringence parameter becomes dependent of the voltage, given by $\beta(V)=\pi d\Delta n(V)/\lambda$, where $\Delta n(V)$ decreases as the voltage increases. In general, the LC director at the input surface is not orientated parallel to the vertical of the laboratory, and the matrix of Eq.(1-5) needs to be rotated a given angle (φ_D). Consequently, the TN-LC cell is modeled with a Jones matrix using three physical parameters: twist angle (α), maximum birefringence parameter (β) and the orientation of the molecular director at the input face (φ_D). In [88], an experimental procedure for calibrating these three parameters is described. Moreover, there exist more complex models of a TN-LC cell [89,90], where they take into account the effect of the pinned molecules at the glass substrates. As final remark, the overall TN-LC system corresponds to an elliptical retarder, whose eigenvectors are elliptical states of polarization [91,92].

1.3.1.3 Ferroelectric LC

A ferroelectric liquid crystal (FLC) employs a smectic C phase with chiral molecules (denoted as SmC*). A molecule is chiral if it is not identical to its mirror image. SmC* phase is analogous to the smectic C phase depicted in Figure 1-1, although there is a gradual change in the direction of the molecular tilt describing an helix, as represented in Figure 1-4(a). The LC director describes a rotation on the surface of a cone defined by the normal to the smectic layers (z axis) and with a tilt angle ($\alpha/2$). There is a spontaneous polarization in the direction given by the vectorial product z x n, where z is the normal to the smectic layers and n is the tilted LC director. Nevertheless, due to the helical structure of the LC bulk form, the local polarization is cancelled on the macroscopic scale. Under external electric field in the direction perpendicular to the surface, the local polarization P is aligned to the field direction, thus the helical structure is unwound, as depicted in Figure 1-4(b). The spontaneous polarization will no longer be a local property but a macroscopic polarization will appear. When reversing the electrical field, the spontaneous polarization is reversed as well, leading to a second configuration represented in

Figure 1-4(c). Therefore, when applying an alternating electric field, the FLC cell has two stable states, in which the LC director is set at two orientations with a relative angle of α.

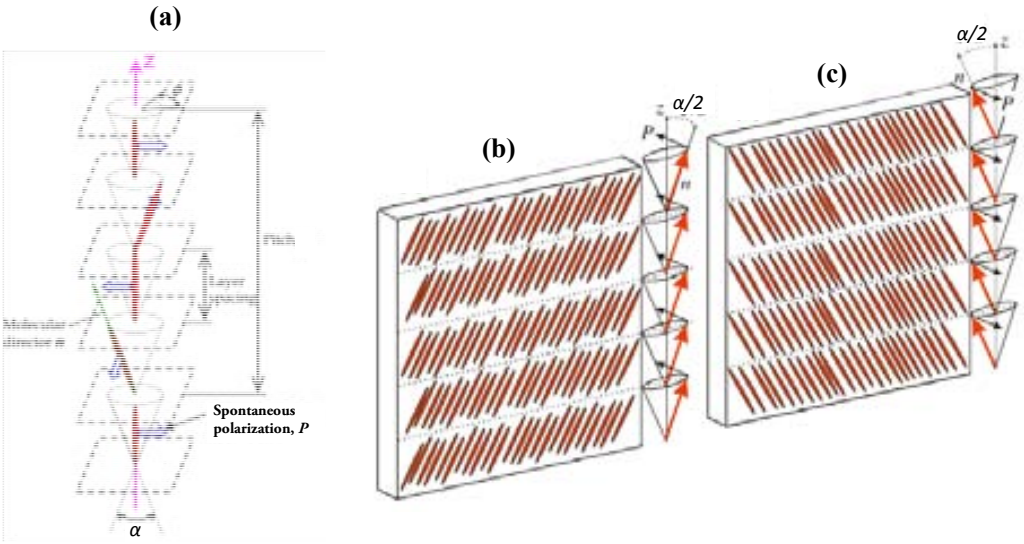

Figure 1-4: Ferroelectric LC when applying : (a) no voltage (helical bulk state), (b) +V (first stable state), and (c) –V (second stable state). *P* is the spontaneous polarization and *n* the LC director [48,93].

In this way, a FLC cell can be modeled as a linear retarder of a given retardance δ and two switchable orientations (θ and $\theta+\alpha$), given by the Mueller matrix M_{LR} of Eq.(1-4). The retardance is constant and depends on the birefringence of the LC molecules, as well as the thickness of the LC cell and the wavelength. Thus, the two matrices modeling the FLC cell when addressing a bipolar voltage are: $M_{LR}(\delta,\theta)$ and $M_{LR}(\delta,\theta+\alpha)$. As consequence, three physical parameters needs to be known for modeling the FLC cell: the retardance (δ), the orientation of the LC director at one of the stable orientations (θ), and the relative angle between the two stable orientations of the LC director (α). There are some experimental calibration procedures to characterize these three parameters, such as in [48].

1.3.2 Polarimeters based on liquid crystals cells

Liquid crystal cells are used in polarimeter architectures, taking advantage of their ability to manipulate polarization of light beams dynamically with an external electrical field. In this way, architectures have no moving elements, so they avoid vibrations, beam wander and orientational alignment errors. In addition, they are operated at low driving voltages and with high switching frequencies.

In the nineties, few works related to polarimeters designs using LC cells were published, specifically they were using TN-LC cells. In 1992, Wolff and Mancini [94] presented an imaging Stokes polarimeter using 2 TN-LC cells with a twist of 90º and 45º. TN-LC cells were used only

in two configurations, when the TN-LC was in its relaxed state (Figure 1-3(a)) and when a high voltage was applied (Figure 1-3(b)), leading to an incomplete polarimeter able to measure only partial linear polarized light (sum of unpolarized and completely linearly polarized states). An extension of this early work was reported in [95,96]. Blakeney *et al*. [97] designed a full Stokes polarimeter using a single TN-LC cell, by using intermediate voltages, leading to TN-LC configurations between the twisted and untwisted configurations (Figure 1-3(a) and (b), respectively).

Polarimeters based on PA-LC cells, referred as well as liquid crystal variable retarders (LCVRs), are frequently reported in the literature. For instance, Bueno and Artal [7] described a Mueller imaging polarimeter using two LC cells for imaging the human eye, although two removable quarter waveplates were required to obtain a complete characterization of the Mueller matrix. Tyo [98–100] developed an imaging Stokes polarimeter using 2 LCVRs, and optimized the polarimeter performance. De Martino *et al*. [101,102], implemented a Mueller polarimeter with no moving parts using 4 LCVRs, whose orientations and retardances were also optimized. An imaging Stokes polarimeter based on two LCVRs was implemented by Goudail *et al*. [103] for target detection and segmentation performance, by Pust and Shaw [104] for studying the effects of differing sky polarizations upon ground-based objects and, by Uribe-Patarroyo and IMaX team [33] for a stratospheric balloon mission to study solar magnetic fields. Moreover, there are some works focused on the error analysis and the optimization of polarimeter architectures based on variable retarders [105,106].

Finally, some publications about polarimeter layouts using ferroelectric liquid crystals are also present in the literature. Among the first designs, Gandofer [107] implemented an image Stokes polarimeter using 2 half-wave FLC retarders and two fixed $\lambda/8$ for solar polarization metrology. FLC modulation frequencies are in the kHz, necessary for applications in solar astronomy to overcome the influence of turbulence in the earth atmosphere. Garcia-Caurel *et al*. [70] implemented a Mueller polarimeter using 4 FLC cells, combined with a dispersion grating in order to take fast spectroscopic measurements. Aas *et al*. [49,108] implemented different prototypes of a near IR (700-1600nm) Mueller matrix polarimeter, with 4 FLC cells combined with 4 waveplates. Gendre *et al*. [73] designed a partial imaging Stokes polarimeter based on a single half-wave FLC cell at 633nm, later in [109] the same prototype was used but at 532nm, away from its FLC designed wavelength, leading to a complete imaging Stokes polarimeter.

1.4 Biaxial crystals

Biaxial crystals (BCs) [1] are anisotropic materials characterized by three different refraction indices corresponding to the three principal axes of the crystal. Light propagating in BCs experiences a refractive index and a phase velocity that depend on the propagation direction, polarization state and wavelength. Figure 1-5 illustrates the index ellipsoid [1] of a BC, with three unequal refractive indices sorted as $n_\alpha < n_\beta < n_\gamma$. There are two particular directions of propagation of a light beam in which the light sees the same refraction index ($n_\beta = n'_\alpha$) independent of its polarization, so no birefringence is seen by the beam. These two directions are the so-called optical axes of the BC, and they are represented in Figure 1-5.

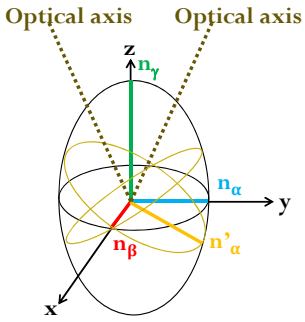

Figure 1-5: Index ellipsoid of a biaxial crystal. The three principal refraction indices are: $n_\alpha < n_\beta < n_\gamma$.

The phenomenon of the conical refraction (CR) [110] is observed in biaxial anisotropic mediums when a light beam travels along one of the optic axes of a BC, propagating conically inside the BC and emerging from the crystal as a hollow cylinder (see Figure 1-6). This phenomenon was predicted by Hamilton in 1832 and observed shortly by Lloyd with a crystal of aragonite [111]. The cross section of the beam exiting from the BC consists in a ring of intensity. The radius of the CR ring, R_0, can be obtained from the product of the length of the crystal, L, and its conicity, α: $R_0 = L\alpha$. The conicity of the crystal depends on the principal refractive indices of the crystal[112]:

$$\alpha = \sqrt{(n_2^2 - n_1^2)(n_3^2 - n_2^2)} / 4n_1n_3 \qquad (1\text{-}8)$$

In general, experimental set-ups to visualize the CR phenomenon use a lens to focalize the beam impinging the BC. In this case, a light ring is observed at the focal plane (also known as Lloyd plane). The ring structure depends on the profile of the incident beam, so let us focus on a Gaussian beam as illumination. One interesting peculiarity of the CR light ring is that it splits into two concentric bright rings separated by a dark ring (Poggendorff ring) under conditions of $R_0 >> w_0$ (see Figure 1-7), where w_0 is the waist radius of the focused input beam. Additionally,

w_0 is also the width of each of these rings. A second interesting feature of the ring is the polarization distribution along the ring. At each point of the CR ring, the electric field is linearly polarized with the polarization plane rotating along the ring such that every two opposite points of the ring have orthogonal polarizations. A third remarkable feature of the CR ring is its intensity distribution along the ring and its dependence with the polarization of the beam impinging the BC. On the one hand, input beams with circularly polarized states or unpolarized lead to uniform bright rings as Figure 1-7. On the other hand, input beams linearly polarized lead to broken bright rings, whose null of intensity corresponds to the position of the ring with orthogonal polarization with respect to the input polarization. As final remark, as the image plane is moved from the focal plane, the intensity pattern changes and it becomes more complex, with two bright spots found symmetrically from the focal plane[113].

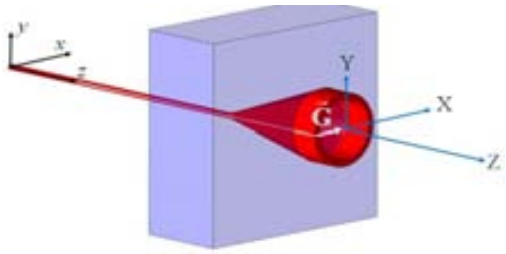

Figure 1-6: Light beam propagating along one of the optical axes of a biaxial crystal, leading to the conical refraction.

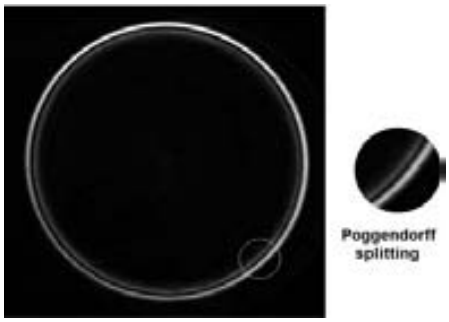

Figure 1-7: Conical refraction ring observed under condition of $R_0 >> w_o$: Two concentric light rings separated by a dark (Poggendorff) ring.

1.5 Main goals of this thesis

This thesis is structured in two main parts. On the one hand, a comprehensive study of polarimeters using materials presenting refraction index anisotropy (first, liquid crystal cells and second, biaxial crystals) is provided. On the other hand, from an exhaustive comparative between all analyzed polarimeters, the best candidate for an imaging polarimeter will be implemented and extended for obtaining polarimetric images with enhanced spatial resolution.

Concerning the first part of this thesis, we will review some existing LC based polarimeter architectures in the literature, introducing some variants to those polarimeter architectures in order to improve their performance, as well as we will design new layouts of LC based polarimeters. In particular, we will focus on three different LC based polarimeters:

i) Stokes polarimeter based on two parallel aligned nematic liquid crystal cells
ii) Stokes polarimeter based on a single twisted nematic liquid crystal cell
iii) Stokes and Mueller polarimeters based on ferroelectric liquid crystal cells

Moreover, the conical refraction phenomenon will be proposed and studied as a new tool for polarization metrology. The new technique will be used as measurement principle of a new division of amplitude polarimeter based on two biaxial crystals.

To provide a meticulous study for all proposed polarimeters, we decide to follow the same scheme of analysis:

i) Design: To propose a design of a complete polarimeter and to provide the corresponding optical model to describe the polarimeter performance. To this aim, it is necessary to experimentally calibrate the liquid crystal (or the biaxial crystal).
ii) Optimization analysis: To optimize the physical parameters of the set-up in terms of minimization of noise amplification from flux measurements. To provide a robustness study of the polarimeter by simulating deviations from the optimized configuration.
iii) Tolerance analysis: To study the polarimeter performance sensitivity to experimental errors during the implementation. In particular, to determine the tolerance of the parameters of the set-up required to achieve an accuracy in the polarization measurements smaller than 0.02 (1% of the total range).
iv) Implementation: To carry out the experimental implementation of the polarimeter and, to calibrate the system. To analyze the experimental measurements and evaluate the repeatability and accuracy.

Concerning the second part of this thesis, a comparative between the different analyzed polarimeters will be given by extracting all the results obtained from the individual studies of the first part of this thesis. Particularly, the comparative will focus on relevant specifications such as equipment needed, cost, transitory time of the LC, possibility to extend to an imaging polarimeter, optimization, robustness, tolerance analysis, accuracy, repeatability and ultimately, strengths and drawbacks for each prototype.

From this comparative, the best candidate for imaging polarimetry will be selected. Finally, we will develop a new experimental configuration which combines an imaging polarimeter and a module used to achieve sub-pixel-resolution imaging in an optical system where the resolution is

limited by detector pixels geometry. To experimentally validate the improvement of resolution in polarimetric images, experimental measurements of resolution test targets will be provided.

1.6 Structure of this thesis

The scientific achievements of this thesis have been published in different international journals in the field of Optics [PAPER A - PAPER F], and they have also led to the application of a patent [PAPER G]. The topic of all papers constituting this thesis is strongly related, leading to a high consistency in its subject of matter. This fact has been the reason to decide to present this thesis as a compilation of papers. This thesis is organized in different chapters, in which the scientific achievements supplied in the papers are explained and expanded, in order to provide a deeper and wider insight as well as to clarify the coherence and unity existing between the papers.

The outline of this thesis is as follows. In Chapter 2, the mathematical formalism and methodologies necessary for the following chapters are provided, including the Mueller-Stokes formalism, the measurement principle of a polarimeter, the optimization, the tolerance analysis and the calibration procedure. Next, the three following chapters correspond to a thorough analysis of the polarimeters based on liquid crystals. Chapter 3 deals with the polarimeter based on parallel aligned liquid crystal panels [PAPER A], Chapter 4 describes the study of the polarimeter based on a twisted nematic liquid crystal panel [PAPER B], and Chapter 5 details the polarimeter based on ferroelectric liquid crystals panels [PAPER C]. Afterwards, Chapter 6 presents and analyze in detail the polarimeter based on the conical refraction phenomenon [PAPER E, PAPER G]. Afterwards, Chapter 7 is divided in three main parts. Section 7.1 presents an exhaustive comparative between the four different prototypes studied along the thesis, and the best candidate for super-resolution imaging polarimetry is selected. Section 7.2 details the implementation of the imaging polarimeter, and later in section 7.3 the performance is extended with an additional module for achieving super-resolved polarimetric images [PAPER F]. Finally, the conclusions of the present work are provided in Chapter 8.

Chapter 2 **Mathematical formalism to model the polarimeters performance**

This chapter introduces the mathematical formalism used in this thesis to describe the polarization of the light, its interaction with materials and to model the performance of polarimeters. First of all, the Mueller-Stokes formalism is introduced, which describes the polarization of a light beam and characterizes the polarimetric properties of a sample. Next, it presents a general formulation of the measurement principle and the data reduction procedure of a polarimeter. In addition, the importance of optimizing the system in order to reduce the amplification of additive noise in the flux measurements during data reduction is addressed in this chapter. In particular, some figures of merit evaluating different aspects of the optimization of the system are reported. Moreover, some guidelines providing how to conduct a study of the system robustness are also reviewed. Afterwards, it includes the methodology for determining the parameters tolerance in order to achieve a particular accuracy in the polarization measurements when considering experimental errors in the set-up. Furthermore, two methods for calibrating the polarimeter are explained.

2.1 Mueller and Stokes formalism

There are different mathematical formalisms to describe the polarization of light and its interaction with matter, such as Jones calculus [114] describing coherent monochromatic light, Berreman formalism [115], the so-called coherence matrices introduced by Wiener [116] and by Wolf [117] or the Stokes-Mueller formalism [1,118–120], among others. Of these formalisms, the Mueller-Stokes formalism is most generally suited for describing polarimeters because of two main reasons. First, polarimeters are irradiance-measuring instruments and the intensity is represented explicitly in this formalism. Second, this calculus describes not only fully polarized light, but also partially and unpolarized light.

In 1858, G. G. Stokes [118] defined four parameters, which now bear his name, to describe the state of polarization (SOP) of a light beam, suitable for incoherent and coherent light. He found that any state of polarized light could be completely described by four observables. These four elements can be defined in terms of these six polarized flux measurements as:

$$S = \begin{pmatrix} S_0 \\ S_1 \\ S_2 \\ S_3 \end{pmatrix} = \begin{pmatrix} P_{0^\circ} + P_{90^\circ} \\ P_{0^\circ} - P_{90^\circ} \\ P_{45^\circ} - P_{135^\circ} \\ P_R - P_L \end{pmatrix} \tag{2-1}$$

where P_x corresponds to the flux measurement when analyzing the x polarization, being x the azimuth of a linearly polarized light or the handedness (right or left) of circularly polarized light. Therefore, S_0 corresponds to the total intensity of the beam, S_1 describes the amount of horizontal or vertical linear polarization, similarly S_2 is the amount of 45º or 135º linear polarization and finally, S_3 describes the amount of right or left circular polarization contained within the light beam. The Stokes vector (S) can be separated mathematically in two vectors representing the fully polarized content (S_p) and the unpolarized content (S_u) of the light beam [1]:

$$S = S_p + S_u = \begin{pmatrix} S_0 \\ S_1 \\ S_2 \\ S_3 \end{pmatrix} = \begin{pmatrix} \sqrt{S_1^2 + S_2^2 + S_3^2} \\ S_1 \\ S_2 \\ S_3 \end{pmatrix} + \left(S_0 - \sqrt{S_1^2 + S_2^2 + S_3^2} \right) \begin{pmatrix} 1 \\ 0 \\ 0 \\ 0 \end{pmatrix} . \tag{2-2}$$

The degree of polarization (DOP) of the beam is defined as:

$$DOP(S) = \frac{\sqrt{S_1^2 + S_2^2 + S_3^2}}{S_0} , \tag{2-3}$$

where DOP ranges from 0 (unpolarized light) to 1 (fully polarized light), and other intermediate values correspond to partially polarized light.

In 1892, Poincaré [121] introduced the concept of using a unit sphere centered in the Cartesian coordinates, whose axes correspond to the normalized Stokes parameters $\{S_{1n},S_{2n},S_{3n}\}$ (i.e. Stokes parameters divided by S_0). Such sphere is nowadays well-known as the Poincaré sphere. It is used to represent any SOP as a point in the three dimensional space, simplifying the analysis of many polarization problems [1]. Figure 2-1 shows the Poincaré sphere with some examples of SOPs. Any point over the surface of the Poincaré sphere corresponds to a fully polarized state. In particular, linear SOPs are represented along the equator, north and south poles are the right and the left circularly polarized SOP respectively, and any other point corresponds to an elliptical SOP. Later, we will see that this geometrical representation will help us to understand the optimization of a polarimeter.

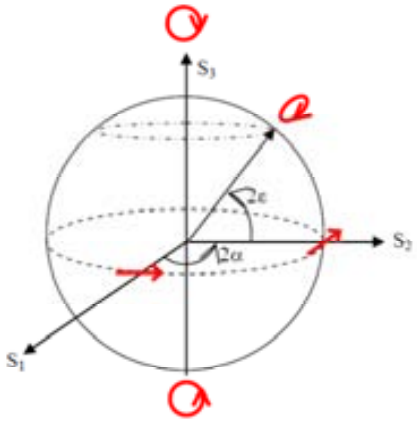

Figure 2-1: Poincaré sphere with some SOPs, whose polarization ellipses are represented in red: linearly polarized SOPs at 0º and at 45º, right and left circularly polarized states and a right-handed elliptical SOP. Azimuth (α) and ellipticity (ε) parameters define the polarization ellipse[1], as well as the point over the Poincaré sphere.

In 1948, Mueller [119] formulated the interaction of a light beam with a polarizing medium by means of a four-by-four real matrix. Later, Parke [120] developed the properties of the so-called Mueller matrices in great detail. In this way, the incident and exiting Stokes vectors to a polarizing sample are linked by the following linear relation:

$$S_{out} = M \cdot S_{in} \ . \qquad (2\text{-}4)$$

Note that the first component of the exiting Stokes vector corresponds to the intensity of the light beam which is transmitted, reflected or scattered by the polarizing sample. Mueller matrix contains information related to all polarization properties of the sample (diattenuation, retardance and depolarization)[1]. The decomposition of Mueller matrices has been addressed by different authors [122–124]. In particular, Lu-Chipman decomposition [124] gives an algorithm for extracting these three main polarization properties from an arbitrary Mueller matrix.

2.2 Polarimetric measurement principle and data reduction procedure

The goal of a Stokes polarimeter is to characterize the Stokes vector of an incident light beam by means of radiometric measurements. The polarization of the incident beam is analyzed by the PSA (polarization state analyzer). In particular, the light is projected over particular configurations of the PSA (such as different retardances of a variable retarder), referred as polarization analyzers (PAs), and a set of flux measurements are acquired. By adopting the nomenclature given in [4] (it is followed throughout this section), we can mathematically describe the response of the polarization analyzer (P_q) to an arbitrary SOP as the dot product of the first row of the Mueller matrix describing the particular configuration q of the PSA (i.e. the polarization analyzer A_q=[$a_{q,0}$,$a_{q,1}$,$a_{q,2}$,$a_{q,3}$]) with the Stokes vector of the incident beam (S):

$$P_q = A_q \cdot S \tag{2-5}$$

To exemplify, this situation is illustrated in Figure 2-2(a). When the Stokes polarimeter uses n PAs, the measurement principle of the instrument is given by the following system of linear equations:

$$P = \begin{pmatrix} P_1 \\ P_2 \\ \vdots \\ P_n \end{pmatrix} = WS = \begin{pmatrix} a_{1,0} & a_{1,1} & a_{1,2} & a_{1,3} \\ a_{2,0} & a_{2,1} & a_{2,2} & a_{2,3} \\ \vdots & \vdots & \vdots & \vdots \\ a_{n,0} & a_{n,1} & a_{n,2} & a_{n,3} \end{pmatrix} \begin{pmatrix} S_0 \\ S_1 \\ S_2 \\ S_3 \end{pmatrix}, \tag{2-6}$$

where S is the Stokes vector of the incident beam (our unknown), W is the polarimetric measurement matrix (whose rows are the n different PAs used during the measurement), and P contains the n measured fluxes, result of projecting the incident beam over the n PAs.

Given a set of flux measurements constituting the vector P and a well-known matrix W (it is necessary to accurately calibrate W, explained in section 2.5), the incident Stokes vector can be estimated by a data reduction procedure. There are two scenarios depending on the rank of the matrix W. On the one hand, when the rank of W is smaller than 4, the polarimeter is incomplete, and only three or fewer properties of the Stokes vector elements are determined. On the other hand, when the rank of W is 4, the polarimeter is complete, and all parameters of the Stokes vector can be determined. Under this last scenario, two cases can be observed depending on the number of PA used (n). First, when n=4, the matrix W is a non-singular square matrix, its inverse W^1 exists and it is unique, leading to the following expression to determine the Stokes vector:

$$S = W^{-1}P \ , \tag{2-7}$$

where W^{-1} is the data reduction matrix. Second, when $n>4$, W is an $nx4$ rectangular matrix, the system is over determined, and in general the solution is not unique. However, we can find the solution that minimizes the mean square error by using the pseudoinverse matrix. Thus, the data reduction procedure is given by this new equation:

$$S = \left(W^T W\right)^{-1} W^T P = \tilde{W}^{-1} P \ , \tag{2-8}$$

where W^{-1}, W^T and $\tilde{W}^{-1}$ are the inverse, the transpose and the pseudoinverse of the matrix W, respectively.

Furthermore, the goal of a Mueller polarimeter is to determine the Mueller matrix of a sample by means of radiometric measurements. The Mueller polarimeter consists of a polarization state generator (PSG), which prepares polarization states incident to the sample (known as polarization generators), and a PSA, which analyzes the SOP of the beam exiting the sample. In this way, the detector of the polarimeter will take a flux measurement (P_q) of the generated Stokes vector (S_q), after being altered by the sample (described by a Mueller matrix M) and projected over a polarization analyzer (A_q), mathematically expressed as $P_q=A_q \cdot M \cdot S_q$, and illustrated in Figure 2-2(b). When the Mueller polarimeter uses the combination of n polarization analyzers and m polarization generators, $n \cdot m$ flux measurements are taken:

$$P = \begin{pmatrix} P_{1,1} & P_{1,2} & \cdots & P_{1,m} \\ P_{2,1} & P_{2,2} & \cdots & P_{2,m} \\ \vdots & \vdots & \ddots & \vdots \\ P_{n,1} & P_{n,2} & \cdots & P_{n,m} \end{pmatrix} = AMS = \begin{pmatrix} a_{1,0} & a_{1,1} & a_{1,2} & a_{1,3} \\ a_{2,0} & a_{2,1} & a_{2,2} & a_{2,3} \\ \vdots & \vdots & \vdots & \vdots \\ a_{n,0} & a_{n,1} & a_{n,2} & a_{n,3} \end{pmatrix} M \begin{pmatrix} S_{0,1} & S_{0,2} & \cdots & S_{0,m} \\ S_{1,1} & S_{1,2} & \cdots & S_{1,m} \\ S_{2,1} & S_{2,2} & \cdots & S_{2,m} \\ S_{3,1} & S_{3,2} & \cdots & S_{3,m} \end{pmatrix}, \tag{2-9}$$

where the rows of matrix A contains the different PAs and the columns of matrix S contains the generated Stokes vectors. Furthermore, this mathematical relation can be rewritten as the following dot product [1,66]:

$$P = \begin{pmatrix} P_1 \\ P_2 \\ \vdots \\ P_{n \cdot m} \end{pmatrix} = W\vec{M} = \begin{pmatrix} w_{1,1} & w_{1,2} & \cdots & w_{1,16} \\ w_{2,1} & w_{2,2} & \cdots & w_{2,16} \\ \vdots & \vdots & \ddots & \vdots \\ w_{n \cdot m,1} & w_{n \cdot m,2} & \cdots & w_{n \cdot m,16} \end{pmatrix} \begin{pmatrix} m_1 \\ m_2 \\ \vdots \\ m_{16} \end{pmatrix} . \tag{2-10}$$

Note that the Mueller matrix is rewritten as a vector of sixteen elements $\vec{M} = \begin{pmatrix} m_1 & \ldots & m_{4(i-1)+j} & \ldots & m_{16} \end{pmatrix}^T$, being $m_{4(i-1)+j}$ the (i-th, j-th) element of the Mueller matrix. In addition, information of matrices A and S is contained in an $n \cdot mx16$ matrix, named the polarimetric measurement matrix (W). When the rank of the matrix W is smaller than 16, the polarimeter is incomplete. On the contrary, when the rank is 16, the polarimeter is complete and all 16 parameters of the Mueller matrix can be determined. Similarly, the data reduction

procedure to determine the Mueller matrix will make use of the inverse or the pseudoinverse matrix of W, depending if $n \cdot m$ is equal or larger than 16, respectively, leading to the following data reduction equations:

$$\vec{M} = W^{-1} \cdot P \tag{2-11}$$

$$\vec{M} = \left(W^T W\right)^{-1} W^T P = \tilde{W}^{-1} P \tag{2-12}$$

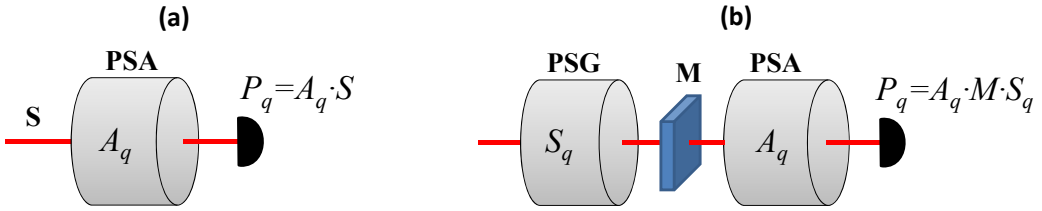

Figure 2-2: General sketch of (a) a Stokes polarimeter and (b) a Mueller polarimeter, when taken a flux measurement (P_q).

2.3 Flux noise: Optimization analysis

An infinite number of matrices W with rank 4 (Eq. (2-7) or (2-8)), for the Stokes polarimeter, or rank 16 (Eq. (2-11) or (2-12)), for the Mueller polarimeter, are valid to describe complete Stokes and Mueller polarimeters, respectively. It can be readily obtained just by selecting one of the infinites PSA configurations set (for Stokes polarimeters) or PSG-PSA configurations set (for Mueller polarimeters), able to build-up a non-singular matrix W. Nevertheless, in presence of noise in the flux measurements, the noise will be transmitted differently to the solution during the data reduction procedure. Different types of noise can be considered during the detection process. Generally, it is assumed an additive Gaussian noise, independent on the level of the signal [99,102,125]. However, in particular systems with low light levels and high acquisition rates a signal-dependent Shot noise becomes the dominant term during the detection process. Some works [126–128] have optimized the polarimetric performance under this scenario, where Shot noise is modelled with a Poisson distribution.

In our polarimetric system, because we work with enough light intensity, we only assume additive noise in the detection process, whereas Shot noise is neglected. Thus, for a Stokes polarimeter, considering an additive flux noise of ΔP, it will be amplified to the Stokes vector estimation by the following relation, when n=4 or n>4, respectively:

$$S + \Delta S = W^{-1}\left(P + \Delta P\right) \tag{2-13}$$

$$S + \Delta S = \tilde{W}^{-1}\left(P + \Delta P\right), \tag{2-14}$$

where ΔS is the solution transmitted noise. Note that the model can be extended to a Mueller polarimeter by replacing the Stokes vector by the Mueller matrix.

Several figures of merit have been widely discussed in the literature [61,79,98,105,129–131] for evaluating the noise propagation during the optimization of Stokes and Mueller polarimeter configurations. These indicators are used for selecting the optimum set of polarization analyzers and generators, determining the optimum values of the optical parameters in the polarimeter set-up, such as the orientations of the optical elements or the retardances introduced by the retarders. Following, we review the figures of merit used in this thesis for the optimization of the polarimeter layouts.

2.3.1 Condition number

When dealing with polarimeters devised not to measure specific SOPs but an arbitrary one, from an optimized performance point of view, the polarimetric measurement matrix should be as far from singular as possible, in other words, it should be well conditioned. This is quantified by the condition number (CN) [132] of matrix W. CN is obtained from the singular value decomposition (SVD) [133] of the matrix W, which consists in a factorization of the form $W = UDV^T$. Where U and V are two unitary matrices and D is a diagonal matrix. The diagonal elements of D are the so-called singular values of W. Actually, the rank of matrix W is the number of non-zero singular values. There are different definitions of the CN [79,98,106], the one used here is:

$$CN\left(W\right) = \frac{\sigma_{\max}}{\sigma_{\min}}, \tag{2-15}$$

where σ_{max} and σ_{min} are the maximum and minimum singular values different from zero. Further insight into the conditioning of W is explained through the SVD and can be found in [106]. Minimizing the CN, one is equalizing and minimizing the noise in the Stokes elements, thereby maximizing the relative importance of each of the flux measurements[98]. Theoretically, the minimum CN is 1, corresponding to an arbitrary unitary matrix and it does not amplify the error. However, polarimetric measurement matrices have some constrains because their constituting rows are not chosen from arbitrary values but they can only be selected from the different polarization analyzers of the system (i.e. they are limited to the Stokes vector form) As a consequence, the value 1 for CN can never be obtained. However, by minimizing the CN, we obtain the best conditioned matrix, and so, the closest to a unitary matrix. Reference [99] includes an appendix demonstrating that the minimum condition number for the polarization measurement

matrix is $(M\text{-}1)^{1/2}$, where M is the number of reconstructed Stokes parameters and it is independent on the number of measurements. Consequently, for a complete Stokes polarimeter (M=4 Stokes parameters), the minimum CN is $\sqrt{3}$. The CN number of a Mueller polarimeter corresponds to the product of the condition numbers of matrices A and S, describing the PSA and PSG respectively [105,106]. As final remark, the use of a ratio in the definition of the CN (Eq. (2-15)) cancels the effect of any overall changes in the size of the singular values. This makes this figure of merit unsuitable for studies of the effect of increasing the number of measurements.

This indicator has been widely used in the literature for the optimization of Stokes and Mueller polarimeter architectures, such as in the optimization of a variable-retardance polarimeter [98,101,106], a rotating waveplate polarimeter [68,79,106], a photo-elastic modulator based PSG on three spectral ranges [102] or a division-of-amplitude prism based PSA [102].

2.3.2 Specific Stokes variances

In order to study the specific sensitivity of each Stokes channel in presence of noise at the radiometric measurements, we can analyze the noise propagation corresponding to the system of linear equations described in Eq. (2-7) or (2-8). Let us rewrite the general case (n>4) as follows:

$$S = \tilde{W}^{-1}P = QP \Rightarrow S_i = \sum_{k=1}^{n} q_{ik}P_k \ , \tag{2-16}$$

with i ={0,1,2,3} and where n is the number of elements of the flux vector P. Moreover, q_{ik} represents the (i-th, k-th) element of the pseudoinverse matrix $\tilde{W}^{-1}$ and S_i is the i-th component of the Stokes vector S. We apply error propagation in Eq.(2-16), considering only error in the flux measurements (δP_k), so we assume that q_{ik} elements have no error (ideal calibration of W). Moreover, we assume that noise at the different flux measurements is uncorrelated and with the same statistical properties ($\delta P_{k=}\ \delta P$), leading to the following expression (already deduced in previous works [98,105,125]):

$$\delta S_i^2 = \sum_{k=1}^{n}\left[\left(\frac{\partial S_i}{\partial P_k}\right)^2 \delta P_k^2\right] = \delta P^2 \cdot \sum_{k=1}^{n} q_{ik}^2 \tag{2-17}$$

Note that this expression gives us the variance amplification associated at every component of the Stokes vector. If a particular Stokes vector component was of interest, the corresponding specific Stokes variance given by Eq. (2-17) would be recommended to use as figure of merit[125].

In a more realistic situation, it is also taken into account the contribution of error in the elements q_{ik} associated to a non ideal calibration of the matrix W or a misalignment of the optical

elements. Some works have considered both error sources, coming from the detection process (δP) and coming from experimental errors in the calibration or alignment (δW) [79,105,106,131,134,135]. However, our approach optimizes the polarimetric system only considering the flux noise, while the experimental errors (causing a variation in the matrix W) and their impact to the polarization measurements are later analyzed (study explained in section 2.4).

2.3.3 Equally weighted variance

When all Stokes vector elements are equally of interest, a figure of merit called equally weighted variance (EWV) is recommended [125]. This indicator is obtained by adding all four Stokes vector component variances with the same weight. Alternatively, this parameter can be also obtained from a SVD point of view:

$$EWV\left(W\right)=\sum_{j=1}^{R}\frac{1}{\sigma_j^2}\ , \tag{2-18}$$

where R is the rank of the matrix W and all its singular values σ_j are contributing in the summation with the same weight. Since singular values appear in the denominator, EWV diverges as W approaches to a singular matrix and so, EWV should be minimized to optimize the polarimeter design. Unlike CN, EWV detects the benefits of increasing the number of measurements. This figure of merit was derived in [125] for optimizing the retardance and orientations of a rotating retarder with a fixed polarizer based polarimeter.

The EWV indicator provides a useful estimation of the global error amplification in the solution vector S when some amount of noise is present in the flux measurements vector P. This global error is the summation of the specific errors transmitted to every component of the Stokes vector. As a consequence, the minimized global transmitted error, obtained by optimizing the EWV indicator, not always corresponds to the possible minimum error of each Stokes parameter.

2.3.4 Poincaré sphere interpretation

Some works have used a geometric approach to analyze how a matrix W is far from a singularity [61,80,98,125]. The concept is to represent PAs describing the matrix W as points on the Poincaré sphere surface. When using 4 PAs, these points are defining a tetrahedron, generally irregular. An optimum choice results if the four points are as equi-spaciated as possible upon the Poincaré surface. This fact maximizes the tetrahedron volume, which maximizes as well the determinant of the matrix, making the matrix as far as possible from singular matrices. The maximum enclosed volume (when $n=4$) corresponds to a regular tetrahedron (when CN takes its minimum value: $\sqrt{3}$). This regular tetrahedron configuration has been reached with different

polarimeter architectures, such as one based on a rotating retarder (with a retardance of 132º) [105,125] and on two variable retarders [98]. On the contrary, when the 4 PAs represented upon the Poincaré sphere are defining a plane, i.e. no volume is enclosed, the determinant of such matrix is zero and it corresponds to an incomplete polarimeter.

2.3.5 Robustness study

It is also interesting to analyze how these quality indicators, such as CN and EWV, are affected when a given polarimeter is experimentally implemented and some experimental errors are taking place. In other words, we want to study the polarimeter robustness. These experimental errors may be due to some miscalibration (on the phase-to-voltage calibration curve of the liquid crystal, on the retardance of a waveplate, etc) or to misalignments (orientational alignment error of the optical elements, small tilt of a polarizing element, etc). The methodology used in this thesis for studying the robustness of the instrument is the following. Let us consider an optimized polarimetric system, described mathematically by its polarimetric measurement matrix W. We simulate a set of polarimeters deviated from the optimized configuration, and for each deviated-polarimeter, its CN and EWV are recalculated. These deviations are conducted by adding a random value to the Stokes parameters describing each optimal PA of the polarimeter. The random value is taken from a zero mean uniform distribution with amplitude of 0.4 (a 20% of the Stokes parameter values range). Finally, for each new deviated PA, it is considered only the fully polarized content of the deviated PA (i.e. S_p from Eq.(2-2)). In conclusion, such simulation allows us to study the robustness of the optimized polarimeters under experimental deviations from the ideal configurations (i.e. the W obtained from the optimization process). Similar study has been done in [105], in order to check the robustness on a rotating retarder polarimeter while varying one of the optimal orientations of the retarder.

2.4 Experimental error: Tolerance analysis

Optimization procedure has considered only additive noise during the detection process. Additional sources of errors in polarimeters are element misalignment and miscalibration. For instance, in [99,134] the angular positioning error of a rotating waveplate based Stokes polarimeter is studied, in [81] the errors in the orientation and retardance of a dual rotating retarder Mueller polarimeter are discussed and, in [136] the extinction ratio of a diattenuator and the spatial and angular variability of the retarding element of an imaging Stokes polarimeter are analyzed.

Our approach to study the polarimeter performance sensitivity to such experimental errors during the implementation is through a tolerance analysis detailed below. The goal is to identify those error sources with largest contributions. In particular, we determine the tolerance of the parameters of the polarimeter set-up in order to achieve a 1% of accuracy in the polarization measurements. The methodology is explained in detail for the Stokes polarimeter, and following it is extended to the Mueller polarimeter.

2.4.1 Theoretical formulation for Stokes polarimeters

The configuration of our Stokes polarimeter is described by the ideal polarimetric measurement matrix *W*, containing the set of optimized PAs. This matrix will depend on a set of parameters of the set-up, which have been optimized through a figure of merit. These parameters could be, depending on the architecture of the polarimeter, the orientation of a linear polarizer, the optimized orientations of a rotating waveplate, the retardance of a constant retarder, the optimized retardances of a variable retardance, among others. Nevertheless, when implementing the polarimeter, the actual parameters in the laboratory will slightly differ from the theoretical values. The reason of those discrepancies can be attributed to multiple experimental factors, as for instance, misalignments, tilts, defects in the optical elements involved, or temperature changes from the one used in the calibration. All these small deviations as a whole will modify the expression of the experimental polarization analyzers, and so the experimental polarimetric measurement matrix will be different (let us call it as W_{exp}). However, when we perform the data reduction process, we will still use the inverse of the ideal matrix *W*. Therefore, the estimated Stokes vector will be as:

$$\vec{S}_{est} = W^{-1} \cdot W_{\exp} \cdot \vec{S} \ . \tag{2-19}$$

Note that for a experimental polarimetric measurement matrix W_{exp} with no errors, this matrix will be equal to *W*, and so $\vec{S}_{est}$ will be identical to the incident Stokes vector, $\vec{S}$. In general, there is a difference between the estimated and the actual incident Stokes vector, called Stokes error ($\vec{e}_S$). This vector is composed by the four errors associated to each Stokes parameter (e_{Sx}):

$$\vec{e}_S = \begin{pmatrix} e_{S0} \\ e_{S1} \\ e_{S2} \\ e_{S3} \end{pmatrix} = \vec{S} - \vec{S}_{est} = \left(Id - W^{-1} \cdot W_{\exp} \right) \cdot \vec{S} \tag{2-20}$$

We want to emphasize that the Stokes error will depend on the incident Stokes vector. For instance, in [127,134] they reported how the Stokes error depends on the incident polarization.

Thus, a study of this error as function of the incident Stokes vector for our polarimetric configuration is very convenient.

We have used a parameterization over the surface of the Poincaré sphere in order to analyze the Stokes error as a function of the incident fully polarized Stokes vector. The Stokes vector is defined by the ellipse polarization parameters [1]: azimuth and ellipticity. Where azimuth, θ, goes from 0 to π, and ellipticity, ε, goes from $-\pi/4$ to $\pi/4$ (from left to right handed).The following set of equations show the parametric equations as functions of the variable k:

$$S_k = \begin{pmatrix} 1 & \cos 2\theta_k \cos 2\varepsilon_k & \sin 2\theta_k \cos 2\varepsilon_k & \sin 2\varepsilon_k \end{pmatrix}^T$$
$$\begin{cases} \varepsilon_k = k \cdot \Delta\varepsilon - \dfrac{\pi}{4}; \quad \Delta\varepsilon = \dfrac{\pi}{2N_\varepsilon N_\theta} \\ \theta_k = k \cdot \Delta\theta; \qquad \Delta\theta = \dfrac{\pi}{N_\theta} \\ k = 1, \ldots, N_\varepsilon N_\theta \end{cases} \tag{2-21}$$

where N_θ is the number of circles around the S_3 axis, and $N\varepsilon$ is the number of steps in each circle around the S_3 axis. In our study, we use N_ε=20 and N_θ=50, so in total we sample 1000 different incident Stokes vectors, which are plotted upon the Poincaré sphere in Figure 2-3.

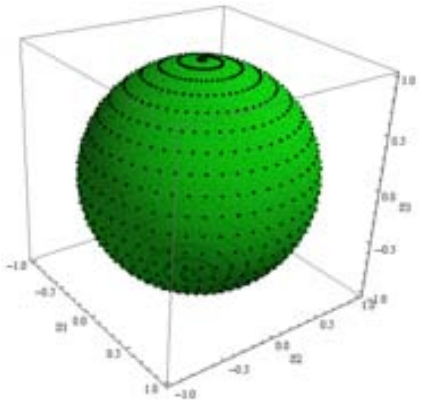

Figure 2-3: Parameterization of the incident Stokes vector over the Poincaré sphere for $N\varepsilon=20$ and $N_\theta=50$.

Many studies can be performed by considering certain deviation in one or diverse of the parameters involved in the set-up. In following chapters, where different architectures of polarimeters are studied in detail, we will show the components of the Stokes error as function of the incident Stokes vector when there is a shift of 1º on one of the parameters of the set-up (as retardance or orientation of the optical elements). In order to determine the accuracy in the polarization measurement, we will look for the maximum error of the four Stokes components, among all the incident Stokes vectors analyzed. We will represent the accuracy versus parameters tolerance, and by calculating a linear regression fitting on the simulated results, we will be able to

determine the tolerance of the parameters in order to achieve a particular value of accuracy. In our case, we will fix an accuracy of 0.02 (1% of the Stokes parameter range) as this value is extensively suitable for most polarimetric applications.

2.4.2 Theoretical formulation for Mueller polarimeters

The methodology detailed in subsection 2.4.1 for determining the parameters tolerance of the Stokes polarimeter can be also conducted for the Mueller polarimeter in the same way by considering the data reduction equation (2-11).

As explained above, due to experimental errors during the implementation, the experimental polarimetric measurement matrix (W_{exp}) will differ from the ideal one (W), obtained in the optimization. Consequently, the estimated and actual Mueller matrix will be slightly different. Thus, we define the Mueller matrix error ($\vec{e}_{mm}$) as the difference between these two Mueller matrices, and it is composed by the 16 errors associated to the 16 elements of the Mueller matrix:

$$\vec{e}_{mm} = \begin{pmatrix} e_{mm00} \\ \vdots \\ e_{mmij} \\ \vdots \\ e_{mm33} \end{pmatrix} = \vec{M} - \vec{M}_{est} = \left(Id - W^{-1} \cdot W_{\exp} \right) \vec{M} \qquad (2\text{-}22)$$

From Eq. (2-22) we note that these errors depend on the particular Mueller matrix that we are measuring. Thus, many studies can be conducted to analyze the dependence of the Mueller polarimeter accuracy with each one of the involved parameters of the polarimeter set-up. When we will implement a Mueller polarimeter, we will show the elements of the Mueller matrix error as function of a particular parameterization of the measured Mueller matrix (as the orientation of a waveplate). In the same way, we will determine the accuracy by looking for the maximum error of the sixteen elements of the Mueller error and by considering all the measured Mueller matrices. We will represent the Mueller accuracy versus parameters tolerance, and by calculating a linear regression fitting on the simulated results, we will be able to determine the tolerance of the parameters in order to achieve a particular value of accuracy. In our case, we will fix an accuracy of 0.02 (a 1% of the Mueller parameter values range).

2.5 Calibration methodology

Polarization elements in the PSA and PSG are not assumed to be ideal polarization elements. Moreover, the implemented set-up will have small misalignments of the optical elements as well as small variations on the retardance of the retarders involved in the set-up. If the polarimetric measurement matrix, W, is determined through an experimental calibration procedure, all these variations will be corrected to certain extent in the data reduction process. Only unavoidable variations between the calibration configuration and the measurement configuration of the polarimeter will still affect to the Stokes measurement error, a part from the noise during detection process. This unavoidable experimental error, caused by of a small variation after the calibration, is the value error which needs to be under the tolerance range calculated through the tolerance analysis. Consequently, the calibration procedure is extremely important, ensuring the desired accuracy in the polarization measurements.

Different experimental calibration procedures are used in the literature [61,137–139], and here we review two methodologies used in this thesis for calibrating the implemented prototypes.

2.5.1 Sequential calibration method

We set the PSA to a particular configuration described by the polarization analyzer A_q, and it is illuminated with four light beams with known polarization: linear polarized light at 0º, 90º and 45º degrees and right circularly polarized beam. Then, 4 flux measurements corresponding to the four input SOPs are taken, and they are denoted as ${P^0}_q$, ${P^{90}}_q$, ${P^{45}}_q$, ${P^{CR}}_q$, respectively. The subscript q is denoting the q-th PA which is being calibrated (with q=1,…,n). Equation (2-5) can be written four times, leading to a system of linear equations. This system can be solved because the four input SOPs are linearly independent. In this way, the 4 parameters describing the polarization analyzer A_q can be expressed as function of the flux measurements by:

$$a_{q,0}=\frac{1}{2}\left(P_q^0+P_q^{90}\right)\ ;\quad a_{q,1}=\frac{1}{2}\left(P_q^0-P_q^{90}\right)\ ;\quad a_{q,2}=P_q^{45}-a_{q,0}\ ;\quad a_{q,3}=P_q^{CR}-a_{q,0} \qquad (2\text{-}23)$$

This procedure is repeated to all the polarization analyzers (i.e. taken q=1,…,n). Finally the polarimetric measurement matrix W is constructed by placing each A_q to the k-th row of the matrix, as shown in Eq.(2-6). This calibration methodology has been followed in some works as in [61,140]. The former using the same set of known SOPs, the later using a set of SOPs generating a regular tetrahedron when plotted over the Poincaré sphere.

When a Mueller polarimeter needs to be calibrated, first we calibrate the PSA using Eqs. (2-23). After that, the PSA is already operative to measure any incident SOP, in particular the polarization generators states generated by the PSG.

2.5.2 Eigenvalue calibration method

A second method for calibrating experimentally the polarimetric measurement matrix is the eigenvalue calibration method, ECM, described in detail in [137]. This calibration is for Mueller polarimeters and, it determines the matrices describing the PSG (S) and the PSA (A) by taken a set of flux measurements when measuring a set of calibration samples (see Eq.(2-9)). In our case, we have used as reference samples a Glan-Thompson polarizer distributed by CASIX and a quarter waveplate. The ECM does not require an accurate alignment of the reference samples because the optical properties of the samples and their orientations are unambiguously determined during the calibration itself. The essential steps of the ECM are the following:

1. A first measurement is taken without any sample: $P^{(0)}=AS$.
2. A set of measurements are carried out with the reference samples, characterized by the Mueller matrix $M^{(i)}$: $P^{(i)}=AM^{(i)}S$.
3. From each measurement $P^{(i)}$, and assuming a knowledge of the matrices of the reference samples, we can determine the characteristics of the reference samples (as orientation, retardance and diattenuation) from the eigenvalues of the matrix product: $[P^{(0)}]^{-1}\cdot P^{(i)}$, (see Ref. [137] for more detail).
4. S matrix is determined as the unique solution of the set of equations (see Ref. [137] for more detail): $M^{(i)}S-S[P^{(0)}]^{-1}\cdot P^{(i)}=0$
5. A matrix is eventually calculated as: $A=P^{(0)}S^{-1}$

This calibration methodology is widely used in the implementation of Mueller polarimeters, as in [49,101].

Chapter 3 **Polarimeter based on parallel aligned liquid crystal panels**

In this chapter, we present a polarimeter architecture based on two parallel aligned liquid crystal (PA-LC) cells. It is a time-sequential polarimeter, and the polarization analyzers are obtained by changing the retardances introduced by the LC cells. The proposed set-up is able to implement any polarization analyzer by properly selecting a pair of retardances introduced by the LC panels. By taking advantage of the versatility of the architecture, many polarization state analyzers (PSAs) have been thoughtfully analyzed. In particular, optimized PSAs with 4, 6, 8, 12 and 20 polarization analyzers have been deduced. In addition, non-optimized PSAs have been also studied, including a PSA to measure only linearly polarized light. A tolerance analysis is detailed in order to get a 1% of accuracy in the polarization measurements. Finally, the polarimeter is implemented using different PSA configurations, and several measurements are provided and discussed.

3.1 Design

In this section we present the design of a Stokes polarimeter based on two variable retarders using parallel aligned liquid crystal (PA-LC) cells. A PA-LC panel can be modeled as a variable linear retarder (LR), i.e. it has a variable retardance depending on the voltage addressed to the device, but the orientation of its fast axis is always constant. Its polarization eigenstates are two orthogonal linear states of polarization (SOPs). The LC molecules structure of the PA-LC cell and its features are explained in detail in subsection 1.3.1.1.

In Figure 3-1 we observe a sketch of the proposed set-up of a polarimeter based on two PA-LC cells. The incident light beam passes through two PA-LC panels orientated at 0º and 45º, as it has been proved that these two orientations are the optimal to analyze any SOP [99]. Their retardances, δ_2 and δ_1 respectively, are variable and they can be controlled by addressing a pair of voltages to the LC devices. After these two LC cells, a linear polarizer (LP) is placed at 0º, this is marking our vertical reference in the laboratory. Finally, a radiometer is measuring the flux transmitted by the last LP.

In order to deduce the expression of the polarization analyzer, first we need to calculate the total Mueller matrix describing the PSA (polarization state analyzer):

$$\begin{aligned} &M_{LP}(0º)\cdot M_{LR}(\delta_1,45º)\cdot M_{LR}(\delta_2,0º)= \\ &=\frac{1}{2}\begin{pmatrix}1&1&0&0\\1&1&0&0\\0&0&0&0\\0&0&0&0\end{pmatrix}\begin{pmatrix}1&0&0&0\\0&\cos\delta_1&0&-\sin\delta_1\\0&0&1&0\\0&\sin\delta_1&0&\cos\delta_1\end{pmatrix}\begin{pmatrix}1&0&0&0\\0&1&0&0\\0&0&\cos\delta_2&\sin\delta_2\\0&0&-\sin\delta_2&\cos\delta_2\end{pmatrix}= \\ &=\frac{1}{2}\begin{pmatrix}1&\cos\delta_1&\sin\delta_1\sin\delta_2&-\sin\delta_1\cos\delta_2\\1&\cos\delta_1&\sin\delta_1\sin\delta_2&-\sin\delta_1\cos\delta_2\\0&0&0&0\\0&0&0&0\end{pmatrix} \end{aligned} \qquad (3\text{-}1)$$

Where M_{LP} is the Mueller matrix of a linear polarizer[1] oriented at 0º and M_{LR} the Mueller matrix of a linear retarder, given by Eq.(1-4). Thus, the polarization analyzer corresponds to the first row of the matrix describing the whole PSA:

$$PA_{PA-LC}=\frac{1}{2}\begin{pmatrix}1&\cos\delta_1&\sin\delta_1\sin\delta_2&-\sin\delta_1\cos\delta_2\end{pmatrix}, \qquad (3\text{-}2)$$

where δ_2 and δ_1 are the retardances introduced by the LC panels. Note that Eq. (3-2), after being normalized with S_0, is analogous to the spherical coordinates where the two retardances are the angles which allow to move around the Poincaré sphere surface. Hence, any locus over the

surface of Poincaré sphere, representing a polarization analyzer, can be implemented by this set-up by properly choosing the pair of retardances introduced by the LC panels.

This feature indicates that our proposed set-up based on PA-LC cells is completely versatile, giving us the flexibility to design any PSA desired. In particular, we have focused on a PSA composed by 4, 6, 8, 12, 20, 40, 60, 80 and 100 analyzers which minimizes the noise propagation. Also, non-optimized PSAs have been studied with this set-up, including an incomplete polarimeter to measure linear SOPs.

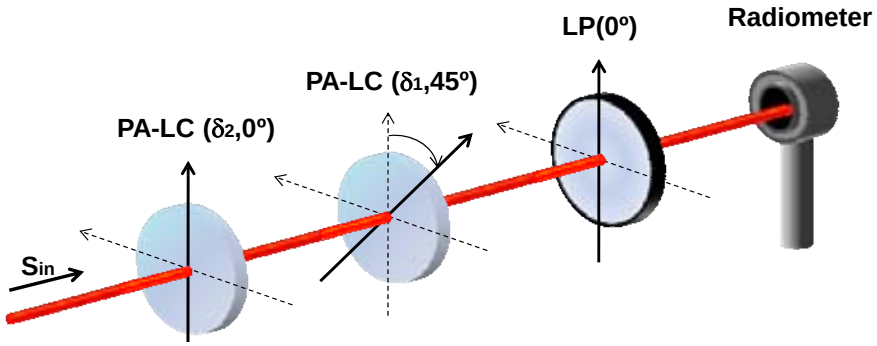

Figure 3-1: Set-up of a Stokes polarimeter based on two PA-LC panels.

3.1.1 Experimental characterization of the LC panel

We have used, as variable retarders, two monopixel parallel aligned nematic liquid crystal cells distributed by Meadowlark Optics (Figure 3-2). PA-LC cells present a tunable retardance by changing the effective birefringence of the material with applied voltage. The variable retarders are constructed using optically flat fused silica windows coated with transparent conductive Indium Tin Oxide (ITO). ITO coating is designed for maximum transmission in our working wavelength. A thin dielectric layer is applied over the ITO and gently rubbed, to provide for LC molecular alignment. Two windows are precisely aligned and spaced a few microns apart. The cavity is filled with birefringent nematic LC material, electric contacts are attached and the device is environmentally sealed.

Figure 3-2: PA-LC cell used in our set-up.

The function relating the voltage addressed to the LC panel and the obtained retardance is provided by the LC supplier company. However, in order to get better accuracy, an experimental calibration of the LC look-up-table is conducted. With this purpose, we implement the set-up of Figure 3-3. The PA-LC panel, orientated at 45º, is illuminated with a linearly polarized light at 0º. Then, we use a Stokes polarimeter to characterize the incident state of polarization (S_{in}). The Stokes polarimeter is composed by a rotating quarter waveplate (QWP) and a linear polarizer (LP) and its working principle is based on the Fourier analysis described in [1]. The QWP orientation is controlled by software and synchronized with the radiometer measurements.

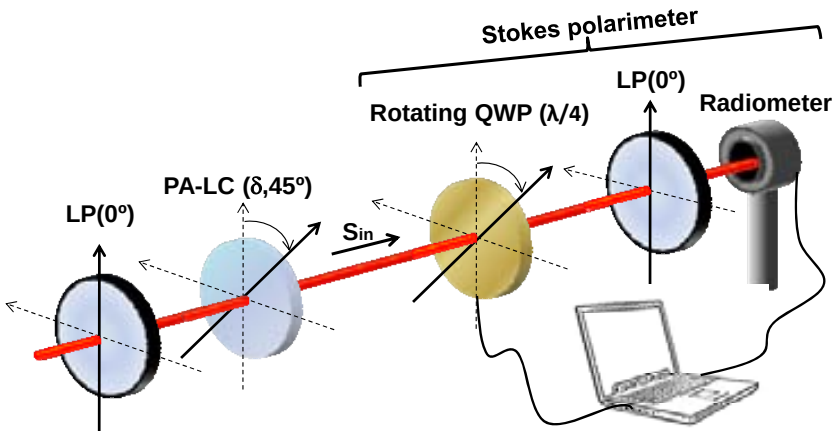

Figure 3-3: Experimental set-up to calibrate the retardance (δ) of the PA-LC panel.

The incident Stokes vector measured by the rotating Stokes polarimeter, which depends on the retardance introduced by the LC cell (and so, on the applied voltage), has the following expression:

$$S_{in} = \begin{pmatrix} S_0 \\ S_1 \\ S_2 \\ S_3 \end{pmatrix} = M_{LR}(\delta,\theta)\cdot \begin{pmatrix} 1 \\ 1 \\ 0 \\ 0 \end{pmatrix} = \begin{pmatrix} 1 \\ \cos^2 2\theta + \cos\delta \sin^2 2\theta \\ (1-\cos\delta)\sin 2\theta \cos 2\theta \\ \sin\delta \sin 2\theta \end{pmatrix}, \tag{3-3}$$

where θ=45º and δ are the orientation and retardance of the PA-LC panel, respectively. The retardance introduced by the LC panel can be expressed as function of the Stokes parameters measured by the polarimeter:

$$\delta = \arctan\left(\frac{S_3 \sin 2\theta}{S_1 - \cos^2 2\theta}\right). \tag{3-4}$$

We have carried out a calibration of the PA-LC cell, illuminating with a He-Ne laser (633nm) and sending an array of voltages from 0.5V to 5.25V in increments of 0.25V. Figure 3-4 shows the experimental values obtained. Moreover, we plot a polynomial function, fitting the experimental data and, it has the following expression:

$$V = -9.458\times10^{-15}\cdot\delta^6 - 3.002\times10^{-13}\cdot\delta^5 + 5.668\times10^{-9}\cdot\delta^4 - \\ -2.679\times10^{-6}\cdot\delta^3 + 5.248\times10^{-4}\cdot\delta^2 - 5.534\times10^{-2}\cdot\delta + 4.952 \quad (3\text{-}5)$$

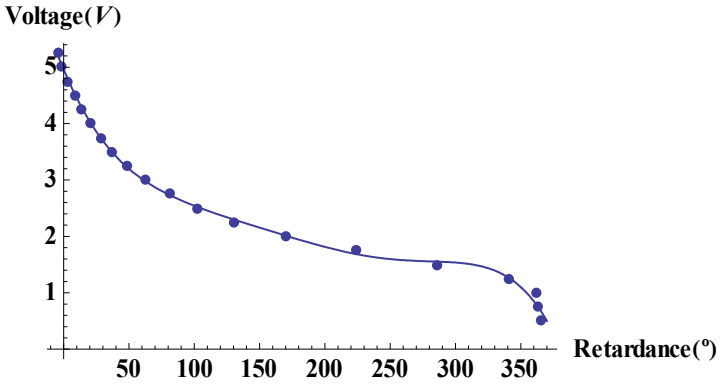

Figure 3-4: PA-LC look-up-table relating voltage addressed with the retardance achieved. Experimental data in points and polynomial fitting in continuous line. 633nm as illumination wavelength.

Note that the plotted *V(δ)* function behaves as mentioned in subsection 1.3.1.1, the higher the voltage, the smaller the retardance achieved. The LC cell has a null of retardance with a high voltage. This value is achievable due to a compensator attached to the liquid crystal cell, a subtractive fixed anisotropic polymer providing a retardance that compensates the residual retardance from the pinned molecules at the surface.

Afterwards, we have measured the transitory time between two stable PA-LC configurations when changing the addressed voltage. The experiment consists in measuring the intensity as function of time when changing the voltage addressed to the LC cell. In order to detect a variation in intensity, we place a LP between the LC cell and the radiometer, being this last element the device that measures the intensity evolution. Figure 3-5 (a) and (b) show the intensity as function of time when, respectively, the voltage is changed from 0 to 1.5V and, from 1.5 to 0V. The measured transitory times of these two cases are of 300 and 80 milliseconds, respectively.

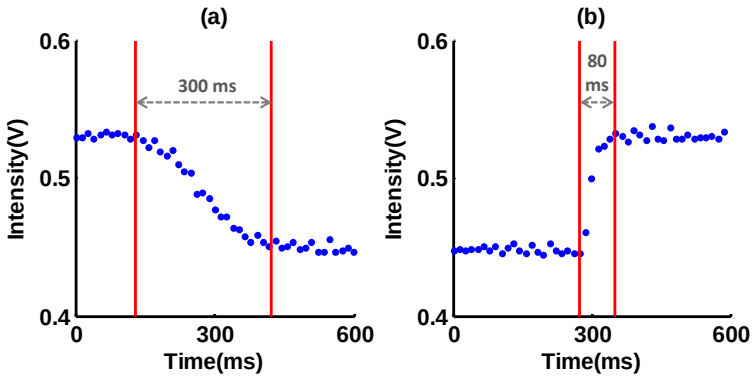

Figure 3-5: Time response of the PA-LC cell when changing voltage: (a) from 0 to 1.5V, (b) from 1.5 to 0V.

3.2 Optimization analysis

In section 2.3 the importance of conducting an optimization of the PSA is explained, in this way there is a reduction of the noise propagation from intensity measurements to the Stokes vector. In addition, set-up of Figure 3-1 allows implementing any fully polarized analyzer by properly choosing the pair of retardances to the LC panels according to Eq. (3-2). This feature allows us to conduct a thorough optimization study of different PSA configurations without any restriction imposed by the polarimeter architecture. This section details the optimization process conducted to different PSAs with different number of polarization analyzers. Afterwards, non-optimized PSAs are also described and their quality indicators are compared with those parameters corresponding to the optimized configurations. All of these analyzed PSAs systems can be implemented with the same polarimeter architecture based on 2 PA-LC panels. Finally, a last subsection studies the sensibility of the PSAs to small deviations from the theoretical configurations.

3.2.1 Optimized polarimeters with different number of measurements

First of all, we focus on optimizing a PSA composed by a set of *n* polarization analyzers by minimizing the condition number (CN) of the polarimetric measurement matrix. This optimization is conducted through a computing process by following these steps:

1. We start with *n* polarization analyzers (PAs) randomly chosen over the surface of the Poincaré sphere.

2. A MATLAB optimization function minimizes the CN for different sets of *n* polarization analyzers, starting from the initial random set of PAs. We fix some parameters to set a termination criterion, including a termination tolerance on the function value and a maximum number of function evaluations. The minimum CN achieved and the corresponding set of PAs are recorded.

3. In order to avoid a local minimum, steps 1 and 2 are repeated *N* times. In step 1 of each iteration, it starts with a new set of random PAs.

4. It gives the global minimum CN after these *N* iterations and the associated set of polarization analyzers.

5. A last minimization is conducted, starting from the set of PAs with the global minimum CN obtained in step 4.

6. Finally, the result of the complete optimization process is the set of PAs given by step 5. Therefore, the polarimetric measurement matrix associated to this set of PAs will have the global minimum CN of the whole process.

In Figure 3-6 we plot the result of the optimization process for diverse PSAs with different number of polarization analyzers (n). The PAs reached by the optimization are plotted over the Poincaré sphere. In particular when n = 4, 6, 8, 12 and 20, the PAs are represented as vertices of inscribed polyhedrons in order to show an interesting property in PSA optimization explained straightaway. When conducting the CN minimization for n=4, the optimization process leads to 4 PAs that, represented over the Poincaré sphere, are the vertices of a regular tetrahedron inscribed into the sphere, as shown in Figure 3-6(a). It has a condition number of 1.73. This result is in agreement with previous works [98,125], showing that the minimum CN of a polarimetric measurement matrix is $\sqrt{3}$. If we repeat the optimization process for this particular case, the solution is always a regular tetrahedron inscribed into the Poincaré sphere, although with different orientation. Therefore, any of the infinite regular tetrahedrons inscribed into the Poincaré sphere gives the best solution when optimizing polarimeters with four polarization analyzers. From now on, we will refer to this regular tetrahedron PSA configuration (CN=1.73) as the best optimized polarimeter for 4 measurements. In further chapters, other set-ups will be studied although with some PAs restrictions, which will constrain the optimization process, leading to PAs sets providing larger CN values. Afterwards, we optimize PSAs with rectangular polarimetric measurement matrix W (i.e. n>4). In particular, we focus on n = 6, 8, 12 and 20 polarization analyzers. We observe that the result of the optimization process corresponds to a set of PAs located at the vertices of the convex regular polyhedron with n vertices inscribed into the Poincaré sphere, also well-known as Platonic solids. That is to say, the PAs are drawing a regular octahedron, cube, icosahedron and dodecahedron respectively in Figure 3-6(b)-(e). These results show the importance of maximizing the volume enclosed by the PAs when representing them over the Poincaré sphere. Essentially, when we are maximizing the volume enclosed by the PAs, the polarimetric measurement matrix is moving away from singular matrices and so, minimizing the CN. Consequently, when optimizing a PSA with n polarization analyzers, if a regular polyhedron with the same number n of vertices exists, this will be the best optimized configuration. In all the other cases, the CN minimization process tends to distribute the PAs over the Poincaré sphere equally separated from the other ones. As an example, in Figure 3-6(f) we show the PSA optimization result when n = 100 PAs. As expected, it exhibits an equidistant distribution, maximizing the enclosed volume for these.

We have extended this study for other number n of polarization analyzers, and the result of the condition number and the equally weighted variance as function of n is shown in Figure 3-7(a) and (b), respectively. Note that the CN is almost constant for all the optimized polarimeters at the

value of $\sqrt{3} = 1.732$, independently of the number of PAs used, in accordance with [99]. Flatness indicates that all optimized polarimeters have a polarimetric measurement matrix similarly well conditioned. In contrast, the EWV is dependent on the number of polarization analyzers used during a Stokes vector measurement. As it is well-known, data redundancy in experiments leads to decrease the variance of measurement and consequently, the EWV decreases as well. Therefore, CN criterion is suitable for each individual optimization, ensuring a well conditioning of the system. Whereas EWV criterion is useful for comparing different polarimeters with different number of polarization analyzers and perceiving the data redundancy benefit.

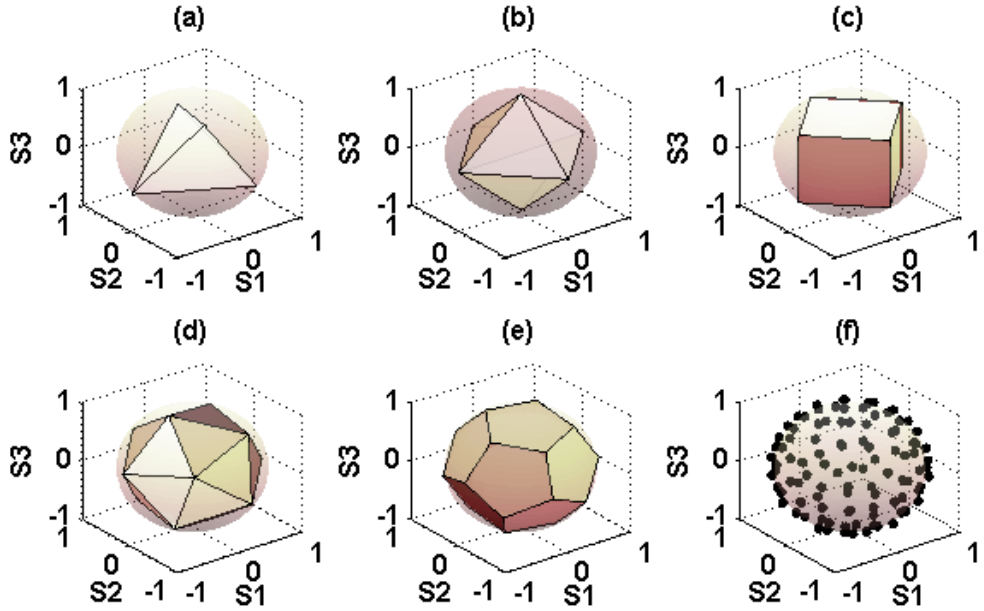

Figure 3-6: Result of the CN optimization process for (a) 4, (b) 6, (c) 8, (d) 12, (e) 20 and (f) 100 polarization analyzers. The vertices of the polyhedrons are representing the PAs, located upon the Poincaré sphere surface.

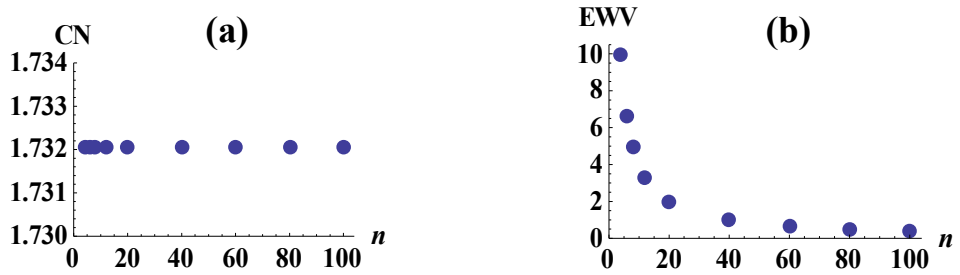

Figure 3-7: (a) Condition number and (b) equally weighted variance of the optimized polarimeters as function of the number of polarization analyzers (*n*).

To complete the analysis of the polyhedrons PSAs, we conduct a last study. We analyze the Stokes parameters variances and their dependency with the orientation of the polyhedron upon the Poincaré sphere. We have rotated each polyhedron over the S_1, S_2 and S_3 axes, and we have examined their Stokes parameters variances as function of the rotation angle. We state that regular

polyhedrons have constant Stokes variances, independent on the orientation of the polyhedron over the Poincaré sphere, and their values are shown in Table 3-1. In addition, the PSA with 100 PAs equally distributed over the Poincaré sphere (Figure 3-6(f)) is also analyzed, and it has the same behavior as the regular polyhedrons, constant Stokes parameters variances independent on the rotation angle. Moreover, S_1, S_2 and S_3 variances take the same value for each polyhedron evaluated. This is due to the regular distribution of the PAs over the Poincaré sphere. Last row of Table 3-1 contains the EWV calculated as the addition of the four Stokes parameters variances. Note that these EWV values coincide with the EWV plot represented in Figure 3-7(b), calculated from the singular values of matrix W (see Eq.(2-18)). We observe a clear decreasing of the EWV as we increase the number of PAs because of the redundancy benefits when we take more measurements.

Table 3-1: Stokes parameters variances and equally weighted variance of the regular polyhedrons PSAs composed by 4, 6 8, 12 and 20 Polarization Analyzers (PAs). Also the PSA with 100 PAs equally distributed over the Poincaré sphere surface.

Number of PAs	**4**	**6**	**8**	**12**	**20**	**100**
$\sigma^2(S_0)$	1.00	0.67	0.50	0.33	0.20	0.04
$\sigma^2(S_1)$	3.00	2.00	1.50	1.00	0.60	0.12
$\sigma^2(S_2)$	3.00	2.00	1.50	1.00	0.60	0.12
$\sigma^2(S_3)$	3.00	2.00	1.50	1.00	0.60	0.12
EWV	10.00	6.67	5.00	3.33	2.00	0.40

3.2.2 Non-optimized polarimeters with four measurements

Next, we studied different PSAs with 4 measurements, although PAs location on the Poincaré sphere is not the optimized configuration (i.e. the regular tetrahedron). Their associated quality indicators are analyzed and compared with the values obtained with the regular tetrahedron PSA.

The different non-optimized PSAs studied are represented into the Poincaré sphere in Figure 3-8 as polyhedrons whose vertices are the polarization analyzers. Figure 3-8(a) describes a PSA with 3 PAs equally distributed on the equator whereas the last PA is at the north pole of the

Poincaré sphere. Figure 3-8(b) represents a PSA with 3 PAs forming an isosceles triangle on the equator whereas the last PA is also at the north pole of the Poincaré sphere. Finally, Figure 3-8(c) depicts a PSA with 4 PAs equally distributed in the equator of the sphere, forming a square. The PSAs represented in Figure 3-8(a), (b) and (c) have a CN of 2.48, 3.23 and infinite, respectively. Regarding these values, we reaffirm that as smaller the CN, better optimization and larger the polyhedron volume. In particular, if the polyhedrons are sorted from the larger to the smaller volume, we obtain the following list: the regular tetrahedron (it has the maximum volume and has the minimum CN), the tetrahedron with an equilateral triangle base, the tetrahedron with an isosceles triangle base and the square (it has null volume and infinite CN). Actually, PSA represented in Figure 3-8(c), with a null of volume, corresponds to an incomplete polarimeter.

Another interesting feature of these non-optimized PSAs is their Stokes variances and their dependency with the rotation angle. In particular, the ones associated to linear polarization measurements (S_1 and S_2) when rotating around the S_3 axis. The Stokes parameters variances and their addition (i.e. the EWV) are represented in Figure 3-9 as function of the rotation angle of the polyhedron around the S_3 axis.

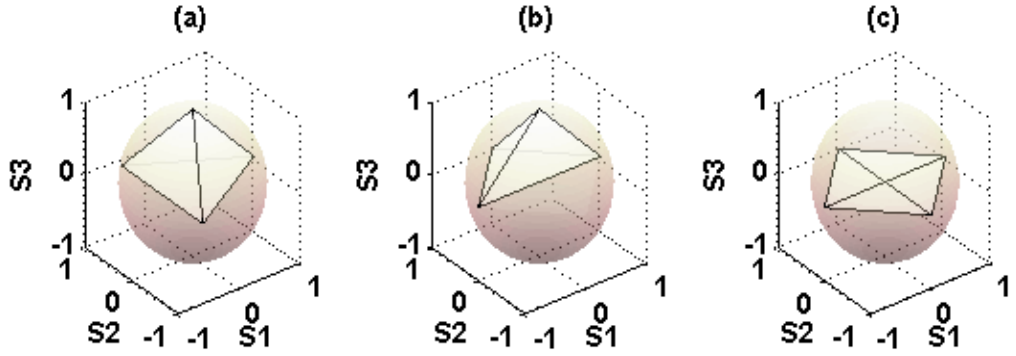

Figure 3-8: Non-optimized PSAs with 4 polarization analyzers: (a) 3 PAs are forming an equilateral triangle on the equator and one PA on the north pole, (b) 3 PAs are forming an isosceles triangle on the equator and one PA on the north pole and, (c) 4 PAs are forming a square on the equator of the Poincaré sphere.

First, the regular tetrahedron (Figure 3-6(a)) Stokes variances are represented in Figure 3-9(a). We observe as mentioned before, that variances and EWV are independent on the rotation angle. Note that Stokes parameter variances S_1, S_2 and S_3 take the same value (3) because their equally distribution over the Poincaré sphere.

Second, the specific variances for the irregular tetrahedron with an equilateral triangle base (Figure 3-8 (a)) are plotted in Figure 3-9(b). S_1 and S_2 variances (2.67) are smaller than the S_3 variance (5.3). This is because 3 PAs are analyzing linear polarization content in front of a single PA measuring circular polarization content. In addition, S_1 and S_2 variances are equal due to the equally separated distribution on the plane S_1-S_2 (the PAs are drawing an equilateral triangle on

the equator plane). In addition, the Stokes variances are independent on the rotation angle around S_3 axis because there is symmetry with respect to this axis.

Third, the variances for the irregular tetrahedron with an isosceles triangle base (Figure 3-8(b)) are plotted in Figure 3-9(c). In this configuration, due to the non-equally separated distribution of the 3 PAs lying on the plane S_1-S_2, S_1 and S_2 variances are dependent on the rotation angle. When the polyhedron is as represented in Figure 3-8(b), 2 PAs are aligned in the S_1 axis, whereas in S_2 axis there is just a single PA as well as in S_3 axis. This is the explanation why at θ=0º, the variances of S_2 and S_3 are equal, and larger than S_1. After rotating $\pi/2$, now is the S_2 axis where there are two PAs and the other orthogonal axes just a single PA. Thus, variances S_3 and S_1 are equal and larger than S_2. In this way, as we rotate the polyhedron the variances S_1 and S_2 vary sinusoidally due to the varying presence of PAs on both axes.

Finally, only the S_0, S_1 and S_2 variances for the square configuration (Figure 3-8 (c)) are plotted in Figure 3-9(d). S_3 variance is not represented because this configuration does not obtain information about circular or elliptical polarization content. S_1 and S_2 variances take the same value (2), being smaller than the value obtained with the tetrahedron configuration. This feature remarks the importance of choosing the proper PSA configuration suitable for your type of measurement. For instance, if the Stokes polarimeter is used for measuring an arbitrary SOP, a regular tetrahedron polarimeter is the recommended one. Nevertheless, if only a certain SOPs are desired to be measured, the recommended PSA should have smaller variances on those Stokes parameters that we want to measure. For instance, if we are only interested in measuring linear polarization, the square PSA is the best option because S_1 and S_2 have smaller variances than the other configurations, including the regular tetrahedron.

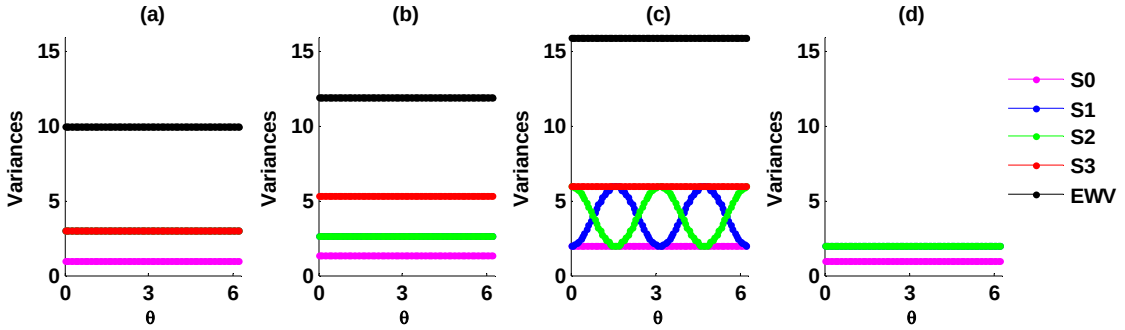

Figure 3-9: Stokes parameters variances and EWV as function of the rotation angle around S_3 axis (θ, in radians) of the PSAs: (a) regular tetrahedron (Figure 3-6(a)) , (b) irregular tetrahedron with an equilateral triangle base (Figure 3-8 (a)), (c) irregular tetrahedron with an isosceles triangle base (Figure 3-8 (b)) and, (d) square on the equator (Figure 3-8 (c)).

3.2.3 Polarimeters robustness

Up to now, we have studied different Stokes polarimeters, described by a PSA-polyhedron, and their quality indicators have been thoroughly analyzed, including optimized PSAs as well as non-optimized PSAs. These PSA configurations, discussed in sections 3.2.1 and 3.2.2, from now on are referred as theoretical configurations or as ideal PSAs. However, it is also interesting to simulate when these PSAs are experimentally implemented and they differ from the theoretical configurations due to experimental errors, later listed. With the aim of quantifying how these small deviations will affect on the optimization of the PSA, we calculate the quality indicators for these deviated PSA sets. There are different reasons why these variations will occur in future implemented PSAs compared to the theoretical configurations, such as small misalignments on the orientation of the optical elements (theoretically, the LP should be at 0º, and the PA-LC cells at 45º and 0º), deviations of the effective retardance produced by the variable retarder compared with the calibrated value (look-up-table in Figure 3-4) due to a small tilt of the LC cells, or a temperature variation compared to the one during the LC calibration (retardance decreases by approximately 0.2% per 1ºC increase in temperature as provided by the LC manufacturer).

Under this scenario, we conduct a study to analyze these variations and their effect on the quality indicators. We take the ideal PSA, composed by n PAs located in particular optimized points over the Poincaré sphere, and we add a given deviation to these PAs. These variations are values taken from a random uniformly distribution, with zero mean and amplitude 0.4 (20% of the Stokes parameter range). From this deviated PSA configuration, we calculate its condition number, its Stokes parameters variances and the equally weighted variance. To have a statistically significant study, this simulation is repeated 50 times for each analyzed PSA.

First, regular polyhedrons presented in Figure 3-6 are used as initial PSAs. Results of the CN and the specific variances of the deviated PSAs are represented in Figure 3-10 and Figure 3-11, respectively. Particularly, subfigures (a), (b), (c), (d), (e) and (f) are the results when the PSA is composed by 4, 6, 8, 12, 20 and 100 PAs, respectively. Obviously, the CN values (and also the variances) of deviated PSAs are always larger than the values obtained for the theoretical configuration, which was obtained after minimizing the CN. Even though the same uniform distribution has been used to deviate the PAs (amplitude of 0.4), we observe as larger the number of PAs used in the PSA, smaller the fluctuations on the quality indicators. However, even for the smallest number of PAs (i.e. the regular tetrahedron, n=4), the variances values and CN values are small enough to ensure an optimum performance of the polarimeter under these circumstances.

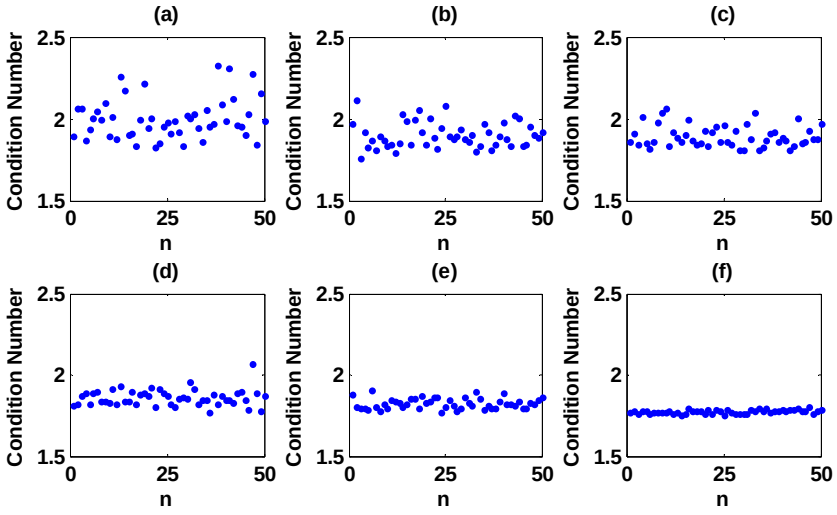

Figure 3-10: Condition number of 50 different simulated PSAs deviated from the theoretical regular polyhedrons configurations of Figure 3-6, when adding to the PAs a value from a zero mean uniform distribution of amplitude 0.4. The PSAs are formed by: (a) 4, (b) 6, (c) 8, (d) 12, (e) 20 and (f) 100 polarization analyzers.

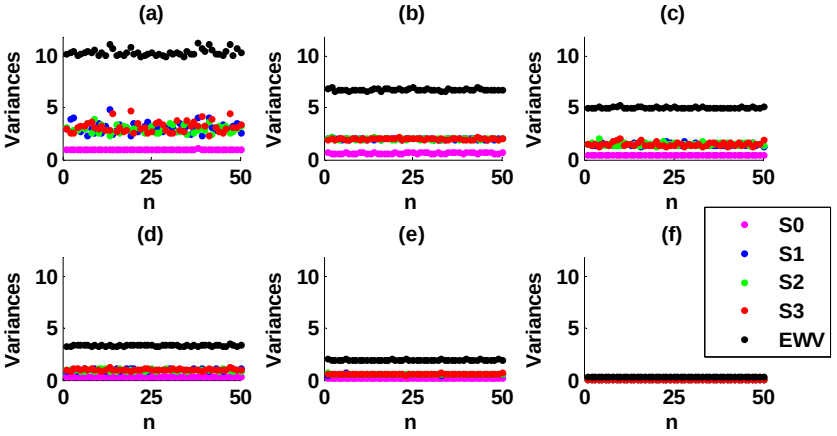

Figure 3-11: Variances of 50 different simulated PSAs deviated from the theoretical regular polyhedrons configurations of Figure 3-6, when adding to the PAs a value from a zero mean uniform distribution of amplitude 0.4. The PSAs are formed by: (a) 4, (b) 6, (c) 8, (d) 12, (e) 20 and (f) 100 polarization analyzers.

We repeat this study with the non-optimized PSAs, represented in Figure 3-8, as ideal PSAs to be deviated. The CN and the variances of the deviated PSAs are shown in Figure 3-12 and Figure 3-13, respectively. Subfigures (a), (b) and (c) corresponds to PSAs of Figure 3-8(a), (b) and (c) respectively, where all three systems use 4 PAs, but their representation over the Poincaré sphere and conditioning are different. As mentioned before, the CN of the PSA with 4 PAs located on the equator of the Poincaré sphere is infinite. Nevertheless, when we generate some deviations to the constituent PAs, the PSA encloses a small volume but different from zero and at the same time, it has a non infinite CN with a very high value. The same happens with S_3 variance and the addition of all variances (EWV). However, as this particular configuration is intentioned to measure only linear polarization content, we have decided to plot only the

variances of the elements S_1 and S_2. Whereas CN, S_3 variance and EWV are not plotted because they are referring to general polarization content. Comparison of Figure 3-12 and Figure 3-13 with Figure 3-10(a) and Figure 3-11(b) revealed that when a non-optimized PSA is implemented, subject to some deviations from the theoretical configuration, the quality indicators worsening is larger than if the initial system is optimized. Therefore, working with an optimized PSA not only minimizes the noise amplification under ideal situation (no deviations), but also the experimental polarimeter is more robust (i.e. the actual experimental values of the CN and the EWV do not differ significantly from those associated to the ideal PSA).

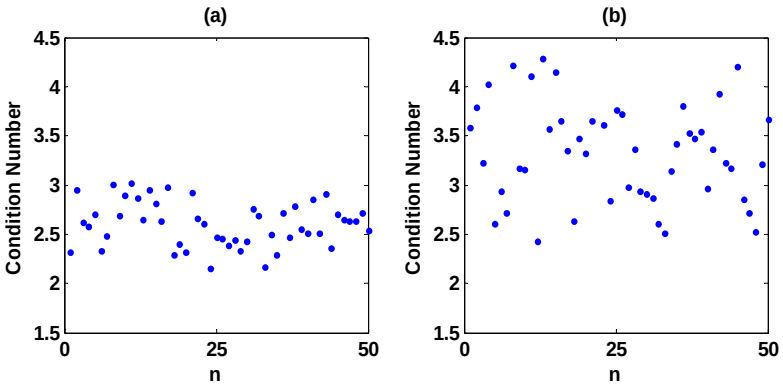

Figure 3-12: Condition number of 50 different simulated PSAs deviated from the theoretical non-optimized PSA configurations of Figure 3-8, when adding to the PAs a value from a zero mean uniform distribution of amplitude 0.4. The PSAs are formed by 4 PAs and their location over the Poincaré sphere is: (a) 3 PAs are forming an equilateral triangle on the equator and one PA on the north pole and, (b) 3 PAs are forming an isosceles triangle on the equator and one PA on the north pole.

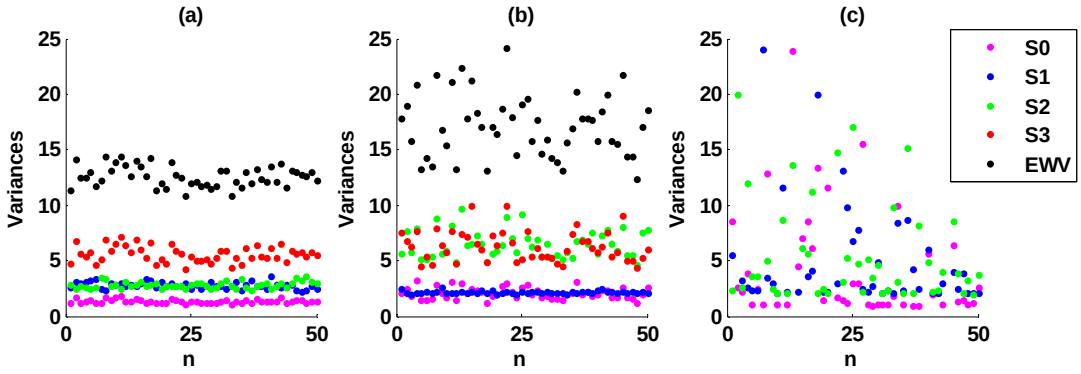

Figure 3-13: Variances of 50 different simulated PSAs deviated from the theoretical non-optimized PSA configurations of Figure 3-8, when adding to the PAs a value from a zero mean uniform distribution of amplitude 0.4. The PSAs are formed by 4 PAs and their location over the Poincaré sphere is: (a) 3 PAs are forming an equilateral triangle on the equator and one PA on the north pole, (b) 3 PAs are forming an isosceles triangle on the equator and one PA on the north pole and, (c) 4 PAs are forming a square on the equator of the Poincaré sphere.

3.3 Tolerance analysis

In this section we report the tolerance analysis of a Stokes polarimeter based on two PA-LC cells. We focus on the PSA of a regular tetrahedron because we have demonstrated it is the best optimized configuration, as well as it is the most robust under experimental variations in the laboratory.

The goal of this study is to quantify the tolerances of the parameters involved in our experimental set-up in order to achieve a given accuracy in the polarization measurement, in particular of 1%. There are four parameters under study, and they are the two orientations (θ) and the two retardances (δ) of both variable retarders (see Figure 3-1). The orientation of the LP is our vertical reference in the laboratory, for this reason it is not subject to misalignment.

First of all, we focus on each individual parameter and how a given tolerance affects on the Stokes vector measurement. As mentioned in section 2.4.1, the Stokes error depends on the polarization of the incident beam to be measured. Thus, we study the Stokes parameter error as function of the incident Stokes vector using the parameterization of Eq.(2-21). In particular, in Figure 3-14 (a), (b), (c) and (d) we show this study with a tolerance of 1º for the parameters θ_1, θ_2, δ_1 and δ_2. We observe that the Stokes parameters errors have a strong polarization dependence. By roughly comparing, it is noticeable that Stokes parameters error is less sensitive to a variation in the retardance (Figure 3-14 (c), (d)) than in the orientation (Figure 3-14 (a), (b)) of the LC cells.

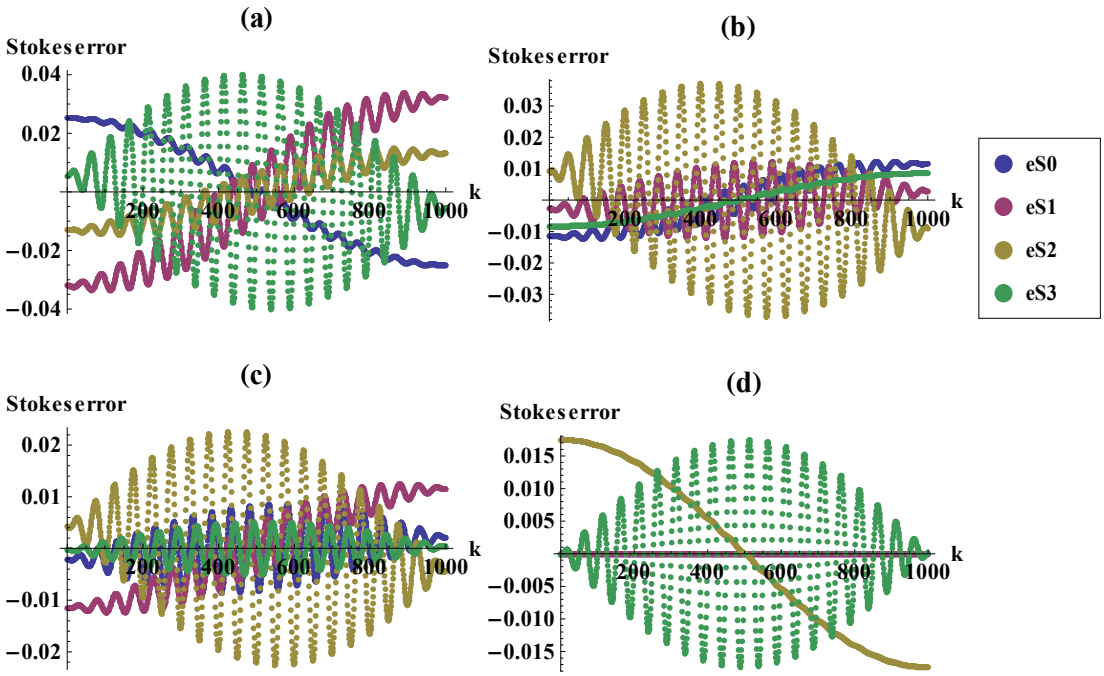

Figure 3-14: Stokes parameters errors with a tolerance of 1º in: (a) the orientation of PA-LC$_1$ (θ_1), (b) the orientation of PA-LC$_2$ (θ_2), (c) the retardance of PA-LC$_1$ (δ_1) and (d) the retardance of PA-LC$_2$ (δ_2). Errors as function of variable k, which parameterizes the incident Stokes vector following Eq.(2-21).

Afterwards, we calculate the accuracy of the polarimetric system for given parameters tolerances. The accuracy is calculated as the highest error of the 4 Stokes errors regarding all the incident polarizations. Figure 3-15 shows the accuracy of the Stokes polarimeter as function of the parameter tolerances. Because of a linear dependency is clearly observed, we have also included a linear regression in the plot. Next, the mathematical expressions of these linear regressions are equaled to an accuracy of 1% (i.e. a Stokes error of 0.02 marked with a red dashed line in Figure 3-15), and the values of the tolerances obtained are shown in Table 3-2. Data shown in the tolerance table asserts that the polarimeter has a larger tolerance on the retardance values (0.89-1.15) than on the orientation of the LC cells (0.50-0.54).

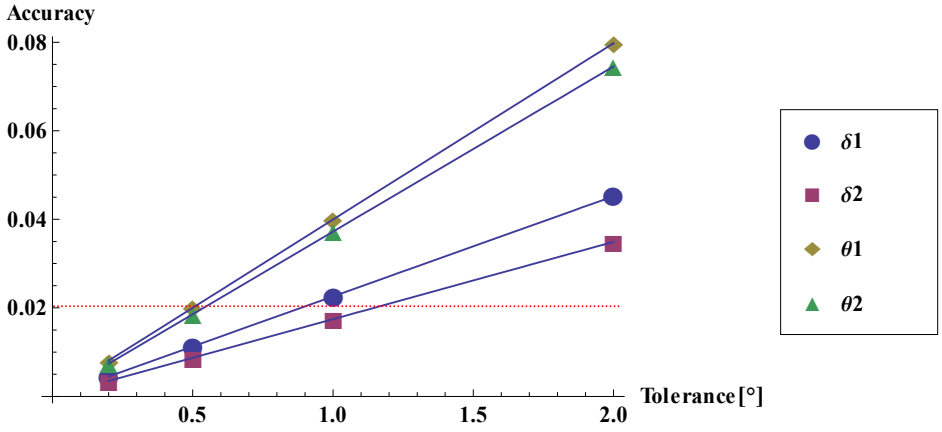

Figure 3-15: Accuracy of Stokes polarimeter based on 2 PA-LC cells with a regular tetrahedron PSA configuration as function of the tolerance of parameters involved in the set-up.

Table 3-2: Tolerance values to achieve an accuracy of 1% in the Stokes vector measurements, concerning the parameters involved in the set-up: orientation (θ) and retardance (δ) of the PA-LC cells (1 and 2).

Parameter	θ_1	θ_2	δ_1	δ_2
Tolerance (º)	0.50	0.54	0.89	1.15

Finally, we focus on our experimental implementation and the actual tolerances of the optical elements available in our laboratory to implement the polarimeter. On the one hand, the PA-LC cells have a retardance which decreases by approximately 0.2% per 1ºC increase in temperature. Ensuring a calibration of the PSA system before starting the set of measurements, we assume a temperature variation of less than 1ºC during the calibration procedure and the measurements. Thus, we work in the tolerance range of the LC retardance to achieve an accuracy of 1%. On the other hand, whereas it is difficult to determine a priori the orientation of the LC cell with a precision of 0.5, after conducting the PSA experimental calibration we assume that the actual LC cell orientation is properly determined under an uncertainty of 0.5. We point out that

LC based polarimeters present an important advantage now evidenced, there are not mechanical movements of the optical elements and so, after an accurate calibration of the system, the optical elements are not subject to future misalignments. Therefore, our Stokes polarimeter is able to measure Stokes vectors with an accuracy of 1%, although is required an accurate calibration of the PSA system before starting to measure. It is also recommended to check the temperature to make sure that temperature variation is smaller than 1ºC during the calibration procedure and the acquisition of measurements.

3.4 Implementation

In this section we describe the implementation of the Stokes polarimeter based on two PA-LC panels. In Figure 3-16, there is a picture of the implemented polarimeter in the laboratory. The polarimetric system is formed by two monopixel PA-LC cells from Meadowlark Optics and a linear polarizer also from Meadowlark Optics. The electrical signal addressed to the LC cells is sent by a control module (D3040 Quad Cell Nematic Liquid Crystal Digital Interface) provided by Meadowlark Optics. This device generates 2-kHz null-offset squarewave signals on four different channels. Squarewaves amplitude is variable, from 0 to 10V, and it is configured on a PC and later communicated to the controller. Thus, the LC retardance is controlled according to the peak-to-peak voltage regarding the calibrated function voltage-retardance of Figure 3-4. In addition, the flux measurements are acquired with a photodiode (silicon detector with a spectral range 400-1100nm, model 818-SL/DB), connected to an optical power meter from Newport. The optical power meter is connected to an analog to digital (A/D) convertor from Keithley. This A/D converter converts the flux measurement value to digital, being able to be read by a PC. Concerning the illumination, a He-Ne laser (633nm) is used as monochromatic light source.

Customized software developed by our group in LabView code is used to control the output signals sent to the LC cells and the input signal from the flux detector. The experimental procedure to send and measure with the polarimeter is the following. First, two electrical signals are addressed to the LC cells by means of the control module (the signals amplitudes were previously chosen through the software). Then, during certain time (1000 milliseconds) we wait until LC molecules are aligned. Note that this waiting time period is much larger than the measured LC transitory time in Figure 3-5 (300ms), avoiding a wrong measurement during transitory states. Finally the radiometer takes 500 flux measurements with a speed of 5000 samples per second.

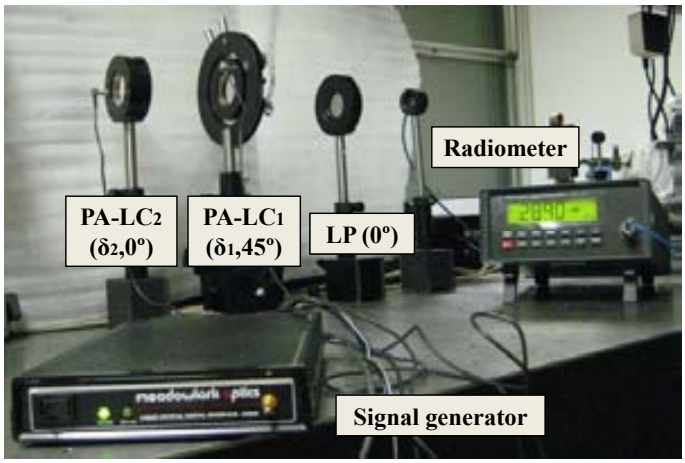

Figure 3-16: Implemented polarimeter set-up in our laboratory. Stokes polarimeter based on two variable retarders (parallel aligned LC cells) and a linear polarizer.

3.4.1 Calibration

We used the sequential calibration method to determine the polarimetric measurement matrix. The calibration procedure, detailed in section 2.5.1, consists in illuminating with 4 known SOPs and solving a system of linear equations.

Among the different PSAs described in sections above (suitable for polarimeter architecture of Figure 3-16), we have selected for implementation the optimized PSAs with 4 (Figure 3-6(a)), 20 (Figure 3-6(e)) and 100 (Figure 3-6(f)) PAs, as well as the incomplete PSA to measure only linear polarization content (Figure 3-8(c)). Respectively, the result of the calibration is plotted in Figure 3-17 (a), (b), (c) and (d). In particular, the theoretical PSA is plotted in green points and the calibrated PSA in red points. We observe a clear correspondence between both red and green colored PAs although there are small differences. These differences might be due to a temperature variation between the LC calibration and the PSA calibration, or a small misalignment of the LC cells. By using the calibrated polarimetric measurement matrix, we will take into account those small experimental differences, leading to more accurate polarization measurements. In this way, we will work on the tolerance range for the different parameters presented in Table 3-2.

Furthermore, Table 3-3 provides the CN of the calibrated PSAs (only corresponding to complete polarimeters). We observe that these small deviations from the theoretical configurations affect differently to the CN depending on the number of PAs. As discussed in Figure 3-17, as larger the number of PAs used in the PSA configuration, more robust is the system, achieving a CN closer to the ideal one (1.73).

Table 3-3: Condition number of the polarimetric measurement matrix experimentally calibrated for different implemented PSAs.

PSA	Tetrahedron	Dodecahedron	100 PAs
Experimental CN	1.89	1.77	1.74

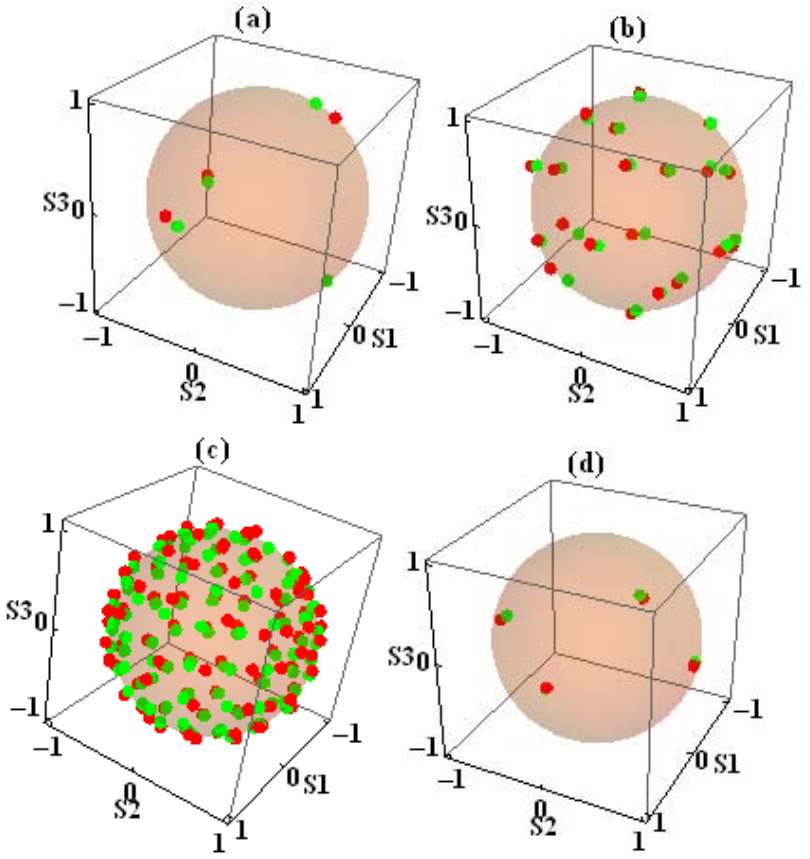

Figure 3-17: Theoretical and calibrated PSAs in green and in red, respectively, for the optimized configurations when using: (a) 4 (regular tetrahedron), (b) 20 (dodecahedron) and (c) 100 PAs, whereas in (d) incomplete polarimeter for measuring linear SoPs.

3.4.2 Experimental measurements

Once the polarimeters are calibrated, the experimental set-up is ready to take measurements. In this section, three different studies are provided and the results are carefully discussed.

First, a comparison of the measurements taken by the three optimized polarimeters (regular tetrahedron, dodecahedron and 100PAs) is detailed in Table 3-4. Each polarimeter is tested by measuring 3 prepared light beams with different polarization: linear, elliptical and circular SOPs. Moreover, these experimental results are compared with those obtained with a

commercial polarimeter (Polarization Analyzer System, PAN 5710 VIS, S/N: M60217605), distributed by Thorlabs. Each Stokes vector of Table 3-4 shows the mean and the standard deviation after taken 100 measurements of the same SOP. Regarding Stokes parameters means, they are in agreement with the reference values given by the commercial polarimeter. Moreover, we point out that the maximum difference between the reference value and the measurement is of 0.04. Regarding the standard deviation of the implemented polarimeters, this is dependent on the number of PAs used by the polarimeter. Standard deviation of the Stokes parameters measured with the tetrahedron, the dodecahedron and the 100PAs polarimeter is, respectively, in the range of 0.010-0.011, 0.004-0.005 and 0.002-0.003. Thus, as more PAs are involved in the polarimeter, better the repeatability of the measurement. Nevertheless, as more PAs are used, the instrument spends more time to measure the SOP. For instance, the 100PAs polarimeter needs 25 times more time than the tetrahedron polarimeter. Therefore, there is a trade-off between repeatability and measurement duration. A reasonable solution is to choose the number of PAs corresponding to a repeatability of the same order as the accuracy of your device (in this case, the regular tetrahedron).

Table 3-4: Stokes vector measurements (mean and standard deviation) corresponding to 3 different incident SOPs.

Polarimeter	**Tetrahedron**	**Dodecahedron**	**100 PAs**	**Commercial**
Linear SOP	$\begin{pmatrix} 1 \\ -0.769 \pm 0.010 \\ 0.630 \pm 0.010 \\ 0.011 \pm 0.010 \end{pmatrix}$	$\begin{pmatrix} 1 \\ -0.755 \pm 0.005 \\ 0.653 \pm 0.005 \\ -0.002 \pm 0.005 \end{pmatrix}$	$\begin{pmatrix} 1 \\ -0.763 \pm 0.003 \\ 0.637 \pm 0.002 \\ 0.006 \pm 0.002 \end{pmatrix}$	$\begin{pmatrix} 1 \\ -0.766 \pm 0.001 \\ 0.643 \pm 0.001 \\ -0.002 \pm 0.001 \end{pmatrix}$
Elliptical SOP	$\begin{pmatrix} 1 \\ 0.001 \pm 0.010 \\ 0.662 \pm 0.011 \\ 0.747 \pm 0.011 \end{pmatrix}$	$\begin{pmatrix} 1 \\ -0.014 \pm 0.004 \\ 0.684 \pm 0.005 \\ 0.732 \pm 0.004 \end{pmatrix}$	$\begin{pmatrix} 1 \\ -0.022 \pm 0.002 \\ 0.674 \pm 0.003 \\ 0.730 \pm 0.003 \end{pmatrix}$	$\begin{pmatrix} 1 \\ 0.014 \pm 0.001 \\ 0.680 \pm 0.001 \\ 0.733 \pm 0.001 \end{pmatrix}$
Circular SOP	$\begin{pmatrix} 1 \\ 0.004 \pm 0.011 \\ 0.000 \pm 0.008 \\ 1.008 \pm 0.011 \end{pmatrix}$	$\begin{pmatrix} 1 \\ -0.015 \pm 0.004 \\ 0.019 \pm 0.004 \\ 0.999 \pm 0.005 \end{pmatrix}$	$\begin{pmatrix} 1 \\ 0.001 \pm 0.002 \\ 0.002 \pm 0.003 \\ 1.003 \pm 0.002 \end{pmatrix}$	$\begin{pmatrix} 1 \\ 0.008 \pm 0.001 \\ 0.005 \pm 0.002 \\ 1.000 \pm 0.001 \end{pmatrix}$

Second, in order to test the usefulness of incomplete polarimeters when measuring a specific range of SOPs, we have experimentally implemented the incomplete polarimeter shown in Figure 3-8(c). As discussed in Figure 3-9(a) and (d), simulations indicate that this incomplete polarimeter gives lower S_1 and S_2 variances than the ones obtained with the regular tetrahedron configuration. Thus, incomplete polarimeter is an appropriate candidate for measuring linear SOPs. In order to show this feature, we have repeated the measurement of the linear SOP from the previous study (light linearly polarized at 70º). The mean and standard deviation of the linear SOP, after taking 100 samples with the incomplete polarimeter is:

$$\begin{pmatrix} 1 \\ -0.743 \pm 0.009 \\ 0.648 \pm 0.009 \\ - \end{pmatrix}. \tag{3-6}$$

Note that the incomplete polarimeter does not provide information about the S_3 element. The SOP measurement indicates a good performance of the incomplete polarimeter, obtaining lower standard deviation than the complete polarimeter for the same number of polarization analyzers (see Table 3-4 for the regular tetrahedron). Then, the incomplete polarimeter shows higher capability of measurement repeatability than the regular tetrahedron configuration for linear polarization metrology. Therefore, an optimization of an incomplete polarimeter by minimizing the error propagation of a particular Stokes parameter is recommended for a decreasing of the noise sensibility in the detection of specific range of SOPs. Generalizing to Mueller polarimeters, if it is of our interest particular elements of the Mueller matrix (as the ones related with retardance or diattenuation), an error propagation minimization is recommended over these Mueller matrix elements in order to decrease the noise sensibility on these particular polarization parameters.

Finally, a last study is carried out with the aim of analyzing the dependence of the standard deviation with the number of intensity measurements averaged with the radiometer. For every pair of retardances (δ_1,δ_2) corresponding to a given polarization analyzer of the PSA, a number m of intensity measurements has been taken with the radiometer. In every case, the intensity mean value has been used for the data reduction calculation. This number m, called sample size, will directly affect on the duration of the polarization measurement. Thus, it is interesting to analyze the actual benefit of increasing that parameter on the standard deviation of the final result without delaying unnecessarily the Stokes vector measurement. We have performed the detection of a linear polarized light at 70º respect to the laboratory vertical with the optimized regular tetrahedron configuration and with the incomplete polarimeter for measuring linear SOPs. The detection has been repeated for eight different values of the radiometer sample

size: 1, 10, 50, 100, 500, 1.000, 5.000 and 10.000 measurements. In all the cases, the SOP is expressed in terms of azimuth of the polarization ellipse and the SOP measurement is repeated 100 times, being calculated its corresponding standard deviation. The relation between the values of the azimuth standard deviation and the sample size is plotted in Figure 3-18, when using the complete optimized and the incomplete polarimeters.

Experimental results show that in the sample size range from 1 to 500 samples, the standard deviation values clearly decrease. Thus, by increasing the sample size range, the SOP measurement repeatability of the system is improved. However, once the sample size is equal to 500, by increasing the number of intensity measurements the standard deviation values remain almost constant. This is because random noise follows the statistic law of *1/m* [125]. Therefore, sample sizes higher than 500 imply an unnecessary increase in the detection time without significant measurement repeatability benefits. Furthermore, in every case the standard deviation values corresponding to the incomplete polarimeter are lower than the obtained with the complete polarimeter, pointing out the benefit of measuring linear SOPS with the incomplete polarimeter. We remark that all experimental measurements shown in previous studies were taken with a sample size of 500.

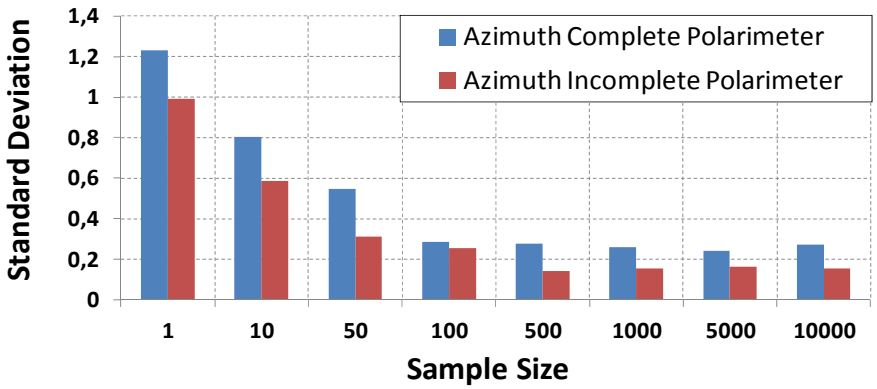

Figure 3-18: Azimuth standard deviation as function of the number of intensity measurements (sample size) taken by the radiometer, when using the regular tetrahedron and the incomplete polarimeter.

Chapter 4 **Polarimeter based on a twisted nematic liquid crystal panel**

Polarimeters based on twisted nematic liquid crystal (TN-LC) are thoughtfully studied in this chapter. By taking advantage that TN-LC introduces a given retardance and as well rotates the polarization ellipse, a complete polarimeter using a single LC panel is possible to build up. However, the available polarization analyzers are restricted to a certain projections curve on the Poincaré sphere. We study different architectures based on the TN-LC panel, leading to alternative projections curves. Their optimized performances are studied to achieve low noise propagation. In particular, we study the influence of illuminating the TN-LC cell in oblique incidence and of performing a double pass through the LC cell. In addition, we analyze the benefit of projecting the light exiting from the TN-LC cell over an elliptical state of polarization. Six different set-ups are designed and optimized. The robustness of each system is studied. Moreover, we detail a tolerance study for measuring with an accuracy of 1%. Finally, we show the implementation of these polarimeters, including experimental measurements with laser and LED illumination. In both scenarios, we test the implemented polarimeters by measuring light fully polarized as well as light partially polarized.

4.1 Design

In this chapter diverse polarimeter architectures have been analyzed, all of them have in common the use of a single twisted nematic liquid crystal (TN-LC) panel. A transmissive TN-LC cell can be modeled as an elliptical retarder (ER) [2]. Thus, its eigenstates are two orthogonal elliptical SOPs [92]. The LC molecules structure of a TN-LC cell and its features are explained in detail in subsection 1.3.1.2.

TN-LC devices enable both to introduce a retardance and to rotate the polarization ellipse orientation to an incident beam. Note that this feature of TN-LC panels reduces the number of required LC panels when constructing LC based polarimeters as for instance for the case of PA-LC based polarimeters explained in Chapter 3.

Different set-ups using a single TN-LC cell are proposed in Figure 4-1. First, the simplest architecture is sketched in Figure 4-1(a), where light impinges on the LC cell in normal incidence and then is projected over a linear polarizer. This polarimeter is restricted to certain set of polarization analyzers, i.e. the available projection SOPs describe a characteristic curve into the Poincaré sphere. Because projection curves configurations enclosing large volumes are related to lower error propagation, we propose to change some physical parameters to the initial set-up in order achieve alternative characteristic curves which may enlarge the volume enclosed, ensuring a better optimization of the system. As first modification, we suggest impinging the LC cell in oblique angle, the corresponding set-up is represented in Figure 4-1(b). As second modification, we suggest working on reflection with the LC cell, by means of a reflection on a mirror, as shown in Figure 4-1(c). Note that these three set-ups, light exiting from the TN-LC cell is projected over a linear SOP (using the LP). Finally, the fact that transmissive TN-LC cells act as an elliptical retarder suggests us including an additional quarter waveplate in the set-up with the aim of projecting light exiting from the TN-LC cell over an elliptical SOP (using a QWP and a LP). This last modification leads us to three new architectures just by including a QWP in the set-ups of Figure 4-1(a), (b) and (c). In particular, Figure 4-1(d) works on normal incidence and includes a QWP, Figure 4-1(e) works on oblique incidence and includes a QWP and, Figure 4-1(f) works on reflection and also includes a QWP. From now on, these set-ups are called A, B, C, D, E and F, respectively.

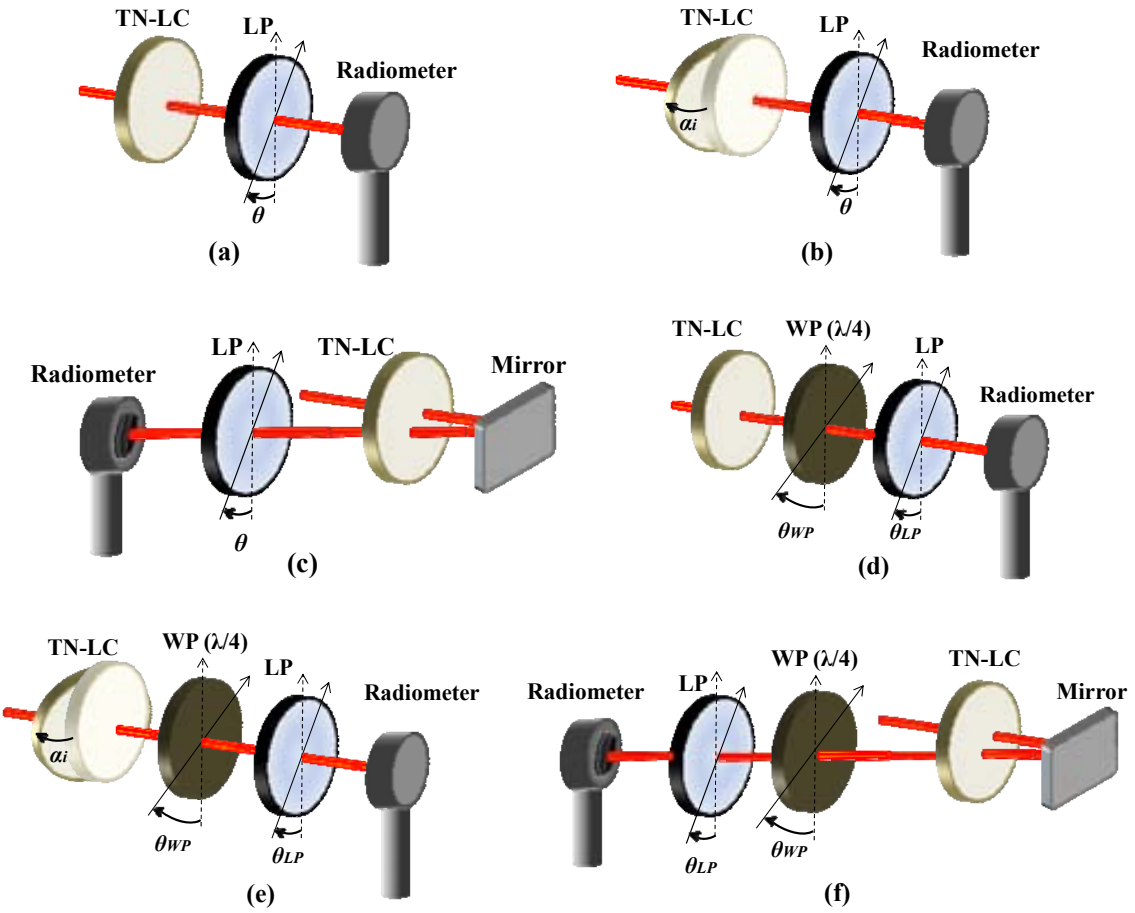

Figure 4-1: Stokes polarimeter architectures containing a single TN-LC cell, a LP and a radiometer. Diverse modifications on the set-up: (a) normal incidence to the TN-LC, (b) oblique incidence to the TN-LC, (c) working on reflection, (d) normal incidence to the TN-LC and including a QWP, (e) oblique incidence to the TN-LC and including a QWP and (f) working on reflection and including a QWP.

The available polarization analyzers for each architecture are expressed as function of the Mueller matrix describing the TN-LC in one of the three configurations: the TN-LC cell in normal incidence, the TN-LC cell in oblique incidence and, the TN-LC cell with a mirror causing a double pass through the LC cell. On the one hand, the Mueller matrix describing the whole polarimetric system is the following for set-ups A, B and C:

$$M_{LP}(\theta)\cdot M_{TN-LC}(V)=\frac{1}{2}\begin{pmatrix}1 & \cos 2\theta & \sin 2\theta & 0\\ \cos 2\theta & \cos^2 2\theta & \sin 2\theta\cos 2\theta & 0\\ \sin 2\theta & \sin 2\theta\cos 2\theta & \sin^2 2\theta & 0\\ 0 & 0 & 0 & 0\end{pmatrix}\cdot M_{TN-LC}(V), \quad (4\text{-}1)$$

where $M_{TN\text{-}LC}$ is the Mueller matrix describing the TN-LC cell in one of the three configurations, and this depends on the voltage addressed to the LC cell. To fulfill this matrix, it can be experimentally calibrated using a Mueller polarimeter or a physical model can be adapted [87].

On the other hand, the expression describing the PSA of set-ups D, E and F includes the quarter waveplate and this is given by:

$$M_{LP}(\theta_{LP})\cdot M_{WP}\left(\delta_{WP}=\frac{\pi}{2},\theta_{WP}\right)\cdot M_{TN-LC}(V)=$$
$$=\frac{1}{2}\begin{pmatrix}1 & \cos 2\theta_{LP} & \sin 2\theta_{LP} & 0\\ \cos 2\theta_{LP} & \cos^2 2\theta_{LP} & \sin 2\theta_{LP}\cos 2\theta_{LP} & 0\\ \sin 2\theta_{LP} & \sin 2\theta_{LP}\cos 2\theta_{LP} & \sin^2 2\theta_{LP} & 0\\ 0 & 0 & 0 & 0\end{pmatrix}\cdot \tag{4-2}$$
$$\cdot\begin{pmatrix}1 & 0 & 0 & 0\\ 0 & \cos^2 2\theta_{WP} & \sin 2\theta_{WP}\cos 2\theta_{WP} & -\sin 2\theta_{WP}\\ 0 & \sin 2\theta_{WP}\cos 2\theta_{WP} & \sin^2 2\theta_{WP} & \cos 2\theta_{WP}\\ 0 & \sin 2\theta_{WP} & -\cos 2\theta_{WP} & 0\end{pmatrix}\cdot M_{TN-LC}(V)$$

Finally, the expression of the PA is the first row of the Mueller matrix describing the whole system (i.e. the first row of matrix of Eq. (4-1) or (4-2), depending on the set-up).

4.1.1 Experimental characterization of the LC panel

We have used a solar-powered flashing LC key ring (Figure 4-2(a)) to extract the monopixel TN-LC cell (Figure 4-2(b)) used in the experimental set-up. Because the TN-LC is an off-the-shelf device, an experimental calibration of its Mueller matrix as function of the voltage is mandatory. With this aim, we have used a Mueller polarimeter with a PSA (polarization state analyzer) and a PSG (polarization state generator), both based on a rotating quarter waveplate and a linear polarizer. Several intensity measurements are acquired for different orientations of the rotating quarter waveplates. Then, a Fourier analysis is carried out as it is explained in[1] and, the 16 elements of the Mueller matrix are determined. The experimental calibration is conducted for a set of voltages (from 1 to 5.5 volts) addressed to the TN-LC cell. The calibrated Mueller matrices as function of the voltage are represented in Figure 4-3, where red points are experimental data. In particular, Figure 4-3(a) represents the Mueller matrix for the TN-LC on normal incidence, whereas in Figure 4-3(b) in oblique incidence. Finally, the Mueller matrix of the LC working in reflection and including the mirror is also calibrated as a single Mueller matrix and, this is represented in Figure 4-3(c). Moreover, we have calculated a polynomial function fitting experimental data for each Mueller matrix element, and these fittings are represented in continuous blue lines in Figure 4-3.

All three matrices are normalized with the element m_{00}. They have in common first column and first row, which are constant for all voltages applied. In particular, first column, related with the polarizance, is always $(1,0,0,0)^T$, indicating that the TN-LC does not polarize an unpolarized

light beam. While, first row is always (1,0,0,0), meaning that LC cell diattenuation is zero. On the contrary, submatrices defined by the elements m_{11}, m_{12}, m_{13}, m_{21}, m_{22}, m_{23}, m_{31}, m_{32}, m_{33} are strongly dependent on the voltage, as well as they differ depending on the system that they are describing. Actually, this set of Mueller matrix elements contains the information about the retarder behaviour. In general terms, Figure 4-3(a) and (b) have a similar evolution of their elements with the voltage, although there are some differences. For instance, element m_{21} of Figure 4-3(a) slightly differs from the one of Figure 4-3(b), particularly in the region from 2 to 5.5V. Regarding the behavior of the matrix elements of Figure 4-3(c), we notice an important difference with respect to the other two matrices. This fact will give us a large variety of available PAs. Finally, we deduce from the graphs of Figure 4-3 that the internal structure of the calibrated TN-LC panel is more active in the region from 1 to 3V, arriving to a practically stationary configuration after 3V.

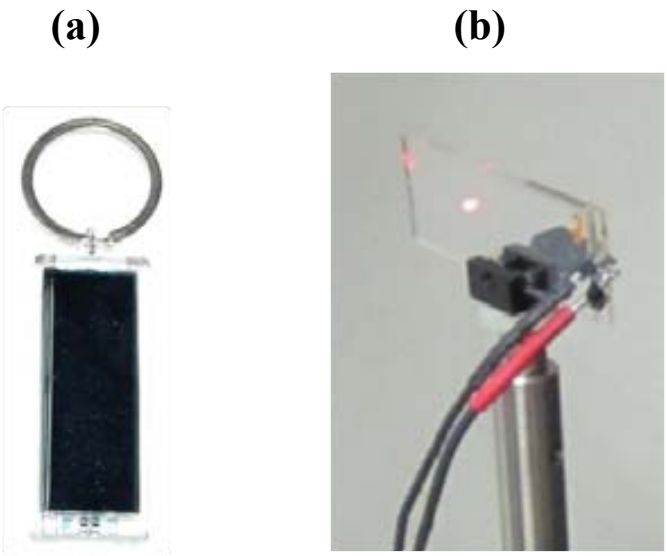

Figure 4-2: (a) Solar-powered flashing LC key ring from where it is extracted the (b) TN-LC cell.

Next, we have experimentally evaluated the transitory time of the TN-LC cell. We have measured the intensity as function of time when changing the addressed voltage to the LC cell. A LP is placed between the LC cell and the radiometer, in order to detect intensity variations. Figure 4-4(a) and (b) show intensity as function of time, when the voltage is changed from 0 to 2V and, from 2 to 0V, respectively. The measured time responses are, respectively, 300 and 80 milliseconds.

(a)

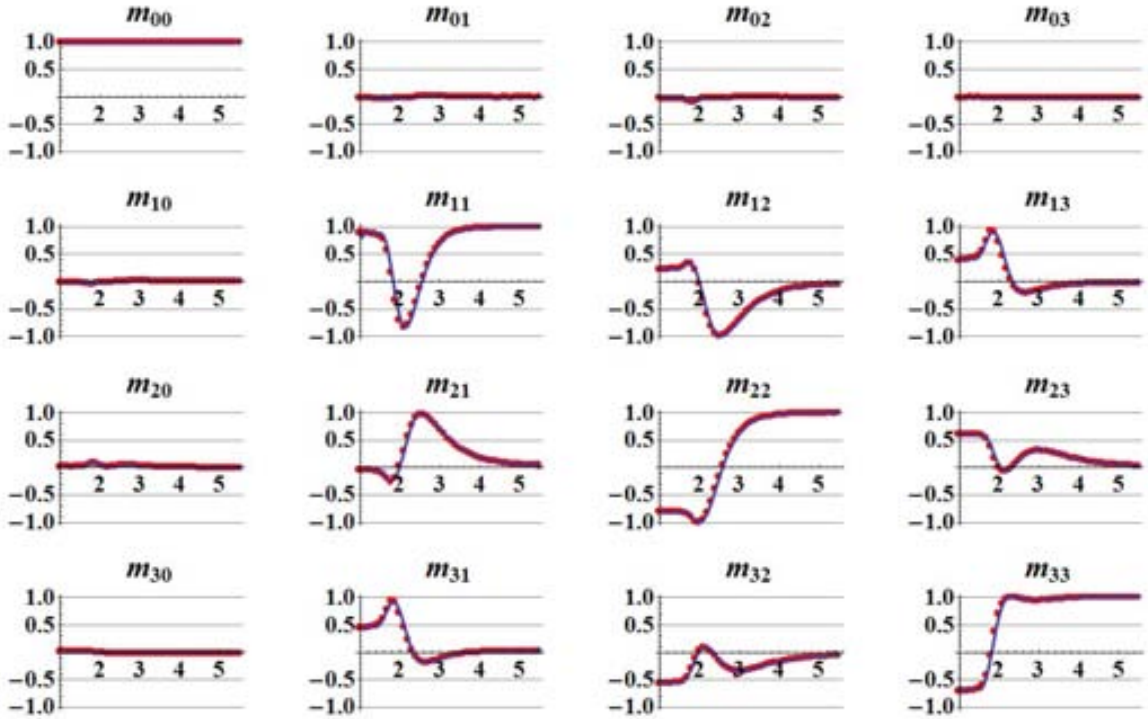
m_{00} m_{01} m_{02} m_{03}
m_{10} m_{11} m_{12} m_{13}
m_{20} m_{21} m_{22} m_{23}
m_{30} m_{31} m_{32} m_{33}

(b)

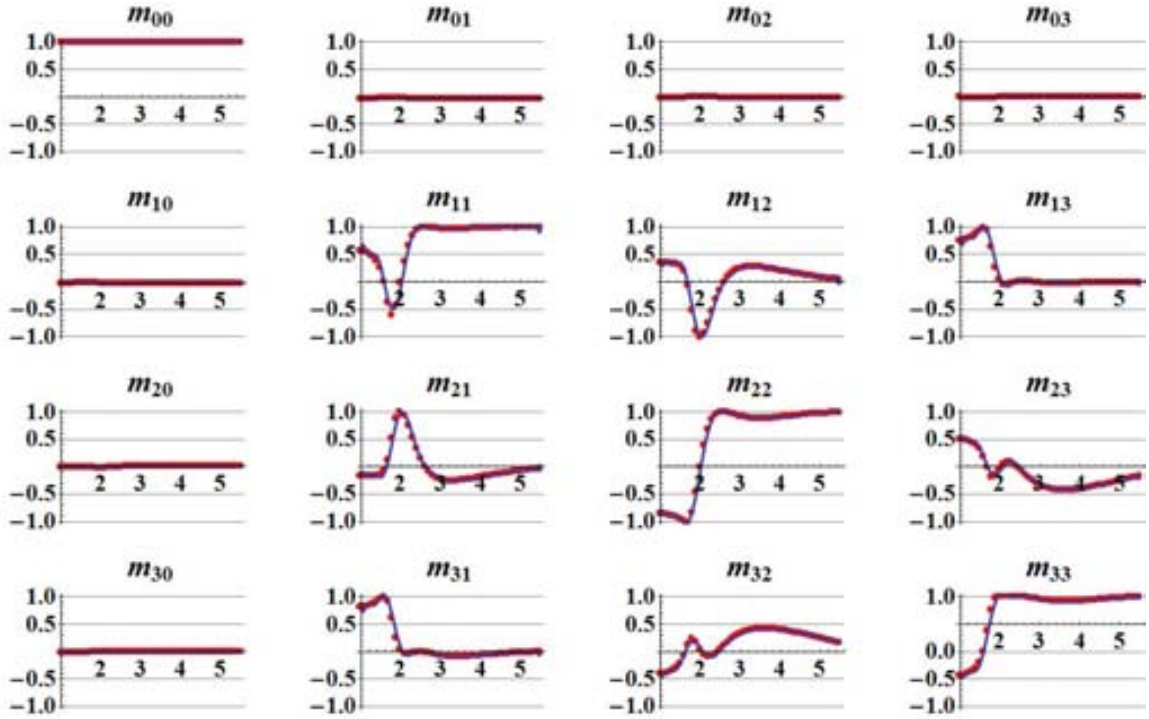
m_{00} m_{01} m_{02} m_{03}
m_{10} m_{11} m_{12} m_{13}
m_{20} m_{21} m_{22} m_{23}
m_{30} m_{31} m_{32} m_{33}

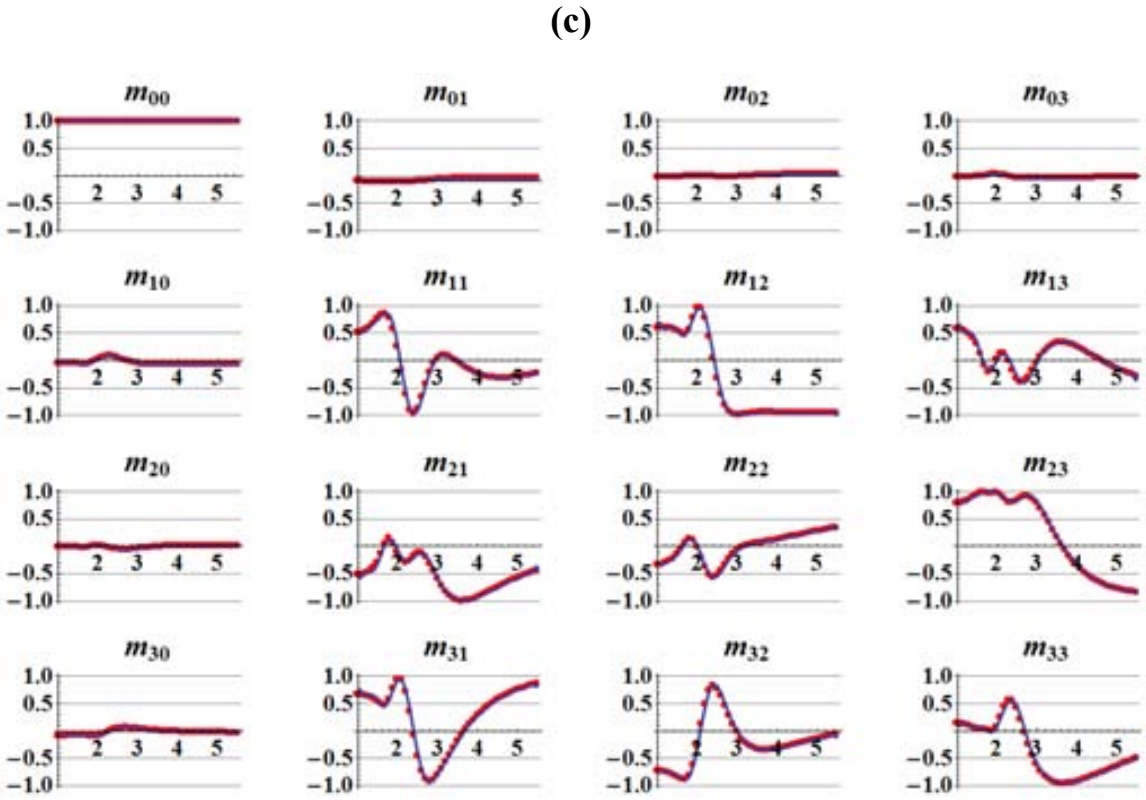

Figure 4-3: Calibrated Mueller matrices as function of the voltage of: (a) TN-LC working in normal incidence, (b) TN-LC working out of normal incidence and (c) TN-LC in reflection configuration. Red points correspond to experimental data and blue line to the polynomial fit.

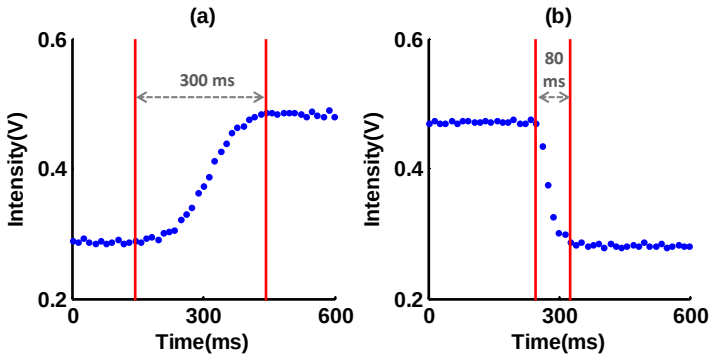

Figure 4-4: Time response of the TN-LC cell when changing voltage: (a) from 0 to 2V and (b) from 2 to 0V.

4.2 Optimization analysis

4.2.1 Optimized polarimeters

From the experimental calibrated TN-LC Mueller matrices and equations (4-1) and (4-2), we have simulated the set of available PAs for the six designed architectures based on a single

TN-LC cell and, we have optimized the set-up parameters as the orientation of the polarizer, the voltages sent to the LC cell and the orientation of the waveplate (only set-ups D, E and F).

As an example, we focus on set-up A (Figure 4-1(a)). In Figure 4-5, we plot 4 sets of PAs when fixing the orientation of the polarizer at 15º (in red), 25º (in magenta), 35º (in green) or 45º (in yellow). Each set of points with the same color corresponds to a particular orientation of the LP and when sending different voltages to the TN-LC cell, defining a characteristic curve for that particular configuration. A strong dependence with the orientation of the LP is observed, generating characteristic curves leading to different volumes.

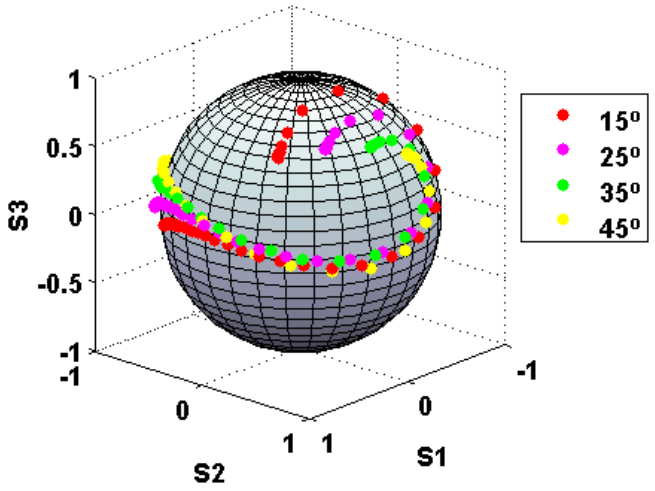

Figure 4-5: Set of available PAs represented upon the Poincaré sphere for set-up of Figure 4-1(a). Each color corresponds to a PSA with a different LP orientation θ, when sending an array of voltages (1 - 5.5V) to the TN-LC cell.

Therefore, as first step in the optimization process, we look for the characteristic curve which maximizes the enclosed volume, ensuring a lower propagation of noise. To this aim, we look for the minimum EWV value, leading to the largest volume. Figure 4-6 (a) plots the EWV of the characteristic curve as function of the orientation of the linear polarizer for the set-up A. Moreover, the EWV dependence with the orientation of the LP is also calculated for set-ups B and C, and plotted in Figure 4-6 (b) and (c), respectively. A black cross is marking the orientation of the polarizer which gives a minimum EWV. Note that around the optimum LP orientation, the EWV is very flat, thus, small variations on the orientation of the polarizer will lead to a polarimeter still well optimized, which can be interpreted in terms of robustness. Furthermore, for set-ups D, E and F, we have calculated the EWV dependence with the orientation of the LP and of the QWP. Respectively, in Figure 4-6 (d), (e) and (f) we map the inverse of EWV as function of the LP and the QWP orientations. The black marker is showing the maximum 1/EWV value (i.e. minimum EWV), marking the optimum orientation for the polarizer and for the waveplate. First and second rows of Table 4-1 summarize the result of this first step in the optimization process, giving the optimum orientations of the LP and the QWP for the six architectures.

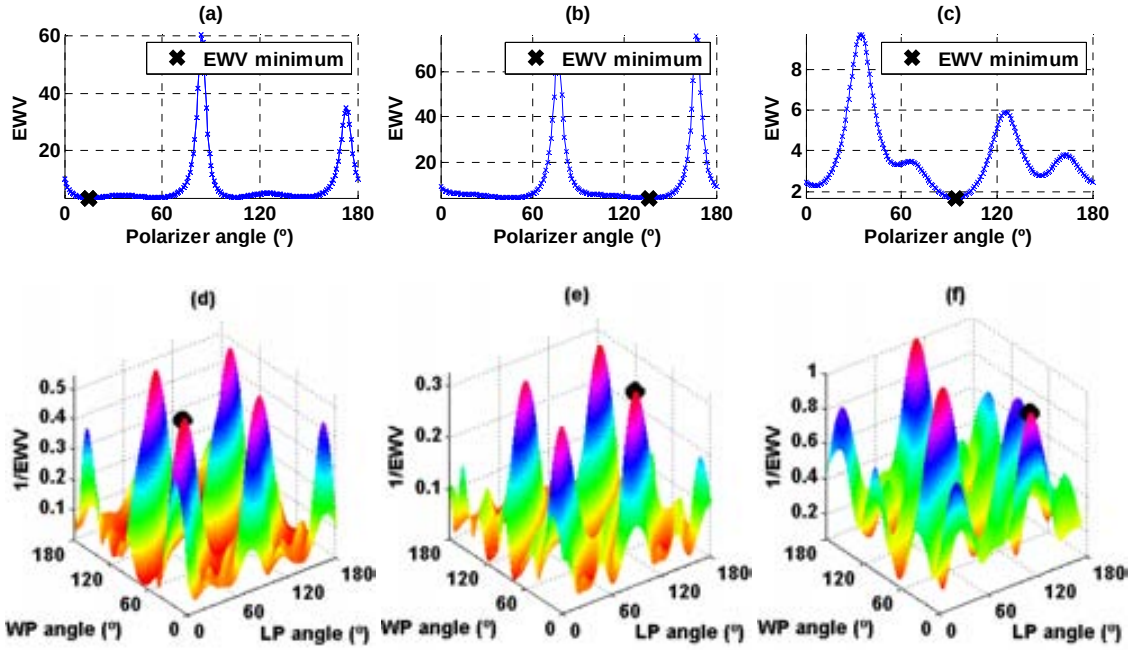

Figure 4-6: EWV as function of the LP orientation, for set-ups based on a TN-LC cell with configuration (a) A, (b) B and (c) C. 1/EWV as function of the LP and QWP orientations, for set-ups based on a TN-LC cell with configuration: (d) D, (e) E and (f) F.

Next, as a second step in the optimization process, from the optimum characteristic curve we have selected the 4 PAs which generates a PSA with the minimum EWV. This process is equivalent to the one explained in 3.2.1, but using the EWV as figure of merit. However, the initial PAs and the ones which are selected in each iteration are not completely random, but they are restricted to belong to the characteristic curve. In Figure 4-7, by using the Poincaré sphere representation, we plot the optimum characteristic curve in black spots, whereas in red points the 4 optimum PAs, result of the optimization process. For a higher visual insight, we have also represented the irregular tetrahedrons which are drawn by the optimum PAs, emphasizing the importance of maximizing the volume enclosed by these points over the Poincaré sphere. Note that this second part of the optimization process, we are selecting the 4 voltages to be addressed to the TN-LC cell during a polarization measurement.

Finally, last two rows in Table 4-1 give the EWV and the CN of the PSAs after selecting the 4 optimum PAs. Comparing polarimeters A and B, we observe smaller quality indicators (QIs) values when illuminating the TN-LC cell in oblique incidence. When light impinges out of normal incidence, the retardance introduced by the TN-LC cell to the light changes due to a variation on the effective LC birefringence and a small change in thickness. This retardance variation leads to an alternative projections curve, which in this case has improved the optimization of the system. The same idea is present in set-up C, where an enlargement of the optical path has lead to a different projection SOPs curve, with significantly lower QIs. We observe that the QIs associated to set-ups using the additional QWP (D, E and F) have improved

with respect to the original set-ups without QWP (A, B and C, respectively). Whereas a significant decrease of the QIs is observed at normal incidence (comparing A and D polarimeters), the improvement at oblique incidence is less relevant (from B to E). This fact can be understood if it is kept in mind that an elliptical retarder can be described as the product of a linear retarder and a rotator of a given angle [2]. In this situation, when the light impinges out of normal incidence, the effective rotator angle may be decreased, so the system tends to act as a linear retarder. In such case, projecting the SOP exiting from the TN-LC over an elliptical polarization state has less influence in the optimization process. Finally, concerning polarimeter F, a slight improvement in the QIs is obtained when comparing with polarimeter C. In this case, the double pass of the light into the TN-LC device may drastically decrease or even cancel the effective rotator [141]. Therefore, the most beneficial contribution of introducing a QWP in the set-up is achieved for normal incidence. We want to emphasize that the diverse modifications applied to the polarimeter set-ups have led to a progressive reduction of the EWV indicator, reaching a minimum value of 11.11 for polarimeter F (and 1.98 of CN). This is an excellent result if one takes into account that the minimum theoretical values that can be achieved for the EWV and the CN are 10 and $\sqrt{3}$ [99,125], respectively.

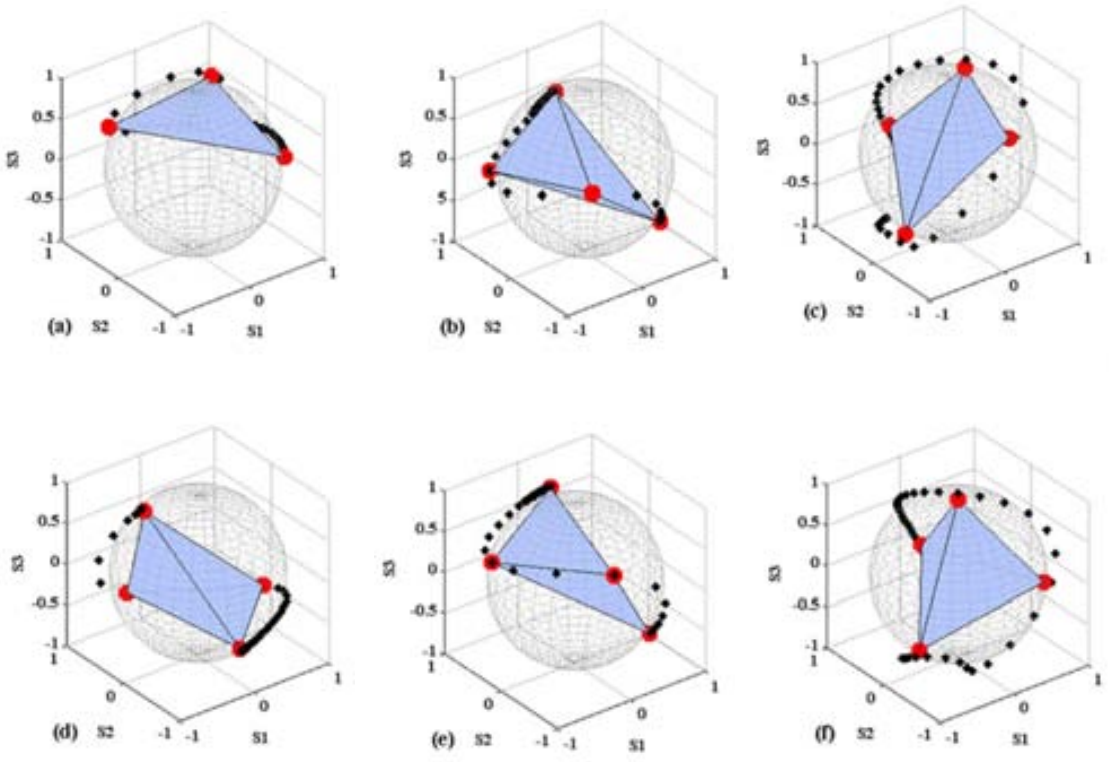

Figure 4-7: In black points, optimized PAs curve by addressing a sequence of voltages (1-5.5V) for polarimeters (a)A, (b)B, (c) C, (d) D, (e) E and (f) F. The vertices of the irregular tetrahedrons (also plotted in red points) are the four optimal PAs obtained during the EWV minimization process.

Table 4-1: Optimization results by minimizing the EWV. Optimum orientations of the linear polarizer and the quarter waveplate for the different polarimeter set-ups. EWV and CN of the optimized PSA (when 4 PAs are used).

Set-up	A	B	C	D	E	F
θ_{LP}	15º	136º	94º	31º	120º	109º
θ_{QWP}	-	-	-	49º	43º	0º
EWV	27.28	19.50	14.82	13.99	15.51	11.11
CN	4.66	3.61	2.69	2.69	3.06	1.98

4.2.2 Polarimeters robustness

Now we analyze the robustness of the designed polarimeters to variations over the optimized configurations. We take the optimized PSAs, composed by the 4 PAs drawn in red points in each subplot of Figure 4-7 (from now on referred as theoretical or ideal configurations), and we deviate them from those initial positions, simulating experimental variations in the laboratory. These modifications can be due to a change of temperature, a misalignment in the orientation of some optical element as the linear polarizer or a variation in the tilt of the TN-LC cell. Thus, the set of deviated PAs simulates a more realistic PSA in the laboratory, and their quality indicators are recalculated. In the simulation, we add to each element of the PA vector a value obtained from a random uniformly distribution, with zero mean and amplitude 0.4 (20% of the Stokes parameter range). For each architecture, 50 different polarimeters are simulated and deviated from the ideal configuration. In Figure 4-8 we represent their condition number values and in Figure 4-9 their variances.

A clear tendency is observed, as lower the QI values of the ideal configuration, more robust is the system, presenting lower deviations on their QIs. In particular, set-up F has the lowest QIs, and the QI values of the deviated polarimeters, represented in Figure 4-8(f) and Figure 4-9 (f), present smaller fluctuations. Whereas, when the system is not so well optimized, as in set-up A and B, the fluctuations of the QIs for the deviated polarimeters are more significant (see Figure 4-8(a), (b) and Figure 4-9 (a), (b)).

We remark that all analyzed PSAs have the same number of PAs (4) and the deviations are taken from the same distribution. Therefore, the robustness is given by the optimization of the theoretical configuration.

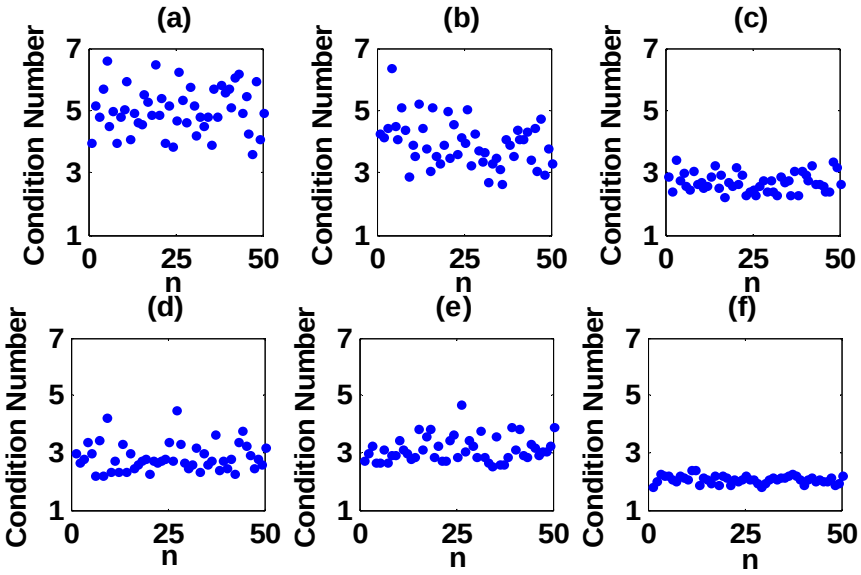

Figure 4-8: Condition number of 50 different simulated PSAs deviated from the theoretical optimized configuration using set-up (a) A, (b) B, (c) C, (d) D, (e) E and (f) F, when adding to the PAs a value from a zero mean uniform distribution of amplitude 0.4.

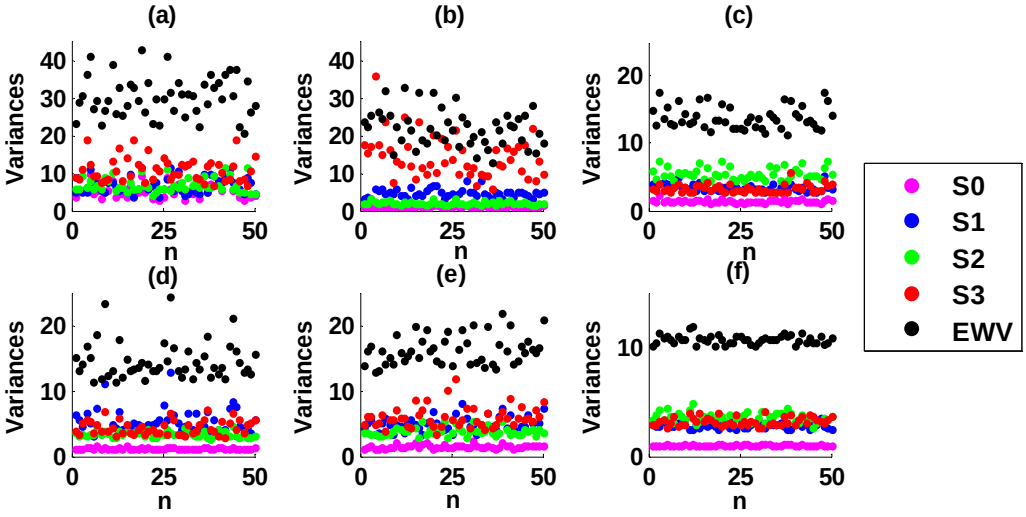

Figure 4-9: Variances of 50 different simulated PSAs deviated from the theoretical optimized configuration using set-up (a) A, (b) B, (c) C, (d) D, (e) E and (f) F, when adding to the PAs a value from a zero mean uniform distribution of amplitude 0.4.

4.2.3 *Simulation of polarimeters by changing some of the TN-LC cell features*

Note that during the optimization, we have only needed the Mueller matrices of the TN-LC cell in the three different configurations (normal incidence, oblique incidence and in reflection), and these matrices were calibrated experimentally as function of the voltage in section 4.1.1. Hence, the PSA optimization is limited by the specific features of our particular TN-LC cell. In order to generalize this chapter of polarimeters based on TN-LC, we decide to extend the

optimization study by including an analysis of the dependence of the polarimeter optimization on the TN-LC physical features.

As told in subsection 1.3.1.2, different physical models can be used for describing the TN-LC cell, particularly we have used the one described in [87]. This model depends of three physical parameters: twist angle, maximum birefringence parameter and orientation of the molecular director at the input face. Thus, we proceed to experimentally calibrate these physical parameters of our TN-LC cell. We have followed the methodology explained in [88]. Briefly, one measures the intensity transmitted by the TN-LC cell sandwiched between two polarizers, whose transmission axes are either parallel or perpendicular between them, and rotated simultaneously. Experimental data is fitted by the theoretical expressions which depend on the twist angle, the maximum birefringence and the orientation of the molecular director at the input face. In order to eliminate unambiguities, 5 different wavelengths (488, 496, 501, 514 and 633nm) have been used [142] by means of an Argon and He-Ne lasers. Figure 4-10 shows experimental data for the different wavelengths. Finally, Table 4-2 shows the calibrated parameters of our TN-LC cell.

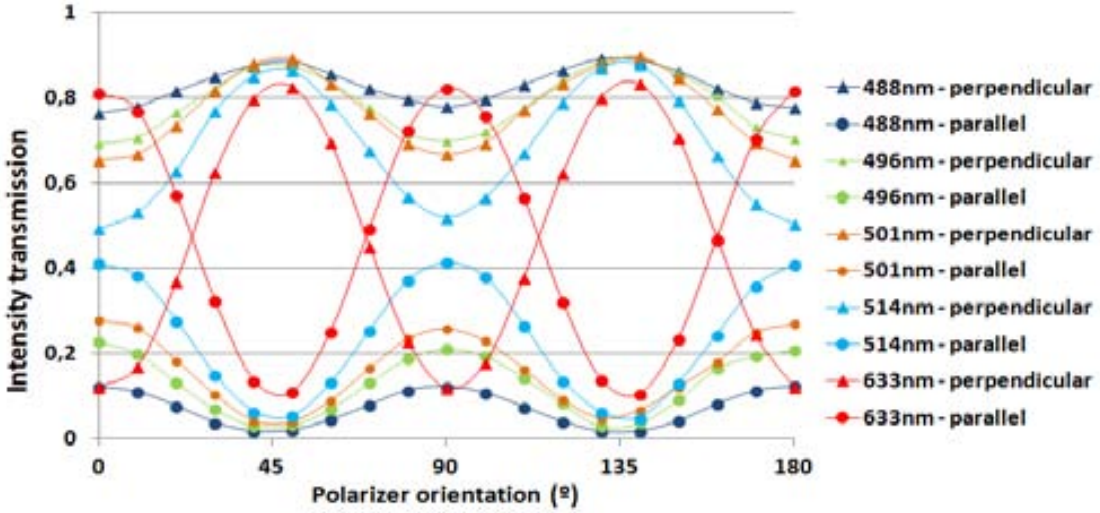

Figure 4-10: Intensity transmission for perpendicular and parallel polarizers sandwiching the TN-LC cell, and using different illumination wavelengths.

Table 4-2: Calibrated physical features of the TN-LC cell used in the implementation of the polarimeters.

Twist angle	Maximum birefringence for 633nm	Orientation of the molecular director at the input face
93.24º	276.51º	48.01º

Afterwards, we have simulated the simplest TN-LC polarimeter set-up (i.e. set-up A), by applying the physical model of the TN-LC cell developed in [87] and summarized in section

1.3.1.2. In particular, we simulate two separate studies with the aim of analyzing the influence of the twist angle and the birefringence of the TN-LC cell on the polarimeter optimized performance. Several characteristic curves are simulated, each one is composed by the same number of PAs (46) and changing one of the TN-LC parameters (twist angle or maximum birefringence). The parameter unchanged is fixed to the calibrated value shown in Table 4-2.

On the one hand, the influence of the twist angle is discussed. Simulations of a TN-LC cell with different twist angle values, from 0° to 180°, are analyzed, and the EWV values of the simulated characteristic curves are plotted in Figure 4-11(a). Notice that TN-LC devices with a twist angle from 40° to 140° give low EWV values of the same order. In addition, the use of a super-twisted nematic LC cell with a twist angle higher than 140° is not an advantage for the optimization of the instrument.

On the other hand, the maximum birefringence is analyzed. Note that when changing the maximum birefringence value, it corresponds to work with different thickness of the TN-LC cell [87]. The EWV of the characteristic curves are calculated for different values of TN-LC birefringence and it is represented in Figure 4-11(b). Note that the EWV is stabilized after 250° of maximum birefringence, approximately. Therefore, it is not necessary to work with higher birefringences (more than 250°). Moreover, working with thicker TN-LC cell leads to a slower response time. We remark that the EWV values achieved in Figure 4-11(a) and (b) are not comparable with those shown in Table 4-1, because the first ones correspond to characteristic curves (using 46 PAs) and the others provided in Table 4-1 are for a set of only 4 PAs.

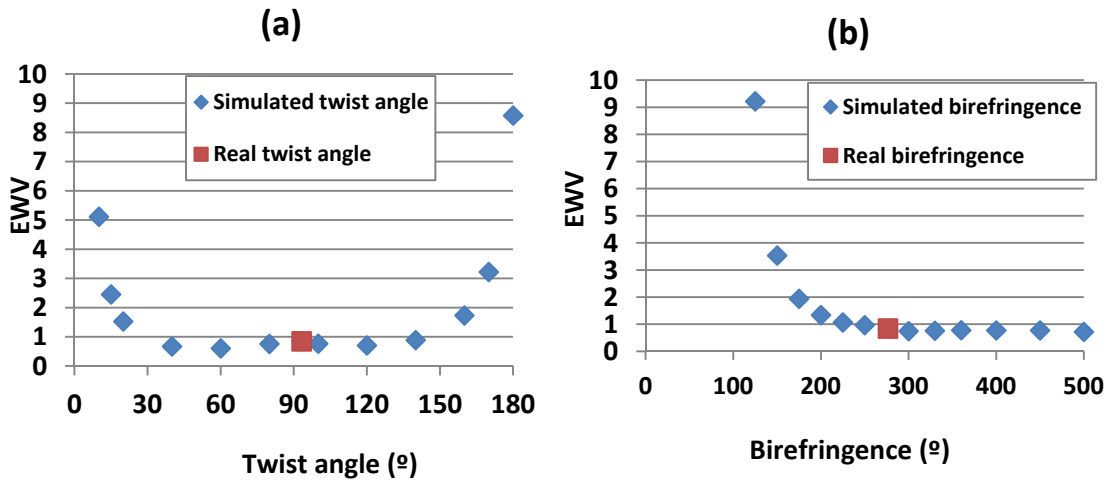

Figure 4-11: (a) EWV as function of the twist angle of the TN-LC cell. Red square is marking the EWV value for the actual twist angle (calibrated value of 93.24º). (b) EWV as function of the maximum birefringence of the TN-LC cell. Red square is marking the EWV for the actual maximum birefringence (calibrated value of 276.51º).

4.3 Tolerance analysis

In this section we detail the tolerance study for the six different polarimeters based on a single TN-LC cell. Our goal consists in determining the tolerance of the parameters involved in the polarimeter in order to get polarization measurements with an error smaller than 0.02.

The parameters to be analyzed are the voltages sent to the LC cell, the orientation of the linear polarizer and, for set-ups D, E and F, the orientation and retardance of the waveplate.

First of all, we focus on set-up D as an example. We analyze the error for each Stokes parameter of the measured Stokes vector when we give a tolerance of a particular parameter of the experimental performance, deviating the actual polarimetric measurement matrix from the theoretical one used during the data reduction calculation. Figure 4-12(a), (b), (c) and (d) show the Stokes parameters errors when we give a tolerance of, respectively, 0.01V to the voltages sent to the TN-LC cell, 1º to the orientation of the polarizer, 1º to the orientation of the waveplate and 1º to the waveplate retardance. Note that 1º over 360º is of the same order than 0.01V over 4.5V (operative LC voltage range). In order to calculate deviations of 0.01V to the initial configuration, we have used the polynomial fits of the calibrated TN-LC Mueller matrix elements, plotted in blue lines in Figure 4-3. Figure 4-12 shows the Stokes errors as function of the variable k, which parameterizes the incident Stokes vector over the whole Poincaré sphere (see Eq. (2-21)). We observe a strong dependence of the Stokes errors with the incident Stokes vector. From results, we conclude that Stokes error is less sensitive to a variation in the waveplate retardance than in the other three parameters.

This analysis is repeated for different tolerances amounts (0.2º, 0.5º and 2º or 0.002V, 0.005V and 0.02V). Next, from each graph it is extracted the maximum Stokes error, giving us the accuracy for that particular tolerance and parameter. Moreover, we repeat this whole tolerance analysis for the other 5 set-ups, and the summary of the accuracy of these polarimeters as function of the parameters tolerance is represented in Figure 4-13. Each color represents a given set-up: A (orange), B (green), C (cyan), D (dark blue), E (purple) and F (red). Markers are showing the accuracy value obtained directly from the analysis, in particular each mark shape represents a given parameter: voltage (circle), polarizer orientation (square), waveplate orientation (filled triangle) and waveplate retardance (unfilled triangle). Next, we calculate a linear regression, fitting each set of accuracy values corresponding to each parameter and set-up, and they are represented in Figure 4-13 as well. The color of these lines corresponds to the set-up and their style to the parameter: thick (voltage), thin (polarizer orientation), dashed (waveplate orientation) and dotted (waveplate retardance). Two x-axes are used: at the top for the voltage tolerance (in volts), and at the bottom for the retardance and orientation tolerances (in degrees).

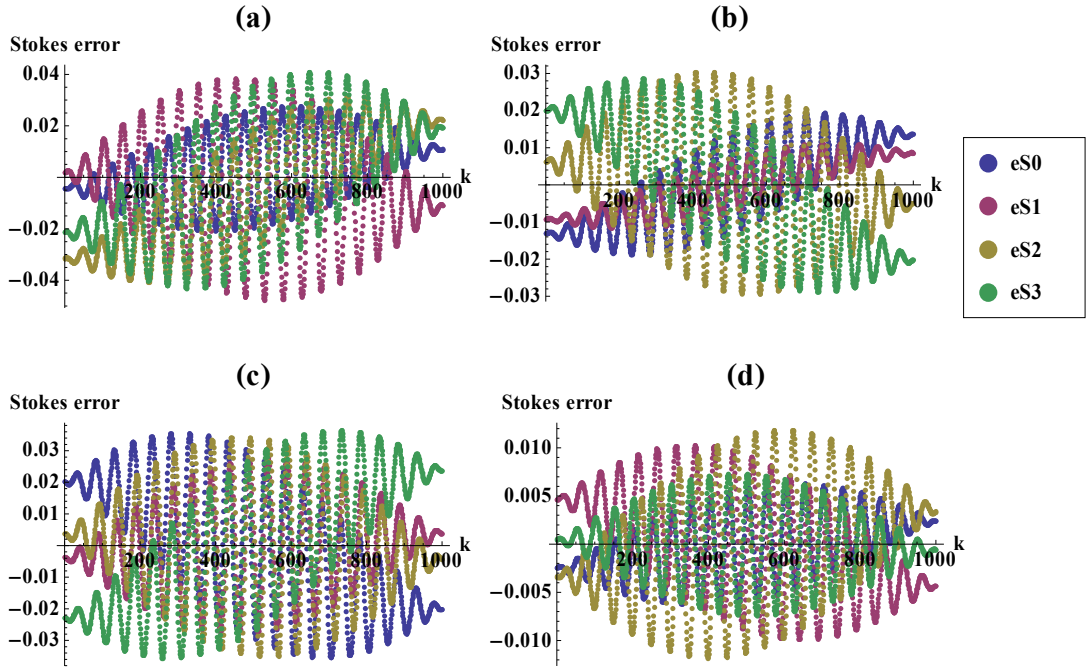

Figure 4-12: Stokes parameters errors, for set-up D, with a tolerance of: (a) 0.01Volts in the 4 voltages addressed to the TN-LC cell, (b) 1º in the orientation of linear polarizer (θ_{LP}), (c) 1º in the orientation of the waveplate (θ_{WP}) and (d) 1º in the retardance of the waveplate (δ_{WP}). Errors as function of variable k, which parameterizes the incident Stokes vector by Eq.(2-21).

We observe how set-up A has the worst accuracy, fact expected because it has the highest CN. Another point to remark is that set-ups D, E and F are very little sensitive to a variation on the waveplate retardance, giving excellent values of accuracy. Furthermore, we equal the linear regression expressions to an accuracy of 0.02 (horizontal black dashed line in Figure 4-13), and the tolerance values for each parameter and set-up are obtained, and shown in Table 4-3. Set-up A is the least accurate, presenting the smallest tolerances. Each set-up has different parameters tolerances, and their relations are also different. We observe that when the waveplate is used (set-ups D, E and F), WP retardance has the larger tolerance values (1.69-2.17º). Then, both WP and LP orientations are relatively of the same order (0.44º-0.66º, excluding set-up A of 0.28). And finally, the voltages addressed to the LC cell have tolerances in the range of 0.0030-0.0049V, excluding set-up F of 0.0072V. By analyzing data given in Table 4-3, we conclude that the best TN-LC based polarimeter architectures are configuration D and F, as they lead to the best result in terms of accuracy-tolerance.

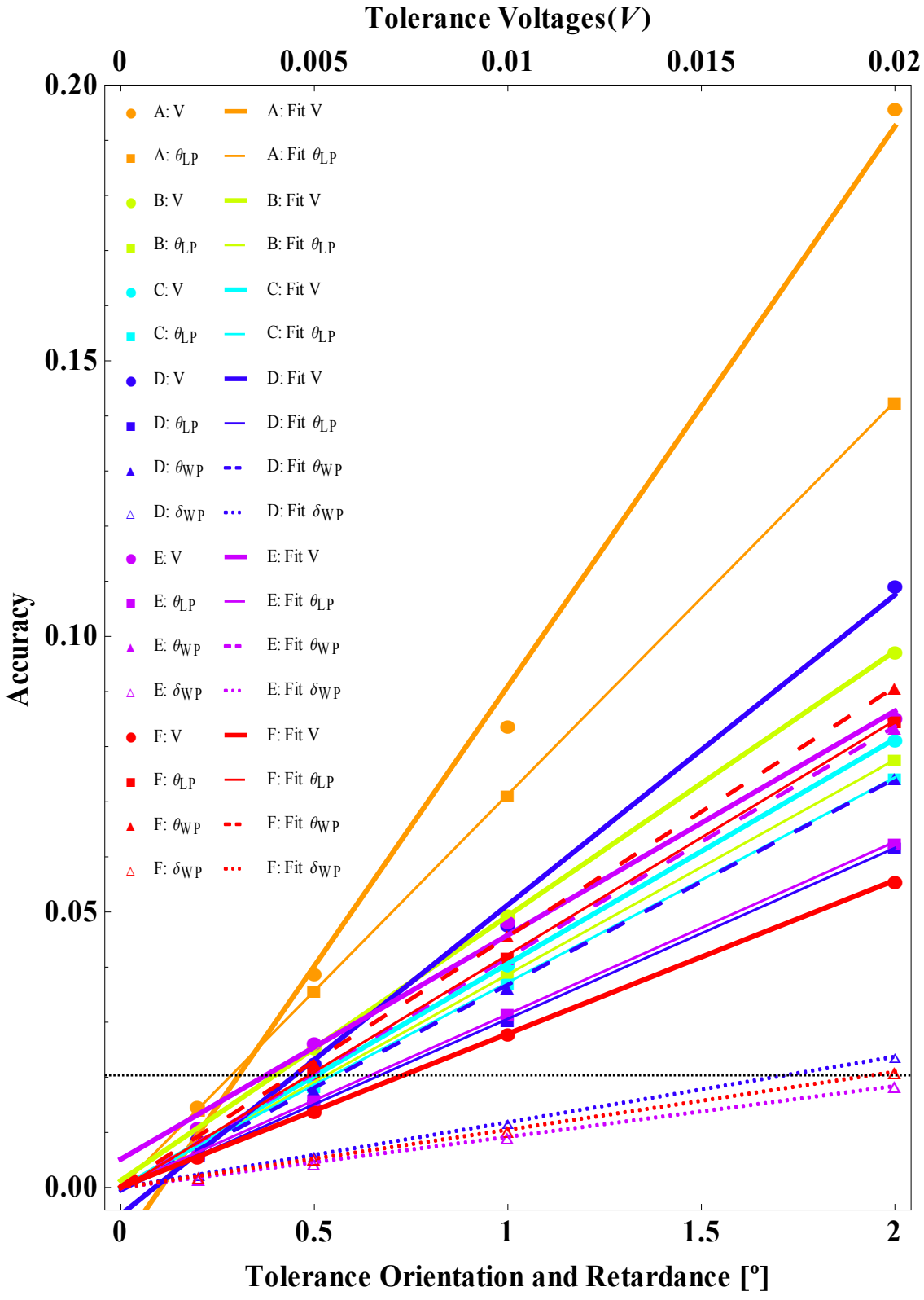

Figure 4-13: Accuracy of 6 Stokes polarimeters (A-F) based on a single TN-LC cell, as function of the tolerance of the parameters involved in each set-up: voltage addressed to the TN-LC cell (V), orientation of the linear polarizer (θ_{LP}), orientation of the waveplate (θ_{WP}) and retardance of the waveplate (δ_{WP}). There are two different x-axes: the top one for voltage and the bottom one for the rest of parameters. Markers indicate the accuracy given by that particular tolerance and parameter from simulated data. Lines (continuous, dotted and dashed) are linear regression fits of simulated data. Horizontal dashed black line is marking an accuracy of 0.02 in the Stokes vector measurement.

Finally, we compare the actual tolerances of our optical elements and they are compared with the ones exposed in Table 4-3. We used a QWP from Meadowlarks, whose retardance accuracy is smaller than λ/350 thus, the retardance error will be smaller than the tolerances shown in the last column of Table 4-3. The LP and the WP are held by a rotation mount with a scale marked at 2º increments. However, thanks to the experimental calibration of the polarimeter, we assume that the orientations of the optical elements are properly determined under an uncertainty of 0.5º. Thus, polarimeters A and F may not reach an accuracy of 1% but, we ensure that accuracy in the polarization measurements for the rest of polarimeters (B-E). Finally, the analog-to-digital converter can send signal with a precision of 0.001V.

Table 4-3: Tolerance values to achieve an accuracy of 0.02 in the Stokes vector measurements, concerning the parameters involved in set-ups A, B, C, D, E and F: voltage addressed to the TN-LC cell (V), orientation of the linear polarizer (θ_{LP}), orientation (θ_{WP}) and retardance of the waveplate (δ_{WP}).

Parameter	V (V)	θ_{LP} (º)	θ_{WP} (º)	δ_{WP} (º)
Polarimeter A	0.0030	0.28	-	-
Polarimeter B	0.0039	0.52	-	-
Polarimeter C	0.0049	0.54	-	-
Polarimeter D	0.0044	0.66	0.55	1.69
Polarimeter E	0.0037	0.63	0.48	2.17
Polarimeter F	0.0072	0.48	0.44	1.90

4.4 Implementation

In this section we describe the implementation of the six different Stokes polarimeters based on a single TN-LC cell. Figure 4-14 shows a picture of polarimeter A implemented in the laboratory.

All implemented polarimeters use an off-the-shelf TN-LC cell and a linear polarizer from Casix, Glan-Thompson type [143]. Two types of light sources are used during the implementation of these polarimeters. On the one hand, we used as monochromatic light source a He-Ne laser (633nm). On the other hand, we used as higher bandwidth light source a collimated red light emitting diode (LED, λo=625nm and Δλ=17 nm), distributed by Thorlabs (Model

M625L2). Set-ups D, E and F are using an achromatic quarter waveplate from Meadowlark Optics with an operating wavelength range centered in 630nm.

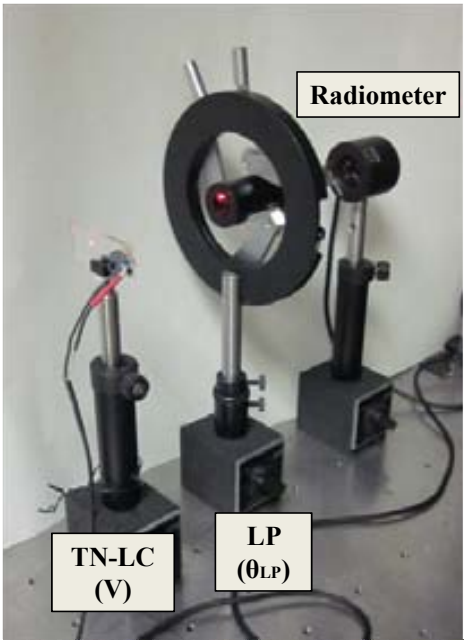

Figure 4-14: Implemented polarimeter A in our laboratory. Stokes polarimeter based on a single TN-LC panel and a linear polarizer.

The electrical signal addressed to the TN-LC cell is sent by the same control module used for the PA-LC cells provided by Meadowlark Optics. Then, the flux measurements are acquired with the same photodiode, connected to the optical power meter, which at the same time is connected to an analog to digital (A/D) convertor from National Instrument.

We developed in LabView the code controlling this second type of polarimeters based on TN-LC, particularly, sending the proper voltages to the TN-LC cell and measuring the flux measurements corresponding to each PA, as well as processing all acquired data (calculating and analyzing the Stokes vectors).

The measurement process of the six implemented polarimeters is the following. The voltage signal is sent to the TN-LC device, we wait 500 milliseconds to achieve a stationary position of the LC molecules (TN-LC transitory time is of 300 milliseconds, measured in Figure 4-4), then, in a rate of 100Hz, 100 measurements of the intensity are acquired and its average is calculated. Since each SOP measurement performed by the polarimeter needs 4 intensities measurements, the process is repeated for the 4 voltages. Therefore, a complete SOP measurement takes 6 seconds.

4.4.1 Calibration

We have calibrated the six implemented polarimeters by following the method explained in section 2.5.1, using as illumination a He-Ne laser (633nm).

In Figure 4-15(a)-(f), we show the result of the calibration of polarimeters A-F, respectively. Green and red points represent the theoretical and the calibrated PSA, respectively. A significant agreement between experimental and theoretical values is observed, although with some discrepancies. Differences may be due to a variation in temperature affecting LC birefringence or a misalignment of some of the optical elements as the polarizer or the waveplate, among others. However, by using the calibrated polarimetric measurement matrix will lead to more accurate measurements. Table 4-4 summarizes the CN and the EWV of the calibrated polarimeters. These values can be compared with those obtained in the optimization process (Table 4-1). In general, as lower the CN, more robust is the system, leading to CNs closer to the theoretical one. Experimental CN and EWV values are of the order of the predicted ones in the robustness simulations of Figure 4-8 and Figure 4-9, respectively. As predicted with theoretical values, set-ups D and F provide the best experimental results in optimization performance.

Finally, polarimeter D has been calibrated again but using the LED as light source. The CN of this new calibrated matrix for LED illumination is 2.79.

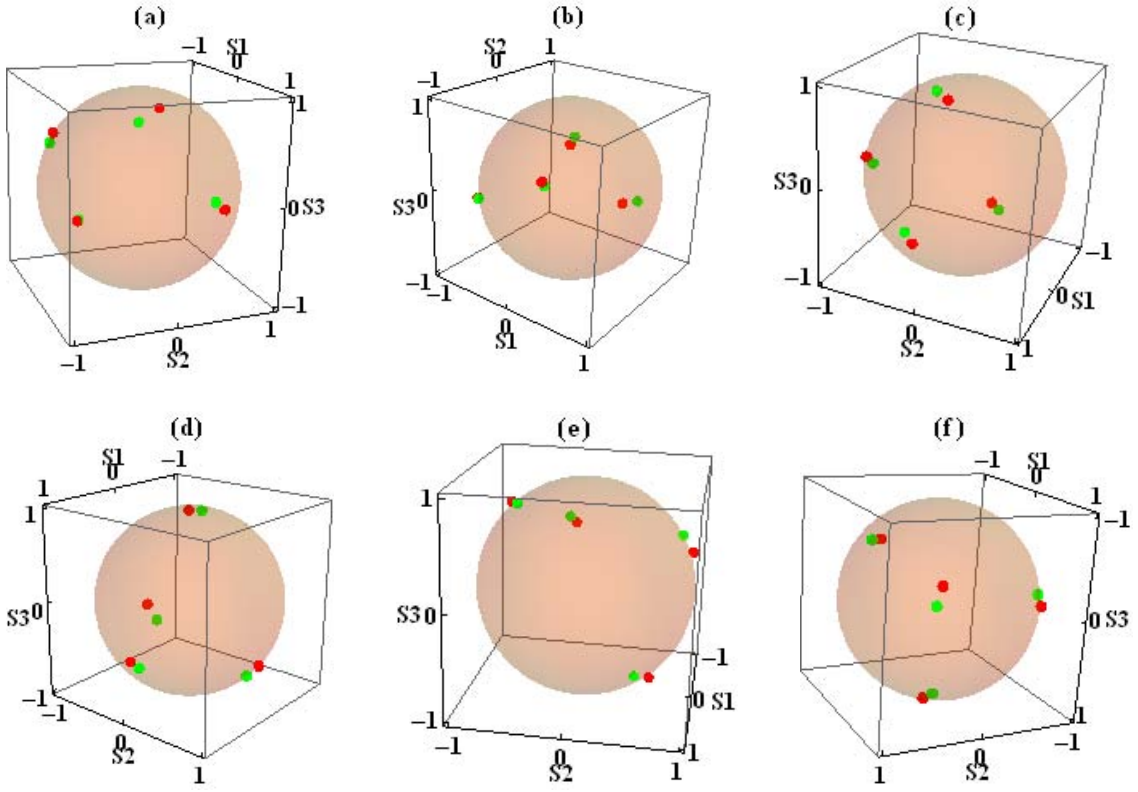

Figure 4-15: Theoretical and calibrated PSAs in green and in red points, respectively, for the optimized polarimeters: (a) A, (b) B, (c) C, (d) D, (e) E and (f) F, based on a single TN-LC cell.

Table 4-4: CN and EWV of the polarimetric measurement matrices experimentally calibrated for different implemented PSAs, when using a He-Ne laser as light source.

PSA	A	B	C	D	E	F
Experimental CN	5.40	3.97	2.83	2.64	3.24	2.21
Experimental EWV	32.29	23.23	15.37	14.29	17.57	11.59

4.4.2 Experimental measurements

In this subsection we detail and discuss all experimental measurements. Measurements can be divided in two blocs according to the type of illumination: monochromatic and LED light sources. For each block, we include measurements of fully polarized light as well as partially polarized light. Concerning fully polarized light, we have addressed three different SOPs: a linear SOP at 30º, an elliptical SOP and a right-handed circular SOP. Whereas concerning partially polarized light, SOPs with different DOP are addressed.

Each SOP measurement process is repeated 100 times. Experimental data provided here corresponds to the mean and the standard deviation of these 100 measurements of the same SOP. Obtained results are compared with the measurements provided by a commercial polarimeter (Thorlabs, Polarization Analyzer System PAN 5710VIS, S/N: M60217605). As well, 100 measurements for each SOP are performed with the commercial polarimeter and so, the mean and the standard deviation are provided as well.

4.4.2.1 Monochromatic illumination

Table 4-5 shows the experimental results when the six implemented polarimeters (A-F) are tested by measuring three fully polarized SOPs generated with a He-Ne laser beam, and experimental data is compared with the measurements provided by the commercial polarimeter. Additionally, in the first row we include the expected values calculated from the orientation of the optical elements set for the SOP to be measured (theoretical prediction).

If we calculate the differences between measurements obtained by the implemented polarimeters with the commercial one (our reference value), we observe that all differences are in the second decimal (excluding polarimeter A when measures S_3 parameter in the elliptical SOP, where the difference is in the first decimal). We have calculated the average of these differences grouped by polarimeter and, for polarimeters B-F differences are 0.02 or smaller, being polarimeter F the one with the smallest difference. This fact points out the importance of the optimization conducted in this chapter for polarimeters based on a single TN-LC.

Table 4-5: Stokes parameters of three different SOPs measured by each implemented polarimeter (A, B, C, D, E, and F), when monochromatic light is employed. SOPs are measured also with the commercial polarimeter (Thorlabs). Stokes vectors are normalized.

	Linear SOP			**Elliptical SOP**			**Circular SOP**		
	S_1	S_2	S_3	S_1	S_2	S_3	S_1	S_2	S_3
Expected values	0.5	0.866	0	0	0.866	0.5	0	0	1
Set-up A	0.487 ± 0.001	0.883 ± 0.004	0.009 ± 0.002	-0.016 ± 0.001	0.883 ± 0.001	0.194 ± 0.001	-0.016 ± 0.005	0.010 ± 0.003	0.984 ± 0.003
Thorlabs	0.5041 ± 0.0003	0.8635 ± 0.0002	0.0159 ± 0.0004	-0.0063 ± 0.0057	0.8625 ± 0.0012	0.5059 ± 0.0020	0.0247 ± 0.0162	-0.0407 ± 0.0171	0.9986 ± 0.0010
Set-up B	0.492 ± 0.002	0.877 ± 0.002	0.019 ± 0.004	-0.027 ± 0.002	0.873 ± 0.001	0.510 ± 0.003	-0.009 ± 0.001	-0.005 ± 0.001	1.005 ± 0.002
Thorlabs	0.4972 ± 0.0005	0.8672 ± 0.0003	0.0265 ± 0.0004	0.0003 ± 0.0007	0.8667 ± 0.0003	0.4988 ± 0.0005	0.0367 ± 0.0023	-0.0515 ± 0.0016	0.9980 ± 0.0001
Set-up C	0.503 ± 0.001	0.868 ± 0.001	-0.005 ± 0.001	-0.004 ± 0.002	0.879 ± 0.002	0.515 ± 0.001	0.025 ± 0.002	0.006 ± 0.001	0.999 ± 0.001
Thorlabs	0.5035 ± 0.0007	0.8637 ± 0.0004	-0.0228 ± 0.0007	-0.0214 ± 0.0011	0.8645 ± 0.0003	0.5021 ± 0.0005	0.0479 ± 0.0011	-0.0752 ± 0.0012	0.9960 ± 0.0001
Set-up D	0.493 ± 0.001	0.872 ± 0.001	-0.006 ± 0.001	-0.027 ± 0.001	0.874 ± 0.001	0.510 ± 0.001	-0.001 ± 0.001	0.000 ± 0.001	1.004 ± 0.002
Thorlabs	0.5195 ± 0.0003	0.8541 ± 0.0002	-0.0244 ± 0.0004	-0.0345 ± 0.0011	0.8711 ± 0.0022	0.4899 ± 0.0062	0.0166 ± 0.0009	-0.0574 ± 0.0007	0.9982 ± 0.0001
Set-up E	0.501 ± 0.001	0.869 ± 0.002	0.000 ± 0.002	-0.032 ± 0.001	0.873 ± 0.001	0.525 ± 0.001	-0.003 ± 0.001	0.000 ± 0.003	1.006 ± 0.003
Thorlabs	0.5081 ± 0.0003	0.8611 ± 0.0002	0.0155 ± 0.0004	-0.0301 ± 0.0005	0.8668 ± 0.0003	0.4978 ± 0.0005	0.0588 ± 0.0012	-0.0441 ± 0.0012	0.9973 ± 0.0001
Set-up F	0.481 ± 0.001	0.850 ± 0.001	-0.004 ± 0.001	-0.027 ± 0.002	0.866 ± 0.001	0.508 ± 0.001	-0.004 ± 0.002	-0.005 ± 0.001	1.007 ± 0.001
Thorlabs	0.4937 ± 0.0011	0.8693 ± 0.0006	-0.0235 ± 0.0008	-0.0309 ± 0.0006	0.8681 ± 0.0002	0.4954 ± 0.0004	0.0269 ± 0.0009	-0.0474 ± 0.0003	0.99851 ± 0.00003

The repeatability of the implemented polarimeters has been studied as well. With this aim, we have calculated the summation of the S_0, S_1, S_2 and S_3 variances for each individual SOP measurement (by using the standard deviations shown in Table 4-5). Then, we have calculated the average of the three summations (i.e. corresponding to the three SOPs) for each polarimeter, leading to the Stokes parameters variance average represented in Figure 4-16. Red rhombuses show the variances average for the polarimeter A, B and C. When the exiting SOP from TN-LC is projected over a linear SOP, the best result is achieved for the double pass set-up (polarimeter C). Green squares show the variances average for polarimeters E, F and G. When the exiting SOP from TN-LC is projected over an elliptical SOP, the standard deviations are smaller than those obtained for linearly polarized light configurations, being this improvement especially relevant in configuration D. We remark that EWV is the summation of the Stokes parameters variances. Therefore, values shown in Figure 4-16 are directly related to the EWV and so, evidencing experimentally the improvement achieved during the optimization process of the six set-ups. Note that tendency observed in plot of Figure 4-16 is in agreement with EWV values of Table 4-1.

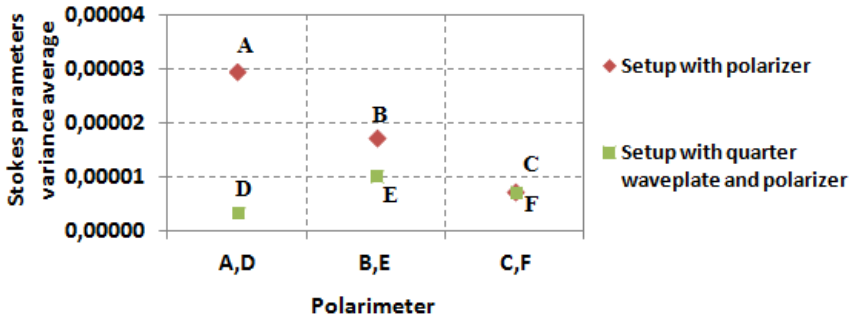

Figure 4-16: Stokes parameters variance average as function of different polarimeters. Using a linear polarized SOP (rhombuses) or an elliptical polarized SOP (squares) to project over the exiting light from the TN-LC.

Finally, we have measured two partially polarized states by using polarimeter D, being the polarimeter providing the lowest average variance (see Figure 4-16). The measured SOPs were generated by illuminating a depolarizer (Thorlabs, DPU-25). This device consists of two crystal quartz wedges, whose optic axes are 45° apart. Thus, light transmitted through this element has a polarization that varies spatially, and since the polarimeter performs an average of a small area, the resulting SOP mean has a certain amount of depolarized light. The DOP measurements obtained are shown in Table 4-6. Notice that DOP values between polarimeter D and the commercial one are very close (differences smaller than 0.02). Moreover, we include the Stokes parameters normalized by $\sqrt{S_1^2+S_2^2+S_3^2}$, providing the fully polarized contribution. Again, the experimental results are in agreement (Stokes parameters maximum difference of 0.04). Small discrepancies between both measurements can be attributed to the difficulty to apply exactly the same measuring area for the two polarimeters. Nevertheless, experimental results evidence the suitability of the polarimeter to measure the polarization of partially polarized light.

Table 4-6: Normalized Stokes parameters (fully polarized contribution) and DOP measurements of two different SOPs partially polarized when measuring with polarimeter D and the commercial polarimeter (Thorlabs), when monochromatic light is used.

		S_1	S_2	S_3	DOP
SOP 1	**Polarimeter D**	0.669 ± 0.002	0.085 ± 0.004	0.739 ± 0.003	0.742 ± 0.001
	Thorlabs	0.6534 ± 0.0008	0.0812 ± 0.0008	0.7526 ± 0.0006	0.724 ± 0.047
SOP 2	**Polarimeter D**	-0.249 ± 0.002	-0.038 ± 0.002	0.968 ± 0.002	0.632 ± 0.001
	Thorlabs	-0.2923 ± 0.0012	-0.0053 ± 0.0007	0.9563 ± 0.0004	0.649 ± 0.042

4.4.2.2 LED illumination

Finally, polarimeter D was tested by illuminating with a higher bandwidth light source (red LED). Since birefringence depends on the wavelength, we have used an achromatic quarter waveplate in the polarimeter set-up, ensuring the desired and unique retardance. However, TN-LC birefringence depends on the wavelength to certain extent. Therefore, first we need to check the TN-LC achromaticity in the LED spectrum, in other words, if the small bandwidth of the LED spectrum affects to the TN-LC birefringence, leading to depolarization in the projection SOPs.

With the aim of testing the achromaticity of TN-LC cell in the LED spectrum, we have generated different SOPs by sending different voltages to the TN-LC cell, being this device illuminated by a LED light beam previously polarized with a LP at 0º. Thus, any state with a DOP lower than 1, would be due to chromatic feature of TN-LC, otherwise we could affirm that TN-LC acts as an achromatic retarder. We have used the rotating QWP based Stokes polarimeter to measure the set of generated SOPs. Figure 4-17 plots the DOP of the measured Stokes vector as function of the voltage sent to the TN-LC panel. DOP values are from 0.96 to 1 (i.e. practically fully polarized light). Analogously, different optical elements were illuminated with the LED source and the output SOP was measured with the commercial polarimeter. First, a chromatic QWP (designed for 633nm) was illuminated with LED light linearly polarized at 45º with respect to the QWP axis. The measured DOP was 0.44. Then, the chromatic QWP was replaced by an achromatic QWP, obtaining a DOP of 0.99. Comparing these values with data shown in Figure 4-17, we affirm that the TN-LC device is acting as an achromatic retarder for our LED bandwidth.

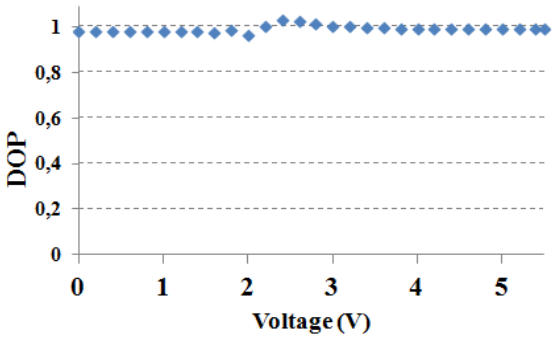

Figure 4-17: Measured degree of polarization (DOP) of generated SOPs with the following PSG: LED light beam, polarizer at 0º and the TN-LC cell when sending an array of voltages.

As mentioned before, we have experimentally calibrated polarimeter D using LED illumination and the corresponding polarimetric measurement matrix is used for data reduction.

Then, we have tested the performance when measuring fully polarized states. The SOPs were generated by modifying the polarization of the light beam with a polarizer and an achromatic retarder, to ensure the same incident SOP for all the wavelengths of the LED spectrum and so, generating a fully polarized mean SOP.

In Table 4-7, we present the measurements of three different fully polarized states. The Stokes parameters obtained with the implemented polarimeter are in accordance to those provided by the commercial polarimeter. Deviations of Stokes parameters measured by polarimeter D and the commercial polarimeter when illuminating with the LED (smaller than 0.05), are of the same order that the ones obtained with laser light.

Finally, we complete the study by measuring two incoming light beams partially polarized. The partially polarized SOPs were generated by illuminating with the LED light beam a polarizer followed by a chromatic QWP. Due to the chromatic QWP has a wavelength dependent retardance, each wavelength generates a different SOP. Since the polarimeter performs an average measurement, the detected mean SOP will have certain amount of depolarization (i.e. DOP < 1).

In Table 4-8, two particular measurements are provided: SOP 1 and SOP 2. In the first case (SOP 1), the studied SOP was generated by illuminating with the LED source a polarizer followed by a chromatic QWP with its fast axis at 45º of the polarizer transmission axis. In such case, circular light is obtained for 633nm (i.e. QWP operational wavelength) but for the other wavelengths in the LED spectrum, different SOPs are generated. The measurement obtained with the polarimeter shows a mean SOP almost circularly polarized, accompanied by a significant content of unpolarized light (DOP equal to 0.4). The second case (SOP 2) was analogous to the first one, but for a different relative angle between the polarizer transmission axis and the QWP fast axis. Differences between measurements from polarimeter D and the commercial one are as maximum of 0.05 in the Stokes parameters and of 0.03 in the DOP value.

To conclude, results given in Table 4-7 and Table 4-8 prove the potential of the implemented polarimeter, which is able to measure partially and fully polarized light with a light source with a small bandwidth.

Table 4-7: Stokes parameters of three different SOPs (the Stokes vectors are normalized) measured by polarimeter D and the commercial polarimeter (Thorlabs), when they are illuminated with a LED light source.

	Linear SOP			**Elliptical SOP**			**Circular SOP**		
	S_1	S_2	S_3	S_1	S_2	S_3	S_1	S_2	S_3
Expected values	0.5	0.866	0	0	0.866	0.5	0	0	1
Set-up D	0.494 ± 0.001	0.878 ± 0.001	-0.001 ± 0.001	0.025 ± 0.001	0.839 ± 0.001	-0.4145 ± 0.0004	0.017 ± 0.001	-0.009 ± 0.001	1.002 ± 0.001
Thorlabs	0.4977 ± 0.0003	0.8673 ± 0.0002	-0.0073 ± 0.0001	0.0459 ± 0.0003	0.89404 ±0.00003	-0.4456 ± 0.0001	-0.0188 ± 0.0001	-0.0344 ± 0.0001	0.99923 ±0.00001

Table 4-8: Normalized Stokes parameters (fully polarized contribution) and DOP measurements of two SOPs partially polarized by means of polarimeter D and the commercial one (Thorlabs), when LED light source is employed.

		S_1	S_2	S_3	**DOP**
SOP 1	**Polarimeter D**	-0.019 ± 0.002	-0.114 ± 0.001	0.993 ± 0.002	0.437 ± 0.001
	Thorlabs	-0.0418 ± 0.0002	-0.0647 ± 0.0002	0.99703 ± 0.00001	0.410 ± 0.003
SOP 2	**Polarimeter D**	-0.044 ± 0.001	0.686 ± 0.001	0.727 ± 0.001	0.5514 ± 0.0004
	Thorlabs	-0.0500 ± 0.0002	0.7120 ± 0.0001	0.7004 ± 0.0001	0.546 ± 0.005

Chapter 5 **Polarimeter based on ferroelectric liquid crystal panels**

This chapter presents a Stokes polarimeter based on two ferroelectric liquid crystal (FLC) panels. In addition, we extended the Stokes polarimeter prototype to a Mueller polarimeter, using two additional FLC panels for the PSG (polarization state generator). FLC devices are very fast in response when compared with other types of LCs, allowing the implantation of dynamic polarimeters with a high velocity in the polarization measurements. We include the experimental characterization of the FLC features. An optimization of the parameters of the set-up is detailed in order to minimize the noise propagation. Moreover, a tolerance analysis of the polarimetric device to get measurements with 1% of accuracy is discussed. Finally, we detail the experimental implementation of the polarimeter. In particular, different experimental concerns are provided: the calibration of the polarimetric measurement matrix, a study of the repeatability in time focusing on the dependence with the temperature, a study of the polarimetric performance dependence with the duration of the measurement and several measurements of Stokes vectors and Mueller matrices.

5.1 Design

In this chapter we focus on the design of a complete polarimeter based on ferroelectric liquid crystals (FLC) panels. FLC cell, described in detail in section 1.3.1.3, can be modeled as a retarder of constant retardance and with two possible orientations for its fast axis, switchable when addressing a bipolar electrical signal. By taking advantage of this behavior, a complete polarimeter free of mechanical movements is designed in Figure 5-1. The polarimetric set-up can be used in two modalities depending on the purpose: as a Stokes polarimeter for determining the polarization of an incident beam or as a Mueller polarimeter for characterizing the polarimetric properties of a sample. The Stokes polarimeter is constituted by a system able to analyze any state of polarization (PSA, polarization state analyzer). The PSA architecture is based on two FLCs of nominal retardances of λ/2 and λ/4, followed by a linear polarizer at 0º (it defines our laboratory vertical) and a radiometer for taking the flux measurements. In order to implement a Mueller polarimeter, besides the PSA, a system which generates controlled polarization states (PSG, polarization state generator) is required. This system is implemented by the same set of elements of the PSA, but in inverse order. That is, following the source of light (in our case a He-Ne laser) we place a linear polarizer at 0º and two FLC panels of nominal retardance of λ/4 and λ/2. Note that the particular positions in the set-up for the λ/4 and λ/2 retarders, as well as their orientations, must not be arbitrarily chosen but optimized, as they are very important for the optimal performance of the polarimeter.

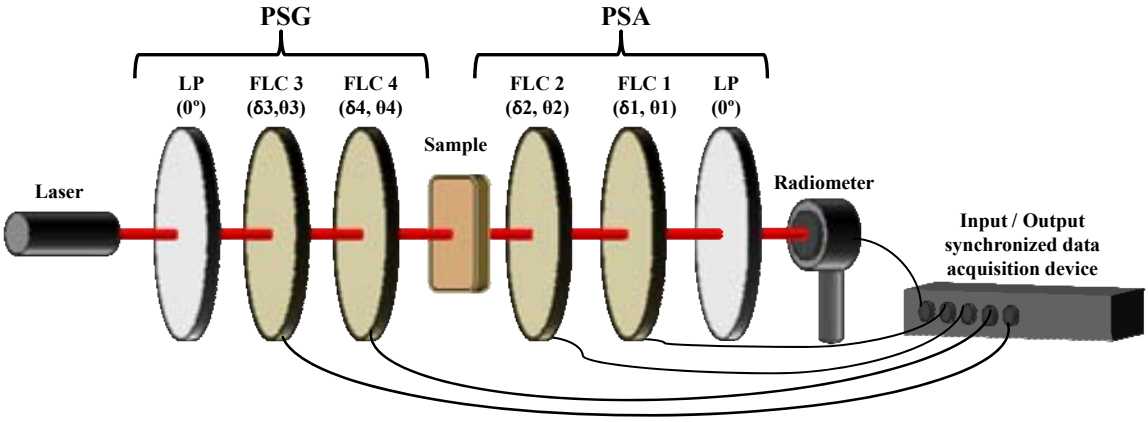

Figure 5-1: Mueller and Stokes polarimeter based on FLC cells. The nominal retardances of the FLC cells are: $\delta_3 = \delta_1 = \lambda/4$ and $\delta_4 = \delta_2 = \lambda/2$.

At this stage, four bipolar squared electrical signals are synchronously sent to the FLC panels. All of them have 20V of amplitude and the periods are related as follows:

$$8T_4 = 4T_3 = 2T_2 = T_1 = T = 0.5s\ , \tag{5-1}$$

where T_n is the period of the n-th FLC and T the duration of the whole measurement process. In general T=0.5s, except in the subsection 5.4.3 where other values have been tested in order to evaluate the dependence of the polarimeter performance with the duration of the measurement. Therefore, in general the signals sent to the 4 FLC cells during this period T are as the ones represented in Figure 5-2.

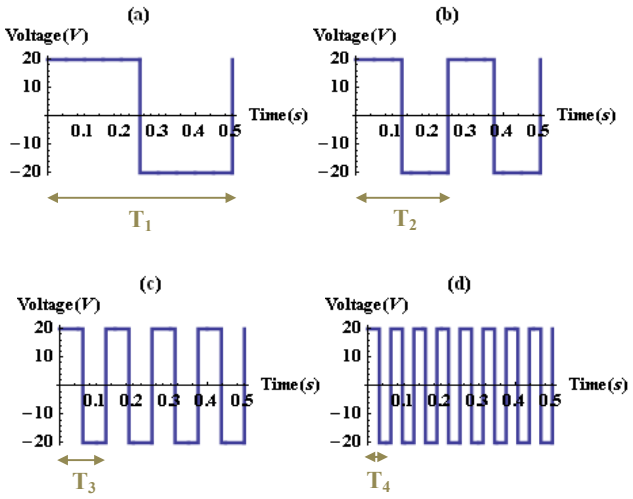

Figure 5-2: Electrical signals sent to the: (a) FLC1, (b) FLC2, (c) FLC3 and (d) FLC4, during a measurement duration of T=0.5s.

Note that for this particular arrangement of signals, we obtain 16 different stationary states, leading to 16 different polarization configurations of the PSG-PSA system. For each one, we take a flux measurement. In this way, 16 sequential flux measurements synchronized with addressed signals are acquired during 0.5s. In fact, each different stationary state corresponds to a particular configuration for the fast axis orientation of the different FLCs in the set-up. Note that depending on the voltage addressed to the FLC panel, its fast axis orientation can switch between two specific positions: θ and $\theta+\alpha$.

As an example we focus on the Stokes polarimeter, and we detail in Table 5-1 the 4 combinations of the fast axis orientations of cells FLC1 and FLC2, leading to the four stationary states of the PSA when a flux measurement is acquired.

Table 5-1: Orientations of the fast axis for the 2 FLC cells involved in the Stokes polarimeter, during the acquisition of the 4 flux measurements.

Measurement	**#1**	**#2**	**#3**	**#4**
FLC1	$\theta 1$	$\theta 1$	$\theta 1+\alpha 1$	$\theta 1+\alpha 1$
FLC2	$\theta 2$	$\theta 2+\alpha 2$	$\theta 2$	$\theta 2+\alpha 2$

The Mueller matrix describing the whole PSA system has the following expression:

$$M_{LP}(0^{\circ}) \cdot M_{FLC1}(\delta_1, \theta_1) \cdot M_{FLC2}(\delta_2, \theta_2), \tag{5-2}$$

where the $M_{LP(0^{\circ})}$ is the Mueller matrix of a linear polarizer at 0º, and $M_{FLC}(\delta,\theta)$ is the Mueller matrix describing the FLC cell and so, it corresponds to the Mueller matrix of a linear retarder (given by Eq.(1-4)) of retardance δ and fast axis orientated at θ or at $\theta+\alpha$, depending on the measurement number (see Table 5-1). Therefore, the polarization analyzer is the first row of the total Mueller matrix indicated in Eq. (5-2).

Furthermore, the states of polarization generated with the PSG have the following expression:

$$M_{FLC4}(\delta_4, \theta_4) \cdot M_{FLC3}(\delta_3, \theta_3) \cdot \frac{1}{2}\begin{pmatrix}1 & 1 & 0 & 0\end{pmatrix}^T \tag{5-3}$$

Note that the combination of the respective two possible values for θ_3 and θ_4, lead to the four available states of polarization generated by the PSG system.

5.1.1 Experimental characterization of the LC panel

We have used FLC cells manufactured by Boulder Nonlinear Systems. Figure 5-3 shows a picture of one of the FLC cell used in our set-up.

The FLC panel is constructed using a sheet glass coated with a deposition of a transparent conductive layer (ITO). These window substrates are then evenly covered with a polymer layer, which is then rubbed, forming tiny microgrooves in the polymer layer. The microgrooves provide the alignment directionality critical in the LCD production. Then, the coated windows are spaced a few microns apart. The cavity between substrates is filled with liquid crystal material and sealed.

Figure 5-3: Ferroelectric liquid crystal cell used in our set-up.

As provided by the fabricant, the nominal retardances of the FLC cells used in our set-up are of λ/4 and λ/2, whereas the rotation of the fast axis (α) under a bipolar square electrical signal should be of 45º. However, in order to take into account possible deviations of the actual optical features values of the FLC cell from the nominal values, we conduct an experimental calibration of the FLC optical features (the actual retardance and the rotation of its fast axis).

The calibration method applied in this section is a modification of the calibration procedure given in [48]. First, we placed the FLC panel between two crossed polarizers. While a squared electrical signal is sent to the LC device, we take synchronously flux measurements. In this way, we separately obtain the flux measurements for the two corresponding stable states. The linear polarizers are simultaneously rotated, and flux measurements are acquired for different polarizer orientations. Figure 5-4 shows an example of intensity versus polarizer orientation plot during the calibration of a half-wave FLC cell, for the two stable positions of the FLC director (data represented in red and in blue, respectively). By doing this, measurements lead to an ambiguity concerning to the orientation of the fast and slow axes. Thus, extra flux measurements are performed when illuminating the FLC with right circularly polarized light. This test leads to the determination of the fast axis orientation. The characterization is conducted for a room temperature of 23ºC and illuminating the system with a monochromatic light source (633nm). In Table 5-2 we show the calibrated retardance and rotation for the four FLC panels characterized.

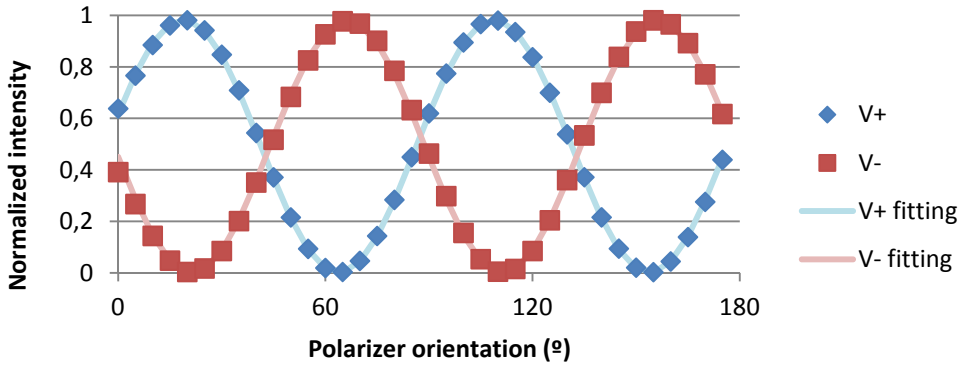

Figure 5-4: Normalized intensity as function of the orientation of the LP, during the calibration of the physical parameters of a FLC cell of nominal retardance λ/2.

Table 5-2: Nominal ($\delta_{nominal}$) and calibrated retardance (δ_{exp}), and fast axis rotation (α_{exp}) of the four FLC cells.

Parameter	$\delta_{nominal}$ (º)	δ_{exp} (º)	α_{exp} (º)
FLC1	90	99	44
FLC2	180	165	47
FLC3	90	104	43
FLC4	180	155	-46

We observe that the actual physical features differ from the nominal values. Thus, a calibration of these parameters before conducting an optimization procedure based on these values is strongly recommended.

Afterwards, we have experimentally measured the transitory time of the FLC cell. To this end, we have measured the intensity as function of time when changing the sign of the square electrical signal. In order to detect variations in the intensity measurements, we placed a LP between the LC cell and the radiometer. Figure 5-5(a) (Figure 5-5 (b)) shows that when the voltage is changed from -20 to 20V (from 20 to -20V), the measured time response is of 0.2 (0.3) milliseconds.

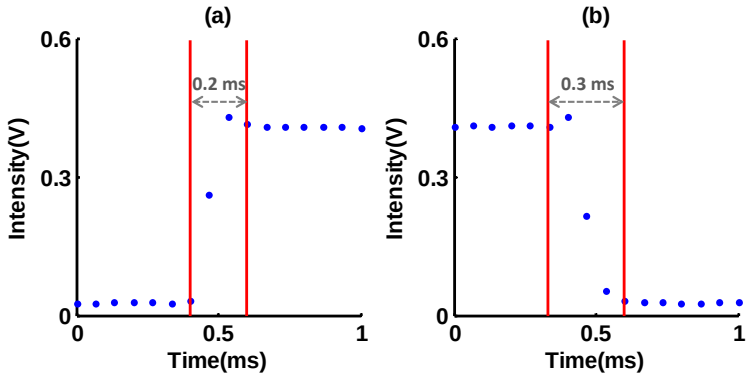

Figure 5-5: Time response of the FLC cell when changing voltage: (a) from -20 to 20V, (b) from 20 to -20V.

5.2 Optimization analysis

The goal of this section is to optimize the polarimetric system in order to reduce the propagation of noise from flux measurements to the estimated Stokes vector (or Mueller matrix). First, in subsection 5.2.1 we detail the optimization carried out to the polarimeter architecture. Next, in subsection 5.2.2, we study the robustness of the optimized polarimeter.

5.2.1 Optimized polarimeters

In order to optimize the Stokes and Mueller polarimeters, we have analyzed the CN of the PSA and the PSG, separately. Three optical elements are involved in each part of the set-up (i.e. in the PSG and in the PSA): two FLC cells and a LP. Concerning the LP, this is set to 0º, whereas the two FLC cells have a given value of retardance (δ) and rotation (α) which have been already calibrated (see Table 5-2). However, the initial orientations of both LC cells have to be chosen (θ_1 and θ_2 for the PSA, and θ_3 and θ_4 for the PSG). Thus, these are the four parameters to be optimized in the architecture of our polarimeter based on FLC cells.

By using Eq. (5-2), we have simulated different PSAs for different combinations of θ_1 and θ_2, and their CN values are calculated and plotted in Figure 5-6(a). Similarly, by using Eq. (5-3), we have simulated different PSGs for different combinations of θ_3 and θ_4, and the CN of the associated systems are calculated and represented in Figure 5-6(b). In both cases, we have used the calibrated values shown in Table 5-2 for the retardance and rotation. We have used a color scale from 1 to 12, in order to enhance small values of CN. Values greater than 12 are mapped to 12. Some combinations of orientations lead to singular matrices (CN is infinite), corresponding to the white areas in the plot. By examining these results, we determine the minimum CN value for the PSA (2.22) and for the PSG (2.25), marked in Figure 5-6 as black points. The optimized orientations of the FLCs corresponding to those minimum CN values are written in Table 5-3. In addition, we include the CN and the EWV for these optimized PSA and PSG. Note that the CN for the PSG is slightly larger than the one obtained for the PSA. This small difference comes from the fact that the FLCs retardances and fast axis rotations used for the simulations are no the nominal ones, but the calibrated ones (see Table 5-2).

Therefore, CN of the Stokes polarimeter is 2.22, whereas the CN of the Mueller polarimeter is 5.00 (product between the CNs describing the PSG and the PSA). Note that the CN for the Stokes polarimeter based on FLC panels is slightly higher than the one corresponding to the best optimization (1.73 corresponding to the regular tetrahedron configuration) implemented in the PA-LC based polarimeter. This is because FLC panels are more restrictive: the retardance is fixed and, once the initial orientation of the fast axis is chosen, the second stable orientation of the fast axis is determined by the rotation angle. Consequently, FLC based polarimeters are limited to certain polarization analyzers. However, after the optimization of the FLC based polarimeter, the CN is very low, ensuring a good optimization for accurate polarization metrology. From now on, we call the optimized configurations (given by parameters from Table 5-3) as theoretical configurations.

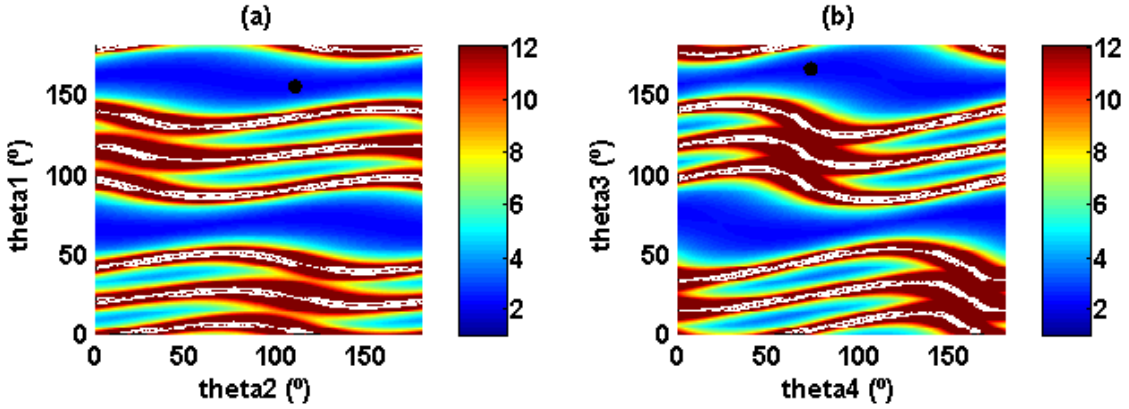

Figure 5-6: CN as function of the two orientations of the FLC cells of: (a) the PSA (θ_1 and θ_2) and (b) the PSG (θ_3 and θ_4). The black points are marking the minimum CN for the PSA and the PSG.

Table 5-3: Result of the optimization process.

	FLC	θ optimized	CN	EWV
PSA	1	154º	2.22	11.18
	2	110º		
PSG	3	165º	2.25	11.10
	4	73º		

5.2.2 Polarimeter robustness

We have also studied the dependence of the polarimeter performance with experimental variations from the theoretical PSA and PSG configurations (given in Table 5-3). In other words, the robustness of our polarimetric system (the PSA and the PSG) is here revised. Note that these variations may be due to a variation on temperature affecting the LC operation, or a small misalignment or tilt of one of the optical elements involved in the set-up.

To this aim, we simulate different deviated PSAs (PSGs), and their quality indicators are recalculated. We add to each element of the PA vector (generated SOP vector) a value obtained from a random uniformly distribution, with zero mean and amplitude 0.4. For both PSA and PSG, 50 different polarimeters are simulated, deviated from the ideal configuration. Figure 5-7 and Figure 5-8 represent their condition numbers and their variances.

Both PSA and PSG present a very robust performance, leading to small variations on their quality indicators. In particular, condition number fluctuations for the deviated PSAs and PSGs have a standard deviation of 0.3 in both cases.

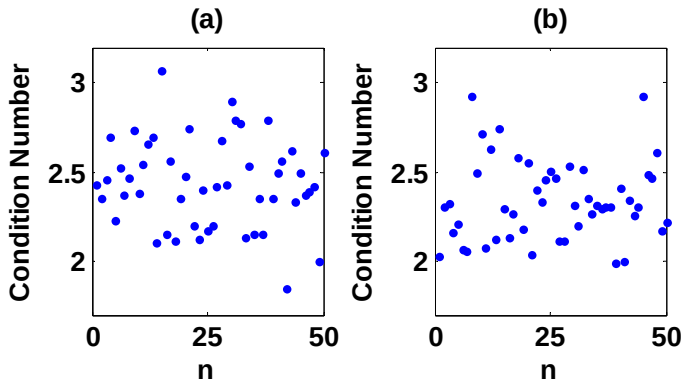

Figure 5-7: Condition number of 50 different simulated (a) PSAs and (b) PSGs deviated from the theoretical optimized configurations, when adding to the PAs or the generated SOPs a value from a zero mean uniform distribution of amplitude 0.4.

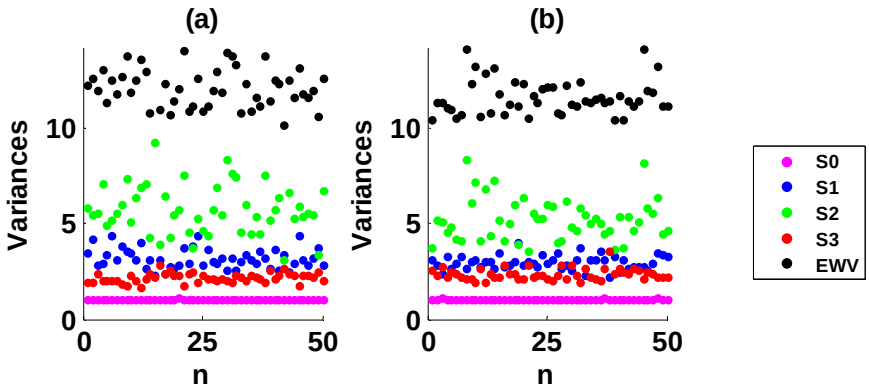

Figure 5-8: Variances of 50 different simulated (a) PSAs and (b) PSGs deviated from the theoretical optimized configurations, when adding to the PAs or the generated SOPs a value from a zero mean uniform distribution of amplitude 0.4.

5.3 Tolerance analysis

In this section we examine the tolerance of the polarimeter parameters in order to achieve an accuracy of 0.02 in the polarization measurements. Two separate studies have been carried out regarding the accuracy in Stokes polarimeter and in the Mueller polarimeter.

First, we analyze the Stokes polarimeter and its accuracy when measuring the Stokes vector elements. We followed the methodology explained in section 2.4.1, where several incident SOPs are tested. In our case, the parameters sensitive to suffer deviations from theoretical values are: the orientation, retardance and rotation of the first and second FLC (θ_1, θ_2, δ_1, δ_2, α_1 and α_2, respectively). Notice that we take as reference the orientation of the linear polarizer at 0º.

As an example, we show a particular study in Figure 5-9: the components of the Stokes error (calculated as Eq. (2-20)) as function of the incident Stokes vector (parameterized by Eq. (2-21)) when there is a shift of 1º on the different parameters involved in the set-up. We observe a strong dependence of the Stokes error with the incident polarization. In addition, from the highest to the smallest Stokes error corresponds to a deviation in the orientation (Figure 5-9(a) and (b)), the rotation (Figure 5-9 (c) and (d)) and finally, the retardance (Figure 5-9(e) and (f)).

In order to determine the accuracy of the polarimeter (defined in section 2.4.1), we look for the maximum error of the four Stokes components and from all the possible incident Stokes vectors (into a certain sampling resolution). For instance, the accuracy for a shift of 1º in the orientation of the FLC2 (Figure 5-9(b)) is of 0.069.

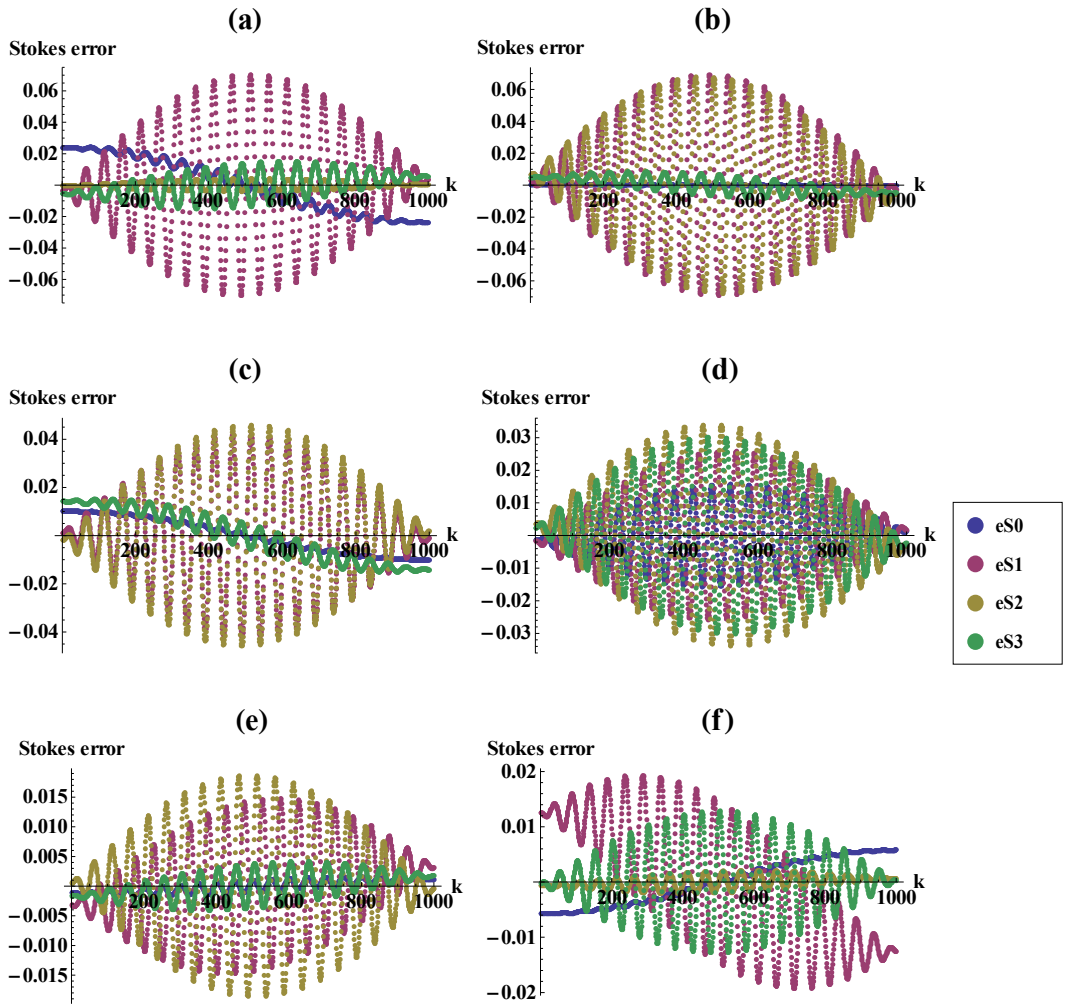

Figure 5-9: Stokes parameters error with a tolerance of 1º for a shift in: (a) fast axis orientation of FLC1 (θ_1), (b) fast axis orientation of FLC2 (θ_2), (c) rotation of FLC1 (α_1), (d) rotation of FLC2 (α_2), (e) retardance of FLC1 (δ_1) and (f) retardance of FLC2 (δ_2). Errors as function of variable k, which parameterizes the incident Stokes vector by Eq.(2-21).

Afterwards, we generalize this study by repeating the same analysis but with other values of tolerance (0.2, 0.5 and 2º). Figure 5-10 shows a summary of the accuracy obtained for the four different values of tolerances evaluated and for the six analyzed parameters in the set-up. We observe a linear dependence between accuracy and tolerance. On one hand, the accuracy of this architecture is especially critical to misalignments on the orientation of the FLCs, as we observe the highest loss of accuracy for this parameter, and then to the rotation of their axes. A stronger dependence on the orientation than on rotation of the fast axis of the FLC is predictable because the four analyzers are dependent on the orientation of the fast axis but just two of them are rotated (see Table 5-1). On the other hand, polarimeter accuracy is very low sensitive to a shift on the retardance of the FLC panels. In particular, a tolerance of 1º on the retardance of each FLC achieves an excellent accuracy of 0.019.

As provided in Figure 5-10, we have also calculated the linear regression for the different parameters. Finally, we chose to fix the accuracy to 0.02 (red dashed line in Figure 5-10), as this value is extensively suitable for most polarimetric applications. Under this scenario, the corresponding tolerance values of the parameters are straightforward determined and shown in Table 5-4. Obviously, if some application requires an accuracy smaller than 0.02, one should recalculate the corresponding new tolerances, obtaining values smaller than the ones presented in Table 5-4.

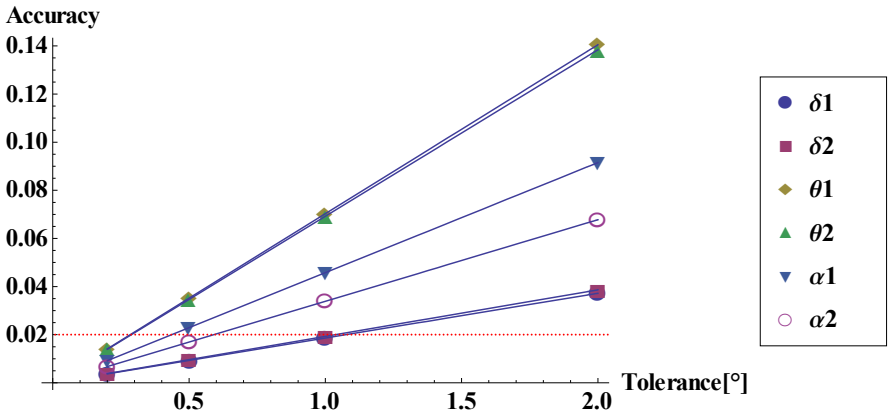

Figure 5-10: Stokes polarimeter accuracy as function of the tolerance of different parameters of the set-up (δ, θ and α are retardance, orientation and rotation, respectively).

Table 5-4: Tolerance values to achieve a 1% of accuracy in the Stokes polarimeter.

Parameter	δ (º)	θ (º)	α (º)
FLC1	1.07	0.28	0.44
FLC2	1.04	0.29	0.59

Second, we analyze the accuracy of the Mueller polarimeter by following the methodology explained in subsection 2.4.2. In the Mueller polarimeter set-up there are 12 parameters that are sensitive to suffer deviations from theoretical values: orientation, retardance and rotation of the four FLC cells involved in the Mueller polarimeter. Mueller matrix error depends on the particular Mueller matrix that we are measuring (as seen in Eq. (2-22)). In addition, many studies can be conducted to analyze the dependence of the accuracy of the Mueller polarimeter with each one of the 12 involved parameters.

As an example, we show a particular case in Figure 5-11: the elements of the Mueller matrix error as function of the fast axis orientation of a quarter waveplate that we have selected as polarimetric target. We assume a shift of 1º on the orientation of the second FLC (θ_2).

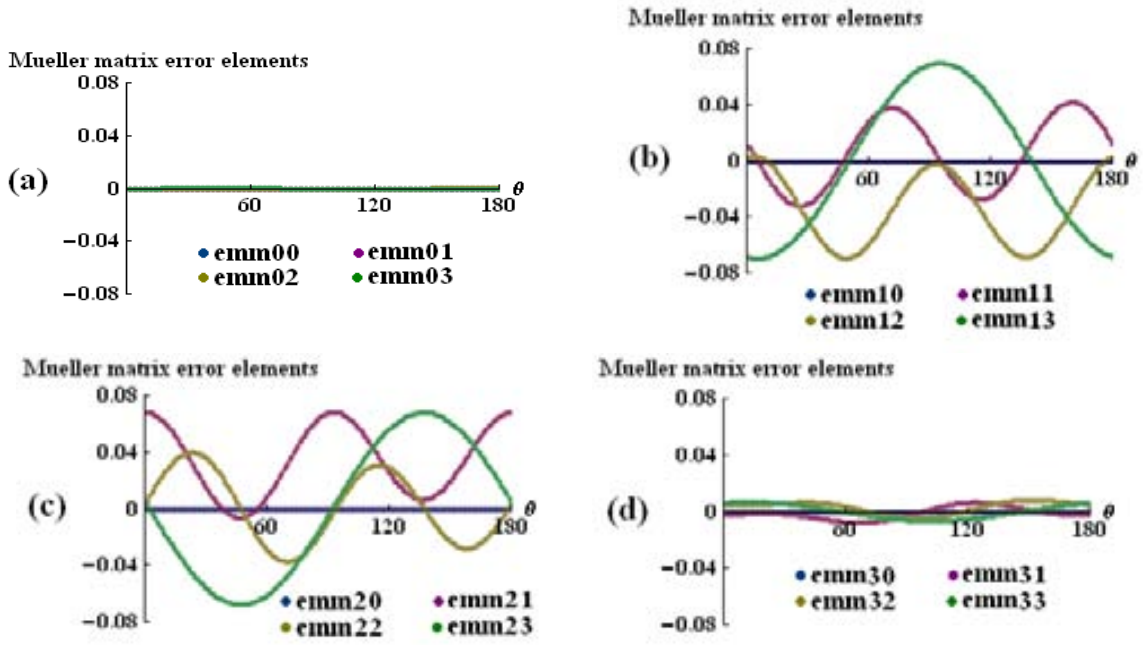

Figure 5-11: Elements of the Mueller matrix error as function of the fast axis orientation (θ) of a quarter waveplate, simulating a shift of 1º on θ_2. (a) First row, (b) second row, (c) third row and (d) fourth row of the Mueller matrix error.

On one hand, we observe that the first row (Figure 5-11(a)) and the first column (e_{mm00}, e_{mm10}, e_{mm20} and e_{mm30} in Figure 5-11) of the Mueller matrix error are practically zero. Also the last row (Figure 5-11(d)) is very close to zero. On the other hand, the other 6 elements of the Mueller matrix error are following a sinusoidal function of the retarder orientation. Finally, as an example, we determine the accuracy for this particular case by looking for the maximum error of the sixteen elements and considering all the analyzed orientations of the retarder. We obtain an accuracy of 0.069.

Afterwards, we complete the analysis for other values of tolerance (0.2, 0.5 and 2º) on the 12 parameters of the set-up, and Figure 5-12 shows the results.

We observe a linear dependence between accuracy of the Mueller polarimeter and tolerance of the parameters. This architecture is more sensitive to a misalignment in orientation of the FLCs panels and then to the rotation of their axes. This dependence can be understood if we consider that all polarization analyzers and generators are supposed to be settled from the initial orientation, but just half of them are rotated. Nevertheless, Mueller polarimeter accuracy is very low sensitive to shifts on the FLC cells retardance.

After calculating the linear regression in Figure 5-12, we fix a desired accuracy of 0.02 (red dashed line in Figure 5-12) and we determine the tolerances of the parameters involved in the set-up, those values are shown in Table 5-5.

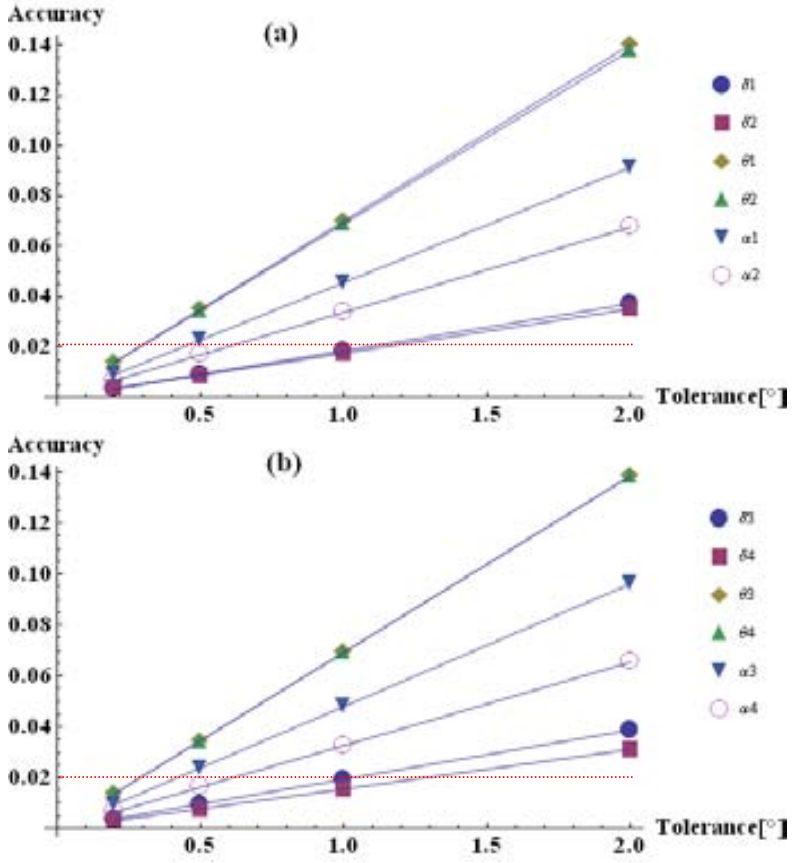

Figure 5-12: Mueller polarimeter accuracy as function of the tolerance of different parameters of the set-up (δ, θ and α are retardance, orientation and rotation, respectively). Tolerance over the parameters concerning: (a) the PSA (FLC1 and FLC2) and (b) the PSG (FLC3 and FLC4).

Table 5-5: Tolerance values to achieve a 0.02 of accuracy in the Mueller polarimeter.

	δ (º)	θ (º)	α (º)
FLC1	1.07	0.28	0.44
FLC2	1.13	0.29	0.59
FLC3	1.03	0.29	0.42
FLC4	1.29	0.29	0.61

To conclude this tolerance study, we discuss the parameters tolerances obtained in Table 5-4 and in Table 5-5 concerning the Stokes and Mueller polarimeters, respectively, and these values are compared with the actual tolerances in the laboratory. Retardance, initial orientation and rotation of the fast axis of the FLC cells were experimentally calibrated (section 5.1.1). Moreover, we conduct a calibration after setting the whole polarimetric set-up in order to characterize the polarimetric measurement matrix (W). Therefore, if we use that calibrated matrix,

we are using a mathematical expression much closer to the actual one that we have in the laboratory, setting smaller tolerances to the system. Actually, after calibrating the polarimetric measurement matrix, no mechanical movements are needed to use the polarimeter, reducing significantly error related to misalignment. Finally, we assume a possible retardance variation smaller than 1º during the calibration and the measurements. This assumption can be justified because, as it will be provided later on, thermal variations in the laboratory are not significant when we use the polarimeter during a short period of time (minutes).

5.4 Implementation

We have experimentally implemented the Stokes polarimeter, and the Mueller polarimeter above described (see Figure 5-13). We have used for each system (the PSA and the PSG), two monopixel FLC cells from Boulder Nonlinear Systems. Their nominal retardances are λ/4 and λ/2, but their calibrated values are the ones indicated in Table 5-2. Then, a linear polarizer (LP) from Meadowlark Optics is used in each system. The 4 electrical signals (Figure 5-2) are generated with the desired periods by an A/D converter from Keithley, and they are sent to an amplifier in order to achieve 4 signals of amplitude 20 volts. Finally, those 4 signals of the proper amplitude and period are sent the 4 respective FLC cells. We have used an optical power meter from Newport. Flux measurements are taken by means of the radiometer, then read with the A/D converter, and later sent to the computer. The input and output signals have to be synchronized and this is possible by means of our own LabView software which is controlling all tasks processed by the A/D converter. Finally, the system is illuminated with a monochromatic light source, a He-Ne laser (633nm).

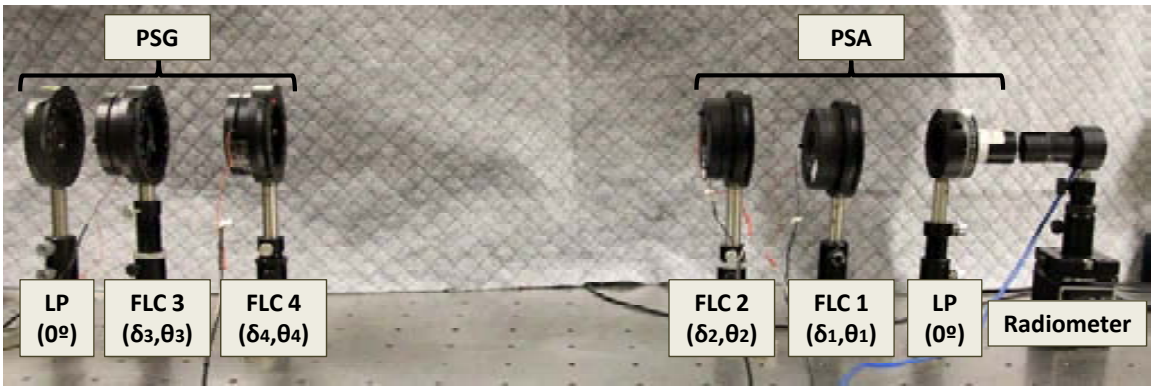

Figure 5-13: Implemented Mueller polarimeter based on two FLC cells in the PSA and two other FLC cells in the PSG.

In next subsection, we detail the experimental calibration of both polarimeters. In addition, we evaluate the repeatability of the Stokes polarimeter over 24 hours of operation, and we include

a discussion of the dependence with the temperature. Also, we include a study related to the speed of measurement. Finally, we provide experimental measurements of several Stokes vectors and Mueller matrices.

5.4.1 Calibration

The polarization elements of the set-up are not assumed to be ideal. For instance, the orientation of the elements can be misaligned with respect to the optimized orientation or the retardance introduced by a FLC can be slightly different from the one previously calibrated because of a variation on the temperature. For this reason, the polarimetric measurement matrix is determined through a calibration procedure and so, misalignments and retardance changes are corrected, to certain extent, in data reduction.

To experimentally calibrate our polarimeter, we used the eigenvalue calibration method [137] (ECM), explained in subsection 2.5.2. This calibration method determines the matrices describing the PSG and the PSA, by performing a set of flux measurements using some reference samples. We have used as reference samples a Glan-Thompson polarizer distributed by CASIX and a quarter waveplate. The ECM does not require an accurate alignment of the reference samples because during the calibration, the optical properties of these reference samples and their orientations are unambiguously determined. In Figure 5-14(a), we plot the theoretical polarization analyzers of the PSA and the experimentally calibrated ones (in green and red, respectively). In Figure 5-14(b), we represent the theoretical and the calibrated SOPs generated by the PSG (in green and red, respectively). The experimental CNs of the calibrated polarimetric measurement matrices describing the PSA and the PSG are, respectively, 2.35 and 2.55, close to the values obtained during the optimization (2.22 and 2.25, respectively as Table 5-3 shows).

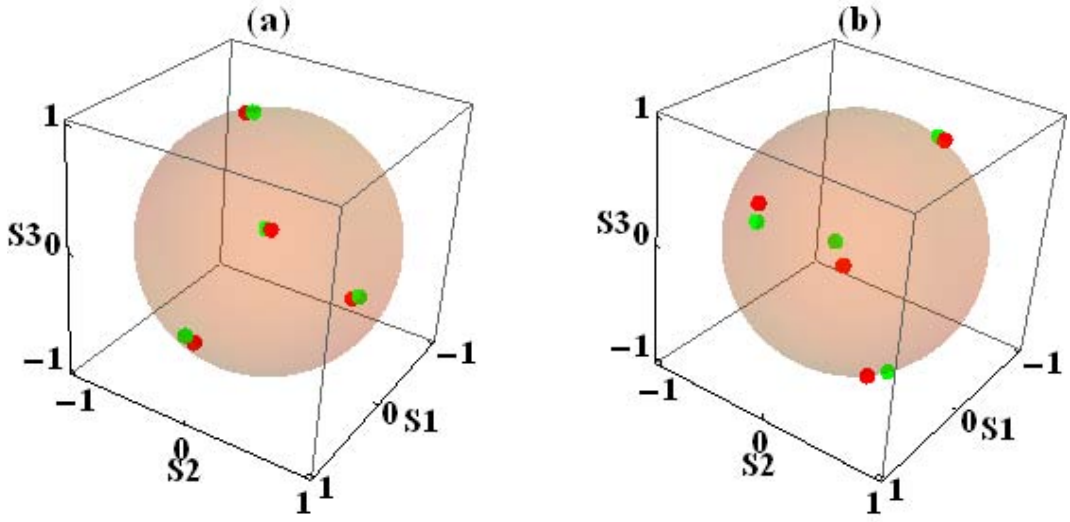

Figure 5-14: (a) PSA and (b) PSG. Theoretical and calibrated SOPs in green and in red points, respectively.

5.4.2 Study of repeatability

To study the dependence of the repeatability of our polarimeter with the temperature, the polarimeter performance is analyzed throughout 24 hours of operation. We focus on the Stokes polarimeter, and we prepared the incident beam as an elliptically polarized state. We separated the measurement procedure in 10 blocks, where 10.000 measurements are taken per block, and with a break of 1 hour between blocks. The purpose of these pauses is to avoid an overheating of the FLC panels. In addition, we have included a LM335 temperature sensor based circuit close to the FLC2 panel. This circuit is synchronized with the measurements of our polarimeter, allowing us to collect the evolution of the temperature during the data acquisition.

The evolution of temperature as a function of time, plotted in Figure 5-15(a), is explained from the room temperature oscillation because the set-up is not thermally insulated. The heating in the laboratory is turned on at 7am and turned off at 9pm approximately, in accordance with the temperature plot. First and last temperature measurements, acquired at similar times of the day, have 1.4ºC of difference. This variation is explained because the second day of acquisition of data was colder than the first one.

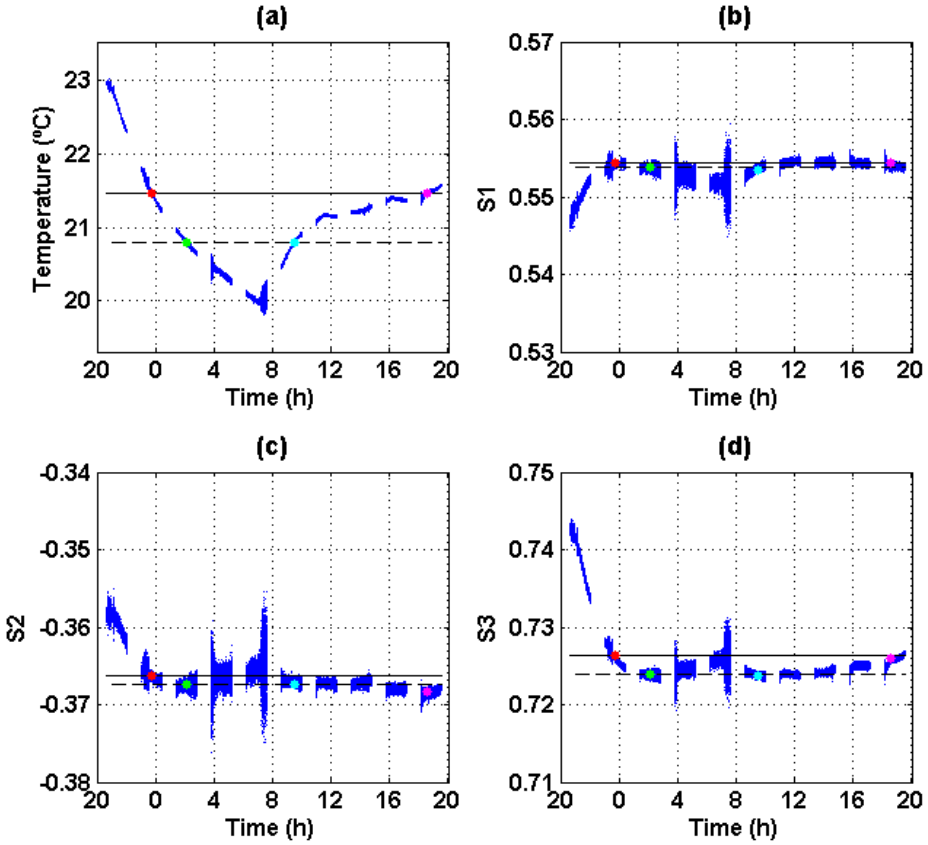

Figure 5-15: (a) Temperature evolution during data acquisition from 8pm of the first day to the 8pm of the second day. Measured Stokes parameters: (b) S_1, (c) S_2 and (d) S_3. By using a horizontal line, we mark a particular temperature reached in two different moments of the day: continuous line at 21.5ºC and dashed line at 20.8ºC. The colored spots are showing the measured values at those times.

The measured Stokes parameters S_1, S_2 and S_3 are plotted in Figure 5-15(b), (c) and (d), respectively. All plotted components have been normalized by S_0. We clearly observe that our polarimeter measurements are temperature dependent. In the analyzed range, there is a 3.2ºC of variation in the temperature, and in the Stokes parameters S_1, S_2 and S_3 there is a variation of 0.015 (0.75% of the Stokes parameter range), 0.021 (1.05%) and 0.025 (1.25%), respectively.

Note that in Figure 5-15 (a), we have also included a continuous and a dashed black lines. Each line is marking a temperature where two different instants of the day reached that particular value. Whereas the temperature of 21.5ºC (continuous line) was reached at two moments of the day (at 23:40:27 plotted with a red spot and, at 18:35:28.5 plotted with a magenta spot), the temperature of 20.8ºC (dashed line) was reached at two new different instants of the day (at 02:03:26.5 plotted with a green spot and, at 09:27:43.5 plotted with a blue spot).

Concerning Figure 5-15(b), (c) and (d), we have also plotted the same four colored spots, showing the Stokes components measurements at those particular times. Then, we included the horizontal continuous line with the same value as the Stokes measurement for the red spot. In this way, we are able to check if the magenta spot, obtained at the same temperature, corresponds to the same Stokes parameter value as the red spot. Simultaneously, we represented the horizontal dashed line with the value of the green spot, using it as reference to check if the blue spot reaches the same value. In other words, we are able to evaluate if the same polarimetric measurement is achieved for the same room temperature, independently of the specific evolution leading to such particular temperature. Finally, by regarding to the particular analyzed times, the maximum difference between two Stokes components at the same temperature is for S_2 at 21.5ºC, being this variation very small (around 0.002).

Furthermore, we analyzed the repeatability by considering 120 measurements during one minute of acquisition data, from 12:00pm to 12:01pm, at 21.2ºC. The standard deviations, shown in Table 5-6, achieves a very small value, being in the fourth decimal.

Table 5-6: Standard deviation of the Stokes components during 1 minute of measurements (120 samples).

$\sigma(S_1)$	$\sigma(S_2)$	$\sigma(S_3)$
1.6E-4	2.0E-4	1.3E-4

Finally, we observe that all the measurements (Stokes parameters and temperature) are noisier around 4am and 7:30am. We think that this behavior is because the electrical current supplied in our laboratory is not completely stable and the noise enters to the analog-to-digital convertor. Note that values of temperature also fluctuate, which is not happening.

Summarizing the data presented in Figure 5-15, we can state that the repeatability of our instrument is in the fourth decimal when we use the polarimeter during a short period of time (minutes) and, a fixed temperature value. When the acquisition is performed at the same room temperature but at larger differences in times (hours), the repeatability is in the thousands. This slight decrease in repeatability may be related to small variations of the optical elements configuration, originated by multiple factors as can be the weights of optical elements, imbalances on the screw holders, etc.

Finally, for temperature variations of few degrees Celsius (about 3ºC), the repeatability of the device is in the hundredth, which still constitutes a very good achievement in terms of polarimetric metrology (~1% of error). As expected, due to the dependence of the LC properties with temperature, variations on the temperature may lead to a decrease in the polarimeter repeatability. Therefore, when highly repeatable polarimetric measurements are required, a precise control and stabilization of the room temperature is recommended. However, in most applications, where repeatability values in the hundredth are extensively acceptable, small temperature variations are not of concern.

5.4.3 Study of temporal dependence

This section is focused on the response of the Stokes polarimeter when the polarization measurement period is decreased (i.e. parameter T from Eq.(5-1)). The frequency clock of the analog-to-digital converter is 12288Hz. Both input and output channels are acquiring the same number of samples, we studied from 6144 to 384 samples (i.e. from a measurement period, T, of 500ms to 31.25ms). There are three input channels: one for acquiring the intensity, another for normalizing the intensity and finally one to measure the temperature. In this way, when we order the A/D converter to read N samples during the whole polarization measurement, each input channel will take $N/3$ samples. The samples acquired through the intensity channel, after being normalized, are divided in 4 subperiods, each one corresponds to a set of intensity measurements obtained with the same polarization analyzer. The FLC presents a transitory time of 0.3ms (measured in Figure 5-5), and so around 4 samples are altered. Because we are synchronizing the input and output signals via the operating system, we are dependent on its velocity response. To avoid using the intensity measurements acquired during the transitory time, we discard 20 samples at the beginning and at the end of each set of intensity measurements with the same polarization analyzer. As an example, when 6144 samples are taken: each input channel reads 2048 samples, the whole polarization measurement lasts 0.5 seconds, each polarization analyzer has 512 intensity measurements, but 20 samples from the beginning and 20 samples from the end are discarded. For the case of 384 samples: each input channel reads 128 samples, the whole polarization measurement lasts 0.03125 seconds, each polarization analyzer has 32 intensity

measurements, but just in this case 10 samples from the beginning and 10 samples from the end are discarded.

We measured 100 times a linearly polarized state at 0º using different polarization measurement periods (T). We plot in Figure 5-16(a) the mean of the S_1 parameter and, in Figure 5-16(b) S_2 and S_3 means as function of the polarization measurement period. We observe a gradual increase of Stokes parameters value when the period is increasing. S_1 increases 0.007, S_2 0.003 and S_3 0.001. In Figure 5-16(c) we represented the standard deviation of those measurements for the three Stokes parameters. When the period is equal or smaller than 62.5ms, the synchronization of the input and output signals is more critical and as a result, standard deviations increase. Moreover, in those cases there are fewer samples per subperiod to average compared to measurements using higher number of samples. Finally, Figure 5-16(d) is showing the degree of polarization (DOP) as function of the measurement period. We observe how the DOP increases as the period of the measurement increases too (total increase of 0.007).

We could not reach the maximum speed of change of the FLC because of the problems of synchronization using the operating system. We suggest for speeding up the measurements to use an external signal trigger. In next subsection presenting the experimental measurements, we have used as polarization measurement period (T) 500 milliseconds.

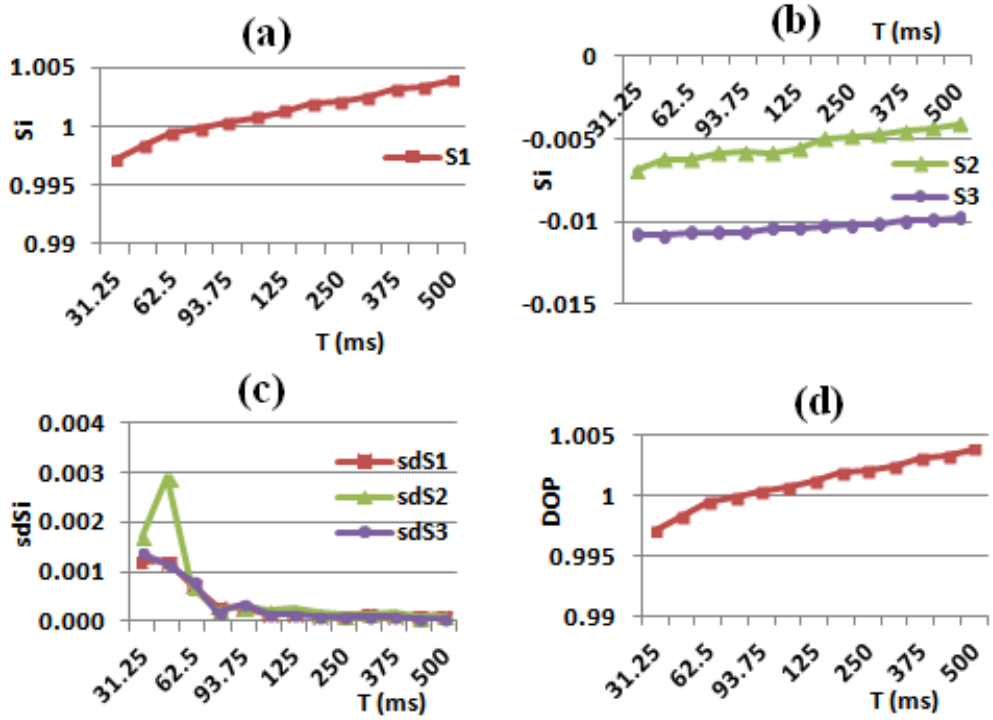

Figure 5-16: Stokes parameters mean: (a) S_1; (b) S_2 and S_3. (c) Standard deviation of the Stokes parameters S_1, S_2 and S_3; and (d) degree of polarization as function of the polarization measurement period (T).

5.4.4 Experimental measurements

5.4.4.1 Stokes vector measurements

Afterwards, to test the validity of the implemented Stokes polarimeter, several measurements of Stokes vectors are performed. In particular, we have generated different incident states of polarization by using a motorized rotating linear polarizer. On the one hand, Figure 5-17(a) shows the estimated Stokes vectors when the polarizer is rotated in steps of 3º, so linearly polarized light with variable azimuth is measured.

On the other hand, Figure 5-17(b) shows the results when rotating the linear polarizer but with a quarter waveplate placed after it. In such case, the measured Stokes vectors are a set of variable elliptically polarized states. We observe that S_1 and S_3 are sinusoidal functions of twice the angle of the polarizer transmission. Moreover, we notice a slight fluctuation in the S_2 component. We fit the experimental measurements to the theoretical Stokes parameters as function of the orientation of polarizer, by adjusting the free parameter of the orientation of the quarter waveplate. We estimated that the QWP fast axis is fixed at -91º. In both plots of Figure 5-17, we have represented the measurements in points and the predicted values in continuous lines. We want to remark that an excellent agreement between experimental and predicted values is achieved, being the maximum difference in the Stokes parameters of 0.04 in Figure 5-17 (a), and of 0.05 in Figure 5-17(b).

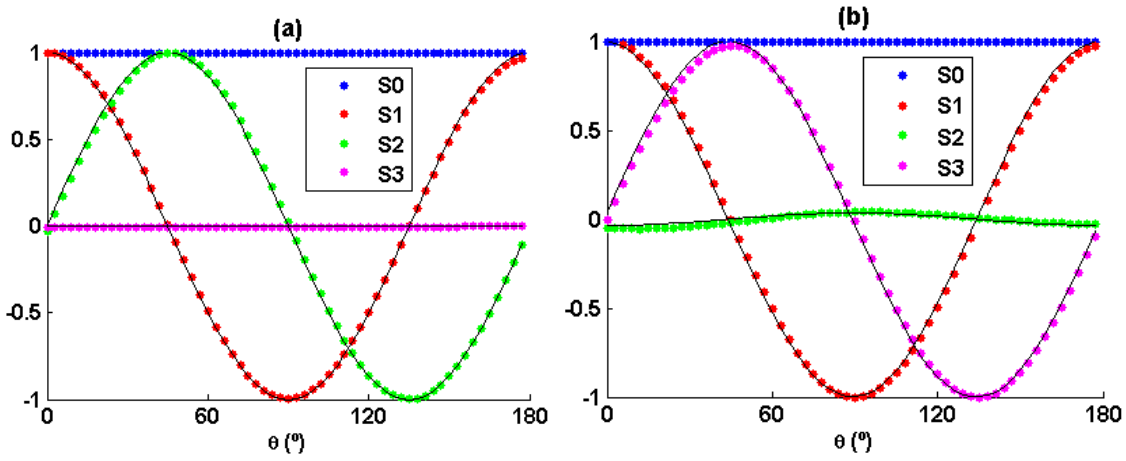

Figure 5-17: Stokes parameters as function of the orientation of the motorized stage which held a linear polarizer and which is used to manipulate the polarization of the incident beam. In points are the Stokes parameters measurements and in continuous lines are the predicted values when: (a) the polarizer is rotated in steps of 3º, or (b) the polarizer is rotated in steps of 3º followed by a quarter waveplate (fast axis fixed at -91º).

5.4.4.2 Mueller matrix measurements

Finally, the Mueller polarimeter is tested by measuring different polarizing optical elements. The analyzed elements are held by a motorized rotating stage, and we have measured its Mueller matrix with a rotation step of 5º.

First, we use as a testing sample a linear retarder. The retardance given by that waveplate was unknown because we used a half waveplate optimized by a different wavelength (514nm) than the one used in the laboratory (633nm). By using the Lu-Chipman decomposition [110,124], we are able to determine its polarization parameters: retardance of 139º and an offset of -8º when the motor is at 0º. In Figure 5-18(a), we have represented in points the measured Mueller elements and in solid lines the theoretical values of a waveplate for a retardance of 139º.

Second, a linear polarizer has been studied as well. Figure 5-18(b) shows the measured Mueller elements in points and they are compared with the theoretical values (in continuous line) obtained from the Mueller matrix of a linear polarizer with a transmission of 0.5.

In both cases, we observe a strong agreement between experimental and theoretical values, being the maximum difference in the Mueller elements of 0.04 in Figure 5-18(a), and of 0.01 in Figure 5-18(b).

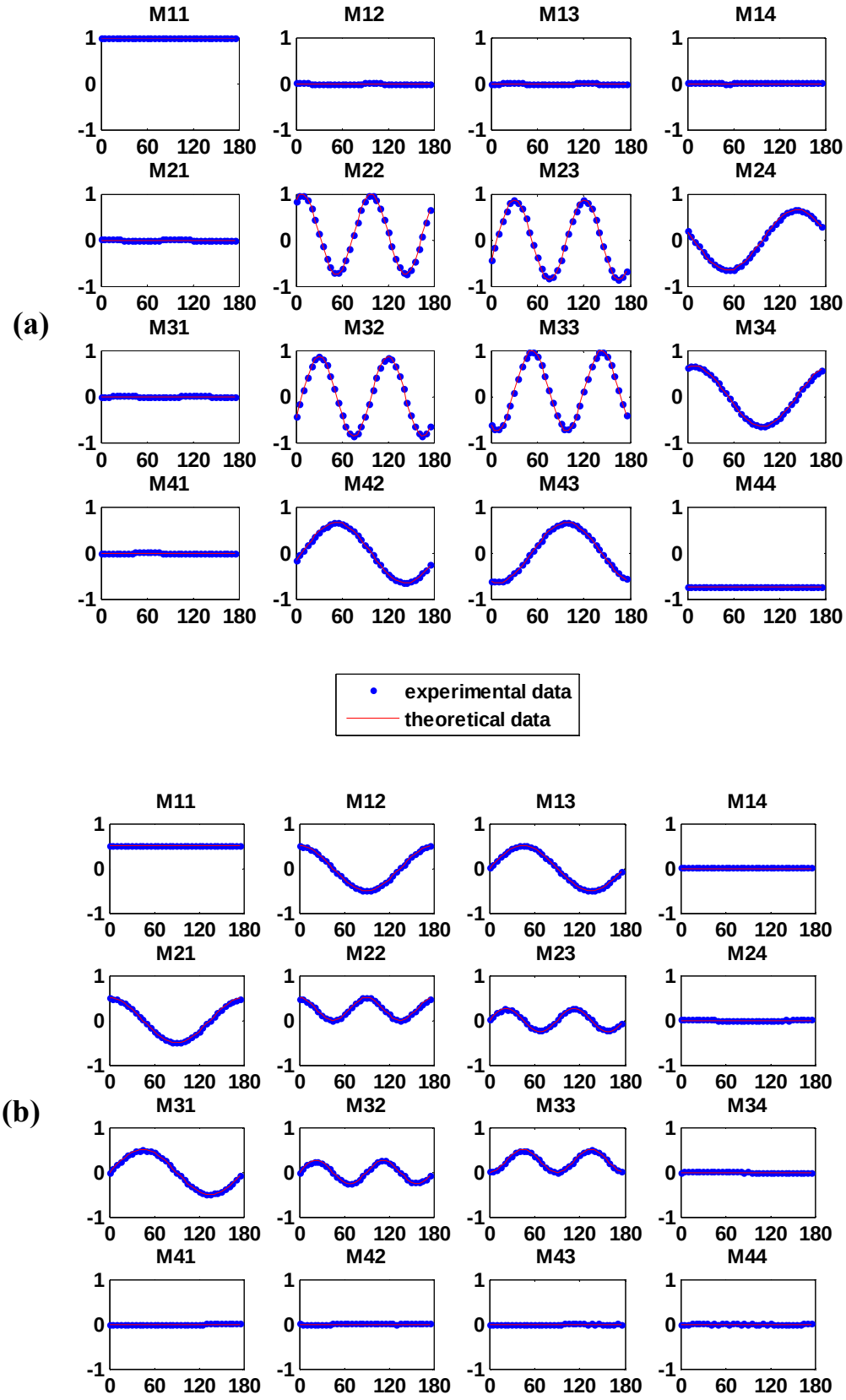

Figure 5-18: Mueller matrix elements as function of the orientation of the motorized stage which held the sample to be measured: (a) a waveplate and (b) a linear polarizer. The polarizing samples are rotated in steps of 5º. In blue points experimental data and in red lines theoretical data.

Chapter 6 **Polarimeter based on the conical refraction**

In this chapter we present a new tool for polarization metrology based on the conical refraction (CR) phenomenon, occurring in biaxial crystals. CR transforms an input Gaussian beam into a light ring whose intensity distribution is linked to the input polarization. We present the design of a division-of-amplitude complete polarimeter composed of two biaxial crystals, whose measurement principle is based on the CR phenomenon. This design corresponds to a static polarimeter, that is, without mechanical movements or electrical signal addressing. Only one division-of-amplitude device is required, besides the two biaxial crystals, to completely characterize any state of polarization, including partially polarized and unpolarized states. Several issues need to be considered during the implementation and alignment of the polarimeter and here discussed, as the image wander or as the fact that the beam splitter introduces some undesired retardance, among others. Moreover, experimental images are provided to validate the capability of the instrument to measure polarization. Finally, several measurements of different polarization states are shown, including fully and partially polarized light.

6.1 Design

In this chapter we present a novel concept to measure the polarization of the light based on the conical refraction (CR) phenomenon occurring in biaxial crystals (BC). The optical features of biaxial crystals, as well as the CR phenomenon are explained in detail in subsection 1.4. Particularly, the fundamental physical property of CR in which our polarimeter is based on is reviewed straightaway.

There is a link between the polarization of the input beam impinging to a biaxial crystal and the transverse intensity distribution along the CR light ring of the output beam [110]. For instance, if the input beam is circularly polarized or unpolarized, the intensity along the ring is constant (Figure 6-1 (a)). In contrast, for linearly polarized input beams the light ring possesses a point of null intensity and a maximum intensity point placed diagonally opposite to the first one (Figure 6-1(b)). Hence, the pass of the incident light through a BC can be described as the projection of the input SOP into an infinite number of linearly polarized states arranged in a circle. Furthermore, Figure 6-1 includes the polarization distribution along the CR ring, illustrated by the orange arrows.

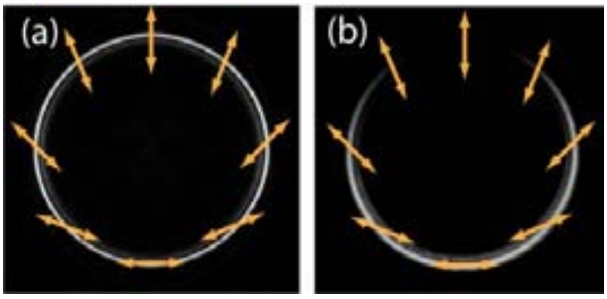

Figure 6-1: CR light ring for: (a) a circularly polarized input beam and (b) a horizontal linearly polarized input beam. Orange double arrows show the polarization distribution at each point along the CR ring.

This new concept to measure polarization based on the CR phenomenon is materialized into the design of a new division of amplitude polarimeter, sketched in Figure 6-2, consisting of two biaxial crystals and a non-polarizing beam splitter.

By means of a division of amplitude device, the analyzed light beam (S_{in}) is split in two sub-beams which are analyzed separately by two different polarizing analyzer arms. Both biaxial crystals (BCs) were cut with one of the optic axes perpendicular to the slab faces (in the following section 6.1.1 we will give more details of the BC specifications). In both arms, lens 1 focuses the beam impinging to the BC, ensuring the proper beam waist (w_0) to satisfy the CR condition: $R_0 >> w_0$ (being $R_0 = L\alpha$, where L is the BC length and α is defined by Eq.(1-8)). Light propagates along one of the optical axes of the BC and, at the system focal plane (plane *P*) the CR

ring is observed. Lens 2 images the CR ring into the CCD camera, with a certain magnification. Thus, the intensity distribution acquired by the cameras will depend on the incident state of polarization (S_{in}). Concerning the first arm, the obtained intensity pattern can be understood as the result of projecting the incident beam over a set of linear polarizers arranged in a circle. The orientation of the transmission axis of those equivalent polarizers is rotated (from 0º to 180º) along the circle (as the orange arrows in Figure 6-1(a)). In order to obtain ellipticity information, we need the second arm, which includes a quarter waveplate (QWP) before the BC. In this way, the intensity pattern in the plane *P* for the second arm can be understood as the result of projecting the incident beam over a QWP and then, over the set of rotated polarizers arranged in a circle.

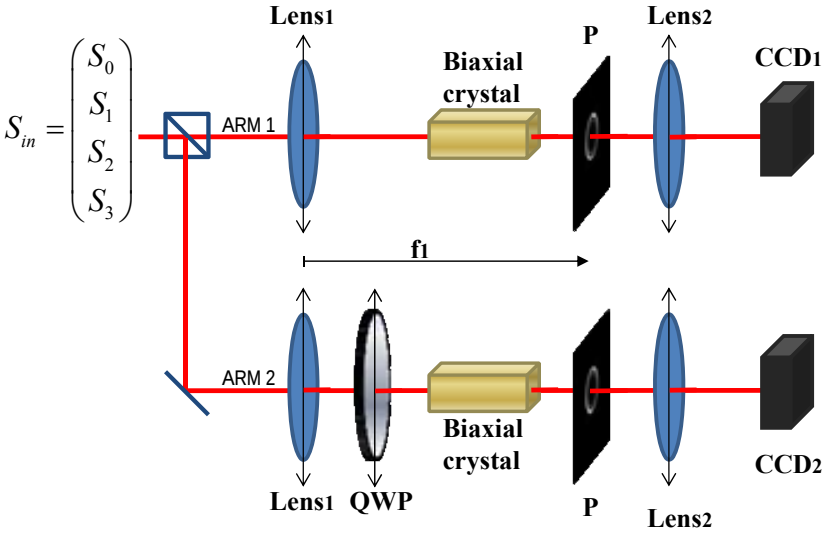

Figure 6-2: Proposed set-up of the polarimeter based on two biaxial crystals. The incident light beam is divided in two arms for being separately analyzed.

By using the Mueller matrices of a QWP and a rotated linear polarizer[1], we can calculate the expressions of the polarization analyzers (PAs) of both arms. These PAs will be expressed as function of φ, the angular position at the ring:

$$PA_1(\varphi) = \frac{1}{2}\begin{pmatrix} 1 & \cos\varphi & \sin\varphi & 0 \end{pmatrix}, \tag{6-1}$$

$$PA_2(\varphi) = \frac{1}{2}\begin{pmatrix} 1 & \cos\varphi & 0 & \sin\varphi \end{pmatrix}, \tag{6-2}$$

where we have fixed the orientation of the QWP at 0º for convenience, but due to the symmetry of the system, any other angle would have led to a complete polarimeter. Thus, the intensity distribution measured by the two cameras will be the projection of the incident Stokes vector (S_{in}) over these PAs. In addition, these expressions can be rewritten as function of the total intensity (S_0), the degree of polarization (DOP), the azimuth (α) and ellipticity (ε) of the incident state of polarization:

$$I_{CCD1}(\varphi)=\frac{1}{2}\begin{pmatrix}1 & \cos\varphi & \sin\varphi & 0\end{pmatrix}\cdot\begin{pmatrix}S_0 & S_1 & S_2 & S_3\end{pmatrix}^T= \\ =\frac{S_0}{2}\left\{1+DOP\cdot\cos 2\varepsilon\left[2\cos^2\left(\frac{\varphi}{2}-\alpha\right)-1\right]\right\} \quad , \tag{6-3}$$

$$I_{CCD2}(\varphi)=\frac{1}{2}\begin{pmatrix}1 & \cos\varphi & \sin\varphi & 0\end{pmatrix}\cdot\begin{pmatrix}S_0 & S_1 & S_2 & S_3\end{pmatrix}^T= \\ =\frac{S_0}{2}+\frac{DOP\cdot S_0}{2}\left[\cos 2\varepsilon\cos 2\alpha\cos\varphi+\sin 2\varepsilon\sin\varphi\right] \quad . \tag{6-4}$$

Note that Eq. (6-3) describes the intensity distribution along the ring due to the CR phenomenon for any input state of polarization. This equation is a generalization of the equations presented in [144], describing the particular cases of: linearly and circularly fully polarized states for the incident light beam.

The available PAs for arm 1 and 2 are plotted in Figure 6-3 upon the Poincaré sphere in red and in blue, respectively. If the orientation of the QWP is rotated an angle θ, the curve of the PAs represented upon the Poincaré sphere corresponding to the arm 2 will be rotated 2θ over the S_3 axis. Note that by using only a single arm, the PAs are disposed in a plane at the Poincaré sphere and consequently, they constitute an incomplete polarimeter. In particular, the PAs from arm 1 (red line in Figure 6-3) do not have information about S_3 and, the ones from arm 2 (blue line) do not measure the S_2 component. However, when we consider the whole system, the polarimeter is complete since the PAs represented upon the sphere are enclosing a certain volume.

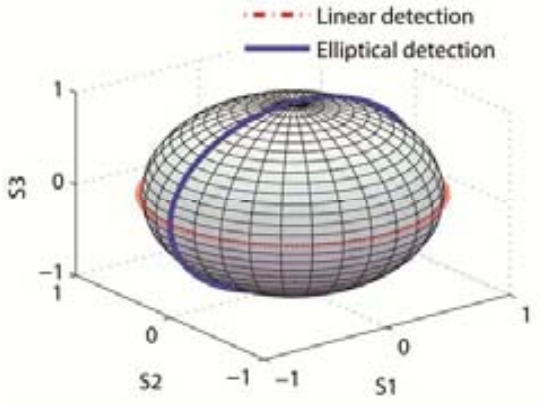

Figure 6-3: PAs represented upon the Poincaré sphere. Red line corresponds to the linear detection arm and blue line to the elliptical detection arm (assuming that the QWP is at 0º).

6.1.1 Experimental characterization of the CR ring

The two biaxial crystals (BCs) used in the implementation of the polarimeter were cut from a monoclinic centrosymmetric $KGd(WO_4)_2$ crystal. Their polished entrances (cross-section 6 mm×4 mm) have parallelism with less than 10 arc sec, and they are perpendicular to one of the

two optic crystal axes within 1.5 mrad misalignment angle. Their lengths, L = 23.38 mm, and their conicity, α = 17 mrad, provide a CR ring of radius R_0 = 397 μm. Figure 6-4 shows a picture of one of the BCs used in the implementation of the polarimeter and the optics mount which is holding the BC. The mount has two adjusters to control the pitch and yaw of the crystal allowing the proper alignment to obtain the CR phenomenon.

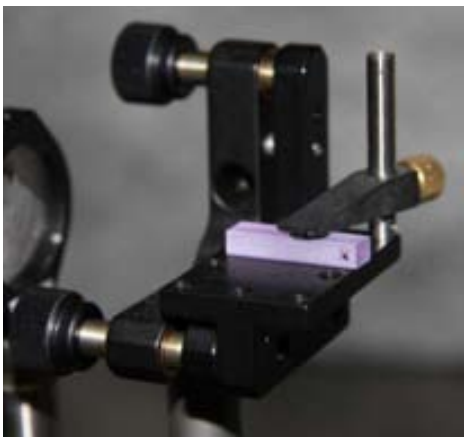

Figure 6-4: Biaxial crystal used in the implementation of the polarimeter.

As mentioned before, the light going through a BC can be described as going through a set of equivalent linear polarizers placed along the ring. In order to check the particular polarization distribution shown in Figure 6-1(a) with the orange arrows, we conduct the following experiment. We have illuminated the BC with a circularly polarized beam and, by means of an imaging Stokes polarimeter, we have measured the polarization distribution of the exiting beam at the focal plane (plane *P*). The imaging Stokes polarimeter used for this measurement is the one described in Figure 3-3, based on a rotating QWP, but extended to an imaging Stokes polarimeter by replacing the radiometer with a CCD camera.

In Figure 6-5, we provide the experimental results. In particular, we show the measured azimuth angle using the color representation according to the colorbar next to the image. In addition, black background represents the area where no light is detected by the camera. Two concentric light rings separated by a dark ring (Poggendorff) are observed (as Figure 1-7). Experimental results agree with the predicted polarization distribution. Each point of the light ring is linearly polarized with the polarization plane rotating along the ring so that every pair of diagonally opposite points has orthogonal polarizations (in agreement with the orange double arrows in Figure 6-1(a)). In other words, at a certain point of the CR ring, given by its azimuthal angle φ, the plane of the electric field, Φ, will be:

$$\Phi = \frac{\varphi + \varphi_C}{2} \tag{6-5}$$

where φ_C is the orientation of the plane of optic axes of the biaxial crystal[144]. As final remark, the distribution of the output beam azimuth will coincide with the orientation of the transmission axes of the equivalent polarizers modeling the effect of the biaxial crystal.

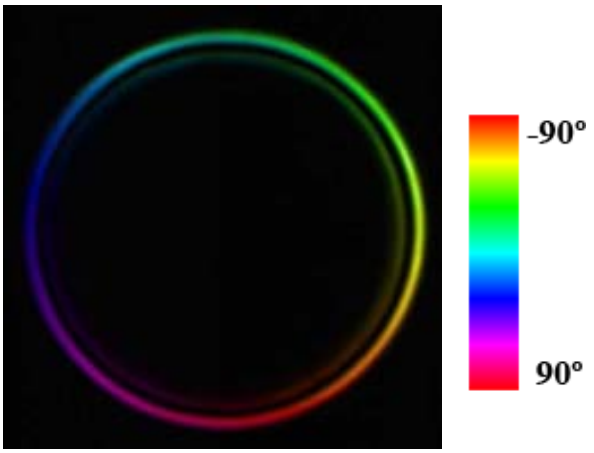

Figure 6-5: Measured azimuth of the CR light ring. Color represents the azimuth angle. Black background corresponds to the area where no light is detected.

6.2 Optimization analysis

This section studies the optimization of the polarimeter based on the CR phenomenon. With this aim, we analyze separately the two polarization analyzer arms and we optimize the parameters involved in each arm.

Arm 1 is only composed by a biaxial crystal. The polarization analyzers in this arm are independent on the orientation of the BC, although they will suffer a rotation along the CR ring, according to Eq.(6-5). Thus, no parameters need to be optimized in the first arm.

Whereas in arm 2, composed by a QWP and a biaxial crystal, the orientation of the QWP can be selected in order to optimize the polarimetric system. In addition, we will check if other values of retardance instead of λ/4 are more suitable for the retarder in arm 2. In the next simulation, we consider the beam splitter as ideal (i.e. it does not affect the polarization of the two split beams). Figure 6-6 plots the CN of the CR polarimeter as function of the retardance (δ) and orientation (θ) of the retarder in arm 2. A minimum value of CN (2.00) is obtained for a retardance of 90º, but the WP orientation is arbitrary.

For a higher visual insight, we have represented different sets of PAs over the Poincaré sphere and the enclosed volume will be related with the polarimeter optimization. Red curve represents the PAs from arm 1, and blue curve represents the PAs from arm 2. Figure 6-7(a) shows the PAs over the Poincaré sphere for different values of the WP retardance δ_{WP} (i.e.

$\delta_{WP} = \{10º, 50º, 90º, 130º, 170º\}$) and with θ_{WP} fixed to 0º, which results in different rotations of the blue circle about the S_1 axis. In turn, Figure 6-7(b) shows an analogous representation but for the PAs related to different values of the WP orientation θ_{WP} (i.e. $\theta_{WP} = \{0º, 22.5º, 45º, 67.5º, 90º\}$), when fixing δ_{WP} to 90º, which results in different rotations of the blue circle about the S_3 axis. As argued in section 2.3.4, the larger the volume enclosed at the Poincaré sphere by the PAs related to a certain polarimeter, the better the conditioning of the system. By analyzing the volume enclosed by the PAs related to the analyzer arm 1 (red circle) and the analyzer arm 2 (blue circle) (Figure 6-7(a) and (b)), some conclusions can be extracted. In particular, Figure 6-7(a) shows that the volume enclosed at the Poincaré sphere strongly depends on the WP retardance. In fact, the largest volume is obtained by the blue circle related to the retardance of 90º, leading to the best possible conditioning. Regarding to Figure 6-7(b), it shows that the volume enclosed at the Poincaré sphere is constant, independently of the WP orientation chosen. Thus, the conditioning of the system is independent of this parameter.

At this point, bearing in mind the discussion related to Figure 6-6 and Figure 6-7, a QWP should be chosen to be inserted in arm 2. Finally, we arbitrarily choose 0º as the QWP orientation.

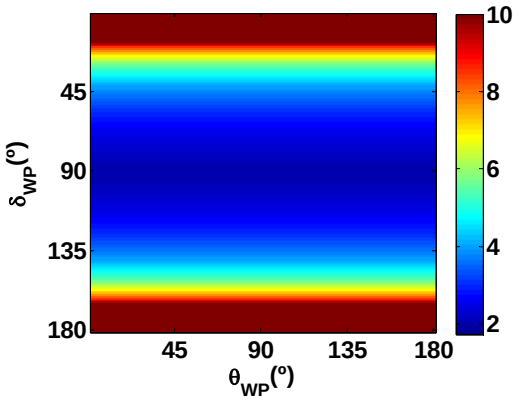

Figure 6-6: CN as function of the retardance (δ) and orientation (θ) of the WP in arm 2 of the CR based polarimeter. Minimum CN (2.00) at δ_{WP}=90º.

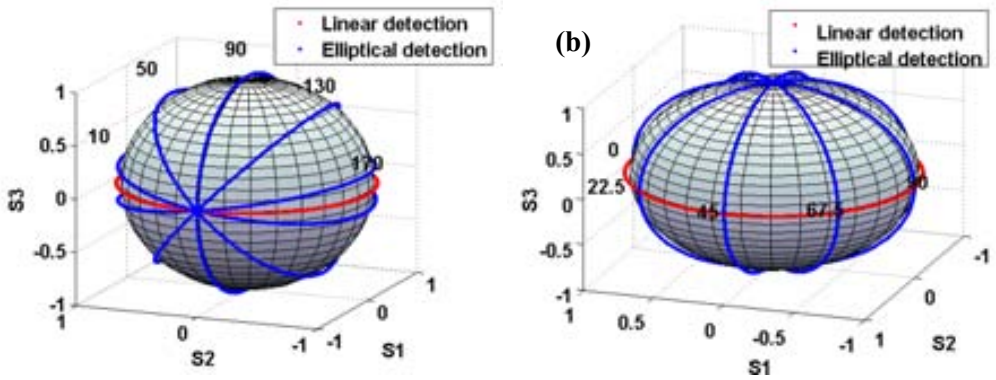

Figure 6-7: CR polarimeter PAs represented over the Poincaré sphere for arm 1 (in red) and arm 2 (in blue) and for different values of: (a) the WP retardance (with θ=0º); (b) the WP orientation (with δ=90º).

Although the CN value of the CR based polarimeter does not depend on the WP orientation (Figure 6-6), the specific Stokes vector variances may be sensitive to this parameter. To obtain higher insight in this issue, the Stokes variances as a function of different QWP orientations are calculated by following Eq.(2-17). In addition, the EWV indicator is also calculated as the equally weighted addition of the four Stokes parameters variances. The obtained results are represented in Figure 6-8, where the EWV indicator is constant as a function of the QWP orientation (black line). In turn, the S_1 (blue curve) and the S_2 (green curve) variances are dependent on the QWP orientation, compensating their value one to each other, and keeping in this way a constant EWV value.

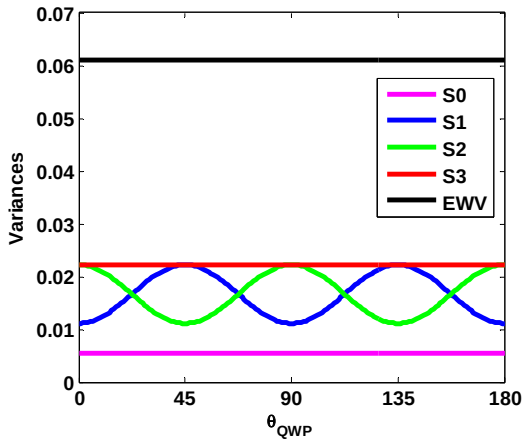

Figure 6-8: Stokes elements variances and EWV as function of the QWP orientation (when N=720PAs).

Therefore, for a general purpose polarimeter which measures a wide variety of Stokes vectors, the QWP orientation is not a significant parameter in terms of optimization (shown by the CN and the EWV indicators). However, if one desires to measure a certain set of Stokes vectors with special interest in some particular Stokes elements, the information provided in Figure 6-8 may be of great interest to reduce the variances associated to those specific Stokes elements.

Finally, to study the influence of data redundancy on the CR polarimeter performance, different polarimeters are simulated by changing the number N of PAs: 8, 12, 20, 100 and 720. Along simulations, the architecture sketched in Figure 6-2 was used, where it was considered that a QWP oriented at 0º was placed at arm 2. For each simulated polarimeter, the CN and the EWV indicators were calculated. The obtained CN is equal to 2.00 for all the cases, independently of the N selected. This result was expected as the CN is not sensitive to data redundancy. Regarding to the EWV indicator, the larger the number of PAs used, the smaller the EWV value obtained. In addition, the Stokes variances for different N were calculated. The obtained results, together with the EWV data, are given in Table 6-1. The S_1 variance is smaller than the ones for S_2 and S_3 (these last two variances are equal). This particular variances weight distribution is understood by taking into account the data provided in Figure 6-8, by bearing in mind that the QWP is oriented at 0º.

We want to emphasize that the polarimeter architecture proposed leads to a snapshot Stokes polarimeter. This scheme allows us to easily increase data redundancy just by increasing the number of PAs selected, which can be readily done without an increase of measuring time. This particular characteristic of the CR polarimeter becomes an outstanding feature, in terms of polarimetric metrology.

Table 6-1: Stokes parameters variances and equally weighted variance of the CR based polarimeter, when *N*=8, 12, 20, 100 and 720 polarization analyzers are used. PAs are equally distributed along the two curves on the Poincaré sphere shown in Figure 6-3.

Number of PAs	**8**	**12**	**20**	**100**	**720**
$\sigma^2(S_0)$	0.5000	0.3333	0.2000	0.0400	0.0056
$\sigma^2(S_1)$	1.0000	0.6667	0.4000	0.0800	0.0111
$\sigma^2(S_2)$	2.0000	1.3333	0.8000	0.1600	0.0222
$\sigma^2(S_3)$	2.0000	1.3333	0.8000	0.1600	0.0222
EWV	5.5000	3.6667	2.2000	0.4400	0.0611

6.2.1 Polarimeters robustness

From now on we will refer to the set of PAs equally distributed along the 2 curves represented in Figure 6-3 as the theoretical configuration.

Next, we study the robustness of this theoretical configuration when using 720 PAs in total (i.e. 360 PAs per arm). We have added to the Stokes elements describing each PA a random value taken from a zero mean uniform distribution of amplitude 0.4. These random deviations are simulating experimental errors in the laboratory. We have simulated 50 different polarimeters deviated from the ideal configuration and, for each new PSA configuration we have recalculated their quality indicators. Figure 6-9(a) and (b) show their condition number values and their variances, respectively. These variances are much smaller than variance values shown for the other robustness studies related to the previous polarimeters architectures (see sections 3.2.3, 4.2.2 and 5.2.2). This is because in this case, the CR based polarimeter has a larger number of PAs (720). Therefore, an important strength of the CR based polarimeter is here highlighted: small variances due to the large redundancy available data obtained when combining the two images.

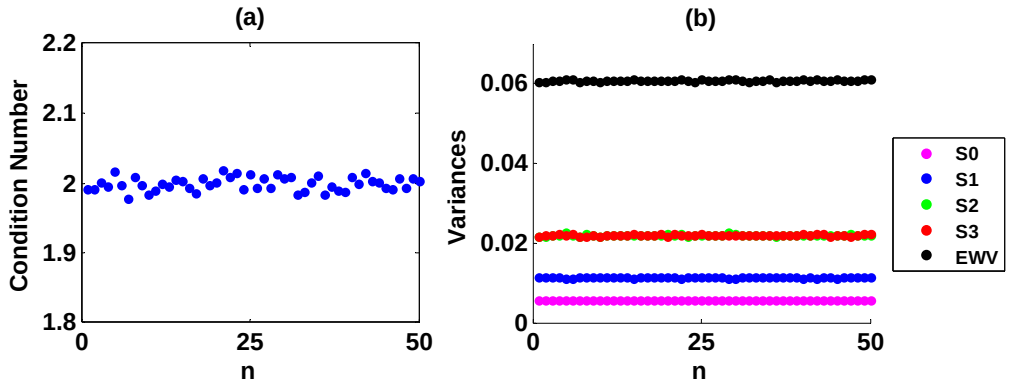

Figure 6-9: (a) Condition number and (b) variances of 50 different simulated PSAs deviated from the theoretical configuration represented in Figure 6-3 (N=720PAs), when adding to the PAs a value from a zero mean uniform distribution of amplitude 0.4.

6.3 Tolerance analysis

Afterwards, we study the tolerance of the different parameters of the set-up in order to achieve a given accuracy in the Stokes vector measurements, in particular of 0.02.

We followed the methodology explained in section 2.4.1. Different studies can be performed by analyzing the Stokes vector elements errors as function of the incident SOP, when we set a given tolerance to the different parameters involved in the set-up. In particular, to the following parameters: orientation and retardance of the QWP (θ_{WP} and δ_{WP}) and, the orientations of the equivalent polarizers located along the first and second light rings (θ_{P1} and θ_{P2}). In the simulation, all equivalent polarizers belonging to the same ring are rotated the same amount, simulating that the whole ring has been rotated that particular angle.

As an example, we show a particular study in Figure 6-10: the components of the Stokes error as function of the incident Stokes vector (using parameterization of Eq. (2-21)) when there is a shift of 1º in the different analyzed parameters. In general, we observe that the Stokes error is higher when the same value of tolerance is given to the orientation of the retarder and to the orientation of the equivalents polarizers compared to the retardance of the QWP.

Next, we extend this study to other values of tolerance (0.2º, 0.5º, and 2º) of the involved parameters. Figure 6-11 summarizes the results obtained, showing the accuracy (i.e. the maximum Stokes element error for all incident SOPs) of the polarimeter as function of the tolerance for the different parameters. We observe that accuracy has a linear tendency with the parameters tolerance. Thus, we have also calculated a linear regression fitting to each parameter, and they are represented in Figure 6-11 as well. It is noticeable that the accuracy of the polarimetric system is

more sensitive to a variation in the orientation of the QWP and the orientations of the equivalents polarizers along the light rings than the retardance of the QWP.

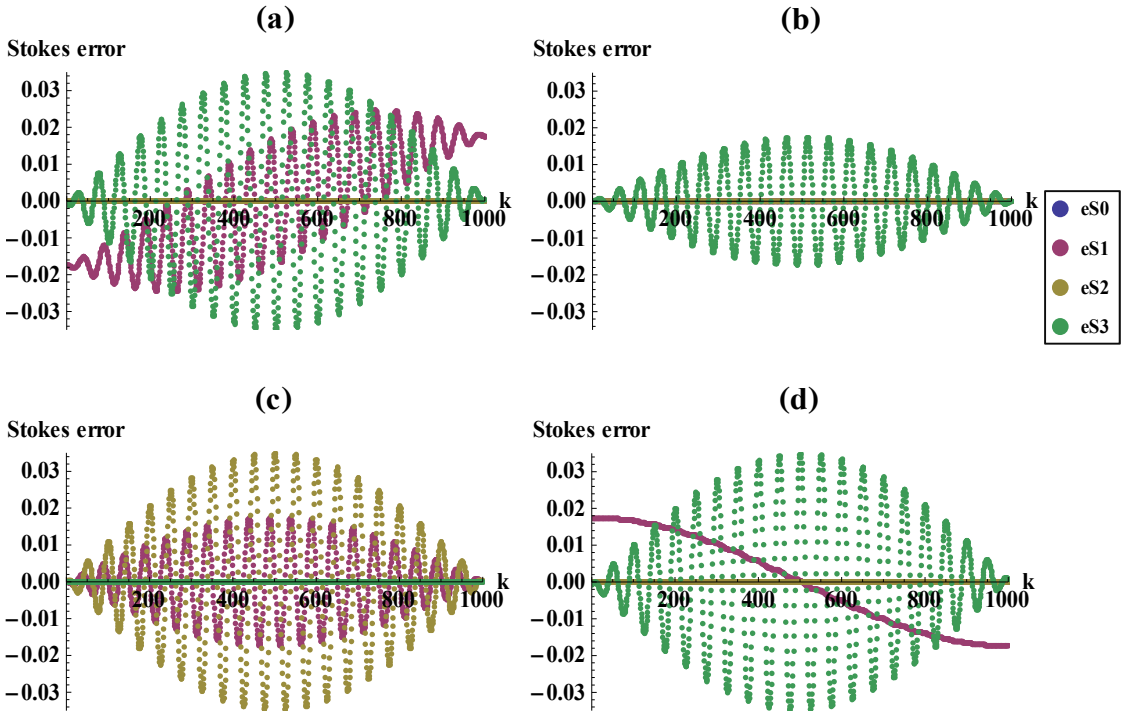

Figure 6-10: Stokes parameters error with a tolerance of 1° in: (a) the orientation of retarder placed at the second arm (θ_{WP}), (b) the retardance of that retarder (δ_{WP}) and, (c) and (d) are the orientations of the equivalents polarizers located along the light rings at the first and second arm (θ_{P1} and θ_{P2}), respectively. Errors as function of variable k, which parameterizes the incident Stokes vector following Eq.(2-21).

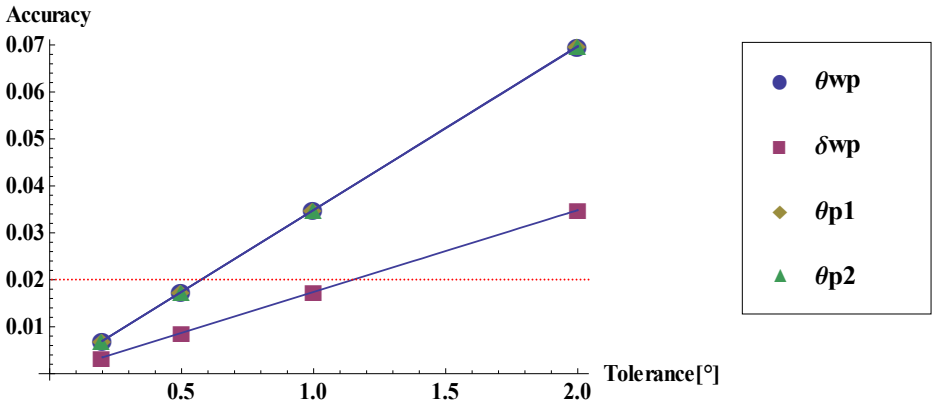

Figure 6-11: Accuracy of Stokes polarimeter based on 2 biaxial crystals as function of the tolerance of parameters involved in the set-up.

Finally, from the 4 equations describing the linear fittings of Figure 6-11, we fix a standard value of accuracy of 0.02 in the polarization measurements (red dashed line in Figure 6-11) and subsequently, the tolerances for the 4 parameters are determined. Table 6-2 shows these calculated tolerances. Retardance tolerance doubles the other three parameters tolerances.

Therefore, in the experimental implementation, a proper orientation of the different optical elements in the system is more crucial than the retardance of the retarder.

Table 6-2: Tolerance values to achieve an accuracy of 0.02 in the Stokes polarimeter.

Parameter	θ_{WP}	δ_{WP}	θ_{P1}	θ_{P2}
Tolerance (º)	0.57	1.15	0.57	0.57

To complete this tolerance study, we discuss the actual experimental tolerances of the optical elements used in the laboratory and they are compared with those values shown in Table 6-2. We want to remark one of the more relevant strengths of the polarimeter here analyzed: the instrument has a static architecture. In other words, no mechanical movements are required, neither optical elements whose configuration changes when addressing an electrical signal (as the liquid crystals). This important feature implies that, after an accurate experimental calibration of the instrument, the orientations of the elements (θ_{WP}, θ_{P1} and θ_{P2}) are not modified, ensuring working in the orientation tolerance range shown in Table 6-2. Moreover, the experimental calibration takes into account the actual value of the retardance of the QWP (δ_{WP}), which is a fixed value.

6.4 Implementation

We have implemented the polarimeter based on two biaxial crystals. Figure 6-12 shows a picture of the experimental set-up. It has been tested with two different input light sources (a 640 nm diode laser coupled to a monomode fiber and a He-Ne laser). Next, we have used a set of optical elements to regulate the intensity of the incident beam and a PSG to manipulate its polarization. PSG (composed by a LP and a QWP) is necessary for calibrating and later testing the Stokes polarimeter. Then, a non-polarizing beam splitter (B-S) is used to split the incident beam into two sub-beams, which will be analyzed separately by the two arms. Before the B-S, we place a lens (L_0) to focus the beam and allowing the proper conditions to obtain the CR phenomenon. Arm 1 consists of a biaxial crystal (BC_1) and a lens (L_1) which is imaging the CR ring to the camera (CCD_1). Arm 2 has the same optical elements as arm 1 (BC_2, L_2 and CCD_2), but with an additional QWP before the BC. The BCs used in the laboratory are as the ones described in section 6.1.1, and the two CCD cameras are distributed by Basler (resolution of 1000x1000pixels and pixel size of 7.4μm).

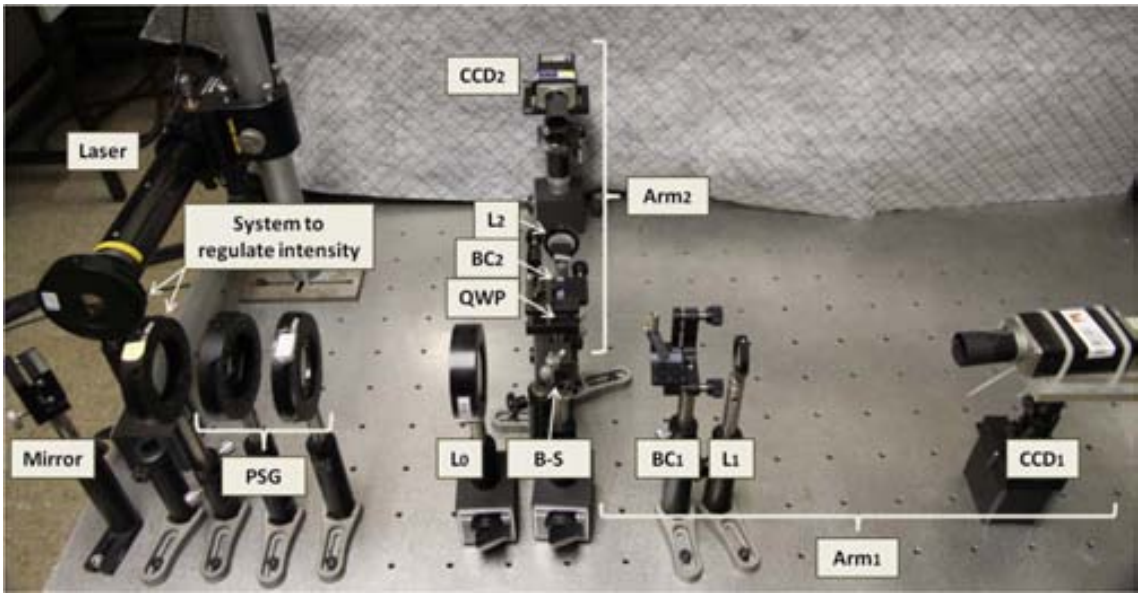

Figure 6-12: Implemented Stokes polarimeter based on two biaxial crystals.

6.4.1 Validation of the measurement principle

To show and prove the measurement principle of the polarimeter design proposed in this chapter, we have experimentally implemented the two arms of the polarimeter and different input SOPs are analyzed. The validation is conducted considering that the B-S is not affecting to the polarization of the incident beam. To experimentally reproduce this ideal scenario, we have removed the B-S from the set-up, and we have measured separately in transmission first, arm 1 and then, arm 2.

Figure 6-13 shows the two experimental images acquired by the two cameras when seven particular SOPs illuminate the system. The SOPs used are: linearly polarized light at 0º, 90º, 45º and 135º, right and left handed circularly polarized light and unpolarized light. The first row of Figure 6-13 corresponds to the first camera, i.e. projecting over linear polarization analyzers. Thus, when this camera analyzes a linear SOP (Figure 6-13 (a)-(d)), the intensity patterns consist in broken rings with a maximum and a null of intensity in diametrically opposite positions in the ring. This broken ring rotates as we rotate the azimuth of the input SOP, as it is described in Eq.(6-3). As explained above, circularly polarized light (Figure 6-13 (e)-(f)) and unpolarized light (Figure 6-13 (g)) result in a ring of constant intensity. Concerning results from the second camera (second row of Figure 6-13), the intensity distributions differ from the first row because of the presence of the QWP. When illuminating with 0º or 90º linear SOPs, the input linear polarization passes through one of the QWP axes, and so the polarization is not modified by the QWP (oriented at 0º), leading to the intensity distributions (Figure 6-13 (h)-(i)) identical to the ones acquired by the first camera. In addition, unpolarized light remains unpolarized after the QWP, so

that a uniform ring is visualized in Figure 6-13 (n). Finally, when projecting the linear SOPs at 45º, 135º, right handed and left handed circular SOPs over the QWP, they are respectively transformed to left handed and right handed circular SOPs and linear SOPs at 45º and 135º. Then, by taking into account the actual SOP impinging to the biaxial crystal, and considering the effect of the crystal over these SOPs as explained above, we understand the intensity distribution of Figure 6-13 (j)-(m).

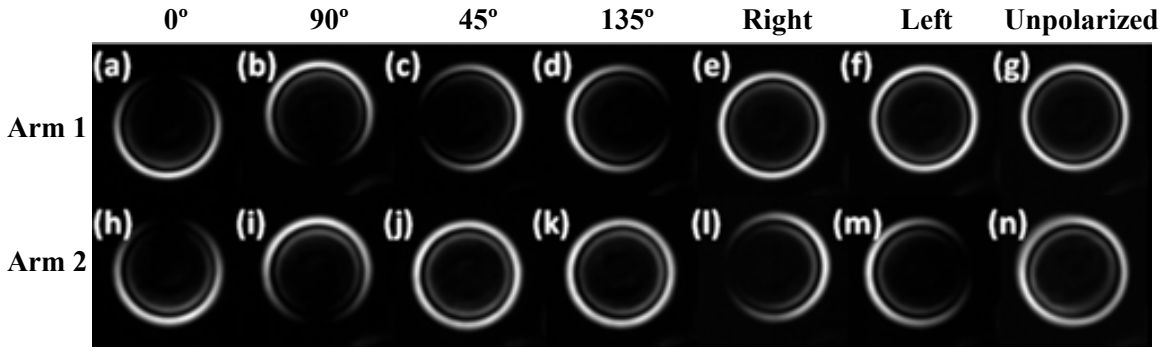

Figure 6-13: Experimental images acquired by cameras of arm 1 (a-g) and arm 2 (h-n) when illuminating with linearly polarized light at 0º (a,h), at 90º (b,i), at 45º (c,j), at 135º (d,k), with circularly polarized light right handed (e,l) and left handed (f,m) and with unpolarized light (g,n). Set-up without B-S.

By analyzing data from these experimental images, we have extracted the intensity profile along the rings, plotted in red points in Figure 6-14. Moreover, we have included in blue continuous line the simulated intensity profiles by using Eqs.(6-1) and (6-2). We observe a good agreement between experimental and simulated intensity profiles.

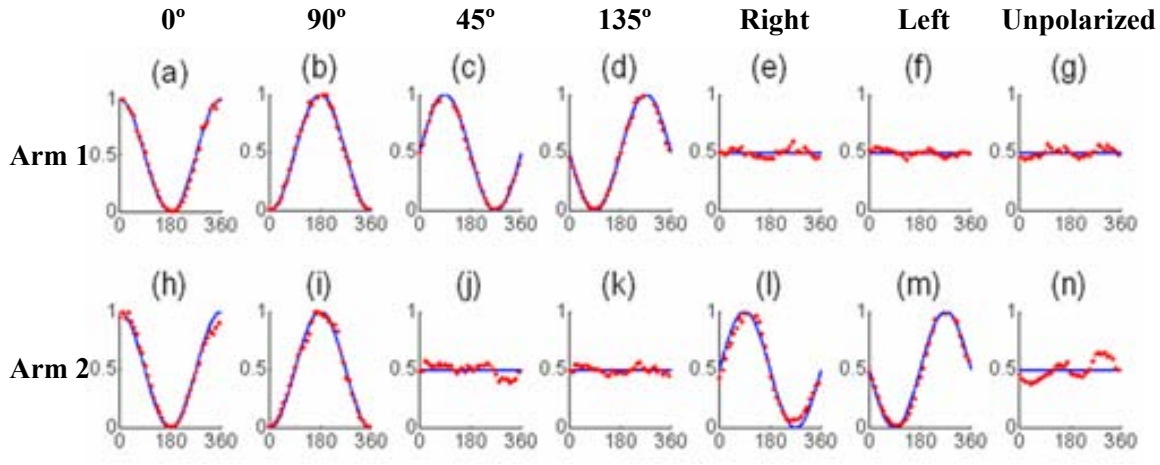

Figure 6-14: Simulated intensity profile in continuous blue line and experimental intensity profile in red spots, as function of φ, the position along the ring of arm 1 (a-g) and arm 2 (h-n); when illuminating with linearly polarized light at 0º (a,h), at 90º (b,i), at 45º (c,j), at 135º (d,k), with circularly polarized light right handed (e,l) and left handed (f,m) and with unpolarized light (g,n). Experimental simulated results without B-S in the set-up.

Note that if only the linear arm is used, there is not distinction between unpolarized light and right and left circularly polarized light (see Figure 6-14 (e-g)). In the same way, the elliptical arm cannot distinguish between linearly polarized light at 45º, 135º and unpolarized light (see Figure 6-14 (j,k,n)). Nevertheless, by combining the information of the two intensity profiles corresponding to both arms, we are able to distinguish each SOP, including unpolarized light beams.

Therefore, results given in Figure 6-13 and Figure 6-14 constitute an experimental prove of the capability of the presented design to perform polarimetric measurements, as the whole polarimetric content of any input SOP can be determined.

6.4.2 Experimental optimization and alignment considerations

After the pretest of the experimental implementation of the 2 separate arms, we proceed to implement the whole polarimetric system, including the B-S (i.e. as the image of Figure 6-12). The presence of the B-S is relevant as it allows us to simultaneously measure the intensity distribution from both arms.

Several issues have been taken into account during the implementation and the alignment of the polarimeter in order to get accurate measurements.

First of all, the B-S does introduce retardance to the incident beam. Consequently, the orientation of the QWP is no longer arbitrary. For this reason, first we have calibrated the Mueller matrix of the B-S in reflection and in transmission by using a QWP rotating based Mueller polarimeter. After conducting the Lu-Chipman decomposition [124], the Jones matrix corresponding to the pure retarder is calculated and finally, the retardance is extracted. The B-S working in transmission introduces a retardance of -10º and, in reflection of -33º. Although the actual system is not able to reproduce the PSA described in section 6.1 and represented in Figure 6-3, the orientation of the QWP can be optimized in order to minimize the CN of the new PSA, and equivalently to maximize the volume enclosed by the new PAs upon the Poincaré sphere. To this end, we have calculated the CN of the new PSA as function of the orientation of the QWP, by considering the B-S calibrated Mueller matrix. This dependency is represented in Figure 6-15, where we can observe how CN fluctuates from 2.08 to 2.54, values slightly higher (i.e. worst conditioning) than the one obtained when considering the B-S as ideal (CN of 2.00). There are two orientations for the QWP which optimize the PSA configuration (at 44º or at 134º). Finally, we have selected the orientation of the QWP at 44º (marked with a red point in Figure 6-15), minimizing the CN of the experimental polarimeter (CN of 2.08).

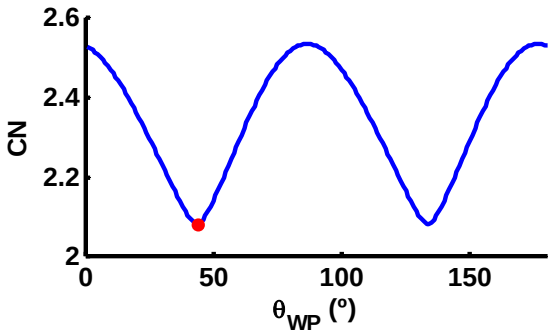

Figure 6-15: CN as function of the orientation of the QWP located at the arm 2 of the experimental set-up, considering the experimental B-S Mueller matrix. Red point is marking the minimum CN (2.08), obtained at 44º.

CR features, as the ring radius and the location of the focal image plane, depend on the wavelength [145] and so, it is important to work with a monochromatic light source. However, if the light source used during the implementation has a small bandwidth, it is recommended to use a bandpass filter.

Furthermore, the focal lengths of the lenses used in the set-up play an important role in the final result. The first lens (L_0) controls the beam waist size (w_0) of the incident beam to the BC, affecting the CR ring width. In addition, the radius of the CR ring (R_0) at the focal image plane is constant because it only depends on the crystal length (L) and on its conicity (α, which is only dependent on the BC refraction indices as defined in Eq.(1-8)). Thus, in order to distinct the CR rings it is necessary to work under conditions of $R_0 >> w_0$, and this is obtained by using the proper lens L_0. Moreover, the other two lenses (L_1 and L_2) image the two CR rings obtained at the focal image planes to the CCD planes with a certain magnification, depending on their focal lengths. We tested different focal lengths and we obtained slightly better results when working with small rings.

We have observed that interference produced by back reflections occurring at the different optical elements of the system may degrade the intensity ring distribution and so, the final SOP measurement. Thus, we have reduced them as best as possible by realigning. As example, a variable neutral density filter, included in the system to regulate the intensity reaching the CCD, was responsible for a set of interference fringes. To get rid of them, the element was replaced by a linear polarizer of better quality, which reduced drastically the artifacts.

As mentioned before, the CR phenomenon is extremely sensitive to the incidence angle to the BC because is only visible when the incident beam propagates parallel to the optical axis of the crystal. We have used the optics mount shown in Figure 6-4 to adjust the pitch and yaw of the BC, ensuring the proper alignment to observe the CR ring. Figure 6-16 shows the intensity distribution during the alignment procedure of the BC. Once the BC is aligned, it is important as well to align the elements constituting the PSG. During the calibration and measurement tests, the

optical elements of the PSG will be rotated and they may cause beam wander at the BC entrance. If the PSG is properly aligned, a nearly normal incidence to the BC will be guaranteed and so, the CR ring will be still observed.

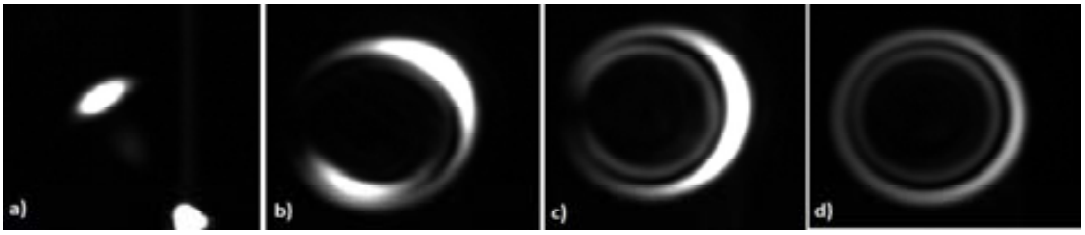

Figure 6-16: Intensity distribution in the focal plane during the alignment procedure to observe the CR ring. From (a) to (d), pitch and yaw of the BC are adjusted, ensuring that light travels parallel to the optical axis of the BC.

As told, when the elements of the PSG are rotated, although the CR ring is not vanished due to the PSG alignment, it may cause small amounts of image wander at the CCD plane [82]. During the calibration, sequential images need to be taken corresponding to different incident SOPs and so, small translations on the registered CR rings are observed. Therefore, if these images were operated to obtain the polarimetric measurement matrix of the system, each pixel would contain mixed information of different PAs, damaging the calibration. In order to overcome this issue, we propose to center the acquired images before the calibration calculation. This centering procedure is achieved by correlating each acquired image (suffering image wander) with a reference image. This operation gives us the displacement of each individual image with respect to the reference image. Two reference images are used during the image correlation, one for each CCD camera because they may have different magnification. These reference images were registered a priori, using an incident SOP which created the whole intensity ring (we used a beam right-hand circularly polarized for CCD_1 and a beam linearly polarized at 0º for CCD_2). Furthermore, when measuring a given incident SOP, the two acquired images are also correlated with those reference images used in the calibration. This procedure ensures a proper correspondence between intensity data and the polarimetric measurement matrix, avoiding mismatching between different PAs.

Another concern is the proper selection of the PAs along both CR rings. The idea is to define a region of interest (ROI) drawing a circle along each light ring, and extract the intensity profile from that ROI. Afterwards, we need to choose the number of points along each intensity profile to be used as polarization analyzers in each arm ($N/2$), leading to a Stokes polarimeter with N PAs. To this aim, we developed an algorithm to define the region of interest (ROI). The algorithm looks for the center and the average radius value of the ring, and these parameters are calculated for both reference images. After defining the two circular ROIs with the parameters obtained by the algorithm, the intensity profiles from the rest of the images (after being centered) are extracted by using those two ROIs.

Finally, we propose two methods to extract the intensity values. First one consists in taking the intensity values at the *N/2* pixels equally distributed along each intensity profile (from now on, called method *A*). This method is the simplest one but it has a weakness point. If some artifacts are present in some of the selected pixels, it may hide the actual values, resulting in a wrong calibration or measurement. With the aim of overcoming this issue, we propose a second method (from now on, method *B*). This consists in working from the intensity profile obtained by calculating radial means (i.e. we calculate the mean along a radius from the center of the CR ring, corresponding to a set of pixels with the same azimuth value). In this way, even though some artifacts may alter some pixels from where we extract the intensity values, the resulting intensity value is balanced when calculating the radial mean.

6.4.3 Calibration

Afterwards, we have calibrated the polarimetric measurement matrix of the polarimeter using the sequential calibration method (explained in 2.5.1). Note that each polarization analyzer corresponds to a pixel (method *A*) or a radial mean (method *B*) along the circular ROI.

Figure 6-17 illustrates upon the Poincaré sphere the simulated (considering the B-S Mueller matrix) and the experimentally calibrated PSA in green and in red points, respectively. Two different calibrations are shown, concerning the two methods to extract the intensity data from the images. On the one hand, Figure 6-17 (a) shows the calibrated PAs when the intensity values are taken in *N* particular pixels equally distributed along the 2 rings (method *A*). On the other hand, Figure 6-17 (b) corresponds to the calibration when calculating the radial mean along *N* positions along the 2 rings (method *B*). In both calibrations, we have used the same number of PAs (*N*=720). The condition number values associated to the calibrated polarimetric measurement matrices are 2.11 (method *A*) and 2.42 (method *B*). Furthermore, we have represented in Figure 6-18 the DOP values of the calibrated PAs when using both methods.

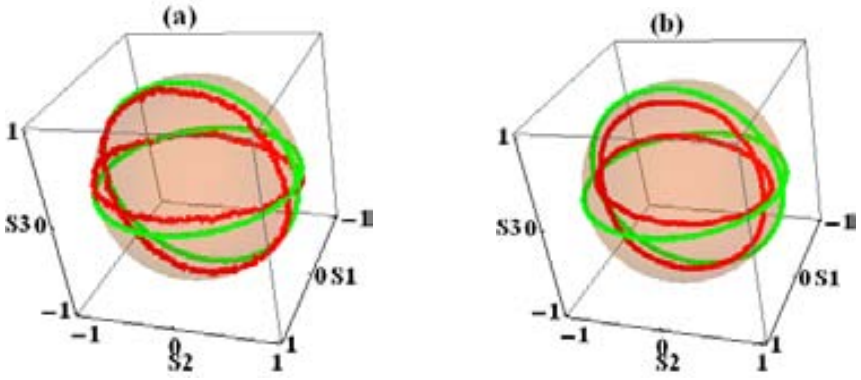

Figure 6-17: In green, theoretical PAs (QWP at 44º and using the calibrated B-S Mueller matrix). In red, experimentally calibrated PAs when intensity is extracted from: (a) the pixel values (i.e. method *A*) and (b) the radial mean values (i.e. method *B*).

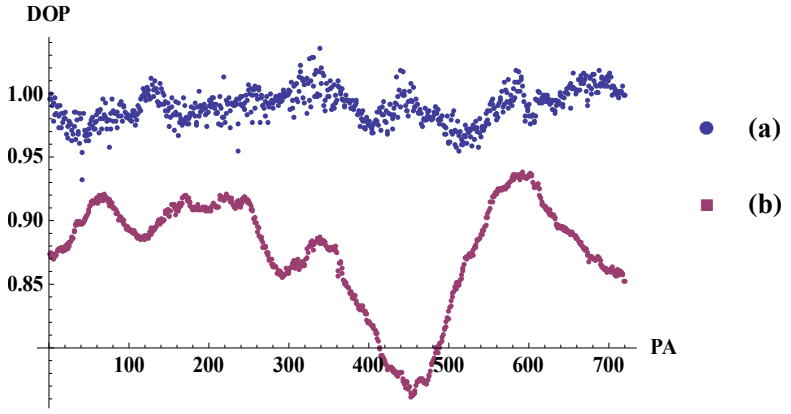

Figure 6-18: Degree of polarization (DOP) of the calibrated 720 PAs constituting the PSA. Calibration procedure by means of intensity data extracted from: (a) the pixel values (method *A*) and (b) the radial mean values (method *B*).

Analysis of data revealed that, method *A* leads to a noisier representation on the Poincaré sphere, although their DOP values are closer to 1 (i.e. PAs are almost fully polarized), and the experimental CN (2.11) is very close to the theoretical one (2.08). On the contrary, method *B*, corresponding to calculate the radial mean values, leads to a more definite PAs curves upon the Poincaré sphere, but their DOP is smaller than 1 (i.e. PAs with a small contain of depolarization), and the experimental CN (2.42) is slightly higher than the theoretical one (2.08). Even though method *A* presents better system conditioning, method *B* is more robust to image wander thanks to the radial means. And this strength is observed when testing the polarimeter, showing better results in terms of accuracy using method *B*. For this reason, we have decided to use method *B* (i.e. radial mean values) in all experimental results shown below.

6.4.4 Experimental measurements

In this last subsection, we provide the experimental measurements obtained with the CR based polarimeter. All acquired images used during the measurements are centered by the correlation with the reference images. In addition, we have used the methodology of extracting the intensity data from radial mean values (method *B*). This methodology is not only used for calibrating the polarimetric measurement matrix, but also for measuring the different SOPs.

The CR polarimeter is tested by measuring different SOPs: fully polarized light (linear and elliptical SOPs) and light partially polarized with a variable DOP.

First of all, we have generated fully polarized light with variable azimuth. This polarized light is obtained by manipulating the incident light beam with a rotating linear polarizer. Figure 6-19 shows the azimuth, ellipticity and DOP of the measured SOP as function of the orientation of the polarizer. We have represented in blue points the experimental data and in red lines the theoretical

values. Despite a small fluctuation in the DOP parameter (values between 0.94 - 1.03), which can be explained due to the calibrating and measuring method based on radial mean values, we observe a great matching between theoretical and experimental measurements. The maximum difference in the Stokes parameters is 0.10.

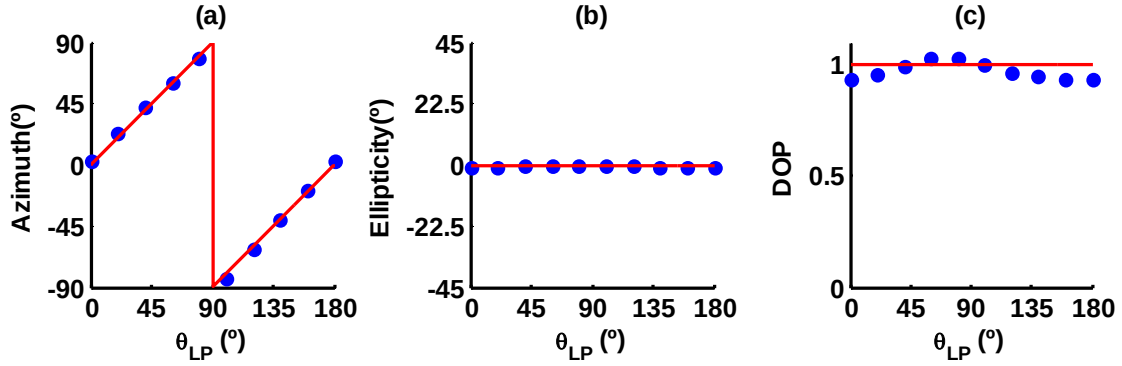

Figure 6-19: Fully polarized light, generated by rotating a linear polarizer (LP orientation in the *x* axis): (a) azimuth, (b) ellipticity and (c) DOP. Blue points are experimental data and red line is predicted data.

Afterwards, we manipulate the incident light to generate fully polarized light with variable ellipticity. This set of SOPs is generated by means of a rotating linear polarizer, followed by a QWP oriented at 45º. Thus, when the LP is at 0º or at 180º, right-hand circularly polarized light is generated. Whereas when the LP is at 90º, a circular SOP with opposite helicity is obtained. In Figure 6-20 (a), (b) and (c) the measured azimuth, ellipticity and DOP are respectively represented as function of the orientation of the LP which is used to generate the proper polarization. We observe how ellipticity, Figure 6-20(b), varies linearly as the polarizer orientation changes. Moreover, the azimuth, Figure 6-20(a), is constant at 45º or at -45º as expected, despite when the light is circularly polarized and so, the azimuth parameter is not defined. The small fluctuation in the DOP parameter (0.96-1.09) is also present in this set of measurements. The maximum difference in the Stokes parameters is 0.15.

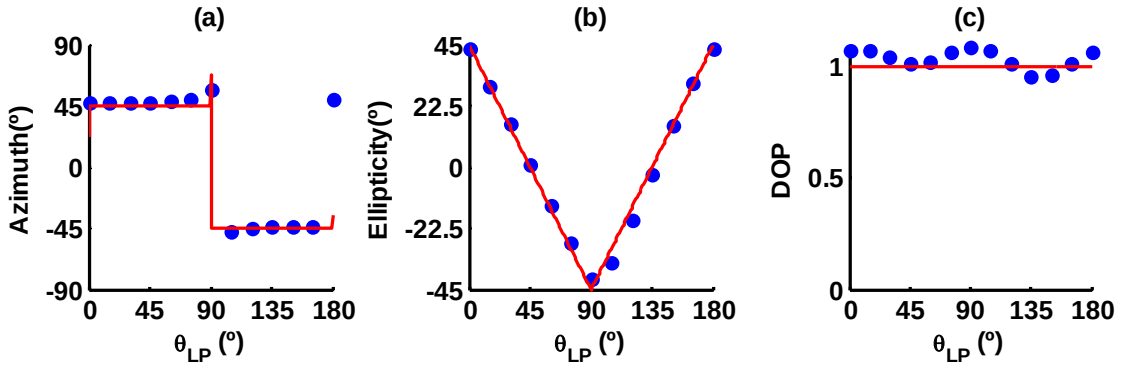

Figure 6-20: Fully polarized light, generated by rotating a linear polarizer (LP orientation in the *x* axis), followed by a QWP at 45º: (a) azimuth, (b) ellipticity and (c) DOP. Blue points and red line are experimental and predicted data, respectively.

Finally, we have generated light partially polarized, with a variable DOP. The DOP is controlled by means of the method explained in [PAPER D], based on the use of a FLC cell of nominal retardance λ/2. By properly aligning the FLC with an incident linear SOP, we can generate two nearly orthogonal SOPs, which are integrated in time, resulting in a SOP with a certain content of depolarization. A rectangular signal is sent to the FLC cell to generate these two orthogonal SOPs and, depending on the duty cycle (t_1/T) of the rectangular signal sent to the FLC, we can control the DOP. Figure 6-21 (a), (b) and (c) show the measured azimuth, ellipticity and DOP, respectively, as function of the duty cycle (t_1/T) of the FLC signal. We observe in Figure 6-21 (c) that the varying DOP measurements (in blue points) are very close to the expected values (red line). Moreover, azimuth and ellipticity parameters are also well determined with the implemented polarimeter, showing a great matching with the simulated values. The maximum difference in the Stokes parameters is 0.17.

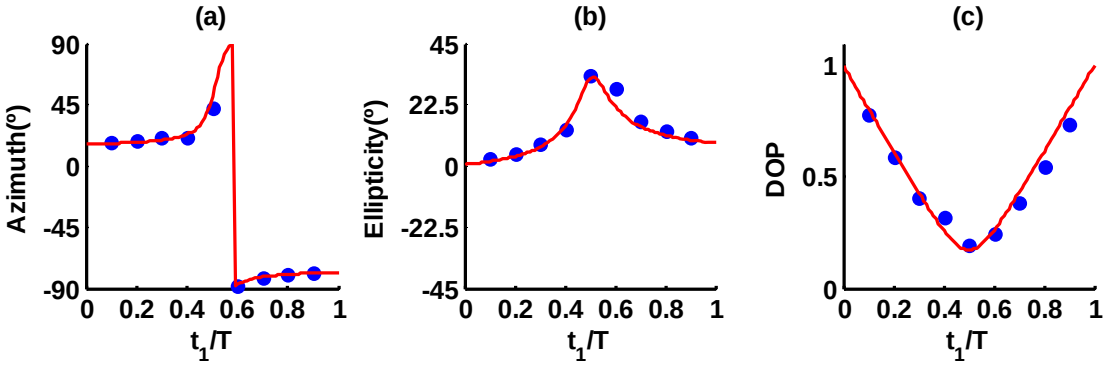

Figure 6-21: Partially polarized light, generated by a λ/2 FLC cell when sending a rectangular signal of duty cycle t_1 over a period of T: (a) azimuth, (b) ellipticity and (c) DOP as function of t_1/T. Blue points are experimental data and red line is the predicted data.

From the experimental results provided in this section, we conclude that the polarimeter based on the CR phenomenon provides accurate measurements of polarization, including fully and partially polarized light. The prototype results in a punctual Stokes and complete polarimeter. Due to the architecture based on the CR phenomenon, it allows to completely determine a SOP of an input light beam without mechanical movements or electrical addressing. In addition, unlike other amplitude division polarimeters [55,60,62,64], it allows to easily increase the number of PAs and so, increase data redundancy, leading to a decrease of variances. Therefore, it constitutes a nice alternative to the existing punctual Stokes polarimeters.

Chapter 7 **Imaging polarimeter and super-resolution polarimetry**

This chapter provides a comprehensive comparative between the four prototypes of polarimeters presented in previous chapters, polarimeters based on materials exhibiting index anisotropy (PA-LC cells, TN-LC cell, FLC cells and biaxial crystals). In particular, we focus on their features such as optimization, transitory time, accuracy, repeatability, parameters tolerance and robustness. The discussion leads to the best candidate to be used for the implementation of an imaging polarimeter. Afterwards, we detail the implementation of an imaging Stokes polarimeter and several experimental measurements are provided of non uniform polarization distributions. Furthermore, we present a new imaging set-up able to obtain super-resolved polarimetric images, when the spatial resolution of the system is limited by the pixel size of the imaging device. The proposed optical set-up performance is implemented and experimentally validated by measuring different spatial resolution test targets (in amplitude and in birefringence). Results are compared with polarimetric images obtained with the regular imaging system.

7.1 Comparative between the different prototypes of polarimeters

Previous chapters have analyzed different prototypes of polarimeters using three different types of LC cells (PA-LC, TN-LC and FLC) and biaxial crystals ($KGd(WO_4)_2$). Each polarimeter presents different features depending on the architecture itself. These features can be broken down into robustness, parameters tolerance, cost, transitory time, accuracy, repeatability, optimization, among others. Depending on the application of the polarimeter, some features become more relevant than others, leading to a best polarimeter candidate for that particular application. For this reason and at this point, it is very valuable to list the features of the different prototypes analyzed. Table 7-1 summarizes the specifications of the four main polarimeter architectures.

Next, we review each listed feature in Table 7-1 and we include a brief discussion of the specifications of the 4 polarimeters.

- **1. Thesis chapter:** First row indicates the number of chapter where it is analyzed in detail each polarimeter, discussing in detail all the results summarized in this table.
- **2. Type:** Polarimeters based on liquid crystal cells (PA-LC, TN-LC, and FLC) are time-division architectures, i.e. the flux measurements are taken sequentially in time when addressing different combination of voltages to the LC cells. Whereas CR based polarimeter is a division of amplitude architecture, i.e. it uses a beam splitter to divide the incident beam into two sub-beams and later, both beams are projected simultaneously over multiple analyzers of polarization by means of the conical refraction phenomenon. Thus, when the analyzed beam rapidly changes its polarization, a snapshot polarimeter is desired (as the CR polarimeter). Otherwise, if the polarization of the incident beam does not change in time, or such change is slower than the measurement time of the polarimeter, a time-sequential polarimeter results in a suitable alternative. Note that time-division polarimeters generally require a single detector (as the LC based polarimeters), reducing the implementation cost.
- **3. Equipment needed:** In order to implement a punctual and complete Stokes polarimeter different optical elements are necessary. LC based polarimeters need a linear polarizer and the radiometer, and the LC elements. In particular, PA-LC and FLC based polarimeters need 2 monopixel LC cells, but the TN-LC based polarimeter only requires a single monopixel LC cell, being one of its advantages. Moreover, TN-LC polarimeter can use an additional QWP for obtaining a better optimization of the system (i.e. lower CN). Finally, to achieve a complete polarimeter, the CR polarimeter architecture needs 2 biaxial crystals, a QWP, lenses, and 2 CCD cameras. However, if users are only interested in linear polarization content, the CR polarimeter architecture can be reduced to a single arm. Thus, the simplest

architecture, in terms of number of optical elements and its simplicity, is the TN-LC based polarimeter.

- **4. Cost:** This feature is connected with the equipment needed to implement the polarimeter. Generally speaking, biaxial crystals, LC cells and CCD cameras are the elements more expensive. However, the cost will strongly depend on the specifications of the optical elements or devices (as the length of the biaxial crystals, the diameter of the LC cells or the resolution of the cameras). Note that in the implementation of the TN-LC based polarimeter, not only has the simplest architecture (only one LC cell), but an off-the-shelf TN-LC cell is used, reducing extremely the cost of implementation. For this reason, we rated as the most economical prototype, although if one desires to improve the accuracy of the polarimeter, a commercial TN-LC cell should be acquired presenting more appealing optical features.
- **5. Transitory time:** CR based polarimeter takes the measurements instantaneously (only limited by the exposure time of the camera), so it is the fastest prototype here presented and the most suitable for time-varying polarization metrology. The LC based polarimeters, because they take time sequential measurements, it is necessary to wait a transitory time while the LC cell changes of configuration (when changing of PA). FLC is the fastest LC cell (0.3ms), leading to a polarimeter suitable for measuring slow-varying or constant in time polarization beams. Finally PA-LC and TN-LC cells are much slower (transitory time of 300ms), leading to polarimeters for measuring static or very slow-varying polarization beams. The total duration of the polarization measurement not only depends on the LC transitory time, but also on the number of intensity measurements acquired for each PA before averaging and the sample rate of the radiometer.
- **6. Extensible to image:** All analyzed polarimeters have been implemented as punctual Stokes polarimeters. Moreover, LC based polarimeters are potential architectures to extend to imaging polarimeters. To this end, the radiometer would be replaced by a CCD camera, and the proper lenses would be used to image the scene plane to the CCD plane. On the contrary, the CR based polarimeter is limited by its own architecture to be a punctual Stokes polarimeter. Thus, if the beam analyzed is uniform, any of the 4 proposed punctual Stokes polarimeters is suitable for characterizing the polarization. Nevertheless, if the beam has a non uniform distribution in polarization, an imaging polarimeter is necessary, and only a LC based polarimeter extended to an imaging polarimeter is suitable for that measurement.
- **7. Configuration selected:** We select one prototype for each polarimeter type (those leading to the best specifications), in order to compare the next features (optimization, robustness, parameters tolerance, accuracy and repeatability). Concerning the PA-LC based polarimeter we choose the regular tetrahedron configuration (Figure 3-6(a)). Concerning the TN-LC based polarimeter we choose the set-up D (Figure 4-1(d)), corresponding to illuminate in normal incidence the LC cell and using an additional QWP. This configuration even though

has a slightly higher CN in comparison with set-up F (Figure 4-1(f)), it has a much simpler architecture. The FLC based polarimeter is the optimized PSA configuration. Finally, CR based polarimeter we choose when N=720PAs (i.e. 360PAs per arm).

- **8. Optimization:** All four architectures allow implementing complete Stokes polarimeters, although with different conditioning. The PA-LC based polarimeter allows implementing the regular tetrahedron configuration (with the minimum theoretical CN achievable with a Stokes polarimeter, 1.73). Other polarimeters have some limitations concerning the available PAs, defining a characteristic curve, because of the restrictions imposed by the architecture, leading to a larger CN. In particular, CR based polarimeter with a CN of 2.00, followed by the FLC based polarimeter with a CN of 2.22. Finally, TN-LC based polarimeter in configuration D leads to a CN of 2.69. It is true that TN-LC based polarimeter in configuration F (double pass through the LC cell by means of a reflection on a mirror and using a QWP) reaches a smaller CN (1.98) but its architecture is more complicated than set-up D. So, generally speaking, for the TN-LC based polarimeters, the configuration D is recommended. All optimized polarimeters are well conditioned because CN is smaller than 3, ensuring a small amplification of the noise during the data reduction to the estimated Stokes vector. In conclusion, the best prototype in terms of general optimization is undoubtedly the polarimeter based on two PA-LC cells, when implementing the regular tetrahedron configuration. Moreover, we remark that PA-LC based polarimeter architecture has a versatile set-up which allows implementing any set of PAs. For instance, it allows implementing the PSA with minimum variances in the Stokes components with linear polarization content, S_1 and S_2 (Figure 3-8(c)). Unlike CN, which only indicates the general optimization, EWV also sees the benefits of data redundancy. For this reason, in terms of variances, the CR based polarimeter presents the best optimization (EWV=0.0611) because of the high data redundancy obtained when using N=720PAs.
- **9. Robustness:** In order to compare the robustness of the polarimeters, we have calculated the standard deviation of the CN related to different simulations of polarimeters deviated from the theoretical configuration. This parameter is related with the number N of PAs used, for this reason we indicate it as: $\sigma(CN,N)$. To conduct a rigorous comparison, the σ related to different polarimeter architectures have to be compared for the same number N. Results show that ordered from the most to the less robust (when N=4), we obtain the PA-LC based polarimeter, the FLC based polarimeter and the TN-LC based polarimeter. Note that they end up sorted from the smaller to the larger CN. Moreover, when more PAs are used in the configuration (N>4), the system becomes more robust. This is easy to understand in terms of volume enclosed by the PAs over the Poincaré sphere in terms of optimization. The same random deviation when using 4 PAs is more noticeable in a decrease of the volume than if we use a larger number of PAs. For this reason, the standard deviation of the CR based

polarimeter is much smaller (i.e. more robust) than the LC based polarimeters. In particular, when N=720PAs, the standard deviation is one order of magnitude smaller than the one for the PA-LC based polarimeter when N=4. In order to make a fair comparison, we have also calculated the standard deviation with N=100 for the PA-LC based polarimeter and for the CR based polarimeter, obtaining the former a slightly smaller standard deviation (σ(CN,100) = 0.015) than the latest (σ(CN,100) = 0.024), pointing out that the first one presents better conditioning. However, we want to emphasize that N=100 leads to long-term measurements when using the PA-LC based polarimeter, whilst this is conducted instantaneously by using the CR based polarimeter. In conclusion, as better conditioning and more redundancy (larger number of PAs), more robust is the polarimeter. Therefore, the CR based polarimeter followed by the PA-LC based polarimeter are recommended in terms of robustness.

- **10. Parameters tolerance:** We conduct the tolerance analysis detailed in section 2.4.1 for the four selected polarimeters. In all the cases, the tolerances of the different parameters are determined in order to have a Stokes error smaller than 0.02. The tolerances of the parameters of the set-up are listed in Table 7-1. In all the cases, the polarimeter accuracy is more sensitive to deviations in the orientation of the optical elements than in the retardance. In order to ensure to work in the tolerance range of the different parameters, it is necessary an experimental calibration of the polarimetric measurement matrix. Because all architectures do not have moving elements, the orientations after being calibrated are kept constant at that position. Additionally, the temperature is controlled in order to keep it as still as possible and so, it does not significantly affect to the LC optical features.

- **11. Accuracy:** We provide the maximum difference between the experimental measurements of the Stokes parameters and the reference Stokes values. LC based polarimeters have the same order of experimental accuracy, in the hundredths. In particular, PA-LC based polarimeter is of 0.04, whereas TN-LC and FLC based polarimeters are of 0.05. Finally, the CR polarimeter configuration implemented lead to an experimental accuracy in the tenths (0.17). However, if required, better results in terms of accuracy could be obtained by improving the polarimeter alignment, being one of the most critical parameters in the CR architecture, in terms of systematic errors. Note that all experimental accuracy values are slightly higher than 0.02, value fixed during the tolerance analysis. This fact is because in the tolerance analysis we only considered individual systematic errors, whereas in the experimental accuracy there may be a combination of systematic errors as well as noise from the flux measurements.

- **12. Repeatability:** Among the LC based polarimeters studied, FLC based polarimeter is the most repeatable instrument followed by the TN-LC based polarimeter and finally by the PA-LC based polarimeter. The main reason of the repeatability magnitude lies on the repeatability of the LC by itself. Nevertheless, other facts need to be kept in mind. First, the

duration of the measurement of the FLC polarimeter (0.5 second) is much faster than the other two LC based polarimeters (around 5 seconds), ensuring a better stability of the laboratory conditions (as fluctuations on the laser source) and so, providing better repeatability. Second, TN-LC based polarimeter only uses one LC element, whereas the other prototypes use 2. Thus, TN-LC polarimeter is more stable in this sense because less dynamic elements are involved compared to the other two set-ups, affecting to some extent to the repeatability of the polarization measurement. CR based polarimeter is a static architecture, in comparison with LC based polarimeters which have dynamic elements, in this way, the repeatability of the former is much better, being nearly undetectable a variation between consecutive Stokes vector measurements.

- **13 and 14. Strengths and weaknesses:** Finally in the two last rows we point out the main strengths and weaknesses of each polarimeter. All 4 prototypes have the appealing feature of measuring the polarization without any moving optical elements and so, they avoid experimental errors associated to misalignments or to beam wander. Furthermore, an appealing characteristic of the CR based polarimeter is that it does not have dynamic elements controllable by an electrical signal, avoiding errors from the phase-to-voltage calibration. First, PA-LC based polarimeter has the best optimization and also allows implementing any configuration of PSA thanks to the versatility of its set-up. This fact may be useful when the measure of a particular Stokes channel is of interest. However, such polarimeter architecture needs of two LC cells and this type of LC is slow when compared with other LC types. The number of LC cells affects the cost of the polarimeter implementation as well as it is strongly related to the light losses due to the reflection on the surface of the LC cell. Second, TN-LC based polarimeter has a single LC cell, which reduces the final cost. Nevertheless, the measurement duration is long because the TN-LC is slow in changing of configuration, limiting to static polarization beams to be measured with accuracy. Third, FLC based polarimeter stands out for its very fast measurements and its high repeatability, although it needs two LC cells (more expensive and more light losses). Finally, CR based polarimeter takes snapshot measurements, allowing to measure varying polarizations, as well as it is possible to increase data redundancy without increasing the measurement time. However, it requires of 2 CCDs to achieve complete polarimetric measurements, the system is very critical to incidence angle tilts and so, it requires a very good alignment and it is not possible to extent to an imaging polarimeter.

Table 7-1: Comparison of the 4 different polarimeter architectures presented in previous chapters.

	PA-LC polarimeter	**TN-LC polarimeter**	**FLC polarimeter**	**CR polarimeter**
1. Thesis chapter	Chapter 3	Chapter 4	Chapter 5	Chapter 6
2. Type	Division of time	Division of time	Division of time	Division of amplitude
3. Equipment needed	2 PA-LC cells LP Radiometer	1 TN-LC cell (QWP), LP Radiometer	2 FLC cells LP Radiometer	2 biaxial crystals QWP 2 CCDs, lenses
4. Cost	Expensive	Economical	Expensive	Expensive
5. Transitory time	(300ms)x4	(300ms)x4	(0.3ms)x4	-
6. Extensible to image	Yes	Yes	Yes	No
7. Configuration selected	Regular tetrahedron	Set-up D	Optimized PSA	720 PAs
8. Optimization	CN = 1.73 EWV = 10.00	CN = 2.69 EWV = 13.99	CN = 2.22 EWV = 11.18	CN = 2.00 EWV = 0.0611
9. Robustness	$\sigma(CN,4) = 0.094$	$\sigma(CN,4) = 0.40$	$\sigma(CN,4) = 0.25$	$\sigma(CN,720)=0.0089$
10. Parameters tolerance	$\theta_{PALC1} = 0.50º$ $\theta_{PALC2} = 0.54º$ $\delta_{PALC1} = 0.89$ $\delta_{PALC2} = 1.15º$	$V_{TNLC} = 0.0044V$ $\theta_{LP} = 0.66º$ $\theta_{WP} = 0.55º$ $\delta_{WP} = 1.69º$	$\theta_{FLC1} = 0.28º$ $\theta_{FLC2} = 0.29º$ $\alpha_{FLC1} = 0.44º$ $\alpha_{FLC2} = 0.59º$ $\delta_{FLC1} = 1.07º$ $\delta_{FLC2} = 1.04º$	$\theta_{WP} = 0.57º$ $\delta_{WP} = 1.15º$ $\theta_{LP1} = 0.57º$ $\theta_{LP2} = 0.57º$
11. Accuracy	0.04	0.05	0.05	0.17
12. Repeatability	$\sigma_{max}(S_i) = 0.01$	$\sigma_{max}(S_i) = 0.002$	$\sigma_{max}(S_i) = 0.0002$	-
13. Strengths	No moving elements, best optimization, it can implement any PSA	No moving elements, single LC cell, economical	No moving elements, very fast, high repeatability	Static set-up, snapshot measurements, high data redundancy
14. Weaknesses	Slow, 2 LC cells	Slow	2 LC cells	Punctual, 2 CCDs, critical to incident beam tilts

7.1.1 Selection of the best candidate for super-resolution polarimetry

Our next step is to choose the best candidate between the 4 prototypes to extend it to an imaging Stokes polarimeter and later, to implement a super-resolution algorithm to obtain polarimetric images with enhanced spatial resolution. With this aim, we have selected the three potential imaging polarimeters (LC based polarimeters), and the CR based polarimeter is discarded. Note that to choose the best polarimeter configuration becomes a subjective decision as strongly depends on the application to be used. Here, we establish an estimation protocol helping us to select the best candidate in terms of imaging polarimetry. In particular, we gather all the results in a single matrix shown in Table 7-2, that we call it decision matrix. We ranked 7 significant features with a number from 0 (worst value) to 10 (best value). The selected features, labeled with the index *k*, and arranged in the first column of Table 7-2, are: transitory time, optimization, accuracy, repeatability, parameters tolerance, robustness and cost.

Table 7-2: Decision matrix. Its coefficient *r(k,j)* corresponds to the rate of the feature *k* when using the polarimeter *j*.

Feature	k	PA-LC polarimeter *j*=1	TN-LC polarimeter *j*=2	FLC polarimeter *j*=3
Transitory time	1	6	6	9
Optimization	2	10	8	9
Accuracy	3	9	8	8
Repeatability	4	8	9	10
Parameters tolerance	5	9	9	9
Robustness	6	9	7	8
Cost	7	8	9	8

Then, we construct a figure of merit to decide the best prototype suited for our specific application (super-resolution polarization imaging). The merit function for the polarimeter *j* is:

$$Merit(j) = \sum_{k=1}^{N} a_k r\left(k, j\right) \ , \tag{7-1}$$

where $r(k,j)$ are the coefficients of the decision matrix and a_k are the different weights assigned to the $N=7$ different features depending on the relevance of them for our particular application. In

our opinion, fast measurements and well optimized system are the two most relevant features. On the one hand, the transitory time, weighted as $a_1=3$, is an important feature because we are interested in implementing a polarimeter able to take fast measurements for potential applications in time-dependent polarization metrology. On the other hand, it is very important to work with a well conditioned polarimeter, which minimizes the amplification of the noise during the data reduction and ensures accurate measurements. Thus, the optimization is weighted as $a_2=2.5$. Next, it will be desirable a reasonable accuracy and repeatability in the polarization measurements ($a_3=1.5$ and $a_4=1.5$, respectively). Following that, it is important the polarimeter sensitivity to systematic errors evaluated with the tolerance analysis by fixing a Stokes error of 0.02 ($a_5=0.5$). Finally, the robustness and the cost of the polarimeter have the same weight ($a_6=0.5$ and $a_7=0.5$, respectively). The cost of the elements is not a significant feature in our conditions because the optical elements were already bought and used in the laboratory for the analysis of the different prototypes working as punctual polarimeters. Moreover, the robustness of the polarimeter, as discussed above, is strongly connected with the conditioning of the polarimetric measurement matrix already taken into account in the optimization feature. By considering the features weights (a_k) and the rates ($r(k,j)$) of Table 7-2, we can calculate the merit for three different prototypes. Figure 7-1 plots the different terms of the merit function of Eq.(7-1) for the three polarimeters. The legend colors indicate the 7 features which have been taken into account in the merit function. We observe that the FLC based polarimeter is the best candidate for this particular application, holding a merit of 89 over 100. The other two polarimeters have a smaller merit value, 81.5 for the PA-LC based polarimeter and 76 for the TN-LC based polarimeter.

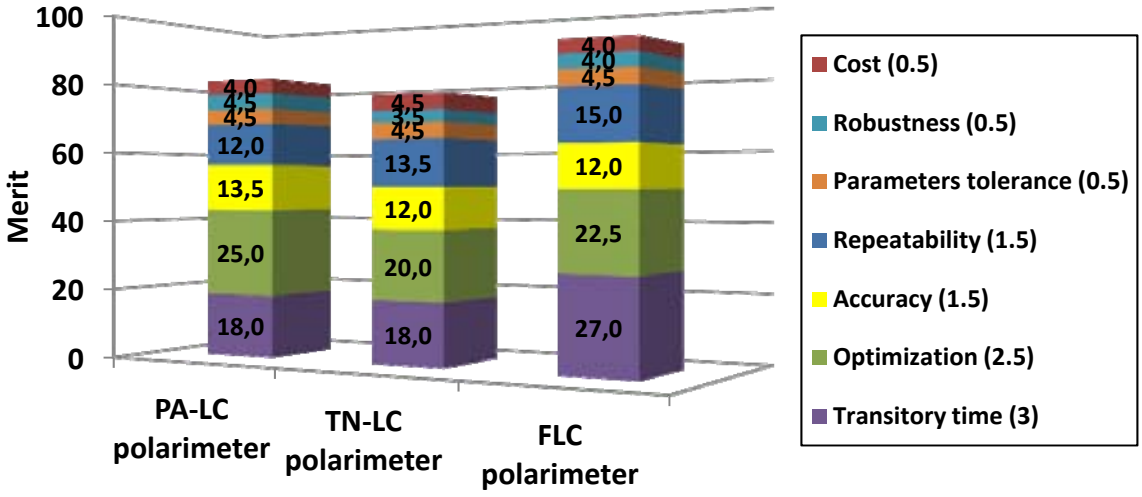

Figure 7-1: Merit for the three polarimeter prototypes. The legend indicates the color representation and the merit function weight (in parenthesis) for each feature.

7.2 Imaging Stokes polarimeter

An imaging Stokes polarimeter seeks the Stokes vector at every pixel in a scene [21]. In this section we describe the extension of the punctual Stokes polarimeter selected from the merit function, which is based on two FLC cells, to an imaging Stokes polarimeter. First, we describe the experimental set-up and next, we provide some experimental measurements of polarimetric images and their corresponding discussions.

7.2.1 Experimental set-up

The basic architecture of the Stokes polarimeter is as the PSA detailed in Chapter 5, and sketched in Figure 5-1, composed by two monopixel FLC cells and a linear polarizer. The orientations of the FLC cells are the optimized angles given in Table 5-3. To adapt the system to imaging polarimetry, the radiometer given in Figure 5-1 is replaced by a charge-coupled device (CCD) camera. In order to spatially measure the polarization of a plane, a convergent lens (L) images the analyzed scene onto the CCD plane. The CCD camera, distributed by Basler, has a resolution of 1000x1000 pixels (7.4μm of pixel size). However, to reduce the processing time, we have selected a smaller region of interest depending on each particular measurement. In addition, the camera acquisition is synchronized with the electrical signals addressed to the FLC cells, ensuring to take the images at the proper times (when the FLC cells are set at the four stable configurations).

The imaging lens is placed after the linear polarizer (LP) of PSA for two reasons. First, rays coming from the scene, which has been illuminated with a collimated beam, are impinging to the elements of the PSA in normal incidence, ensuring the same polarization change for all the rays. Whereas if the imaging lens would have been placed before the PSA, rays exiting from the scene would have been tilted and so, they would have been impinged with different incident angles to the elements of the PSA. Consequently, each ray would have been projected over a different PA because retardance is dependent with the optical path length[136]. Second, the lens may introduce some small polarization aberration when light goes through, but if the lens is placed after the LP of the PSA, light is already projected over the polarization analyzer of the PSA and the transmitted intensity, which is going to be measured with the camera, is not affected by the polarization aberration.

7.2.2 Calibration

Two different light sources are tested in the implementation. Firstly, a He-Ne laser (633nm) and secondly, a collimated red light emitting diode (LED, λ_o=625 nm and $\Delta\lambda$=17 nm). It is necessary to calibrate the PSA system for the two different light sources, because the optical elements may have small wavelength dependence. Both new PSA calibrations are represented over the Poincaré sphere in Figure 7-2 (in red and blue when illuminating with laser and LED, respectively), whereas we have also plotted the theoretical PSA (in green), optimized in section 5.2.1. The CN of the calibrated PSAs are 2.58 and 2.51 for laser and LED respectively, values close to the theoretical counterpart (2.22). Concerning the DOP of the PAs, not only the ones implemented when illuminating with a laser are fully polarized (DOP values of 1), but also the ones obtained when using the LED source can be considered fully polarized (DOP values larger than 0.96).

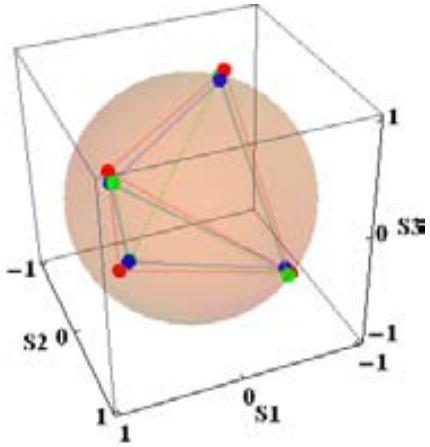

Figure 7-2: Calibrated PSA when illuminating with a laser (in red) and with a LED source (in blue), as well as the theoretical PSA (in green).

We have tested both calibrations by measuring a uniform polarization distribution. This is generated by a linear polarizer at 0º. In Figure 7-3(a) and (b), we show the S_0 element when illuminating with the laser and the LED, respectively. It is appreciable that when using a laser, the total intensity image is degraded with diffraction of dust or small imperfections (as scratches) on the optical elements surfaces. On the contrary, when using the LED source, the intensity image is much cleaner. This is because the light source is less monochromatic and so, the diffraction effects are less noticeable. To complete this analysis of the light source suitability, we have analyzed the uniformity given by both Stokes vector image measurements. Table 7-3 provides the mean and the standard deviation of three parameters (DOP, azimuth and ellipticity) of the measured SOP (related to the different pixels) when illuminating with the laser and the LED. Concerning the DOP parameter, in both cases the mean value is close to the expected one (i.e. 1 because it is fully polarized light), and the associated standard deviations are of the same order.

Regarding the azimuth parameter, the mean value is not comparable because the polarization rotation mount has increments of 2º, and for each measurement we have reoriented the LP. However, we can state that the laser measurement is less uniform because the azimuth standard deviation is much larger than the counterpart for the LED measurement. This fact may be related to diffraction phenomenon stated above, being less significant when working with a slightly less coherent light source (LED). Finally, ellipticity parameter should be 0 because the beam is linearly polarized with a LP and, it is the LED measurement which gives a value much closer to the expected one. In addition, we observe as well that the LED measurement presents better uniformity (i.e. smaller standard deviation) in the ellipticity parameter. By taking into account all the discussed points above, we conclude that the LED is the most suitable light source to illuminate the imaging Stokes polarimeter. Therefore, the following experimental measurements are obtained by using the LED as light source.

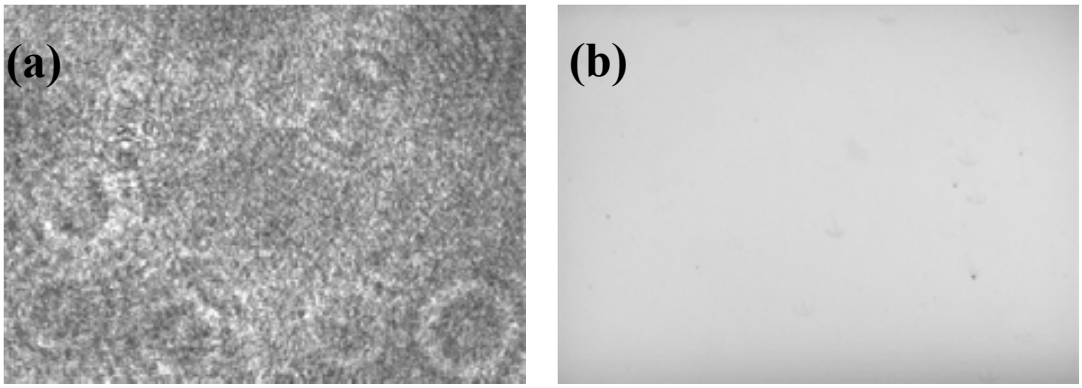

Figure 7-3: S_0 Stokes parameter of a uniform light beam linearly polarized using as light source: (a) He-Ne laser and (b) LED.

Table 7-3: Histogram analysis of a uniform distribution measurement of a linearly polarized light at 0º, when illuminating with a laser and a LED. Mean and standard deviation (σ) of the measured DOP, azimuth and ellipticity.

	DOP mean	Azimuth mean	Ellipticity mean	DOP σ	Azimuth σ	Ellipticity σ
Laser	1.001	0.692	1.635	0.059	2.058	1.022
LED	1.022	-0.171	0.164	0.011	0.417	0.143

7.2.3 Experimental measurements

Measurements provided by any complete imaging Stokes polarimeter have four channels, containing the full polarization characterization, typically the four Stokes elements (S_0, S_1, S_2 and S_3). Thus, the interpretation of this multidimensional content is difficult to grasp at once. In [146],

they proposed to represent three polarization parameters in a single synthesized image using the HSV color space shown in Figure 7-4. HSV color space represents each color by three attributes:

- The hue (H) is related to the color perception. This is the angular dimension, starting at red (0º), passing through green (120º), blue (240º), and finally wrapping back to the red (360º).
- The saturation (S) is related to the degree of the color purity. This parameter corresponds to the distance to the axis, going from white or a particular grey level depending on the V value (0), to the pure color (1).
- The value (V) is related to light quantity in a color. This parameter corresponds to the height, going from dark (0) to bright (1).

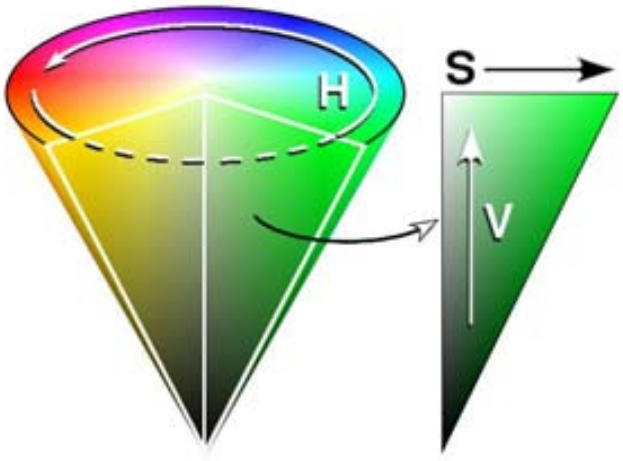

Figure 7-4: Geometrical representation of the HSV color space used for encoding 3 polarization parameters channels [146].

The election of the three polarization parameters (or a combination of them) to be represented in the synthesized image using the HSV model depends on the samples which are being analyzed. The objective of this election is to enhance the contrast of the polarization image. In our case, we have used the correspondence between color attribute and polarization parameters shown in Table 7-4. The main information, azimuth or ellipticity, is encoded with the hue parameter, whereas the total intensity and the DOP modifies the pure color by changing the value and saturation, respectively. Moreover, it is necessary to normalize the three polarization parameters (azimuth or ellipticity, DOP and total intensity) in the corresponding range of each color attribute (i.e. $0º \leq H \leq 360º$, $0 \leq S \leq 1$ and $0 \leq V \leq 1$). By using this color correspondence, the interpretation of ellipticity and azimuth images becomes easier because it avoids misinterpretation in particular regions of the image where low intensity values reach the camera (the color will be darker) or where light contains a significant content of depolarization (the color will be bleached). From now on, we will refer as azimuth HSV image or ellipticity HSV image when we use this

HSV model using the color correspondence detailed in Table 7-4, and the hue will be encoding the azimuth or the ellipticity, respectively.

Table 7-4: Correspondence between the HSV color attributes and the polarization parameters used in our representation of Stokes images measurements.

Color attribute	Color attribute range	Polarization parameter	Polarization parameter range
Hue (H)	0º≤H≤360º	Azimuth (χ)	-90º≤χ≤90º
		Ellipticity (ε)	-45º≤ε≤45º
Saturation (S)	0≤S≤1	DOP	0≤DOP≤1
Value (V)	0≤V≤1	Total intensity (S_0)	0≤ S_0≤1

After introducing the HSV color representation, we provide a set of Stokes vector images measurements of different non uniform polarization distributions.

Firstly, we measure the beam transmitted through a polarizer divided in 8 circular sectors, where each sector has a particular transmission axis orientation which rotates along 360º. The azimuth and ellipticity HSV images, obtained from the experimental measurements, are represented in Figure 7-5(a) and (b), respectively. We observe that the exiting beam has a non uniform polarization distribution, with 8 distinct circular sectors with different azimuth values distributed along (-90º, 90º), labeled with black numbers. In addition, all sectors present a null ellipticity, as we are dealing with linear polarizations. Moreover, the edges between circular sectors are darker because less light is transmitted through these particular regions. In order to see in more detail the uniformity along the circular sectors, we have represented the cross section along the black circle plotted in Figure 7-5. Cross sections of azimuth, ellipticity and DOP are plotted in Figure 7-6(a), (b) and (c), respectively. Azimuth function is clearly divided in 8 regions with 8 constant values, corresponding to the 8 circular sectors (indicated with the number labels), and there is a link between consecutive regions with intermediate azimuth values. Ellipticity function is kept constant at 0º (small fluctuations around -1.1 and 1.3), highlighting the linear polarizance of the optical element. Finally, DOP function shows how the light transmitted through the circular sectors is fully polarized, but light going through the edges is partially polarized (DOP reduced until 0.85 approximately).

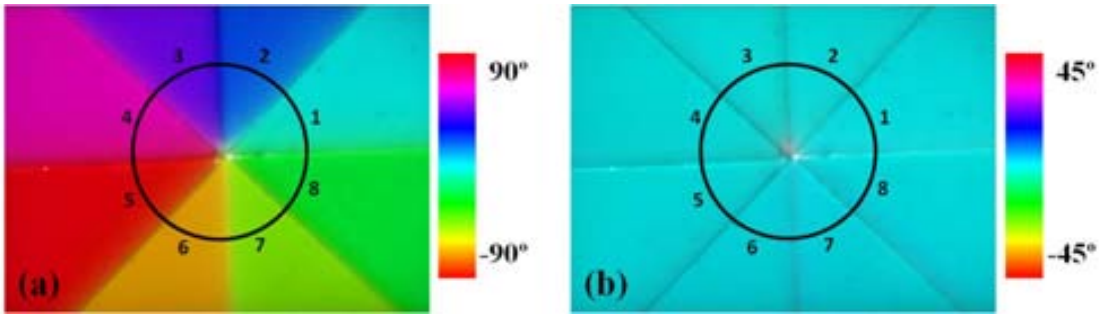

Figure 7-5: (a) Azimuth HSV image and (b) ellipticity HSV image of a beam transmitted through a polarizer divided in 8 circular sectors with different transmission axis orientation (labeled with a number from 1 to 8). The color legend bar corresponds to the azimuth and ellipticity angle, respectively, encoded by the hue attribute using the HSV model. Cross section of the black circle is plotted in Figure 7-6.

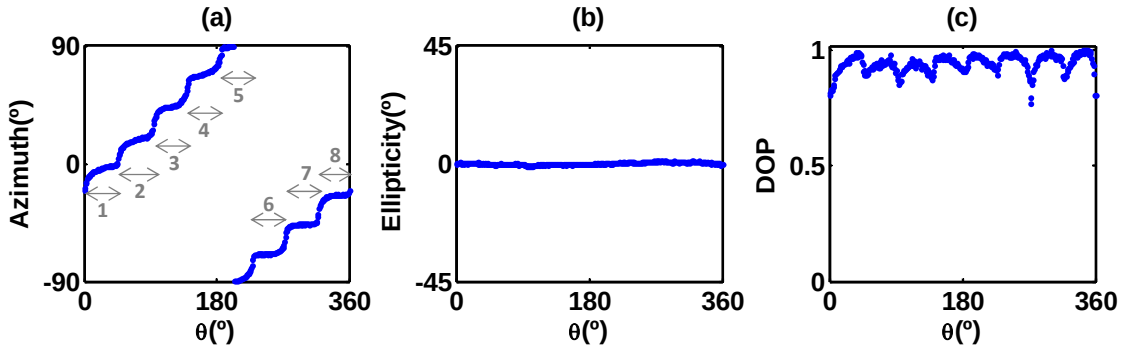

Figure 7-6: Circular cross section of the Stokes vector measurement shown in Figure 7-5: (a) azimuth, (b) ellipticity and (c) DOP as function of the angle over the circular cross section (θ). Numbers are indicating the 8 distinct regions of the image in Figure 7-5.

Secondly, we analyze the polarization distribution of a linearly polarized beam transmitted through a plastic ruler, being this a polarimetric sample showing spatial variations in the birefringence due to stress. Figure 7-7(a) and (b) show the azimuth and ellipticity HSV images, respectively. There are four distinct regions labeled with white numbers. Region 1 has a uniform linear polarization (ellipticity is null) corresponding to the light going through a hole on the plastic ruler. Therefore, the light polarization is not altered by the material and so, the measurement in that region corresponds to the polarization of the incident beam. Then, in region 2 very little light is transmitted without being deviated trough a circular thick flange in the ruler, resulting in a dark area in HSV images. In region 3 there is also a circular flange, although thinner than the one in region 2, allowing some light going through, and several scratches are observed on the surface of that particular region. Finally, in region 4 few scratches are also observed and this corresponds to the uniform layer of the plastic ruler. Both regions 3 and 4 have a striking color distribution in both polarization HSV images, result of the birefringence stress induced during the manufacturing process of the ruler. Birefringence stress is a well-known material property of plastics, that upon the application of stresses, the material exhibits birefringence. In this way,

when light is transmitted through this piece of plastic, the exiting beam exhibits a spatial variation in azimuth as well as in ellipticity according to the non uniform birefringence stress distribution. In particular, we observe that region 3 presents a faster variation in the spatial distribution of polarization in comparison with region 4. This is because the section 3 presents a larger deformation of the plastic (propinquity of the hole) than the section 4 (uniform layer of the ruler), as a stronger stress was applied to generate the flange during the manufacturing process. Furthermore, an analysis of the cross section of the vertical line plotted in Figure 7-7 is conducted. In particular, we show in Figure 7-8 the DOP evolution as function of the *y* position along the vertical line. The four regions described above are also marked in Figure 7-8. Region 1 and 4 correspond to fully polarized light (DOP=1), in contrast to regions 2 and 3, where light is partially polarized. The decrease of the DOP in these last two regions can be originated by different causes, as for instance, by the diffraction produced by the scratches, by the sharp shape of the plastic in these particular regions, or due to the spatial average of polarizations related to the pixel area.

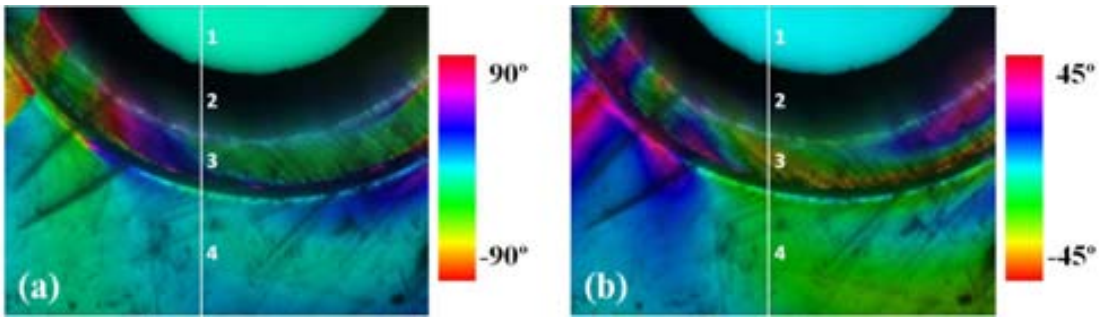

Figure 7-7: (a) Azimuth HSV image and (b) ellipticity HSV image of a linearly polarized beam transmitted through a plastic ruler. The color legend bar corresponds to the azimuth and ellipticity angle, respectively, encoded by the hue attribute using the HSV model. Numbers are labeling four distinct regions of the image. Cross section of the white line is plotted in Figure 7-8.

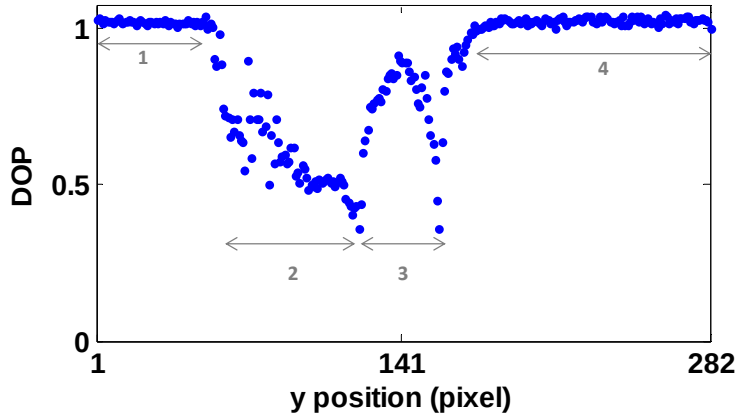

Figure 7-8: Vertical cross section of the Stokes vector measurement shown in Figure 7-7. DOP as function of the position along the *y* axis. Numbers are indicating the four distinct regions of the image in Figure 7-7.

Afterwards, we generate a more pronounced non uniform polarization distribution by applying an external mechanical strain with a screw on a plastic bar. The beam transmitted through this plastic bar under stress is measured with the imaging Stokes polarimeter. Figure 7-9(a) and (b) show the azimuth and ellipticity image, respectively (without using the HSV model to avoid a bleached image related to the low DOP values). We observe a nice banded distribution with rapid changes, more prominent on the left side of both images, due to the birefringence stress. Moreover, it is easy to observe a tendency of the bands wrapping a point on the left side, which actually corresponds to the position where the screw was pressing. Therefore, azimuth and ellipticity images give a fairly accurate picture of the stress distribution in the plastic bar. Additionally, in Figure 7-10(a) we have represented the DOP distribution. The cross section along the horizontal line marked in Figure 7-10(a) is represented in Figure 7-10(b). DOP data shows that light on the left side is less polarized than on the right side. This difference can be explained because on the left side polarization changes more rapidly and so, the pixel of the camera does a spatial average of these mixed SOPs, leading to a SOP with a higher content of depolarization.

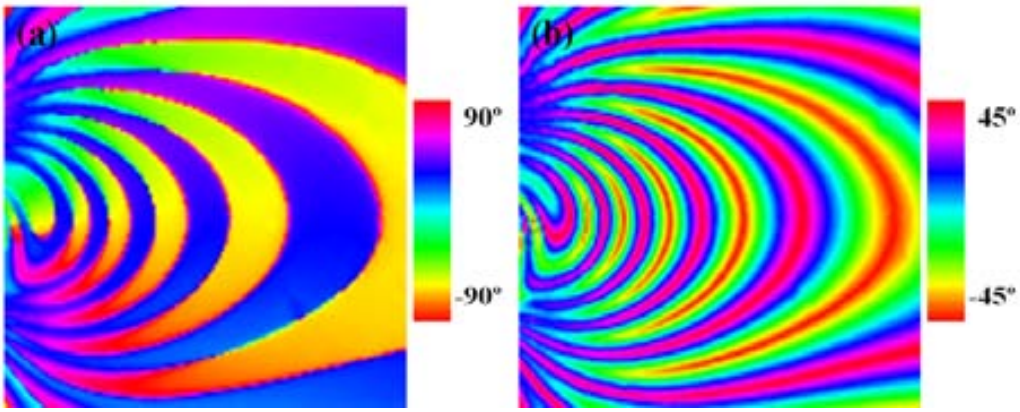

Figure 7-9: (a) Azimuth image and (b) ellipticity image of a linearly polarized beam transmitted through a plastic bar under mechanical stress.

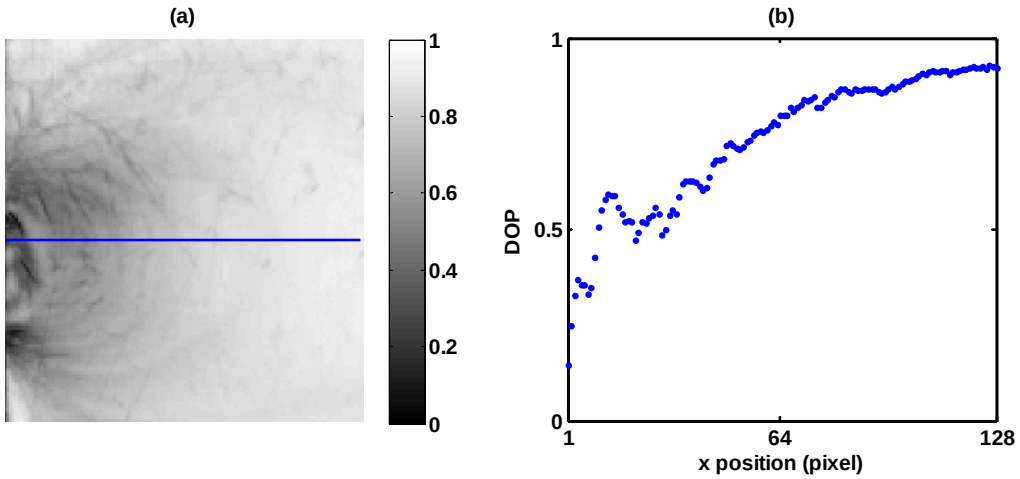

Figure 7-10: (a) DOP image of a linearly polarized beam transmitted through a plastic bar under mechanical stress. (b) DOP cross section as function of the *x* position along the horizontal blue line plotted in (a).

Finally, we have measured the beam exiting from a depolarizer, when this is illuminated with a linear SOP. In particular we used an achromatic depolarizer distributed by Thorlabs (DPU-25). This element consists of two crystal quartz wedges, one of which is twice as thick as the other. The optical axis of each wedge is perpendicular to the flat for that wedge, and the relative angle between the optical axes of the two wedges is 45º. In this way, when illuminating the element with a polarized beam, it generates a spatially varying polarization distribution. The design of this element leads to depolarized light when spatially averaging these varying SOPs. In addition, if we use a source with a certain bandwidth (as our illumination source, a LED of $\Delta\lambda$=17 nm), certain depolarization content will be added due to the wavelength-dependent retardation of the light transmitted through the quartz wedges. The measured azimuth and ellipticity images are represented in Figure 7-11(a) and (b), respectively. A set of bands with similar polarization are observed. The polarization changes in one direction (azimuth and ellipticity), according to the relation between the depolarizer orientation and the polarization of the incident beam. Nevertheless these two images only reflect the contribution of fully polarized light, which actually is very small in comparison with the unpolarized light content. In order to analyze this second content, in Figure 7-12(a) it is represented the DOP image of the output beam, and in Figure 7-12(b) the cross section of the vertical line plotted in Figure 7-12(a), as a function of the pixel position in the *y* axis. Note that the output beam has a very high content of depolarized light (DOP < 0.05), due to the pixel average and wavelength-dependent retardation discussed above.

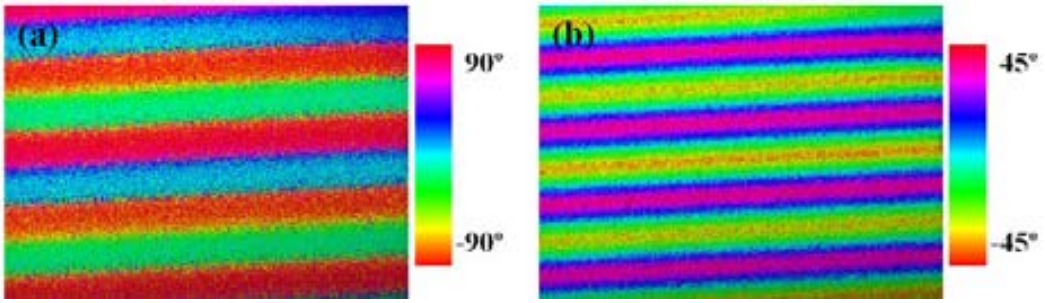

Figure 7-11: (a) Azimuth and (b) ellipticity images of a linearly polarized beam transmitted through a depolarizer.

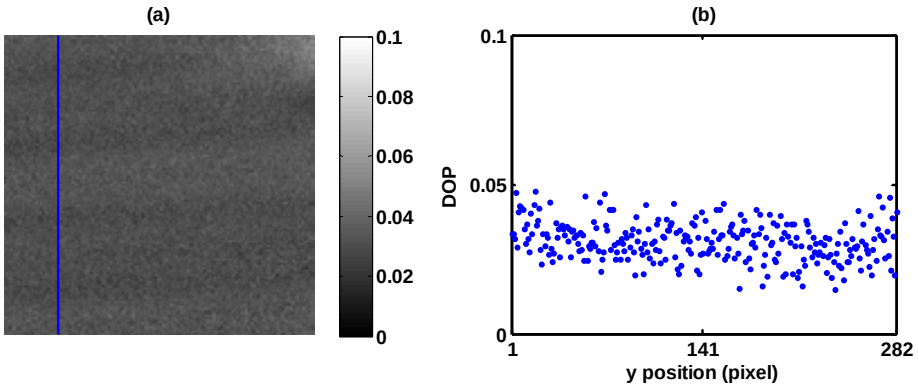

Figure 7-12: (a) DOP image of a linearly polarized beam transmitted through a depolarizer. (b) DOP cross section as function of the *y* position along the vertical blue line plotted in (a).

7.3 Super-resolution imaging Stokes polarimeter

Spatial resolution (SR) is a measure for the ability to distinguish two separated points in an image. SR is limited by diverse factors: numerical aperture of the imaging system, the wavelength of the employed light, misalignments and aberrations of the optical components, geometrical properties of the camera pixel (size, shape and pitch) among others [147]. High resolution devices are required for many purposes in imaging based applications, such as in remote sensing applications [148] or for medical purposes [149]. Different approaches have been reported to attempt to overcome the resolution of an imaging system. As well known, one of the main limitations for the SR is the diffraction limit of the optical system. To overcome this limitation different super-resolution methods have been presented in the literature, as for instance those based on the use of diffraction gratings [150,151], structured illumination [152,153] and time multiplexing super-resolution techniques [154]. In the case of modern imaging systems, they usually include CCD cameras as the main devices to capture the images. In such cases, the pixel dimension of the camera may also impose a geometrical limitation in resolution. In particular, many optical systems have detector pixels relatively large compared to the point spread function (PSF) of the optical system, resulting in a system that is undersampled. In such systems, the optical system passes higher spatial frequencies than those that the detector can correctly sense. Undersampled systems are used in some applications because they may present some interesting advantages, such as improved sensitivity leading to faster integration times and higher signal-to-noise ratio, larger fields-of-view, better image quality and less expensive [155,156]. When the SR is limited by the detector pixels, geometry multiframe super-resolution algorithms can be employed to improve the resolution of the imagery, as for instance sight-and-add, interlacing, Drizzle algorithm [157], techniques based on the maximum likelihood [158,159], projection onto convex sets [160,161], non uniform interpolations [162,163], stochastic reconstruction method [164,165], code-division multiplexing [166], among others [156,167,168].

In general, imaging systems only analyze the intensity information of an object. However, extra image information, as an accurate knowledge of the light polarization content, may be of interest in some applications. For instance, in medical applications [8,169], polarimetric images provide valuable data for diagnosis, being this information hidden in regular intensity images of the sample. Imaging polarimeters are the basic devices to perform these polarization images, as those described in [73,104] or the one described and implemented in the previous section 7.2.

In this section, we propose for the first time, to the best of our knowledge, a new experimental set-up able to provide polarization images with enhanced spatial resolution. This

new imaging set-up is based on LC technology and it is suitable when the main limitation in resolution is imposed by the pixel pitch of the CCD camera.

7.3.1 Experimental set-up

The proposed set-up used for implementing the super-resolution imaging polarimeter is sketched in Figure 7-13. The system is illuminated with a LED source (λ_o=625 nm and $\Delta\lambda$=17 nm) because intensity images appear much cleaner, as discussed in the imaging Stokes polarimeter in section 7.2.1. Then, a polarization state generator (PSG), consisting of a linear polarizer (LP_1) and a quarter waveplate (QWP), is used to control the polarization of the incident beam illuminating the scene. The scene is a polarimetric object which generates a particular polarization distribution to be measured with the polarimeter.

Afterwards, the super-resolution polarimetric imaging system is set. The idea is to achieve polarimetric images with enhanced spatial resolution. To this aim, the experimental set-up combines two different modules: a super-resolution module (which reconstructs a single high resolution intensity image of a scene from a set of regular intensity images recorded at lower resolution) with the imaging Stokes polarimeter described in section 7.2 (which determines the polarization spatial distribution of a light beam from a set of super-resolved intensity images obtained with the super-resolution module).

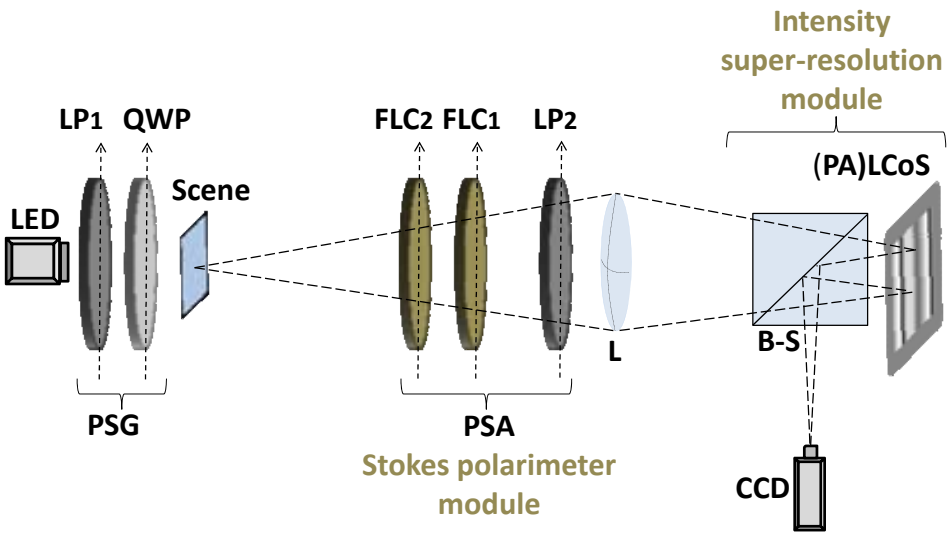

Figure 7-13: Set-up used to implement the polarization imaging system with enhanced spatial resolution. This consists of two parts: an imaging Stokes polarimeter (two ferroelectric liquid crystal cells and a polarizer) and an intensity super-resolution module (LCoS spatial light modulator).

The imaging Stokes polarimeter, implemented in 7.2, obtains polarimetric images with a SR limited by the pixel size of the CCD. Nevertheless, in our proposed super-resolution imaging polarimeter sketched in Figure 7-13, we include an extra module for enhancing the spatial

resolution of the intensity images taken by the camera. In this module the light is transmitted by a 50/50 non polarizing beam splitter (B-S) towards a parallel aligned liquid crystal on silicon (PA-LCoS) display. This device is a pure phase spatial light modulator (SLM) that allows the introduction of linear phases very precisely controlled. The reflected light goes back to the B-S and is redirected to the detector. As the lens *L* images the scene plane at the CCD plane, the linear phases addressed to the PA-LCoS generate sub-pixel displacements of the low-resolution images at the CCD plane. By properly interlacing the different shifted images and applying an anti-aliasing algorithm it is possible to reconstruct a final super resolved intensity image of large dimension. Finally, by combining 4 super-resolved intensity images, and conducting the polarimetric data reduction calculation, a super-resolved polarimetric image is obtained.

The PA-LCoS display used in this work, pictured in Figure 7-14, is a PLUTO SLM distributed by HoloEye Systems with a diagonal display of 1.8 cm, a resolution of 1920x1080 pixels, with a pixel pitch of 8 μm and a fill factor of 87%. To operate with the PA-LCoS in the phase-only regime, the LP_2 is orientated at the same direction than the LC molecules extraordinary axis. Consequently, the two FLC cells are also rotated the same angle to preserve the optimization of the PSA. In Figure 7-15 we include a picture of the super-resolution imaging Stokes polarimeter implemented in our laboratory.

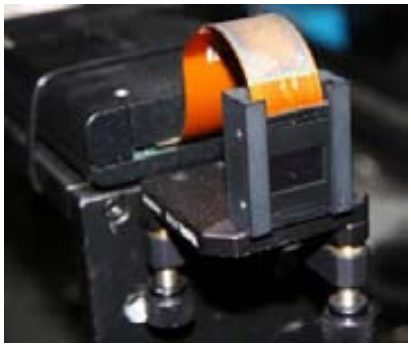

Figure 7-14: PA-LCoS spatial light modulator.

The ideal experimental set-up should use a transmissive liquid crystal display (LCD), avoiding the use of the B-S and its corresponding light losses. However, the available LCD in our laboratory is a PA-LCoS display working in reflection. So, a set-up configuration working in reflection is required. Under this scenario, two possible configurations could be used: a B-S based set-up or an off-axis illumination based set-up. However, the LCD phase modulation range decreases as the incidence angle increases [170], for this reason we have selected the layout of Figure 7-13.

We are looking for the increase of resolution at the image plane, where the pixel size and point spread function (PSF) size are of concern. For the optical imaging system configuration

employed, the PSF is about a quarter of the pixel size. Thus, the spatial resolution of our imaging system is limited by the pixel size of the camera.

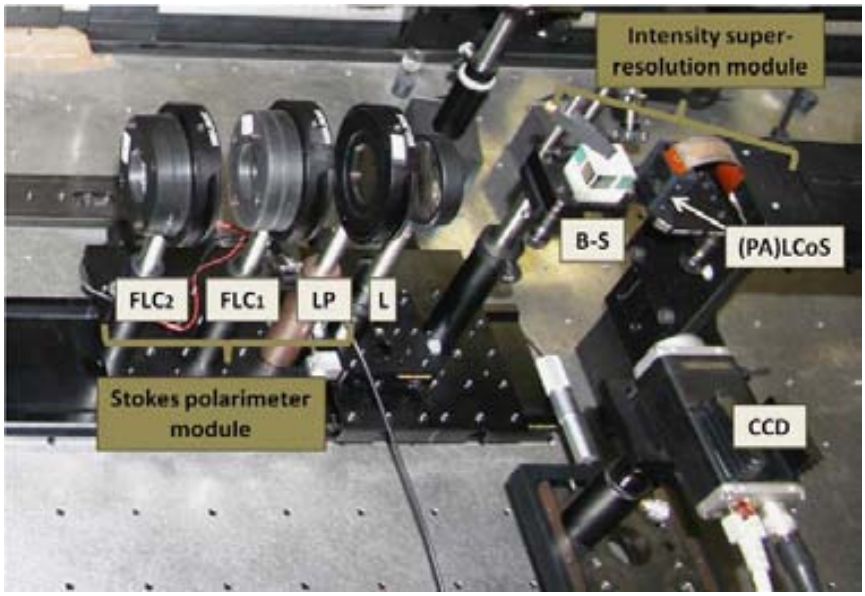

Figure 7-15: Implemented super-resolution imaging Stokes polarimeter.

7.3.2 Super-resolution algorithm

To achieve super-resolved intensity images of a scene by means of the super-resolution module included in Figure 7-13, we apply the imaging super-resolution algorithm described in [171]. This algorithm is suitable for increasing the spatial resolution (SR) of the final scene image when the SR is mainly limited by the CCD pixels dimension. Basically, a linear phase is introduced by the PA-LCoS to shift the image over the CCD plane a sub-pixel distance. To this end, the SLM phase-to-voltage response must be accurately calibrated by following some LCoS display calibration technique [46,172]. In addition, the relationship between the linear phase displayed at the PA-LCoS and the corresponding image displacement produced at the CCD plane must be calibrated as well. Once the sub-pixel displacements are controlled, a set of $n_x \cdot n_y$ sub-pixel 2-D displacements are generated with the SLM, where n_x and n_y are the number of sub-pixel displacements in x and y directions, respectively. In this situation, $n_x \cdot n_y$ images are recorded. The dimension of each raw image is (s_x, s_y). Afterwards, raw images are interlaced in a larger image of dimension $(n_x \cdot s_x,\ n_y \cdot s_y)$. Note that all raw images suffer the intensity spatial average due to the pixel size, causing blurring effect [167,171]. Thus, the final image of larger dimension, created by properly interlacing those raw images, will be consequently affected by the same blurring effect. From a mathematical point of view, the intensity detected by the camera can be described as the convolution of the scene intensity distribution ($I(x,y)$) with the shape of the camera pixel ($p(x,y)$):

$$I_d(x,y) = I(x,y) \otimes p(x,y) \tag{7-2}$$

In order to remove this blurring effect, an inverse filtering process is applied in the frequency domain [173,174]. The goal of the algorithm is to isolate the intensity distribution (*I(x,y)*), eliminating as much as possible the effect of the pixel size (*p(x,y)*). To this aim, we first multiply the Fourier transform (FT) of the intensity detected by the camera ($\tilde{I}_d(u,v)$) with the filter (*f*(*u,v*)), as shown in [171,174]:

$$\tilde{I}_{filtered}(u,v) = \tilde{I}_d(u,v) \cdot f(u,v) = \frac{\tilde{I}_d(u,v)\,\tilde{p}^*(u,v)}{\left|\tilde{p}(u,v)\right|^2 + \sigma}\,, \tag{7-3}$$

where $\tilde{I}_{filtered}(u,v)$ is the FT of the synthesized intensity image of the object, $\tilde{p}^*(u,v)$ and $\left|\tilde{p}(u,v)\right|$ are the complex conjugate and absolute value of the FT of the pixel shape respectively and, σ is a parameter which takes small values and is used to avoid possible zeros at the denominator of Eq. (7-3). In fact, *f*(*u,v*) is the so-called Wiener filter [174], where we have considered that the images are mainly affected by white noise and the constant σ is related with its spectral density. When the spectral density is not known, it is necessary to select a proper value of this constant. If it is too small, the noise will be much amplified, on the contrary when it is too big, the blurring effect is not removed.

Finally, we perform the inverse Fourier transform of $\tilde{I}_{filtered}(u,v)$, obtaining the synthesized intensity image of the object. By applying this technique we are able to obtain super-resolved images of the object due to the blurring effect has been removed to certain extent.

Note that one of the main novelties present in our method lies on not using regular intensity images for the data reduction process (described in section 2.2) but using the high resolved intensity images provided by the super-resolved module present in Figure 7-13. In this way, we apply super-resolved intensity images of the scene for the polarimetric data reduction calculation and consequently, we are able to achieve a final polarimetric image with enhanced spatial resolution. To provide super-resolved images of the scene, we are using the super-resolution algorithm reviewed above. This method is very useful when the main resolution limitation in the system is related to the pixel dimensions of the CCD camera. However, we want to emphasize the potential of including a PA-LCoS display in the proposed set-up. In particular, different super-resolution techniques based on LCoS technology are proposed in the literature [153,175], which are not addressed to detector-limited resolution but to diffraction-limited resolution. Therefore, by conducting some modifications in the super-resolution module in the experimental set-up, the concept of using super-resolved images for polarimetry analysis could be adapted and tested for other origins of the optical system resolution limit.

7.3.3 Calibration

Particularly, in our work the enhanced SR technique is achieved by producing sub-pixel displacements of 1/12 the pixel size in both *x* and *y* directions. We want to note that the timing imaging and processing in our experimental set-up depends on different factors, as the transitory time of the FLC panels, the number of *n* sub-pixels selected, the exposure time of the camera, the number of images to be averaged and the processing time of the computer, among others. For the experimental results provided in this work, none of these parameters have been optimized in terms of time minimization. On the contrary, we have set some security times to ensure a proper synchronization between the FLC panels and the camera, and ultimately a suitable performance for the super-resolution imaging polarimeter. Therefore, the complete measuring and processing time leading to the super-resolved polarimetric images is roughly about 5 minutes. However, if this time needs to be reduced for requirements of a particular application, the number of sub-pixel displacements as well as the others parameters stated above could be optimized.

Some preliminary steps are conducted before testing the SR enhancement in polarimetric images. First, we have used the sequential calibration method, explained in 2.5.1, to determine the polarimetric measurement matrix *W*. Afterwards, our polarimeter is validated by studying its capability of measuring different incident SOPs. In particular, different beams with spatially uniform polarization are generated with the PSG system, and later, measured with the Stokes polarimeter, obtaining a standard deviation smaller than 10^{-3}.

7.3.4 Experimental measurements

Afterwards, the polarimetric system with the intensity super-resolution module is validated by measuring two different spatial resolution tests: the first one has non uniform spatial transmission and uniform polarimetric properties and the second one has uniform transmission but non uniform spatial polarimetric properties.

First, in order to test the spatial resolution enhancement achieved in the intensity content by applying the above described technique, a 1951-USAF resolution target (Newport, model RES-1) was used as amplitude scene. The object consists on several arrangements of 3 horizontal and 3 verticals lines, labeled with a number that sorts them by the spatial frequency of each particular arrangement. The Stokes vector element S_0 (i.e. the total intensity of the beam) obtained with regular imaging is represented in Figure 7-16(a), whereas the counterpart obtained with the enhanced resolution algorithm is shown in Figure 7-16(b). We observe a clear improvement in the spatial resolution in both directions. Focusing on the right side of the images, it is noticeable that the different groups of frequencies not resolved in Figure 7-16(a) are better resolved in Figure 7-16(b). In order to quantitatively demonstrate this improvement, the cross sections of the red

lines marked in Figure 7-16 are represented in Figure 7-17. Comparing both plots present in Figure 7-17, we observe that groups labeled with the number 3, 4 and 5 (circled with dashed lines) when applying the enhanced SR technique (Figure 7-17(b)) are resolved, whereas when applying the regular imaging (Figure 7-17(a)) are not resolved. In particular, the enhanced SR technique reaches to the element 5 (12.70 cycles/mm), whereas the regular technique only reaches to the element 2 (8.98 cycles/mm), leading to an improvement of resolution by a factor of 1.4. Consequently, we assert that the algorithm improves the spatial resolution in intensity images.

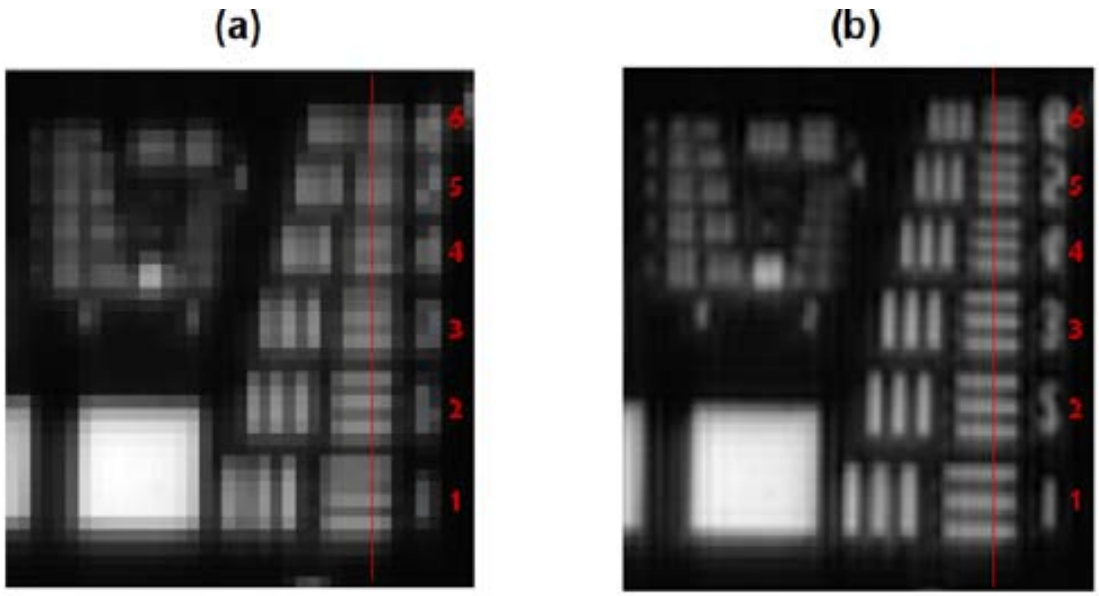

Figure 7-16: S_0 Stokes element of USAF resolution test by applying (a) the regular technique and (b) the enhanced resolution technique. Cross sections of the red lines are plotted in Figure 7-17.

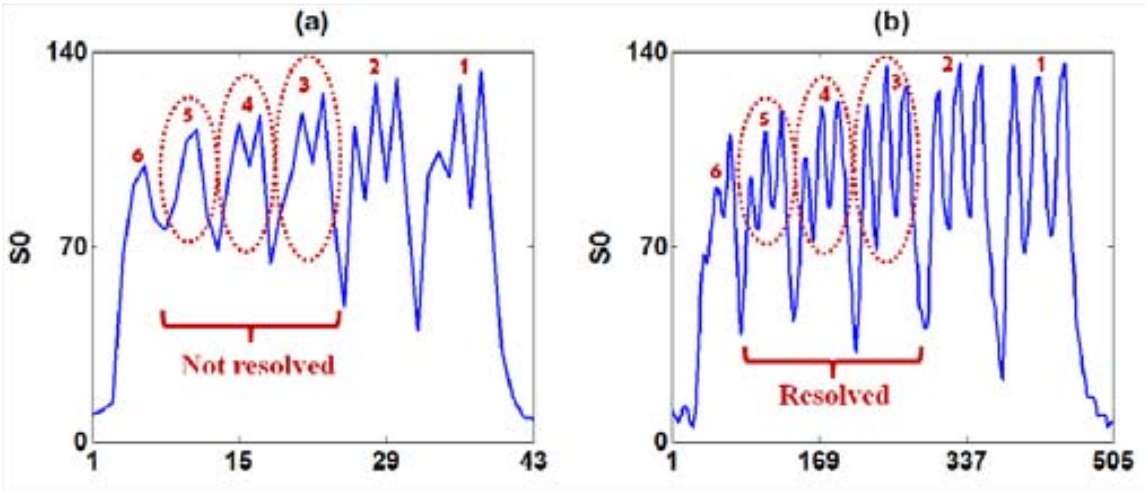

Figure 7-17: Cross section of the S_0 element of the USAF test as function of the y pixel position (red line in Figure 7-16). Experimental data when applying: (a) the regular technique and (b) the enhanced resolution technique.

Second, with the aim of testing the resolution enhancement in polarimetric images, a birefringence resolution target (Thorlabs model NBS 1963A) is used as a scene. It consists on a

birefringent pattern sandwiched between two glass substrates. The pattern includes different groups of birefringent material, each one with different spatial frequencies but with uniform transmission. Each group, sorted in two sets of five horizontal lines and five vertical lines, is labeled with a number referring to the cycles per millimeter.

The Stokes vector of the input object was measured when the scene was illuminated with linearly polarized light. Figure 7-18 shows the Stokes vector elements obtained from regular polarization measurement (Figure 7-18(a,c,e,g)) and from the enhanced SR measurement (Figure 7-18(b,d,f,h)). As expected, the object has uniform S_0, due to the uniform transmission of the pattern. Moreover, it is noticeable that the different frequency groups are only distinguishable through the S_1, S_2 and S_3 channels, because of the non-uniform polarimetric spatial distribution.

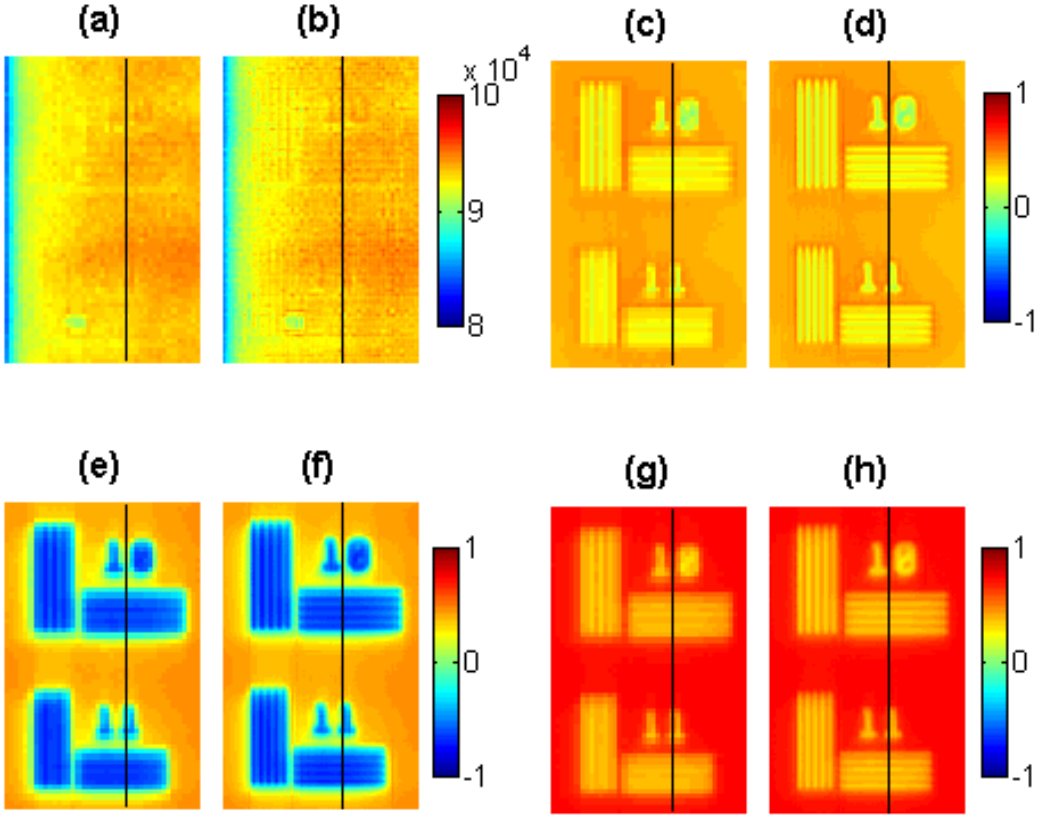

Figure 7-18: Polarization image of a birefringent resolution test obtained by applying the two techniques. Regular resolution Stokes parameters: (a) S_0, (c) S_1, (e) S_2 and (g) S_3. Enhanced resolution Stokes parameters: (b) S_0, (d) S_1, (f) S_2 and (h) S_3. Cross sections of the black lines are plotted in Figure 7-19.

To differentiate polarimetric data from intensity images, as those depicted in Figure 7-16, and to emphasize that the resolution improvement is achieved in polarimetric images, we have used a pseudocolor mapping to show the Stokes elements S_0, S_1, S_2 and S_3. In general, it is observed that the images obtained with the proposed technique offers much better resolution for the Stokes channels than the ones obtained from regular measurements. In order to show in more detail the resolution enhancement in the polarimetric images, the vertical cross sections

corresponding to the black lines marked in Figure 7-18 are plotted in Figure 7-19. Note that cross sections of S_1-S_3 Stokes parameters in Figure 7-19 are zoomed in the y axis including a range of 0.5 (the full Stokes scale goes from -1 up to 1). This is done to better visualize how the different frequency arrangements of interest are resolved by the experimental system.

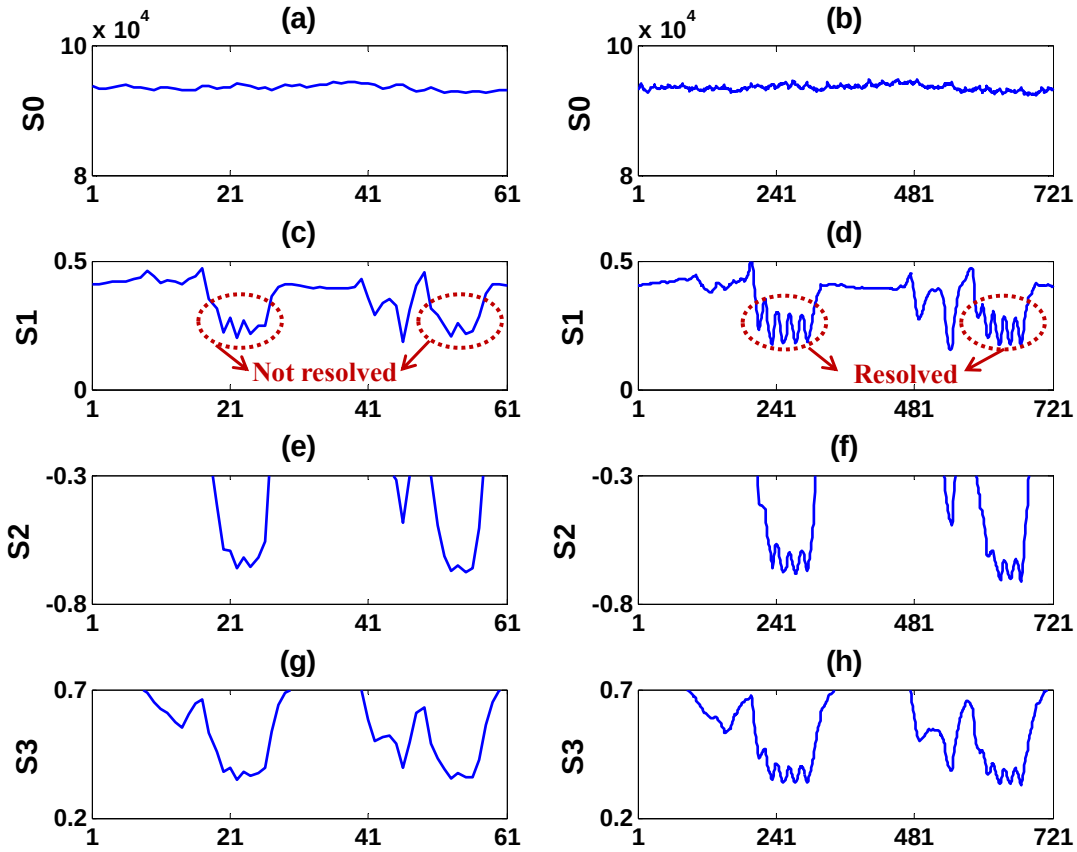

Figure 7-19: Cross section of the birefringent resolution test measurements shown in Figure 7-18. Regular resolution Stokes parameters: (a) S_0, (c) S_1, (e) S_2 and (g) S_3. Enhanced resolution Stokes parameters: (b) S_0, (d) S_1, (f) S_2 and (h) S_3. All Stokes elements are given as function of the y pixel position.

It is observed that Stokes elements S_1, S_2 and S_3 (Figure 7-19(d,f,h), respectively) are much better resolved when applying the super resolution technique than the ones using the regular technique (Figure 7-19(c,e,g), respectively). As an example, the dashed circles plotted in Figure 7-19 point out that whereas the 5 consecutive lines per group are clearly resolved when applying the enhancing SR algorithm (Figure 7-19(d)), they cannot be resolved by applying a regular method (Figure 7-19(c)). Note that Figure 7-18 and Figure 7-19 represent a region of interest of the whole birefringent resolution target. This sample area is selected to highlight the resolution improvement that we have observed between both techniques. When the polarimetric images corresponding to the entire resolution test are analyzed, we observe that the largest resolved frequency in the best case (S_1 channel) reaches 9 cycles/mm for regular imaging, whereas super-resolving imaging reaches 12.5 cycles/mm, leading to an improvement of resolution by a factor of

1.4. Certainly, the polarization measurement with enhanced resolution technique resolves intermediate states of polarization between two birefringent lines, whereas in regular images those zones are not resolved.

Note that S_1 and S_3 channels present better resolution than S_2 channel. This fact may be due to the inhomogenous noise response of the Stokes polarimeter, in agreement with the Stokes variances of S_0, S_1, S_2 and S_3 (1.0, 3.1, 4.9 and 2.1, respectively). Moreover, polarimetric data is given in multichannel images, thus the contrast of these images depend on the channel analyzed, as it can be observed in Figure 7-19. Particularly, S_1 has larger contrast than S_2 and S_3 channels. This contrast not only depends on the original object, but also could depend on the coordinate system chosen to define the state of polarization. In addition, it will depend on the state of polarization of the beam illuminating the scene, which could be also optimized as function of the scene to be measured [176]. This study is an interesting perspective, although it is beyond the scope of this work.

Chapter 8 **Conclusions**

This manuscript gathers the main scientific contributions achieved through the current PhD thesis and framed in the field of the polarimetry. These research achievements have been published in different scientific international journals in the field of Optics [PAPER A- PAPER F], as well as have give rise to the application of a patent [PAPER G].

In the first part of this thesis, we have presented individual exhaustive studies of four different polarimeters based on different materials exhibiting refraction index anisotropy: three types of liquid crystals (parallel aligned nematic, twisted nematic and ferroelectric) and biaxial crystals. All four analyzed polarimeter architectures have in common that they are free of moving elements, avoiding experimental errors such as beam wander or orientational misalignments of the optical elements.

In the second part of this thesis, we provide a comprehensive comparative table between the four analyzed polarimeters as well as a detailed discussion of their specifications, becoming a very valuable summary for all those users who are interested in implementing a polarimeter based on liquid crystals or biaxial crystals. Moreover, it provides a new experimental configuration which combines an imaging Stokes polarimeter with an extra module for overcoming the spatial resolution limit due to the detector geometry and so, leading to polarimetric images with enhanced spatial resolution.

Among the several results provided along this thesis, we emphasize the following main conclusions from each chapter:

Chapter 2:

- It consists of a valuable overview of the mathematical formalism, significant analysis and experimental procedures related to the modeling, optimization and implementation of a polarimeter.
- In particular, we have reviewed the mathematical basics, based on the Mueller-Stokes formalism, used for describing polarimeters, including the measurement principle and data reduction.
- In addition, the importance of an optimization of the system in terms on noise from the detection process is remarked, giving a survey of important figures of merit.
- A general methodology to evaluate the robustness and tolerance performance of polarimeters to a particular architecture is provided.
- Finally, two calibration methodologies are explained to experimentally determine the polarimetric measurement matrix of a polarimeter.

Chapter 3:

- A complete Stokes polarimeter based on two parallel aligned nematic liquid crystal (PA-LC) cells is studied, implemented and discussed. The two PA-LC cells are oriented at 45º and 0º, and their retardances are controlled electronically. This architecture is completely versatile because it allows implementing any polarization analyzer (PA) by addressing the proper pair of voltages to the LC cells.
- It is a time-division polarimeter architecture. We have measured the transitory time of our PA-LC cells and it is around 300 milliseconds.
- We have optimized polarization state analyzers (PSAs) by minimizing the condition number of the system, when different number n of polarizing analyzers (PAs) are used. In particular, we show as when n=4, 6, 8, 12 and 20, the location of the polarization analyzers over the Poincaré sphere corresponds to the vertices of a regular polyhedron with n vertices inscribed in the sphere. All these optimized PSAs have a condition number (CN) of $\sqrt{3}$, the minimum value. However, the equally weighted variance (EWV) of such optimized configurations decreases as the number of PAs increases, revealing the benefit of data redundancy with larger number of PAs. Stokes parameters variances for each optimized PSA are equal, remarking the advantage of distributing equally separated the PAs over the Poincaré sphere. Thus, the optimized PSAs (corresponding to regular polyhedrons) are configurations suitable for measuring an arbitrary polarization.
- Moreover, non-optimized PSAs have been analyzed as well, and we have proved the interest that incomplete polarimeters may present for some particular applications. In

particular, an incomplete polarimeter where the 4 PAs are equally distributed in the S_1-S_2 plane is studied. Because of this particular PSA distribution, the S_1 and S_2 variances of the incomplete polarimeter are smaller than the ones for the optimized polarimeter (i.e. regular tetrahedron), being the former a perfect PSA candidate for measuring light with linear polarization.

- From the robustness study of the different PSAs, we have concluded that: First, as more PAs in the system, more robust becomes the system to small variations from the optimum configurations. Second, an optimization of the PSA gives more stability to the system under these small variations than if the system is non-optimized.
- From the tolerance analysis, we assert that the polarimeter has a larger tolerance on the retardances of the liquid crystals than on the orientation of the optical elements. In particular, for an accuracy in the Stokes vector measurement of 0.02 (1% of the total range), the tolerances of the retardances are 0.89º and 1.15º, and of the orientations are 0.50º and 0.54º, respectively for the first and second PA-LC cells oriented at 45º and 0º.
- Three optimized PSAs are implemented (tetrahedron, dodecahedron and 100PAs), as well as the incomplete polarimeter for linear SOPs. From the calibration of the polarimetric measurement matrix, the experimental CNs are calculated. Experimental CN values of the optimized polarimeters are much closer to the theoretical ones as the number of PAs is larger, experimentally validating the statement of polarimeter robustness linked with the number of PAs.
- The accuracy and repeatability of the three implemented optimized polarimeters (tetrahedron, dodecahedron and 100PAs configuration) is evaluated. The repeatability of the instrument improves as the number n of PAs increases. The standard deviation of the measured Stokes vectors is in the range of: 0.010-0.011 for n=4 (regular tetrahedron), 0.004-0.005 for n=20 (regular dodecahedron) and 0.002-0.003 for n=100PAs. Note that there is a trade-off between duration of the measurement (it increases with n) and the repeatability. The accuracy of the implemented polarimeters is evaluated using a commercial polarimeter as a reference, and it is in the order of the hundredths (0.04 is the maximum Stokes parameter deviation).
- The usefulness of the incomplete polarimeter designed for measuring linear SOPs is tested and compared with the optimized PSA with the same number of PAs (i.e. 4 PAs, corresponding to the regular tetrahedron). The standard deviation of a measured linear polarization state is lower when measuring with the incomplete polarimeter rather than the optimized polarimeter, showing the suitability for measuring specific SOPs with the incomplete polarimeter.

- Finally, we have studied the effect of the sample size on each flux measurement on the standard deviation of the final polarization measurement. As larger the sample size, lower the standard deviation until reaching the sample size value of 500 measurements, where beyond this value the standard deviation remains constant.

Chapter 4:

- A complete Stokes polarimeter based on a single TN-LC cell is proposed. The initial architecture is proposed in normal incidence on the LC cell. We have proposed some modifications on the initial set-up to study the influence of some physical parameters on the polarimeter performance. The idea is to achieve alternative characteristic curves which enlarge the volume enclosed, improving the optimization of the system. First, we impinged the LC cell in oblique angle. Second, we worked on reflection with the LC cell, by means of a reflection on a mirror. Note that in all these three set-ups, light exiting from the TN-LC cell is projected over a linear SOP (using the linear polarizer (LP)). Next, we included an additional quarter waveplate (QWP) in the set-up with the aim of projecting light exiting from the TN-LC cell over an elliptical SOP (using a QWP and a LP). This modification led to corresponding three new architectures.
- Therefore, 6 complete Stokes polarimeters based on a single twisted nematic liquid crystal (TN-LC) cell have been proposed, 5 of them are new architectures. All of them have in common the use of a single off-the-shelf LC cell, leading to interesting advantages such as simplicity, reduced light losses and reduced cost.
- They are time-division polarimeter architectures. We have measured the transitory time of our TN-LC cells and it is around 300 milliseconds.
- We have optimized the 6 different polarimeters by minimizing the EWV. To this aim, two different parameters are revised: first, the orientation of the linear polarizer (and the orientation of the QWP if used) and second, the 4 voltages to be addressed to the LC. The CN for the different configurations achieved has been calculated as well. Whereas the initial set-up (normal incidence) presents a CN of 4.66, the new modified and optimized polarimeters lead to CN values much smaller (smaller than 2.7 in most of the cases). Thus, we have proved that a significant improvement in the minimization of noise propagation is achieved by modifying the optical path, the incidence angle or the projection polarization states. The best optimized polarimeter (CN of 1.98) corresponds to work on reflection and with a QWP, following there are two configurations with the same CN (2.69): first, LC working on reflection but with only the LP and second, normal incidence but including the QWP, being this last one (set-up D) very appealing architecture for implementing due to its simplicity.

- From the robustness study, we reaffirm the statement of more stability as better optimization presents the PSA.
- We have analyzed the influence of the physical parameters of the TN-LC cell (maximum birefringence and twist angle) on the optimization of the polarimeter via numerical simulations. The most suitable TN-LC cell for a polarimeter implementation has a twist angle from 40° to 140°, and a birefringence larger than 200º, although there is no need to be larger than 250° since no improvement in the optimization is observed. Thus, the use of a super-twisted nematic LC cell, to be used for polarimeter implementations, is not required.
- From the tolerance analysis, we assert that TN-LC based polarimeters have a larger tolerance on the retardances of the liquid crystal and of the QWP than on the orientation of the optical elements. Particularly, for the polarimeter using normal incidence to the TN-LC cell and a QWP (set-up D), for an accuracy in the Stokes vector measurement of 0.02 (1% of the total range), the tolerance of the voltage addressed to the LC is of 0.0044V, the WP retardance is 1.69º, the orientation of the linear polarizer is 0.66º and of the QWP is 0.55º.
- The optimized polarimeters have been experimentally implemented and calibrated. Their CN values are very close to the theoretical ones, in particular set-up D reached the CN of 2.64.
- Experimental measurements have been taken for validating their performance under monochromatic light. Concerning the accuracy of the polarimeter, measurements are compared with the values given by a commercial polarimeter, and the differences are in the hundredths (excluding set-up A for a particular measurement). The repeatability of the 6 polarimeters showed the same tendency of the theoretical values of EWV, so experimentally evidencing the improvement achieved in the proposed modifications from respect the initial set-up. In particular, set-up D has a repeatability of 0.002. Moreover, light with a certain degree of polarization (DOP) has been measured as well, obtaining the equivalents results in accuracy and repeatability.
- Finally, experimental measurements have been taken for validating their performance using a light source with a small bandwidth (LED illumination). The polarimeter D have measured fully polarized light and partially polarized, and in both tests excellent results for accuracy (in the hundredths) and repeatability (0.002) have been obtained.

Chapter 5:

- A complete Stokes and Mueller polarimeters based on two and four ferroelectric liquid crystal (FLC) cells have been proposed, respectively.

- Both polarimeters are time-division polarimeters architectures. The transitory time of our FLC cells has been measured, and it is around 0.3 milliseconds. Thus, FLC based polarimeters are appealing instruments for polarimetric applications where fast measurements are required.
- We have applied a minimization of the condition number of the polarimetric measurement matrix. In such way, the optimal values for the optical model, being in this case the orientation of the FLC cells present in the set-up, are determined. We have obtained a CN of 2.22 for Stokes polarimeter and of 5.00 for the Mueller polarimeter.
- From the robustness study, we have observed that both PSA and PSG have similar stability conditions under small deviations with respect to the optimized configurations.
- From the tolerance analysis, we assert that the FLC based polarimeter has a larger tolerance on the retardances than on the orientations and rotations of the FLC cells. In particular, for ensuring an error in the Stokes measurement lower than 0.02, the tolerance of the optical parameters of the FLC panels are restricted to the following values: 1º for the retardance, 0.3º for the orientation of the fast axis and 0.4º-0.6º for the rotation of the fast axis. Moreover, the tolerances for the Mueller polarimeter to get an accuracy of 0.02 are also obtained: 1º-1.3º for the retardance, 0.3º for the orientation of the fast axis and 0.4º-0.6º for the rotation of the fast axis.
- PSA and PSG have been implemented in the laboratory and calibrated. Their experimental CNs are respectively 2.35 and 2.55, close to the values obtained during the optimization.
- Regarding to the repeatability of the implemented Stokes polarimeter, we have observed certain dependence both on room temperature and time of acquisition. The worst repeatability result is in the hundredth, and with the following measurements conditions: without thermal insulation (i.e. through a variation of few degrees Celsius) and during 24 hours of acquisition. However, when the measurements are taken at a fixed room temperature (21.2ºC) the repeatability is significantly improved, reaching the fourth decimal. Therefore, when very sensitive polarimetric measurements are required, a stabilized room temperature is strongly recommended.
- Furthermore, we have presented a set of Stokes vector measurements as function of the speed of taking the measurements (from 500 to 31ms), showing the potential of FLC based polarimeters for fast measurement requirements.
- Finally, the Mueller and Stokes polarimeters are experimentally tested by measuring different polarization states and polarizing samples, and an excellent agreement between experimental and theoretical values are obtained. The maximum difference in the Stokes parameters is of 0.05 and in the Mueller matrix elements of 0.04.

Chapter 6:

- It presents a new tool for Stokes vector metrology by means of analyzing the characteristic intensity pattern associated to the conical refraction (CR) phenomenon occurring in biaxial crystals.
- This idea is developed by proposing a new design of a division of amplitude complete and punctual Stokes polarimeter based on a beam splitter and two biaxial crystals. The set-up requires of two cameras to acquire the intensity distribution along the CR light rings. Although other punctual polarimeters only require one radiometer, this drawback is compensated by the strengths of the CR based polarimeter, namely: no electrical addressing is needed, snapshot polarimeter, static measurements (no moving elements) avoiding misalignments errors and large data redundancy (leading to small variances for the different Stokes channels).
- It is a snapshot Stokes polarimeter, only limited by the exposure time of the camera, and data redundancy can be increased without an increase of the measuring time.
- The optimization of the CR polarimeter performance is conducted by minimizing the CN of the polarimeter. The result of the optimization have led to a CN of 2.00, and it has been shown the suitability of using a QWP before the biaxial crystal in the second arm of the polarimeter with an arbitrary orientation. The orientation of the QWP is optimized in a second step, when considering the B-S as a non ideal element and its Mueller matrix is calibrated.
- In addition, a comprehensive study of the robustness of the CR polarimeter is provided, showing the benefits of including data redundancy to the system, which in these devices can be done without increasing the measuring time.
- From the tolerance analysis, we assert that CR based polarimeters have a larger tolerance on the retardance of the QWP than on the QWP orientation and on the orientation of both rings. In particular, to achieve an accuracy in the Stokes vector measurement of 0.02 (1% of the total range), the tolerance of the QWP orientation is 0.57º, of the QWP retardance is 1.15º and of the rings orientation of 0.57º.
- The CR polarimeter has been experimentally implemented and calibrated. 720 PAs have been used in total, meaning 360 PAs per ring. The CN obtained from the calibration depends on the method of extracting the intensity from the images. When each PA corresponds to a single pixel, the calibration is noisier although the DOPs of the calibrated PAs are much closer to 1 and the CN is 2.11. Whereas when each PA corresponds to an average of pixels along a radius from the center of the ring and with the same azimuth, the calibration is less noisy but their DOP is smaller and the CN is 2.42.

Even though first calibration shows better conditioning, second calibration is preferred because it is more robust to image wander and spurious pixels thanks to the radial means. Moreover, some concerns about the assembling, alignment and calibration are discussed.

- Finally, the capability of the CR polarimeter has been tested by measuring different incident states of polarization, including fully and partially polarized light. The good agreement observed between experimental measurements and theoretical prediction validates the suitability of the CR polarimeter to be used for polarimetric metrology, being the maximum difference in the Stokes parameters of 0.17.

Chapter 7:

- A comprehensive comparative table between the 4 analyzed polarimeters is given, and their specifications and features are broken down into type of polarimeter, equipment needed, cost, transitory time, their capability to be extended to an imaging polarimeter, optimization, robustness, tolerance parameters, accuracy, repeatability, strengths and weaknesses. This gathered information is very valuable as guidelines for all those users who are interested in implementing a polarimeter based on liquid crystals or biaxial crystals.
- The three potential imaging polarimeters (LC based polarimeters) have been evaluated with a decision matrix and a merit function to find the best candidate for implementing an imaging Stokes polarimeter for super-resolution polarization metrology, being the FLC based polarimeter the best option.
- As first step, we have implemented the imaging Stokes polarimeter. The system has been calibrated with a laser and a LED as illumination sources. LED illumination is selected because intensity images are no degraded due to diffraction of impurities.
- Due to polarimetric data is multidimensional, we have proposed to represent three channels in a single synthesized image using the HSV color space: hue (H), saturation (S) and value (V) are encoding azimuth (or ellipticity), DOP and total intensity, respectively.
- Different polarizing samples are measured with the imaging Stokes polarimeter based on FLC cells, and their particular results are described and discussed. In particular, we have showed the potential of sensing the stress birefringence in plastics.
- A new experimental set-up able to obtain super-resolved polarimetric images, when the spatial resolution of the system is limited by the pixel size of the imaging device is presented. The proposed experimental set-up is based on the combination of two main modules: an imaging Stokes polarimeter and an intensity super-resolution module.
- Concerning the intensity super-resolution module, it is based on a parallel aligned liquid crystal on silicon (PA-LCoS) display where different linear phases are addressed. After calibrating the response of the spatial modulator, it is possible to generate sub-pixel

displacements of the image at the CCD plane. By combining a set of shifted images of low resolution and after applying a deconvolution process, a final super-resolved image of larger dimension than the original ones is obtained. The technique leads to a significantly improvement in the spatial resolution of an image when this is limited by the pixel geometry of the CCD camera.

- Our novel approach consists of using the super-resolved intensity images in the polarimetric data reduction calculation, obtaining as a result, polarimetric images with enhanced spatial resolution.
- Different spatial resolution test targets (in amplitude and in birefringence) have been measured. The experimental results show a significant improvement in spatial resolution by a factor of 1.4 for intensity and polarimetric images, when the proposed technique is applied.

List of acronyms

Acronym	Meaning
A/D	Analog to digital
BC	Biaxial crystal
B-S	Beam splitter
CCD	Charge-coupled device
CN	Condition number
CR	Conical refraction
DOP	Degree of polarization
ECM	Eigenvalue calibration method
EWV	Equally weighted variance
FLC	Ferroelectric liquid crystal
FT	Fourier transform
IR	Infrared
ITO	Indium tin oxide
LC	Liquid crystal
LCD	Liquid crystal display
LCVR	Liquid crystal variable retarder
LED	Light emitting diode
LP	Linear polarizer
PA	Polarization analyzer
PA-LC	Parallel aligned liquid crystal
PA-LCoS	Parallel aligned liquid crystal on silicon
PSA	Polarization state analyzer
PSG	Polarization state generator
QI	Quality indicator
QWP	Quarter waveplate
ROI	Region of interest
SLM	Spatial light modulator
SOP	State of polarization
SR	Spatial resolution
SVD	Singular value decomposition
TN-LC	Twisted nematic liquid crystal
WP	Waveplate

List of papers of this doctoral thesis

[PAPER A] A. Peinado, A. Lizana, J. Vidal, C. Iemmi, and J. Campos, "Optimization and performance criteria of a Stokes polarimeter based on two variable retarders," *Opt. Express* **18**(10), 9815–9830 (2010) [doi:10.1364/OE.18.009815].

[PAPER B] A. Peinado, A. Lizana, J. Vidal, C. Iemmi, and J. Campos, "Optimized Stokes polarimeters based on a single twisted nematic liquid-crystal device for the minimization of noise propagation," *Appl. Opt.* **50**(28), 5437–5445 (2011) [doi:10.1364/AO.50.005437].

[PAPER C] A. Peinado, A. Lizana, and J. Campos, "Optimization and tolerance analysis of a polarimeter with ferroelectric liquid crystals," *Appl. Opt.* **52**(23), 5748–5757 (2013) [doi:10.1364/AO.52.005748].

[PAPER D] A. Peinado, A. Lizana, and J. Campos, "Use of ferroelectric liquid crystal panels to control state and degree of polarization in light beams," *Opt. Lett.* **39**(3), 659–662 (2014) [doi:10.1364/OL.39.000659].

[PAPER E] A. Peinado, A. Turpin, A. Lizana, E. Fernández, J. Mompart, and J. Campos, "Conical refraction as a tool for polarization metrology," *Opt. Lett.* **38**(20), 4100–4103 (2013) [doi:10.1364/OL.38.004100].

[PAPER F] A. Peinado, A. Lizana, C. Iemmi, and J. Campos, "Polarization imaging with enhanced spatial resolution," *Optics Communications,* in Press.

[PAPER G] J. Mompart, A. Turpin, T. Kirilov, A. Peinado, A. Lizana, and J. Campos, "A polarimeter based on conical refraction and a method for determining the polarization state of an input electromagnetic radiation," PCT (Patent Cooperation Treaty) application number: PCT/EP2014/065918, 02 August 2013.

Bibliography

[1] D. H. Goldstein, *Polarized Light*, Second, Mercel Dekker, New York (2010).

[2] S. Huard, *Polarisation de la lumière*, Masson, Ed. (1994).

[3] R. Bartholin, *Experimenta Crystalli Islandici disdiaclastici, quibus mira et insolita refractio detegitur*, p. 60 (1669).

[4] R. A. Chipman, "Polarimetry," in *Handbook of Optics*, 2nd ed., McGraw-Hill, New York (1995).

[5] N. Ghosh and I. A. Vitkin, "Tissue polarimetry: concepts, challenges, applications, and outlook," *J. Biomed. Opt.* **16**(11), 110801 (2011) [doi:10.1117/1.3652896].

[6] V. V. Tuchin, L. Wang, and D. A. Zimnyakov, *Optical Polarization in Biomedical Applications*, Springer, New York (2006).

[7] J. M. Bueno and P. Artal, "Double-pass imaging polarimetry in the human eye," *Opt. Lett.* **24**(1), 64 (1999) [doi:10.1364/OL.24.000064].

[8] K. M. Twietmeyer, R. A. Chipman, A. E. Elsner, Y. Zhao, and D. VanNasdale, "Mueller matrix retinal imager with optimized polarization conditions," *Opt. Express* **16**(26), 21339 (2008) [doi:10.1364/OE.16.021339].

[9] O. K. Naoun, V. L. Dorr, P. Allé, J.-C. Sablon, and A.-M. Benoit, "Exploration of the retinal nerve fiber layer thickness by measurement of the linear dichroism," *Appl. Opt.* **44**(33), 7074 (2005) [doi:10.1364/AO.44.007074].

[10] M. Anastasiadou, A. De Martino, D. Clement, F. Liège, B. Laude-Boulesteix, N. Quang, J. Dreyfuss, B. Huynh, A. Nazac, et al., "Polarimetric imaging for the diagnosis of cervical cancer," *Phys. status solidi* **5**(5), 1423–1426 (2008) [doi:10.1002/pssc.200777805].

[11] A. Pierangelo, A. Nazac, A. Benali, P. Validire, H. Cohen, T. Novikova, B. H. Ibrahim, S. Manhas, C. Fallet, et al., "Polarimetric imaging of uterine cervix: a case study," *Opt. Express* **21**(12), 14120–14130 (2013) [doi:10.1364/OE.21.014120].

[12] M.-R. Antonelli, A. Pierangelo, T. Novikova, P. Validire, A. Benali, B. Gayet, and A. De Martino, "Mueller matrix imaging of human colon tissue for cancer diagnostics: how Monte Carlo modeling can help in the interpretation of experimental data," *Opt. Express* **18**(10), 10200–10208 (2010) [doi:10.1364/OE.18.010200].

[13] A. Pierangelo, A. Benali, M.-R. Antonelli, T. Novikova, P. Validire, B. Gayet, and A. De Martino, "Ex-vivo characterization of human colon cancer by Mueller polarimetric imaging," *Opt. Express* **19**(2), 1582–1593 (2011) [doi:10.1364/OE.19.001582].

[14] J. C. Ramella-Roman, D. Duncan, and T. A. Germer, "Out-of-plane polarimetric imaging of skin: surface and subsurface effects," in *Proc. SPIE 5686,* pp. 142–153 (2005) [doi:10.1117/12.592399].

[15] S. L. Jacques, R. Samatham, S. Isenhath, and K. Lee, "Polarized light camera to guide surgical excision of skin cancers," in *Proc. SPIE 6842*, p. 68420I–68420I–7 (2008) [doi:10.1117/12.761823].

[16] W. P. Van De Merwe, D. R. Huffman, and B. V Bronk, "Reproducibility and sensitivity of polarized light scattering for identifying bacterial suspensions," *Appl. Opt.* **28**(23), 5052–5057 (1989) [doi:10.1364/AO.28.005052].

[17] W. S. Bickel and M. E. Stafford, "Polarized light scattering from biological systems: A technique for cell differentiation," *J. Biol. Phys.* **9**(2), 53–66 (1981) [doi:10.1007/BF01987283].

[18] G. L. Coté, M. D. Fox, and R. B. Northrop, "Noninvasive optical polarimetric glucose sensing using a true phase measurement technique," *IEEE Trans. Biomed. Eng.* **39**(7), 752–756 (1992) [doi:10.1109/10.142650].

[19] B. D. Cameron and G. L. Cóte, "Noninvasive glucose sensing utilizing a digital closed-loop polarimetric approach," *IEEE Trans. Biomed. Eng.* **44**(12), 1221–1227 (1997) [doi:10.1109/10.649993].

[20] J. R. Schott, *Fundamentals of Polarimetric Remote Sensing*, SPIE Press, Bellingham (2009).

[21] J. S. Tyo, D. L. Goldstein, D. B. Chenault, and J. A. Shaw, "Review of passive imaging polarimetry for remote sensing applications," *Appl. Opt.* **45**(22), 5453 (2006) [doi:10.1364/AO.45.005453].

[22] P.-Y. Gerligand, M. Smith, and R. Chipman, "Polarimetric images of a cone," *Opt. Express* **4**(10), 420 (1999) [doi:10.1364/OE.4.000420].

[23] T. L. Ainsworth, D. L. Schuler, and J.-S. Lee, "Polarimetric SAR characterization of man-made structures in urban areas using normalized circular-pol correlation coefficients," *Remote Sens. Environ.* **112**(6), 2876–2885 (2008) [doi:10.1016/j.rse.2008.02.005].

[24] F.-M. Breon, D. Tanre, P. Lecomte, and M. Herman, "Polarized reflectance of bare soils and vegetation: measurements and models," *IEEE Trans. Geosci. Remote Sens.* **33**(2), 487–499 (1995) [doi:10.1109/36.377949].

[25] R. Hegedüs, A. Barta, B. Bernáth, V. B. Meyer-Rochow, and G. Horváth, "Imaging polarimetry of forest canopies: how the azimuth direction of the sun, occluded by vegetation, can be assessed from the polarization pattern of the sunlit foliage," *Appl. Opt.* **46**(23), 6019 (2007) [doi:10.1364/AO.46.006019].

[26] G. W. Kattawar, "Genesis and evolution of polarization of light in the ocean," *Appl. Opt.* **52**(5), 940–948 (2013) [doi:10.1364/AO.52.000940].

[27] R. Hegedüs, S. Akesson, and G. Horváth, "Polarization patterns of thick clouds: overcast skies have distribution of the angle of polarization similar to that of clear skies," *J. Opt. Soc. Am. A. Opt. Image Sci. Vis.* **24**(8), 2347–2356 (2007).

[28] T. Sakai, T. Nagai, M. Nakazato, Y. Mano, and T. Matsumura, "Ice Clouds and Asian Dust Studied with Lidar Measurements of Particle Extinction-to-Backscatter Ratio, Particle Depolarization, and Water-Vapor Mixing Ratio over Tsukuba," *Appl. Opt.* **42**(36), 7103 (2003) [doi:10.1364/AO.42.007103].

[29] K. Sassen, "The Polarization Lidar Technique for Cloud Research: A Review and Current Assessment," *Bull. Am. Meteorol. Soc.* **72**(12), 1848–1866 (1991) [doi:10.1175/1520-0477(1991)072<1848:TPLTFC>2.0.CO;2].

[30] F. J. Iannarilli, Jr., H. E. Scott, and S. H. Jones, "Passive IR polarimetric hyperspectral imaging contributions to multisensor humanitarian demining," in *Proc. SPIE 4394,* pp. 346–352 (2001) [doi:10.1117/12.445486].

[31] T. Gehrels, Ed., *Planets, Stars and Nebulae Studied with Photopolarimetry*, University of Arizona Press (1974).

[32] J. C. Kemp, G. D. Henson, C. T. Steiner, and E. R. Powell, "The optical polarization of the Sun measured at a sensitivity of parts in ten million," *Nature* **326**(6110), 270–273 (1987) [doi:10.1038/326270a0].

[33] N. Uribe-Patarroyo, A. Alvarez-Herrero, R. L. Heredero, J. C. del Toro Iniesta, A. C. López Jiménez, V. Domingo, J. L. Gasent, L. Jochum, and V. Martínez Pillet, "IMaX: a polarimeter based on Liquid Crystal Variable Retarders for an aerospace mission," *Phys. Status Solidi* **5**(5), 1041–1045 (2008) [doi:10.1002/pssc.200777771].

[34] J. Tinbergen and F. der W. en Natuurwetenschappen, "Interstellar polarization in the immediate solar neighbourhood," *Astron. Astrophys.* **105**, 53–64 (1982).

[35] J. Greaves, W. Holland, T. Jenness, and T. Hawarden, "Magnetic field surrounding the starburst nucleus of the galaxy M82 from polarized dust emission," *Nature* **404**(6779), 732–733 (2000) [doi:10.1038/35008010].

[36] D. Gisler, H. M. Schmid, C. Thalmann, H. P. Povel, J. O. Stenflo, F. Joos, M. Feldt, R. Lenzen, J. Tinbergen, et al., "CHEOPS/ZIMPOL: a VLT instrument study for the polarimetric search of scattered light from extrasolar planets," in *Proc. SPIE 5492,* pp. 463–474 (2004) [doi:10.1117/12.550366].

[37] S. V. Berdyugina, A. V. Berdyugin, D. M. Fluri, and V. Piirola, "First Detection of Polarized Scattered Light from an Exoplanetary Atmosphere," *Astrophys. J.* **673**(1), L83–L86 (2008) [doi:10.1086/527320].

[38] O. Guyon, G. Schneider, R. Belikov, and D. J. Tenerelli, "The EXoplanetary Circumstellar Environments and Disk Explorer (EXCEDE)," in *Proc. SPIE 8442* (2012).

[39] W. B. Sparks, "A direct way to measure the distances of galaxies," *Astrophys. J.* **433**, 19 (1994) [doi:10.1086/174621].

[40] R. M. A. Azzam and N. M. Bashara, *Ellipsometry and polarized light*, North Holland, Amsterdam (1977).

[41] R. M. A. Azzam, "Mueller-matrix ellipsometry: a review," in *Proc. SPIE 3121,* pp. 396–405 (1997) [doi:10.1117/12.283870].

[42] A. Lizana, M. Foldyna, M. Stchakovsky, B. Georges, D. Nicolas, and E. Garcia-Caurel, "Enhanced sensitivity to dielectric function and thickness of absorbing thin films by combining total internal reflection ellipsometry with standard ellipsometry and reflectometry," *J. Phys. D. Appl. Phys.* **46**(10), 105501 (2013).

[43] J. F. Elman, J. Greener, C. M. Herzinger, and B. Johs, "Characterization of biaxially-stretched plastic films by generalized ellipsometry," *Thin Solid Films* **313-314**, 814–818 (1998) [doi:10.1016/S0040-6090(97)01001-8].

[44] M. Schubert, A. Kasic, T. Hofmann, V. Gottschalch, J. Off, F. Scholz, E. Schubert, H. Neumann, I. J. Hodgkinson, et al., "Generalized ellipsometry of complex mediums in layered systems," in *Proc. SPIE 4806*, pp. 264–276 (2002) [doi:10.1117/12.472993].

[45] N. A. Beaudry, Y. Zhao, and R. Chipman, "Dielectric tensor measurement from a single Mueller matrix image," *J. Opt. Soc. Am. A. Opt. Image Sci. Vis.* **24**(3), 814–824 (2007).

[46] A. Márquez, I. Moreno, C. Iemmi, A. Lizana, J. Campos, and M. J. Yzuel, "Mueller-Stokes characterization and optimization of a liquid crystal on silicon display showing depolarization," *Opt. Express* **16**(3), 1669–1685 (2008) [doi:10.1364/OE.16.001669].

[47] I. Moreno, A. Lizana, J. Campos, A. Márquez, C. Iemmi, and M. J. Yzuel, "Combined Mueller and Jones matrix method for the evaluation of the complex modulation in a liquid-crystal-on-silicon display," *Opt. Lett.* **33**(6), 627 (2008) [doi:10.1364/OL.33.000627].

[48] A. Martínez, N. Beaudoin, I. Moreno, M. D. M. Sánchez-López, and P. Velásquez, "Optimization of the contrast ratio of a ferroelectric liquid crystal optical modulator," *J. Opt. A Pure Appl. Opt.* **8**(11), 1013–1018 (2006) [doi:10.1088/1464-4258/8/11/013].

[49] L. M. S. Aas, P. G. Ellingsen, and M. Kildemo, "Near infra-red Mueller matrix imaging system and application to retardance imaging of strain," *Thin Solid Films* **519**(9), 2737–2741 (2011) [doi:10.1016/j.tsf.2010.12.093].

[50] P. A. Williams, "Rotating-Wave-Plate Stokes Polarimeter for Differential Group Delay Measurements of Polarization-Mode Dispersion," *Appl. Opt.* **38**(31), 6508 (1999) [doi:10.1364/AO.38.006508].

[51] V. Gruev, R. Perkins, and T. York, "CCD polarization imaging sensor with aluminum nanowire optical filters," *Opt. Express* **18**(18), 19087–19094 (2010) [doi:10.1364/OE.18.019087].

[52] F. Gori, "Measuring Stokes parameters by means of a polarization grating," *Opt. Lett.* **24**(9), 584 (1999) [doi:10.1364/OL.24.000584].

[53] A. G. Andreou and Z. K. Kalayjian, "Polarization imaging: principles and integrated polarimeters," *IEEE Sens. J.* **2**(6), 566–576 (2002) [doi:10.1109/JSEN.2003.807946].

[54] M. W. Kudenov, L. Pezzaniti, E. L. Dereniak, and G. R. Gerhart, "Prismatic imaging polarimeter calibration for the infrared spectral region," *Opt. Express* **16**(18), 13720 (2008) [doi:10.1364/OE.16.013720].

[55] R. M. A. Azzam, "Arrangement of four photodetectors for measuring the state of polarization of light," *Opt. Lett.* **10**(7), 309 (1985) [doi:10.1364/OL.10.000309].

[56] G. P. Nordin, J. T. Meier, P. C. Deguzman, and M. W. Jones, "Micropolarizer array for infrared imaging polarimetry," *J. Opt. Soc. Am. A* **16**(5), 1168 (1999) [doi:10.1364/JOSAA.16.001168].

[57] V. L. Gamiz, "Performance of a four-channel polarimeter with low-light-level detection," in *Proc. SPIE 3121*, pp. 35–46 (1997) [doi:10.1117/12.283869].

[58] D. J. Diner, A. Davis, B. Hancock, G. Gutt, R. A. Chipman, and B. Cairns, "Dual-photoelastic-modulator-based polarimetric imaging concept for aerosol remote sensing," *Appl. Opt.* **46**(35), 8428 (2007) [doi:10.1364/AO.46.008428].

[59] A. M. El-Saba, R. M. A. Azzam, and M. A. G. Abushagur, "Parallel-slab division-of-amplitude photopolarimeter," *Opt. Lett.* **21**(21), 1709 (1996) [doi:10.1364/OL.21.001709].

[60] T. Todorov and L. Nikolova, "Spectrophotopolarimeter: fast simultaneous real-time measurement of light parameters," *Opt. Lett.* **17**(5), 358 (1992) [doi:10.1364/OL.17.000358].

[61] R. M. A. Azzam, I. M. Elminyawi, and A. M. El-Saba, "General analysis and optimization of the four-detector photopolarimeter," *J. Opt. Soc. Am. A* **5**(5), 681–689 (1988) [doi:10.1364/JOSAA.5.000681].

[62] R. M. A. Azzam and K. A. Giardina, "Photopolarimeter based on planar grating diffraction," *J. Opt. Soc. Am. A* **10**(6), 1190 (1993) [doi:10.1364/JOSAA.10.001190].

[63] R. M. A. Azzam, "Oscillating-analyzer ellipsometer," *Rev. Sci. Instrum.* **47**(5), 624 (1976) [doi:10.1063/1.1134702].

[64] R. M. A. Azzam and A. De, "Optimal beam splitters for the division-of-amplitude photopolarimeter," *J. Opt. Soc. Am. A* **20**(5), 955 (2003) [doi:10.1364/JOSAA.20.000955].

[65] O. Arteaga, J. Freudenthal, B. Wang, and B. Kahr, "Mueller matrix polarimetry with four photoelastic modulators: theory and calibration," *Appl. Opt.* **51**(28), 6805 (2012) [doi:10.1364/AO.51.006805].

[66] R. M. A. Azzam, "Photopolarimetric measurement of the Mueller matrix by Fourier analysis of a single detected signal," *Opt. Lett.* **2**(6), 148 (1978) [doi:10.1364/OL.2.000148].

[67] M. W. Kudenov, M. J. Escuti, N. Hagen, E. L. Dereniak, and K. Oka, "Snapshot imaging Mueller matrix polarimeter using polarization gratings," *Opt. Lett.* **37**(8), 1367–1369 (2012) [doi:10.1364/OL.37.001367].

[68] M. H. Smith, "Optimization of a Dual-Rotating-Retarder Mueller Matrix Polarimeter," *Appl. Opt.* **41**(13), 2488 (2002) [doi:10.1364/AO.41.002488].

[69] E. Garcia-Caurel, A. De Martino, and B. Drevillon, "A broadband ellipsometer/polarimeter system," EP1963822 A1 (2008).

[70] E. Garcia-Caurel, A. De Martino, and B. Drévillon, "Spectroscopic Mueller polarimeter based on liquid crystal devices," *Thin Solid Films* **455-456**, 120–123 (2004) [doi:10.1016/j.tsf.2003.12.056].

[71] R. C. Thompson, J. R. Bottiger, and E. S. Fry, "Measurement of polarized light interactions via the Mueller matrix," *Appl. Opt.* **19**(8), 1323–1332 (1980) [doi:10.1364/AO.19.001323].

[72] F. Delplancke, "Automated high-speed Mueller matrix scatterometer," *Appl. Opt.* **36**(22), 5388 (1997) [doi:10.1364/AO.36.005388].

[73] L. Gendre, A. Foulonneau, and L. Bigué, "Imaging linear polarimetry using a single ferroelectric liquid crystal modulator," *Appl. Opt.* **49**(25), 4687 (2010) [doi:10.1364/AO.49.004687].

[74] D. W. Thompson and B. D. Johs, "Infrared ellipsometer/polarimeter system, method of calibration, and use thereof," US5706212 A, US (1998).

[75] L. L. Deibler and M. H. Smith, "Measurement of the Complex Refractive Index of Isotropic Materials with Mueller Matrix Polarimetry," *Appl. Opt.* **40**(22), 3659 (2001) [doi:10.1364/AO.40.003659].

[76] G. Corti and M. Romoli, "Characterization of Materials for a Vacuum-Ultraviolet Polarization Analyzer," *Appl. Opt.* **42**(19), 3950 (2003) [doi:10.1364/AO.42.003950].

[77] L. B. Wolff, "Polarization camera for computer vision with a beam splitter," *J. Opt. Soc. Am. A* **11**(11), 2935 (1994) [doi:10.1364/JOSAA.11.002935].

[78] G. Myhre, W.-L. Hsu, A. Peinado, C. LaCasse, N. Brock, R. A. Chipman, and S. Pau, "Liquid crystal polymer full-stokes division of focal plane polarimeter," *Opt. Express* **20**(25), 27393 (2012) [doi:10.1364/OE.20.027393].

[79] A. Ambirajan, "Optimum angles for a polarimeter: part I," *Opt. Eng.* **34**(6), 1651 (1995) [doi:10.1117/12.202093].

[80] A. Ambirajan, "Optimum angles for a polarimeter: part II," *Opt. Eng.* **34**(6), 1656 (1995) [doi:10.1117/12.202098].

[81] D. H. Goldstein and R. A. Chipman, "Error analysis of a Mueller matrix polarimeter," *J. Opt. Soc. Am. A* **7**(4), 693 (1990) [doi:10.1364/JOSAA.7.000693].

[82] M. H. Smith, J. B. Woodruff, and J. D. Howe, "Beam wander considerations in imaging polarimetry," in *Proc. SPIE 3754,* pp. 50–54 (1999) [doi:10.1117/12.366359].

[83] E. Compain and B. Drevillon, "High-frequency modulation of the four states of polarization of light with a single phase modulator," *Rev. Sci. Instrum.* **69**(4), 1574 (1998) [doi:10.1063/1.1148811].

[84] S. J. Woltman, G. D. Jay, and G. P. Crawford, *Liquid Crystals: Frontiers in Biomedical Applications*, World Scientific Publishing Company, London (2007).

[85] S.-T. Wu and D.-K. Yang, *Fundamentals of Liquid Crystal Devices*, Wiley, England (2006).

[86] H. Kawamoto, "The history of liquid-crystal displays," *Proc. IEEE* **90**(4), 460–500 (2002) [doi:10.1109/JPROC.2002.1002521].

[87] B. E. A. Saleh and K. Lu, "Theory and design of the liquid crystal TV as an optical spatial phase modulator," *Opt. Eng.* **29**(3), 240–246 (1990) [doi:10.1117/12.55584].

[88] C. Soutar and K. Lu, "Determination of the physical properties of an arbitrary twisted-nematic liquid crystal cell," *Opt. Eng.* **33**(8), 2704–2712 (1994) [doi:10.1117/12.173544].

[89] J. A. Coy, M. Zaldarriaga, D. F. Grosz, and O. E. Martínez, "Characterization of a liquid crystal television as a programmable spatial light modulator," *Opt. Eng.* **35**(1), 15–19 (1996) [doi:10.1117/1.600886].

[90] A. Máquez, J. Campos, M. J. Yzuel, I. Moreno, J. A. Davis, C. Iemmi, A. Moreno, and A. Robert, "Characterization of edge effects in twisted nematic liquid crystal displays," *Opt. Eng.* **39**(12), 3301–3307 (2000) [doi:10.1117/1.1321197].

[91] J. L. Pezzaniti and R. A. Chipman, "Phase-only modulation of a twisted nematic liquid-crystal TV by use of the eigenpolarization states," *Opt. Lett.* **18**(18), 1567 (1993) [doi:10.1364/OL.18.001567].

[92] J. A. Davis, I. Moreno, and P. Tsai, "Polarization Eigenstates for Twisted-Nematic Liquid-Crystal Displays," *Appl. Opt.* **37**(5), 937–945 (1998) [doi:10.1364/AO.37.000937].

[93] S. Pirkl and M. Glogarova, "Ferroelectric Liquid Crystals with High Spontaneous Polarization," in *Ferroelectr. - Phys. Eff.*, Mickaël Lallart, Ed., InTech (2011) [doi:10.5772/942].

[94] L. B. Wolff and T. A. Mancini, "Liquid crystal polarization camera," in *Proc. IEEE Work. Appl. Comput. Vis.*, pp. 120–127 (1992) [doi:10.1109/ACV.1992.240320].

[95] L. B. Wolff and A. G. Andreou, "Polarization camera sensors," *Image Vis. Comput.* **13**(6), 497–510 (1995) [doi:10.1016/0262-8856(95)94383-B].

[96] L. B. Wolff, T. A. Mancini, P. Pouliquen, and A. G. Andreou, "Liquid crystal polarization camera," *IEEE Trans. Robot. Autom.* **13**(2), 195–203 (1997) [doi:10.1109/70.563642].

[97] S. Blakeney, S. Day, and J. Stewart, "Determination of unknown input polarisation using a twisted nematic liquid crystal display with fixed components," *Opt. Commun.* **214**, 1–8, (2002).

[98] J. S. Tyo, "Noise equalization in Stokes parameter images obtained by use of variable-retardance polarimeters," *Opt. Lett.* **25**(16), 1198–1200 (2000) [doi:10.1364/OL.25.001198].

[99] J. S. Tyo, "Design of Optimal Polarimeters: Maximization of Signal-to-Noise Ratio and Minimization of Systematic Error," *Appl. Opt.* **41**(4), 619 (2002) [doi:10.1364/AO.41.000619].

[100] J. S. Tyo and T. S. Turner, Jr., "Imaging spectropolarimeters for use in visible and infrared remote sensing," in *Proc. SPIE 3753*, pp. 214–224 (1999) [doi:10.1117/12.366312].

[101] A. De Martino, Y.-K. Kim, E. Garcia-Caurel, B. Laude, and B. Drévillon, "Optimized Mueller polarimeter with liquid crystals," *Opt. Lett.* **28**(8), 616 (2003) [doi:10.1364/OL.28.000616].

[102] A. De Martino, E. Garcia-Caurel, B. Laude, and B. Drévillon, "General methods for optimized design and calibration of Mueller polarimeters," *Thin Solid Films* **455-456**, 112–119 (2004) [doi:10.1016/j.tsf.2003.12.052].

[103] F. Goudail, P. Terrier, Y. Takakura, L. Bigué, F. Galland, and V. DeVlaminck, "Target Detection with a Liquid-Crystal-Based Passive Stokes Polarimeter," *Appl. Opt.* **43**(2), 274 (2004) [doi:10.1364/AO.43.000274].

[104] N. J. Pust and J. A. Shaw, "Dual-field imaging polarimeter using liquid crystal variable retarders," *Appl. Opt.* **45**(22), 5470 (2006) [doi:10.1364/AO.45.005470].

[105] J. Zallat, A. S, and M. P. Stoll, "Optimal configurations for imaging polarimeters: impact of image noise and systematic errors," *J. Opt. A Pure Appl. Opt.* **8**(9), 807–814 (2006) [doi:10.1088/1464-4258/8/9/015].

[106] K. M. Twietmeyer and R. A. Chipman, "Optimization of Mueller matrix polarimeters in the presence of error sources," *Opt. Express* **16**(15), 11589 (2008) [doi:10.1364/OE.16.011589].

[107] A. M. Gandorfer, "Ferroelectric retarders as an alternative to piezoelastic modulators for use in solar Stokes vector polarimetry," *Opt. Eng.* **38**(8), 1402 (1999) [doi:10.1117/1.602183].

[108] L. M. S. Aas, P. G. Ellingsen, M. Kildemo, and M. Lindgren, "Dynamic response of a fast near infra-red Mueller matrix ellipsometer," *J. Mod. Opt.* **57**(17), 1603–1610 (2010) [doi:10.1080/09500340.2010.515750].

[109] L. Gendre, A. Foulonneau, and L. Bigué, "Full Stokes polarimetric imaging using a single ferroelectric liquid crystal device," *Opt. Eng.* **50**(8), 081209 (2011) [doi:10.1117/1.3570665].

[110] M. V. Berry and M. R. Jeffrey, "Conical diffraction: Hamilton's diabolical point at the heart of crystal optics," in *Prog. Opt.* **50**, pp. 13–50, Elsevier, Bristol (2007) [doi:10.1016/S0079-6638(07)50002-8].

[111] M. Born and E. Wolf, *Principles of Optics*, 7th ed., Cambridge University Press, London (1999).

[112] T. K. Kalkandjiev and M. A. Bursukova, "Conical refraction: an experimental introduction," in *Proc. SPIE 6994*, p. 69940B (2008) [doi:10.1117/12.780793].

[113] A. Turpin, V. Shvedov, C. Hnatovsky, Y. V Loiko, J. Mompart, and W. Krolikowski, "Optical vault: a reconfigurable bottle beam based on conical refraction of light," *Opt. Express* **21**(22), 26335–26340 (2013) [doi:10.1364/OE.21.026335].

[114] R. C. Jones, "A New Calculus for the Treatment of Optical Systems," *J. Opt. Soc. Am.* **31**(7), 488 (1941) [doi:10.1364/JOSA.31.000488].

[115] D. W. Berreman, "Optics in Stratified and Anisotropic Media: 4 × 4-Matrix Formulation," *J. Opt. Soc. Am.* **62**(4), 502 (1972) [doi:10.1364/JOSA.62.000502].

[116] N. Wiener, "Generalized harmonic analysis," *Acta Math.* **55**(1), 117–258 (1930) [doi:10.1007/BF02546511].

[117] E. Wolf, "Optics in terms of observable quantities," *Nuovo Cim.* **12**(6), 884–888 (1954) [doi:10.1007/BF02781855].

[118] G. G. Stokes, "On the composition and resolution of streams of polarized light from different sources," *Trans. Cambridge Philos. Soc.* **9**, 399–416 (1852).

[119] H. Mueller, "The foundation of optics," *J. Opt. Soc. Am.* **38**(7), 661 (1948).

[120] N. G. Parke, "Optical algebra," *J. Math. Phys.* **28**, 131–139 (1949).

[121] H. Poincaré, *Traite de la lumiere*, p. 165, Paris (1892).

[122] J. J. E. B. Gil, "Obtainment of the polarizing and retardation parameters of a non-depolarizing optical system from the polar decomposition of its Mueller matrix," *Optik (Stuttg)* **76**(2), 67–71 (1987).

[123] Z.-F. Xing, "On the Deterministic and Non-deterministic Mueller Matrix," *J. Mod. Opt.* **39**(3), 461–484, (1992) [doi:10.1080/09500349214550471].

[124] S.-Y. Lu and R. A. Chipman, "Interpretation of Mueller matrices based on polar decomposition," *J. Opt. Soc. Am. A* **13**(5), 1106 (1996) [doi:10.1364/JOSAA.13.001106].

[125] D. S. Sabatke, M. R. Descour, E. L. Dereniak, W. C. Sweatt, S. A. Kemme, and G. S. Phipps, "Optimization of retardance for a complete Stokes polarimeter," *Opt. Lett.* **25**(11), 802–804 (2000) [doi:10.1364/OL.25.000802].

[126] F. Goudail, "Noise minimization and equalization for Stokes polarimeters in the presence of signal-dependent Poisson shot noise," *Opt. Lett.* **34**(5), 647–649 (2009) [doi:10.1364/OL.34.000647].

[127] D. Lara and C. Paterson, "Stokes polarimeter optimization in the presence of shot and gaussian noise," *Opt. Express* **17**(23), 21240 (2009) [doi:10.1364/OE.17.021240].

[128] G. Anna and F. Goudail, "Optimal Mueller matrix estimation in the presence of Poisson shot noise," *Opt. Express* **20**(19), 21331–21340 (2012) [doi:10.1364/OE.20.021331].

[129] D. S. Sabatke, A. M. Locke, M. R. Descour, W. C. Sweatt, J. P. Garcia, E. L. Dereniak, S. A. Kemme, and G. S. Phipps, "Figures of merit for complete Stokes polarimeter optimization," in *Proc. SPIE 4133,* pp. 75-81 (2000) [doi:10.1117/12.406613].

[130] M. R. Foreman, C. Macias Romero, and P. Török, "A priori information and optimisation in polarimetry," *Opt. Express* **16**(19), 15212 (2008) [doi:10.1364/OE.16.015212].

[131] E. Chironi and C. Iemmi, "Bounding the relative errors associated with a complete Stokes polarimeter," *J. Opt. Soc. Am. A. Opt. Image Sci. Vis.* **31**(1), 75–80 (2014) [doi:10.1364/JOSAA.31.000075].

[132] P. Taylor, *Theory and Applications of Numerical Analysis*, 2nd ed., Academic Press, London (1996).

[133] G. E. Forsythe, M. A. Malcolm, and C. B. Moler, *Computer Methods for Mathematical Computations*, 1st ed., Prentice Hall, New Jersey (1977).

[134] P. Li and J. S. Tyo, "Experimental measurement of optimal polarimeter systems," in *Proc. SPIE 5158,* pp. 103–112 (2003) [doi:10.1117/12.507165].

[135] H. Dong, P. Shum, Y. Gong, and Q. Sun, "Measurement errors induced by retardance deviation in a rotatable retarder fixed polarizer Stokes polarimeter," *Opt. Eng.* **51**(3), 033001 (2012) [doi:10.1117/1.OE.51.3.033001].

[136] J. S. Tyo and H. Wei, "Optimizing imaging polarimeters constructed with imperfect optics," *Appl. Opt.* **45**(22), 5497 (2006) [doi:10.1364/AO.45.005497].

[137] E. Compain, S. Poirier, and B. Drevillon, "General and self-consistent method for the calibration of polarization modulators, polarimeters, and mueller-matrix ellipsometers," *Appl. Opt.* **38**(16), 3490–3502 (1999) [doi:10.1364/AO.38.003490].

[138] Y. Zhang, H. Zhao, and N. Li, "Polarization calibration with large apertures in full field of view for a full Stokes imaging polarimeter based on liquid-crystal variable retarders," *Appl. Opt.* **52**(6), 1284–1292 (2013) [doi:10.1364/AO.52.001284].

[139] B. Boulbry, J. C. Ramella-Roman, and T. A. Germer, "Improved method for calibrating a Stokes polarimeter," *Appl. Opt.* **46**(35), 8533–8541 (2007) [doi:10.1364/AO.46.008533].

[140] S. Davis, R. Uberna, and R. Herke, "Retardance sweep polarimeter and method," in *US Pat. 6,744,509* **2**(12), United States (2004).

[141] S. Stallinga, "Equivalent retarder approach to reflective liquid crystal displays," *J. Appl. Phys.* **86**(9), 4756–4766 (1999) [doi:10.1063/1.371440].

[142] J. Davis, D. Allison, K. D'Nelly, M. Wilson, and I. Moreno, "Ambiguities in measuring the physical parameters for twisted-nematic liquid crystal spatial light modulators," *Opt. Eng.* **38**(4), 705–709 (1999) [doi:10.1117/1.602113].

[143] J. M. Bennett, "Polarizers," in *Handb. Opt.*, 3rd ed., M. Bass, Ed., pp. 3.1–3.70, McGraw-Hill, New York (2010).

[144] A. Turpin, Y. V. Loiko, T. K. Kalkandjiev, and J. Mompart, "Multiple rings formation in cascaded conical refraction," *Opt. Lett.* **38**(9), 1455 (2013) [doi:10.1364/OL.38.001455].

[145] R. T. Darcy, D. McCloskey, K. E. Ballantine, B. D. Jennings, J. G. Lunney, P. R. Eastham, and J. F. Donegan, "White light conical diffraction," *Opt. Express* **21**(17), 20394–20403 (2013) [doi:10.1364/OE.21.020394].

[146] S. Aïnouz, J. Zallat, A. de Martino, and C. Collet, "Physical interpretation of polarization-encoded images by color preview," *Opt. Express* **14**(13), 5916–5927 (2006) [doi:10.1364/OE.14.005916].

[147] Z. Zalevsky and D. Mendlovic, *Optical Superresolution*, Springer, New York (2003).

[148] A. Tatem, "Super-resolution land cover pattern prediction using a Hopfield neural network," *Remote Sens. Environ.* **79**(1), 1–14 (2002) [doi:10.1016/S0034-4257(01)00229-2].

[149] H. Greenspan, "Super-Resolution in Medical Imaging," *Comput. J.* **52**(1), 43–63, Oxford University Press (2008) [doi:10.1093/comjnl/bxm075].

[150] W. Lukosz, "Optical Systems with Resolving Powers Exceeding the Classical Limit," *J. Opt. Soc. Am.* **56**(11), 1463–1471 (1966) [doi:10.1364/JOSA.56.001463].

[151] W. Lukosz, "Optical Systems with Resolving Powers Exceeding the Classical Limit II," *J. Opt. Soc. Am.* **57**(7), 932–939 (1967) [doi:10.1364/JOSA.57.000932].

[152] V. Mico, Z. Zalevsky, P. Garcia-Martinez, and J. Garcia, "Single-step superresolution by interferometric imaging," *Opt. Express* **12**(12), 2589 (2004) [doi:10.1364/OPEX.12.002589].

[153] A. Hussain, J. L. Martínez, A. Lizana, and J. Campos, "Super resolution imaging achieved by using on-axis interferometry based on a Spatial Light Modulator," *Opt. Express* **21**(8), 9615–9623 (2013) [doi:10.1364/OE.21.009615].

[154] A. Calabuig, V. Micó, J. Garcia, Z. Zalevsky, and C. Ferreira, "Single-exposure super-resolved interferometric microscopy by red-green-blue multiplexing," *Opt. Lett.* **36**(6), 885–887 (2011) [doi:10.1364/OL.36.000885].

[155] R. D. Fiete, "Image quality and λfn/p for remote sensing systems," *Opt. Eng.* **38**(7), 1229–1240 (1999) [doi:10.1117/1.602169].

[156] Sung Cheol Park, Min Kyu Park, and Moon Gi Kang, "Super-resolution image reconstruction: a technical overview," *IEEE Signal Process. Mag.* **20**(3), 21–36 (2003) [doi:10.1109/MSP.2003.1203207].

[157] A. F. Hook and R. N. Hook, "Novel image-reconstruction method applied to deep Hubble space telescope images," in *Proc. SPIE 3164*, pp. 120–125 (1997) [doi:10.1117/12.292751].

[158] M. S. Alam, J. G. Bognar, S. Cain, and B. J. Yasuda, "Fast Registration and Reconstruction of Aliased Low-Resolution Frames By Use of a Modified Maximum-Likelihood Approach," *Appl. Opt.* **37**(8), 1319 (1998) [doi:10.1364/AO.37.001319].

[159] S. Farsiu, M. D. Robinson, M. Elad, and P. Milanfar, "Fast and Robust Multiframe Super Resolution," *IEEE Trans. Image Process.* **13**(10), 1327–1344 (2004) [doi:10.1109/TIP.2004.834669].

[160] H. Stark and P. Oskoui, "High-resolution image recovery from image-plane arrays, using convex projections," *J. Opt. Soc. Am. A* **6**(11), 1715 (1989) [doi:10.1364/JOSAA.6.001715].

[161] A. M. Tekalp, M. K. Ozkan, and M. I. Sezan, "High-resolution image reconstruction from lower-resolution image sequences and space-varying image restoration," in *Proc. IEEE Int. Conf. Acoust. Speech, Signal Process.* **3**, pp. 169–172 vol.3, IEEE (1992) [doi:10.1109/ICASSP.1992.226249].

[162] H. Ur and D. Gross, "Improved resolution from subpixel shifted pictures," *CVGIP Graph. Model. Image Process.* **54**(2), 181–186 (1992) [doi:10.1016/1049-9652(92)90065-6].

[163] T. Komatsu, K. Aizawa, T. Igarashi, and T. Saito, "Signal-processing based method for acquiring very high resolution images with multiple cameras and its theoretical analysis," *Commun. Speech Vision, IEE Proc. I* **140**(1), 19–24 (1993).

[164] P. Cheeseman, B. Kanefsky, R. Kraft, J. Stutz, and R. Hanson, "Super-Resolved Surface Reconstruction from Multiple Images," in *Maximum Entropy and Bayesian Methods*, G. R. Heidbreder, Ed., pp. 293–308, Springer Netherlands, Dordrecht (1996) [doi:10.1007/978-94-015-8729-7].

[165] R. C. Hardie, K. J. Barnard, and E. E. Armstrong, "Joint MAP registration and high-resolution image estimation using a sequence of undersampled images," *IEEE Trans. image Process.* **6**(12), 1621–1633 (1997) [doi:10.1109/83.650116].

[166] J. Solomon, Z. Zalevsky, and D. Mendlovic, "Geometric Superresolution by Code Division Multiplexing," *Appl. Opt.* **44**(1), 32 (2005) [doi:10.1364/AO.44.000032].

[167] A. Shemer, D. Mendlovic, Z. Zalevsky, J. Garcia, and P. Garcia Martinez, "Superresolving Optical System with Time Multiplexing and Computer Decoding," *Appl. Opt.* **38**(35), 7245 (1999) [doi:10.1364/AO.38.007245].

[168] A. Borkowski, Z. Zalevsky, and B. Javidi, "Geometrical superresolved imaging using nonperiodic spatial masking," *J. Opt. Soc. Am. A* **26**(3), 589 (2009) [doi:10.1364/JOSAA.26.000589].

[169] A. Pierangelo, S. Manhas, A. Benali, C. Fallet, J.-L. Totobenazara, M.-R. Antonelli, T. Novikova, B. Gayet, A. De Martino, et al., "Multispectral Mueller polarimetric imaging detecting residual cancer and cancer regression after neoadjuvant treatment for colorectal carcinomas," *J. Biomed. Opt.* **18**(4), 046014 (2013) [doi:10.1117/1.JBO.18.4.046014].

[170] A. Lizana, N. Martín, M. Estapé, E. Fernández, I. Moreno, A. Márquez, C. Iemmi, J. Campos, and M. J. Yzuel, "Influence of the incident angle in the performance of Liquid Crystal on Silicon displays," *Opt. Express* **17**(10), 8491–8505 (2009) [doi:10.1364/OE.17.008491].

[171] M. Sohail, A. Lizana, and J. Campos, "Super-resolution imaging technique based on a Liquid Crystal on Silicon display: increase of Charge-Coupled Device resolution limit," *Óptica Pura y Apl.* **46**(3), 223–230 (2013).

[172] C. Ramirez, B. Karakus, A. Lizana, and J. Campos, "Polarimetric method for liquid crystal displays characterization in presence of phase fluctuations," *Opt. Express* **21**(3), 3182–3192 (2013) [doi:10.1364/OE.21.003182].

[173] J. C. Russ, *The Image Processing Handbook*, CRC Press, Boca Raton (2011).

[174] R. C. Gonzalez and R. E. Woods, *Digital Image Processing*, 3rd ed., Prentice Hall, New Jersey (2008).

[175] A. Hussain, J. L. Martinez, and J. Campos, "Holographic superresolution using spatial light modulator," *J. Eur. Opt. Soc. Rapid Publ.* **8**, 13007 (2013) [doi:10.2971/jeos.2013.13007].

[176] F. Goudail, "Optimization of the contrast in active Stokes images," *Opt. Lett.* **34**(2), 121 (2009) [doi:10.1364/OL.34.000121].